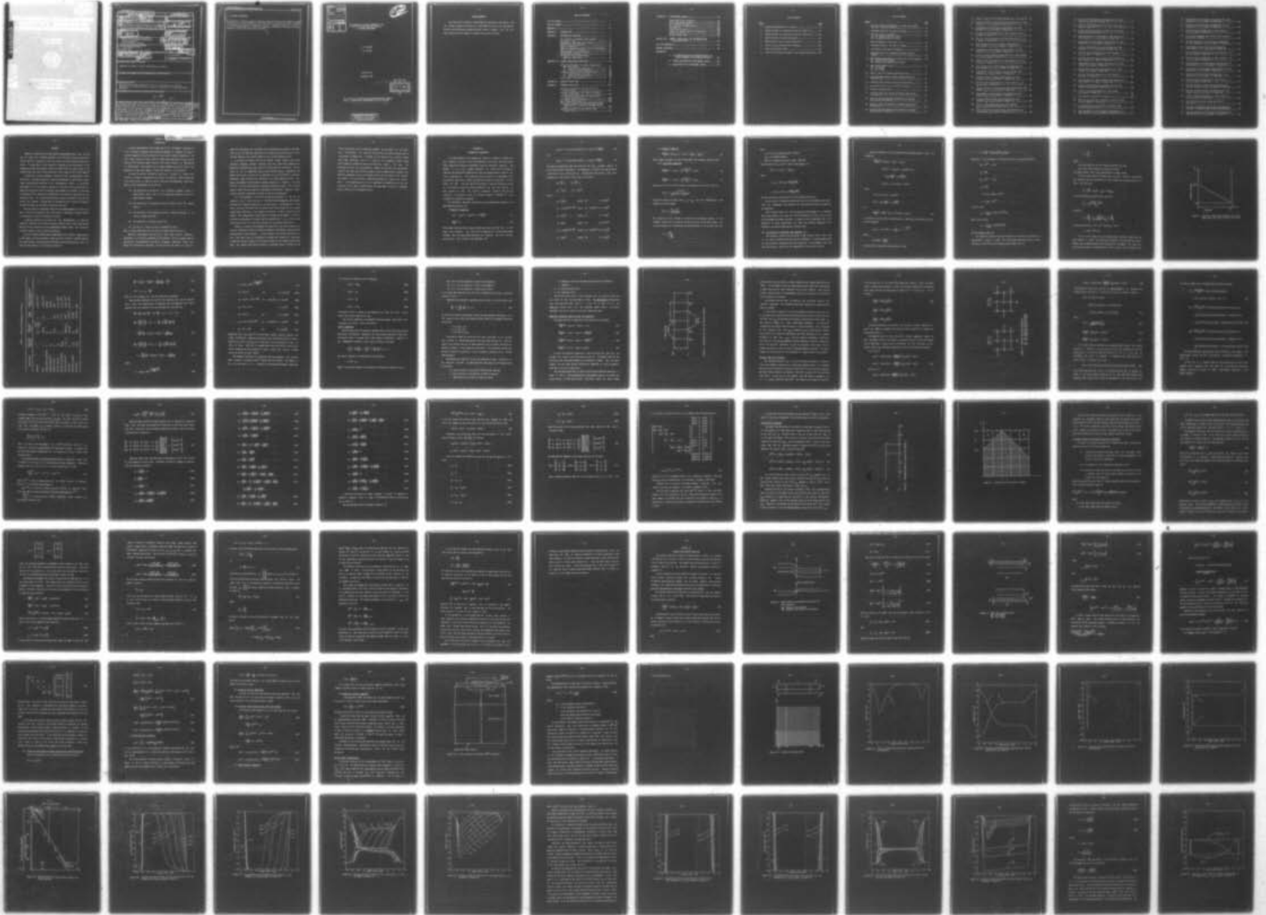
AD-A053 539 PURDUE UNIV LAFAYETTE IND SCHOOL OF ELECTRICAL ENGI--ETC F/G 9/1
THE ANOMALOUS VOLTAGE RESPONSE OF THE P(+)N-N(+) DEVICE AND ITS--ETC(U)
DEC 77 G W NEUDECK, L R RAZOUK DAAG29-77-G-0191
UNCLASSIFIED TR-EE-77-40 ARO-15322.1-A-EL NL
1 OF 3
AD
A053539

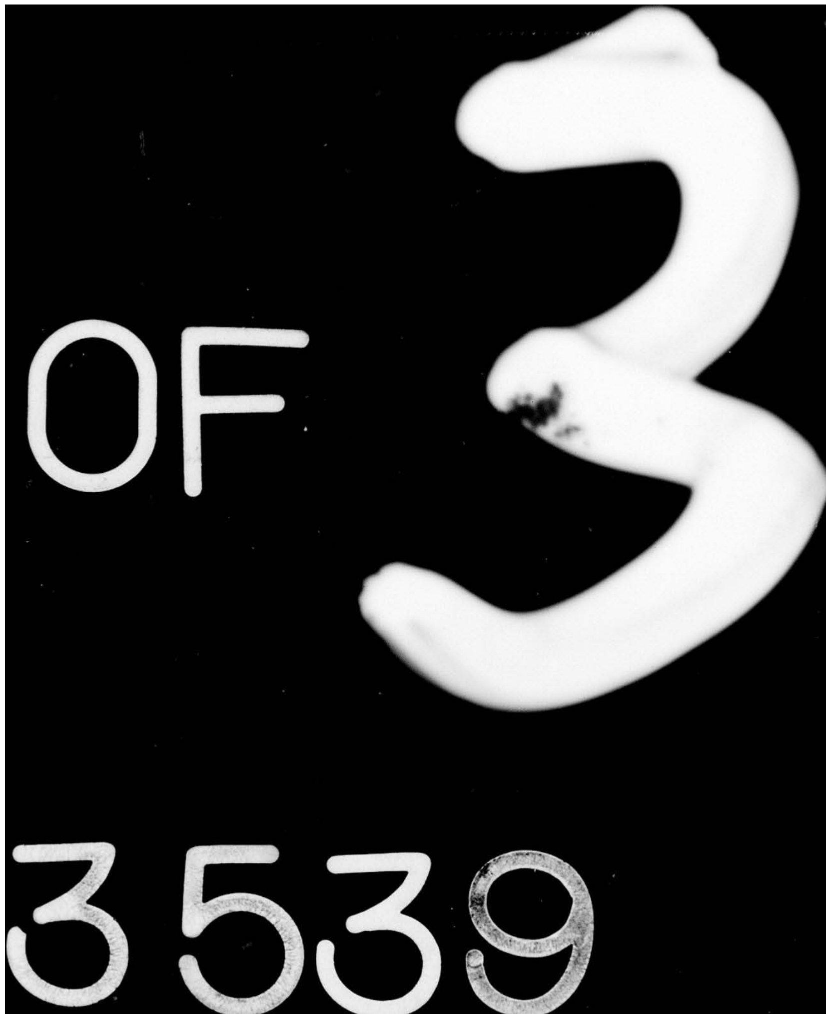
OF 3
3539

AD A053539

Unclassified

SECURITY CLASSIFICATION OF THIS PAGE (When Data Entered)

REPORT DOCUMENTATION PAGE

READ INSTRUCTIONS BEFORE COMPLETING FORM

1. REPORT NUMBER: (19) 15322.1-A-EL	2. GOVT ACCESSION NO. (18) ARO
3. RECIPIENT'S CATALOG NUMBER (9)	
4. TITLE (and Subtitle) (6) The Anomalous Voltage Response of the $P^+_{\sqcup}N^-_{\sqcup}N^+_{\sqcup}$ Device and its Effects on Second Breakdown.	5. TYPE OF REPORT & PERIOD COVERED: Final Report. 1 Aug [illegible] - 30 Nov 77
	6. PERFORMING ORG. REPORT NUMBER
7. AUTHOR(s) (10) G. W. Neudeck, L. R. Razouk	8. CONTRACT OR GRANT NUMBER(s) (15) DAAG29-77-G-0191
9. PERFORMING ORGANIZATION NAME AND ADDRESS: School of Electrical Engineering, Purdue University, West Lafayette, Indiana	10. PROGRAM ELEMENT, PROJECT, TASK AREA & WORK UNIT NUMBERS (14) TR-EE77-40
11. CONTROLLING OFFICE NAME AND ADDRESS: U. S. Army Research Office, P. O. Box 12211, Research Triangle Park, NC 27709	12. REPORT DATE (11) Dec [illegible] 77
	13. NUMBER OF PAGES 214 (12) 229 p.
14. MONITORING AGENCY NAME & ADDRESS (if different from Controlling Office) (16) Z99QAXT (17) B087	15. SECURITY CLASS. (of this report) unclassified
	15a. DECLASSIFICATION/DOWNGRADING SCHEDULE

16. DISTRIBUTION STATEMENT (of this Report)

Approved for public release; distribution unlimited.

17. DISTRIBUTION STATEMENT (of the abstract entered in Block 20, if different from Report)

18. SUPPLEMENTARY NOTES

The findings in this report are not to be construed as an official Department of the Army position, unless so designated by other authorized documents.

19. KEY WORDS (Continue on reverse side if necessary and identify by block number)

1000 1,000,000 sq. cm.

20. ABSTRACT (Continue on reverse side if necessary and identify by block number)

Numerical simulations and experimental measurements have been carried out to study the transient behavior of the $P^+_{\sqcup}N^-_{\sqcup}N^+_{\sqcup}$ structure under different levels of injection in both the reverse and the forward pulsed directions. A major part of this research is devoted to the explanation of the anomalous voltage that appears across the diode terminals when pulsed in the forward direction with current densities in the range of 10^3 to 10^6 amp/cm^2. A numerical iterative method of solution of the one-dimensional basic two-carrier transport equations, coupled with Maxwell's and Poisson's equations, describing the behavior of the semiconductor device

292 000

DD FORM 1 JAN 73 1473 EDITION OF 1 NOV 65 IS OBSOLETE

Unclassified

20. ABSTRACT CONTINUED

is presented. The pure implicit technique along with the Newton-Raphson iteration are used to solve the equations, while the explicit technique is used to obtain a first guess to start the iterative solution. A numerical method is arrived at for the determination of effective transient lifetimes in the case of excess diffusion due to very high current density.

ACCESSION for
NTIS White Section
DDC Buff Section
UNANNOUNCED
JUSTIFICATION
BY
DISTRIBUTION/AVAILABILITY CODES
Dist. AVAIL. and/or SPECIAL
A

12

THE ANOMALOUS VOLTAGE RESPONSE OF THE P^{+} N^{-} N^{+} DEVICE AND ITS EFFECTS ON SECOND BREAKDOWN

G. W. Neudeck

L. R. Razouk

TR-EE 77-40

December 1977

62704 H

DDC
RECEIVED
MAY 4 1978
D

This work was sponsored by the Defense Nuclear Agency
under: Subtask Code Z99QAXTB087 and Work Unit 7.

DISTRIBUTION STATEMENT A
Approved for public release;
Distribution Unlimited

ACKNOWLEDGEMENTS

The authors are pleased to acknowledge the assistance, the advice, and the constant support provided by Dr. Dave Mathews and the U.S. Army Missile Research and Development Command Redstone Arsenal, Alabama. Also the U.S. Army Research office, Research Triangle Park, North Carolina.

TABLE OF CONTENTS

LIST OF TABLES v

LIST OF FIGURES vi

ABSTRACT xii

CHAPTER I. INTRODUCTION 1

CHAPTER II. MATHEMATICAL EQUATIONS 4

- The dielectric relaxation time constant " $_r$ " 7
- The transit time " $_t$ " 9
- Mathematical equations to be solved 12
- Normalized basic equations 13
- Type of equations 17
- Numerical Techniques used to solve the equations .. 19
- The pure implicit technique 21
- Newton-Raphson iteration method 26
- The explicit technique 35
- Literature review for different numerical techniques 38

CHAPTER III. THERMAL EQUILIBRIUM CONDITION 48

- Using the same points as space charge points and field points 56
  - (i) using Poisson's equation 57
  - (ii) using the current equation 58
- Different charge points and field points 58
  - (i) using Poisson's equation 58
  - (ii) using the current equation 59
- Device under consideration 59

CHAPTER IV. REVERSE PULSED CASE 68

CHAPTER V. FORWARD PULSED CASE 109

- External excitation in the form of a low current stop 114
- External excitation in the form of extremely high current step 121
- The excess diffusion stage and the transient lifetime prediction 135
- The impact ionization stage 138
- Near steady state stage 140
- The use of transient lifetime and band-to-band recombination in case of an extreme current step 140
- External excitation in the form of high current step 155

CHAPTER VI. EXPERIMENTAL RESULTS.............................. 170

Diode Fabrication Procedure........................ 171
MOS-C Fabrication Procedure........................ 172
N_D from MOS Measurements........................ 173
N_D from Diode C-V Measurements.................. 177
The Width W.. 183
Diode Testing Results.............................. 185
Comparison between theory and experiment........... 187
Reverse pulsed case................................ 189
Forward pulsed case................................ 190

CHAPTER VII. SUMMARY, CONCLUSIONS, AND RECOMMENDATIONS FOR FURTHER STUDY.............................. 196

LIST OF REFERENCES.. 201

GENERAL REFERENCES.. 202

APPENDICES

A. THE FORMULATION FOR THE CONSTRUCTION OF THE MATRIX ELEMENTS IN THE IMPLICIT METHOD..... 205

B. THOMAS ALGORITHM FOR TRIDIAGNONAL MATRIX...... 209

C. ALGORITHM FOR TRI-TRIDIAGONAL MATRIX.......... 210

LIST OF TABLES

Table		Page
1	Normalized Parameters for Silicon	14
2	Output Voltage as a Function of Time for Figure 19	93
3	Output Voltage as a Function of Time for Figure 39	107
4	Specifications of the Silicon Wafer	171
5	MOS Analysis of N_D for Starting Material	177
6	Results for N_D Using Different Methods	181
7	Angle Lap and Stain Data	185
8	Results of Pulsing the Diodes in the Forward Direction	187

LIST OF FIGURES

Figure		Page
1	Minority carrier distribution in a short base under low level injection condition	11
2	Time-space mesh for the implicit method	20
3	Electron and hole movements (a) for negative electric field (b) for positive electric field	23
4	Newton's Method to solve F(x) = 0	27
5	Time-space mesh for the explicit method	36
6	Limitation of the explicit method	37
7	Time-space mesh for the generalized pure implicit scheme	40
8	Band diagram and potential variation for P^+-N structure (a) electron band diagram (b) potential variation with distance	49
9	Donor and acceptor levels (a) for N-type (b) for P-type	51
10	Spacial steps for thermal equilibrium case	54
11	Using the same points as space charge points and field points	54
12	Different space charge points and field points	54
13	Cross section of a typical $P^+N^-P^+$ junction	60
14	Uniform time-space mesh	63
15	Electric field distribution at thermal equilibrium for diode #1	64
16	Electron and hole density distribution of thermal equilibrium for diode #1	65
17	Electric field distribution at thermal equilibrium for diode #2	66
18	Electron and hole density distributions at thermal equilibrium for diode #2	67

19 Output voltage for the reverse biased case (first device) 70

20 Electron and hole current density distributions for time instants t_1 to t_6 as shown in Figure 19.................. 71

21 Displacement current density distribution for time instants t_1 to t_6 as shown in Figure 19.................. 72

22 Electron and hole densities for time instants t_1 to t_6 as shown in Figure 19.................................... 73

23 Electric field distribution for time densities t_1 to t_6 as shown in Figure 19.................................... 74

24 Electron and hole current density distribution for time instants t_7 to t_{13} as shown in Figure 19........... 76

25 Displacement current density distributions for time instants t_7 to t_{13} as shown in Figure 19................ 77

26 Electron and hole density distributions at time instants t_7 to t_{13} as shown in Figure 19......................... 78

27 Electric field distribution at time instants t_7 to t_{13} as shown in Figure 19.................................... 79

28 Electron and hole current density distributions for time instants t_{14} to t_{19} as shown in Figure 19.......... 81

29 Displacement current density distribution for time instants t_{14} to t_{19} as shown in Figure 19................ 82

30 Electron and hole density distributions for time instants t_{14} to t_{19} as shown in Figure 19................ 83

31 Electric field distribution for time instants t_{14} to t_{19} as shown in Figure 19............................ 84

32 Electron and hole current density distributions for time instants t_{20} to t_{22} as shown in Figure 19................ 85

33 Displacement current density distribution for time instants t_{20} to t_{22} as shown in Figure 19................ 86

34 Electron and hole density distributions for time instants t_{20} to t_{22} as shown in Figure 19................ 88

35 Electric field distribution for time instants t_{20} to t_{22} as shown in Figure 19......................... 89

36 Electron and hole current density distributions for time instant t_{23} as shown in Figure 19.................. 90

37 Electron and hole density distributions for time instant t_{23} as shown in Figure 19........................ 91

38 Electric field distribution for time instant t_{23} as shown in Figure 19.. 92

39 Current density and output voltage for the reverse biased case (second device)............................ 95

40 Electron and hole current density distributions for time instants t_1 to t_5 as shown in Figure 39............ 96

41 Displacement current density distribution for time instant t_1 to t_5 as shown in Figure 39.................. 97

42 Electron and hole density distributions for time instants $t = 0$ to t_5 as shown in Figure 39............. 98

43 Electric field distribution for time instants $t = 0$ to t_5 as shown in Figure 39.............................. 99

44 Electron and hole current density distributions for time instant t_6 as shown in Figure 39.................... 100

45 Displacement current density distribution for time instant t_6 as shown in Figure 39......................... 101

46 Electron and hole density distributions for time instant t_6 as shown in Figure 39............................ 102

47 Electric field distribution for time instant t_6 as shown in Figure 39... 103

48 Electron and hole current density distributions for time instant t_7 as shown in Figure 39.................... 104

49 Electron and hole density distributions for time instant t_7 as shown in Figure 39............................ 105

50 Electric field distribution for time instant t_7 as shown in Figure 39.. 106

51 Pure implicit technique flow chart......................... 108

52 Electron and hole drift velocity vs. electric field for pure samples of Ge and Si.......................... 111

53 J(t) and V(t) for a relatively low current step in the forward direction.................................. 116

54 Electron and hole current density distributions for time instants t_1 to t_6 as shown in Figure 53............ 117

55 Displacment current density distribution for time instants t_1 to t_6 as shown in Figure 53.................. 118

56 Electron and hole density distributions for time instants t_1 to t_6 as shown in Figure 53.................. 119

57 Electric field distribution for time instants t_1 to t_6 as shown in Figure 53.............................. 120

58 V(t) for an extremely high current step using the equilibrium lifetime...................................... 123

59 Electron and hole current density distributions for time instants t_1 to t_3 as shown in Figure 58......... 124

60 Displacement current density distribution for time instants t_1 to t_3 as shown in Figure 58............ 125

61 Electron and hole densities for time instants t = 0 to t_3 as shown in Figure 58.............................. 126

62 Electric field distribution for time instants t = 0 to t_3 as shown in Figure 58.............................. 127

63 Electron and hole current density distributions for time instants t_4 to t_7 as shown in Figure 58............ 128

64 Displacement current density distribution for time instants t_4 to t_7 as shown in Figure 58.................. 129

65 Electron and hole density distributions at time instants t_4 to t_7 as shown in Figure 58.................. 130

66 Electric field distribution for time instants t_4 to t_7 as shown in Figure 58.............................. 131

67 Electron and hole current density distributions for time instants t_8 and t_9 as shown in Figure 58........ 132

68 Electron and hole density distributions for time instants t_8 and t_9 as shown in Figure 58.................. 133

69 Electric field distribution for time instants t_8 to t_9 as shown in Figure 58.............................. 134

70 The lifetime variation inside the P^+-N^--N^+ structure.. 139

71 V(t) for an extremely high current step using the transient lifetime and band-to-band recombination........ 142

72 Electron and hole current density distributions for time instants t_1 to t_5 as shown in Figure 71............ 143

73 Displacement current density distribution for time instants t_1 to t_5 as shown in Figure 71.................. 144

74 Electron and hole density distributions for the instants $t = 0$ to t_5 as shown in Figure 71.............. 145

75 Electric field distribution for time instant $t = 0$ to t_5 as shown in Figure 71................................ 146

76 Electron and hole current density distributions for time instants t_6 to t_9 as shown in Figure 71............ 147

77 Displacment current density distributions for time instants t_6 to t_9 as shown in Figure 71................ 148

78 Electron and hole density distributions for time instants t_6 to t_9 as shown in Figure 71.................. 149

79 Electric field distributions for time instants t_6 to t_9 as shown in Figure 71................................ 150

80 Electron and hole current density distributions for time instants t_{10} to t_{12} as shown in Figure 71........... 151

81 Displacement current density distribution for time instants t_{10} to t_{12} as shown in Figure 71............... 152

82 Electron and hole density distributions for time instants t_{10} to t_{12} as shown in Figure 71............... 153

83 Electric field distribution for time instants t_{10} to t_{12} as shown in Figure 71.............................. 154

84 V(t) for a high current step with different lifetimes.. 156

85 Electron and hole current density distributions for time instants t_1 to t_7 as shown in Figure 84............. 157

86 Displacement current density distribution for time instants t_1 to t_5 as shown in Figure 84.................. 158

87 Electron and hole density distributions for time instants $t = 0$ to t_7 as shown in Figure 84............... 159

88 Electric field distribution for time instants $t = 0$ to t_7 as shown in Figure 84......................... 160

89 Electron and hole current density distributions for time instants t_8 to t_{12} as shown in Figure 84........ 161

90 Displacement current density for time instants t_9 to t_{11} as shown in Figure 84.......................... 162

91 Electron and hole density distributions for time instants t = 0 to t_{12} as shown in Figure 84.............. 163

92 Electric field distribution for time instants t = 0 to t_{12} as shown in Figure 84.............................. 164

93 Electron and hole current density distributions for time instant t_{13} as shown in Figure 84........................ 166

94 Electron and hole density distributions for time instant t_{13} as shown in Figure 84........................ 167

95 Electric field distribution for time instant t_3 as shown in Figure 84.. 168

96 MOS Capacitor Geometry.. 174

97 Capacitance for MOS Wafer #3.................................... 175

98 Capacitance vs. Voltage for Diode Wafer #3.................. 178

99 Log C vs. Log V for Diode Wafer #3.......................... 179

100 $1/C^2$ vs. volt for diode wafer #3.......................... 182

101 Geometry of Angle Lap and Stain.............................. 184

102 External applied current and output voltage for experimental data.. 186

103 Pulsed reverse biased characteristics for diode wafer #3.. 188

104 V(t) obtained experimentally for diode #3................ 191

105 Computer simulation result for v(t) using $_0 = 3.1 \times 10^{-10}$ sec. 193

106 Computer simulation result for v(t) using the transient lifetime and $_0 = 4 \times 10^{-10}$ sec. 194

ABSTRACT

Numerical simulations and experimental measurements have been carried out to study the transient behavior of the $P^{+}-N^{-}-N^{+}$ structure under different levels of injection in both the reverse and the forward pulsed directions. A major part of this research is devoted to the explanation of the anomalous voltage that appears across the diode terminals when pulsed in the forward direction with current densities in the range of 10^{3} to 10^{6} amp/cm^{2}.

A numerical iterative method of solution of the one-dimensional basic two-carrier transport equations, coupled with Maxwell's and Poisson's equations, describing the behavior of the semiconductor device is presented. The method is of a very general character, with none of the conventional assumptions and restrictions introduced, and freedom is available in selecting the doping profile, generation-recombination law, mobility dependencies, and injection level. For a specified arbitrary current excitation, the solution yields the terminal voltage and all the quantities of interest throughout the entire device as functions of position and time.

The pure implicit technique along with the Newton-Raphson iteration are used to solve the equations, while the explicit technique is used to obtain a first guess to start the iterative solution.

A numerical method is arrived at for the determination of effective transient lifetimes in the case of excess diffusion due to very high current density. As the transient solution approaches steady state, the transient lifetimes reduce to their equilibrium values.

The use of band-to-band Auger recombination as a process complementary to the impact ionization process, along with the transient lifetimes explain the large terminal voltage across the diode structure when pulsed with intense current density in the forward direction.

CHAPTER I

INTRODUCTION

Present semiconductor device modeling of the volt-ampere characteristics, transient response, and avalanche breakdown is adequate for predicting the response of junction devices in the normal region of operation. For very high injection levels, such as diodes operating under intense current pulses in the forward biased direction with current density of 10^3 amp/cm^2 to 10^6 amp/cm^2, these models are no longer adequate and do not predict the anomalous voltage that appears across the terminals of thed device.

In order to achieve analytical results for a diode in a closed form solution, a number of assumptions are usually introduced. These assumptions limit the solution to specific device structures and operating conditions. Some of these assumptions are as follows:

(a) The separation of the device into different regions: either a space-charge layer that is fully depleted of mobile carriers or quasi-neutral regions.

(b) The neglecting of the majority carrier current in the low doping region.

(c) The limitation of the doping profiles to abrupt junctions or to linearly graded junctions.

(d) The assumption of constant mobilities.

(e) The use of a linear low level recombination rate.

Most of these assumptions are not valid for high-injection levels.

Numerical techniques, with the aid of high speed digital computers, represents an alternative approach to the problem. This is accomplished by solving the one-dimensional two carrier transport equations, along with Maxwell's and Poisson's equations. By using either the implicit or explicit

numerical techniques, one can obtain the transient and the spatial distributions of all the physical quantities of interest such as the electric field, the hole density, the electron density, the current densities, etc.

A. De Mari [1] solved this set of coupled second ordered non-linear equations assuming constant electron and hole mobilities, absence of a generation-recombination term, and with the application of external excitations of low to moderately high current density values. Scharfetter and Gummel [2] solved a similar set of equations for a Silicon N^+-N-P structure operating under reversed bias conditions as a Read diode oscillator. Lee, Lomax, and Haddad [3] developed a computer program to simulate a Silicon N^+-P-N^+ structure operating as an avalanche diode oscillator. All of these authors used different numerical techniques, and different boundary conditions to achieve a numerical solution to the set of equations.

It is the purpose of this work to develop a solution to the set of equations that is free from any of the traditional assumptions and thereby simulate the transient behavior of a current driven one-dimensional solid state structure starting from the thermal equilibrium condition (or a known steady-state condition). This computer simulation is used to explain and to predict the unexpectedly large transient voltage, which appears in the experimental measurements of diodes that are pulsed with a very narrow and large current pulse in either the reversed or the forward directions.

Chapter II presents the mathematical equations to be solved numerically and the literature review for different numerical techniques, along with the methods used in this research . It also exposes the various sources of errors that could result in divergence or instability. Chapter III describes a numerical method to obtain an accurate solution of the thermal equilibrium case. The thermal equilibrium solution is necessary since it serves as the

initial conditions for the transient problem. As an example of the numerical calculations, the transient solution for the reverse biased case is illustrated in Chapter IV. In Chapter V, the theory of the forward biased case under different levels of injection is discussed in detail along with a numerical method to predict an effective transit life time. The transient solution is also presented. Chapter VI describes the experimental results, the diode fabrication procedure, and the method used to measure the physical parameters such as the doping profile and the width of the low doping region. It also contains a comparison between the theory and experiment. In the appendices (A to C) are gathered the formulation for the construction of the matrix coefficients, the algorithms to solve a tridiagonal matrix, and the tri-tridiagonal matrix.

CHAPTER II

MATHEMATICAL EQUATIONS

It is the purpose of this chapter to present a numerical method for the transient solution of the one-dimensional two carrier continuity equations coupled with Maxwell's equations and with Poisson's equation. The method is of a very general character. It allows for the freedom of choosing the generation recombination laws, the doping profile, and the mobility dependencies. The transient solution results in a knowledge of all the physical quantities, between the device contacts, as functions of distance and time. The pure implicit technique is used to iteratively solve for the electric field, the electron density, and the hole density at each instant of time. The explicit technique is used to initiate the iteration. A literature review for different numerical methods is also included for comparative purposes.

The fundamental equations that govern the one-dimensional behavior of a semiconductor material are

(i) Maxwell's Equations

$$J(t) = J_n(x,t) + J_p(x,t) + \varepsilon \frac{\partial E(x,t)}{\partial t} \tag{1}$$

$$\frac{\partial J(t)}{\partial x} = 0 \tag{2}$$

which shows that the total current density may vary with time but is constant with distance. The third term of equation (1) is the displacement current. The first and second terms are the electron and hole currents respectively. Their current flow equations are

$$J_n(x,t) = e\,\mu_n(x,t)\,n(x,t)E(x,t) + e\,D_n(x,t)\,\frac{\partial n(x,t)}{\partial x} \tag{3}$$

and

$$J_p(x,t) = e\,\mu_p(x,t)P(x,t)E(x,t) - e\,D_p(x,t)\,\frac{\partial P(x,t)}{\partial x} \tag{4}$$

The above two equations show that electron and hole currents consist of drift and diffusion components. The dependence of mobilities and diffusion coefficients ($\mu(x,t)$ and $D(x,t)$) on distance and time follows from their dependence on the electric field $E(x,t)$ as follows

$$D_p = \frac{KT}{q}\,\mu_p \qquad D_n = \frac{KT}{q}\,\mu_n$$

$$\mu_p = |v_p/E| \qquad \mu_n = |v_n/E|$$

where

$$v_n = 1500\,E \quad \text{cm/sec} \quad \text{for} \quad E < 3.5\times10^3$$

$$v_n = 1.45\times10^6\,E^{0.1525} \quad \text{cm/sec} \quad \text{for} \quad 3.5\times10^3 < E < 1.4\times10^5$$

$$v_n = 9\times10^6 \quad \text{cm/sec} \quad \text{for} \quad E > 1.4\times10^5$$

$$v_p = 600\,E \quad \text{cm/sec} \quad \text{for} \quad E < 3.5\times10^3$$

$$v_p = 4.68\times10^4\,E^{0.445} \quad \text{cm/sec} \quad \text{for} \quad 3.5\times10^3 < E < 1.4\times10^5$$

$$v_p = 9\times10^6 \quad \text{cm/sec} \quad \text{for} \quad E > 1.4\times10^5$$

(ii) Poisson's Equation

$$\frac{\partial E(x,t)}{\partial x} = \frac{e}{\varepsilon}\,[p(x,t) - n(x,t) + N_D^+(x) - N_A^-(x)] \tag{5}$$

where, $N_D^+(x)$ and $N_A^-(x)$ are the ionized donor and acceptor impurities/cm^3

(iii) Continuity Equations

$$\frac{\partial n(x,t)}{\partial t} = -\,U(x,t) + \frac{1}{e}\frac{\partial J_n(x,t)}{\partial x} + G(x,t) \tag{6}$$

$$\frac{\partial P(x,t)}{\partial t} = -\,U(x,t) - \frac{1}{e}\frac{\partial J_P(x,t)}{\partial x} + G(x,t) \tag{7}$$

where $U(x,t)$ is the net hole-electron recombination, typically given as,

$$U(x,t) = \frac{np - n_i^2}{\tau_{po}(n+n_i) + \tau_{no}(p+n_i)}$$

If the life times are equal, then $\tau_{no} = \tau_{po}$, and the recombination term reduces to the following:

$$U(x,t) = \frac{np - n_i^2}{\tau_n(n+p+2n_i)}$$

The minority carrier lifetime is a function of the doping density in the diffused region and is therefore shorter than that of the bulk region. The relation between the lifetime and the doping density is as follows [4] [5]:

$$\tau_n = \frac{\tau_{nb}}{1 + \frac{N_B}{AN1}}$$

where

τ_{nb} is the low doping region lifetime

N_B is the doping density

AN1 is a constant typically $1.894 \times 10^{14}/cm^3$

The generation term, with no light on the sample, is

$$G(x,t) = \alpha \, |J_n| \, n + \beta |J_p| \, p$$

where

$$\alpha = 3.8 \times 10^6 \exp\left(\frac{-1.75 \times 10^6}{E}\right)$$

$$\beta = 2.25 \times 10^7 \exp\left(\frac{-3.26 \times 10^6}{E}\right)$$

are the ionization coefficients for the electrons and holes.

At this point it should be noted that only six of the above seven equations are independent since equation (2) can be derived from the remaining six equations.

With the application of a current pulse to a P^+-N diode (i.e., changing the current density with time) the transient behavior of E(x,t), p(x,t), and n(x,t) becomes of primary interest. In order to fully understand the time variation of these quantities, one must pay special attention to the dielectric relaxation time and the transit time.

(1) <u>The dielectric relaxation time constant</u> "τ_r":

This quantity cotnrols the variation of the electric field with time in the case of constant electron and hole densities. An approximate value for the dielectric relaxation time can be derived if one assumes that the hole and electron mobilities are independent of the electric field.

Combining equations (1), (3), and (4) for the displacement current divided by ξ

$$\frac{\partial E(x,t)}{\partial t} = \frac{1}{\varepsilon}[J(t) - J_n(x) - J_p(x)]$$

$$= \frac{1}{\varepsilon}[J(t) - e(\mu_n n(x) + \mu_p p(x))E(x,t)$$

$$+ e(D_p \frac{\partial P(x)}{\partial x} - D_n \frac{\partial n(x)}{\partial x})]$$

$$= \frac{1}{\varepsilon}[J(t) - \sigma(x)\, E(x,t) + D(x)]$$

where

$$\sigma(x) = e(\mu_n\, n(x) + \mu_p\, P(x))$$

$$D(x) = e(D_p \frac{\partial P(x)}{\partial x} - D_n \frac{\partial n(x)}{\partial x})$$

or,

$$\frac{\partial E(x,t)}{\partial t} + \frac{\sigma(x)}{\varepsilon}\, E(x,t) = \frac{1}{\varepsilon}[J(t) + D(x)] \quad (8)$$

If a positive current step of magnitude J_s is applied, the solution of equation (8) becomes

$$E(x,t) - E(x,t=0^-) = -\frac{J_s}{\sigma(x)}[1 - e^{-\frac{\sigma(x)}{\varepsilon}}]$$

where

$$E(x,t=0^-) = \frac{D(x)}{\sigma(x)}$$

The dielectric relaxation time constant is then

$$\tau_r = \frac{\varepsilon}{\sigma(x)} = \frac{\varepsilon}{e(\mu_n\ n(x) + \mu_p\ P(x))}$$

Therefore, if one considers a P^+-N diode with the following parameters:

$$N_A = 10^{18} \quad = p(x)$$

$$\mu_p \doteq 200$$

$$N_D = 10^{15} \quad = n(x)$$

$$\mu_n \doteq 1500$$

$$\varepsilon = 11.8 \times 8.854 \times 10^{-14}$$

$$e = 1.602 \times 10^{-19}$$

In the P side:

$$\tau_{rp} \cong \frac{\varepsilon}{e\mu_n N_A} = 3.261 \times 10^{-14} \text{sec.}$$

and, in the N side:

$$\tau_{rn} \cong \frac{\varepsilon}{e\mu_n N_D} = 4.347 \times 10^{-12} \text{sec.}$$

(2) <u>The transit time</u> "τ_t":

This quantity controls the time variation of the minority carriers in a semiconductor region of width (W), with a time invariant electric field. The general definition of the steady state transit time is:

$$\tau_t = \frac{Q_m}{J_m}$$

where

Q_m is the minority carrier charge contained in W, and

J_m is the current density of minority carrier.

The above transit time can be approximated in simple cases:

(i) For a short base P^+-N diode under low level injection conditions, the minority carrier distribution in the N region can be approximated as in Fig. 1. In this case,

$$Q_n \doteq \frac{e\,W_n}{2}\,(p_n(0) - p_{no}) + e\,W_n p_{no}$$

J_m is the diffusion current and is given by:

$$J_m = e\,D_p \frac{(p_n(0) - p_{no})}{W_n}$$

Therefore,

$$\tau_t = \frac{W_n^2}{2\,D_p} + \frac{W_n^2\,p_{no}}{D_p\,(p_n(0) - p_{no})} \doteq \frac{W_n^2}{2\,D_p}$$

In the case where $W_n = 10 \times 10^{-4}$ cm and $D_p = 15.54$

$$\tau_t = 3.22 \times 10^{-8} \text{ sec.}$$

(ii) For a P^+-N diode, with an N region under avalanche conditions, the base region is under very high-level injection and the minority carrier density can be approximated by an average value throughout the width W_n. The minority current is considered as a drift current, and the minority car-

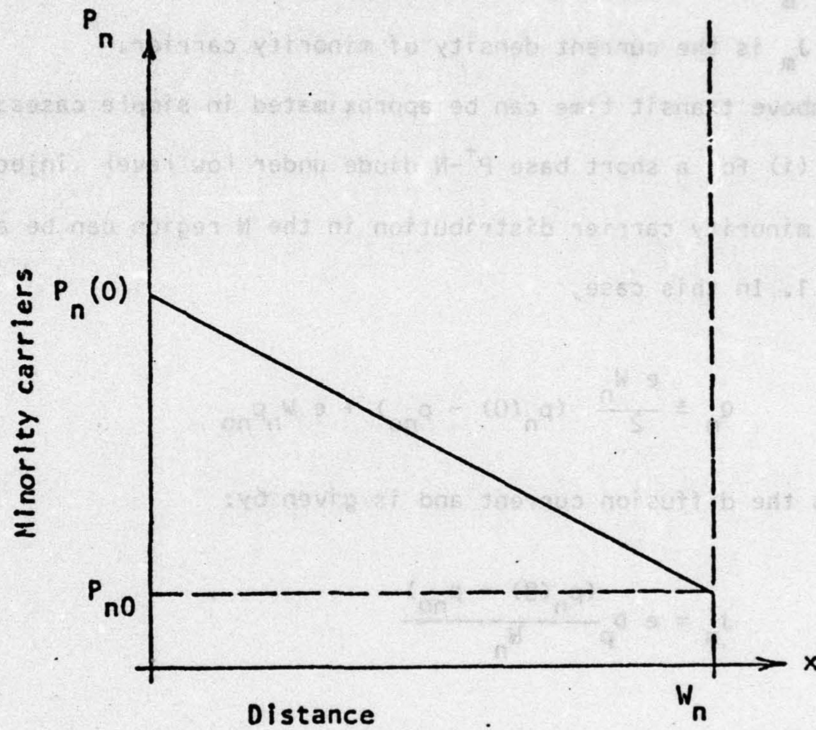

Figure 1. Minority carrier distribution in a short base under low level injection condition

rier velocity is taken as the scattering limited saturation velocity (v_s). Therefore,

$$Q_m \doteq e p_n W_n$$

$$J_m \doteq e p_n v_s$$

$$\tau_{tf} = W_n / v_s$$

The above is the full transit time, the average transit time is about one half this value,

$$\tau_t = \frac{W_n}{2v_s} = 5 \times 10^{-11} \text{sec.}$$

As shown from the above calculations, the relaxation time is smaller than the transit time. Therefore, the time variation of the minority carriers follows the time variation of the electric field.

<u>Mathematical Equations to be Solved</u>

From the previous discussion, it is obvious that the electric field E and the carrier densities are all functions of distance and time. These quantities cannot be solved in the N region alone because the boundary conditions near the transition region have an unknown time dependence. Therefore, one must try to solve for n, p, and E for the entire P^+-N device assuming the ohmic contacts as boundaries on both sides of the device.

To reduce the redundant calculations, the parameters of the basic equations are normalized. The normalization factors used here are the same as

those used by A. De Mari (1). The following definitions have been made:

D_0 = unit of carrier diffusion constant (cm^2/sec)

$D_n(D_p)$ = diffusion constant

$-e$ = electron charge

K = Boltzman's constant

L_D = intrinsic debye length

n_i = intrinsic carrier density (= 1.18×10^{10} for Si)

v_t = thermal voltage ($- \frac{KT}{e}$ = 0.0259 volt)

ε = permitivity (= $11.8 \times 8.85 \times 10^{-14}$ F/cm for Si)

$\mu_n(\mu_p)$ = mobility of carriers

Table 1 lists the symbols, units, and their values for silicon at room temperature. The basic equations (1) to (7) can be normalized and rewritten as follows:

<u>Normalized Basic Equations</u>

$$J_n = -v_n n - \left|\frac{V_n}{E}\right| \frac{\partial n}{\partial x} \tag{9}$$

$$J_p = -v_p p + \left|\frac{V_p}{E}\right| \frac{\partial p}{\partial x} \tag{10}$$

$$\frac{\partial E}{\partial x} = p - n + N_D - N_A \tag{11}$$

$$\frac{\partial n}{\partial t} = \alpha \left|V_n\right| n + \beta \left|v_p\right| p - \frac{np-1}{\tau_n(2+n+p)} - \frac{\partial Jn}{\partial x} \tag{12}$$

Table 1. Normalized Parameters for Silicon

Description	Normalized Quantity	Normalized Symbol	Factor Units	Values of Normalized factors for Si
position	x	$L_D = \sqrt{\frac{\varepsilon V_t}{e n_i}}$	cm	3.782×10^{-3}
time	t	L_D^2/D_0	sec.	1.435×10^{-5}
electrostatic potential	ψ	V_t	V	0.0259
barrier potential	V_d	V_t	V	0.0259
electric field	E	V_t/L_D	V/cm	6.85
carrier density	n, p	n_i	cm^{-3}	1.18×10^{10}
acceptors and donors	N_A, N_D	n_i	cm^{-3}	1.18×10^{10}
current densities	J, J_n, J_p	$-eD_0 n_i/L_D$	A/cm^2	-5.77×10^{-7}
G-R rate	U	$D_0 n_i/L_D^2$	$cm^{-3} sec^{-1}$	8.23×10^{14}
diffusion constant	μ_n, μ_p	D_0	cm^2/sec	1
mobilities	μ_n, μ_p	D_0/V_t	$cm^2/V.sec$	38.6

$$\frac{\partial P}{\partial t} = \alpha \left| V_n \right| n + \beta \left| V_p \right| P - \frac{np - 1}{\tau_n (2+n+p)} + \frac{\partial J_p}{\partial x} \tag{13}$$

$$J(t) = J_n + J_p - \frac{\partial E}{\partial t} \tag{14}$$

where all the variables are now the normalized variables.

Substituting equations (9) and (10) into equation (11), we get equation (15). Also, the substitution of equation (9) into equation (12), and of equation (10) into equation (13) yields equations (16) and (17).

$$\frac{\partial E}{\partial t} = \frac{1}{|E|} [|V_p| \frac{\partial P}{\partial x} - |V_n| \frac{\partial n}{\partial x}] - V_n\, n - V_p\, p - J(t) \tag{15}$$

$$\frac{\partial n}{\partial t} = \left| \frac{V_n}{E} \right| \frac{\partial^2 n}{\partial x^2} + [V_n + [- \frac{V_n}{E^2} + \frac{1}{E} \frac{dV_n}{dE}] \frac{\partial E}{\partial x}] \frac{\partial n}{\partial x}$$

$$+ [\frac{dV_n}{dE} \frac{\partial E}{\partial x} + \alpha |V_n|] n + \beta |V_p| P - \frac{np-1}{\tau_n (2+n+p)} \tag{16}$$

$$\frac{\partial p}{\partial t} = \left| \frac{V_p}{E} \right| \frac{\partial^2 p}{\partial x^2} + [-V_p + [- \frac{V_P}{E^2} + \frac{1}{E} \frac{dV_p}{dE}] \frac{\partial E}{\partial x}] \frac{\partial P}{\partial x}$$

$$+ [- \frac{dV_p}{dE} \frac{\partial E}{\partial x} + \beta |V_p|] P + \alpha |V_n| n - \frac{np-1}{\tau_n (2+n+p)} \tag{17}$$

Where

$$\alpha = 1.436 \times 10^4 \, e^{\frac{-2.555 \times 10^5}{|E|}} \tag{18}$$

$$\beta = 8.51 \times 10^4 \, e^{\frac{-4.76 \times 10^5}{|E|}} \tag{19}$$

$$V_n = 37.3\, E \qquad \text{for} \qquad E < 5.11 \times 10^2 \tag{20a}$$

$$V_n = 7.351 \times 10^3 \, E^{.1525} \qquad \text{for} \qquad 5.11 \times 10^2 < E < 2.2 \times 10^4 \tag{20b}$$

$$V_n = 3.4 \times 10^4 \qquad E > 2.2 \times 10^4 \tag{20c}$$

$$V_p = 12.3\, E \qquad \text{for} \qquad E < 5.11 \times 10^2 \tag{21a}$$

$$V_p = 4.16 \times 10^2 \, E^{.445} \qquad \text{for} \qquad 5.11 \times 10^2 < E < 2.2 \times 10^4 \tag{21b}$$

$$V_p = 3.4 \times 10^4 \qquad \text{for} \qquad E > 2.2 \times 10^4 \tag{21c}$$

Equations (15), (16), and (17) are the three second ordered coupled non-linear differential equations that have to be solved numerically to determine $E(x,t)$, $n(x,t)$, and $p(x,t)$ at each point in the structure at each instant of time. Once this is accomplished, then the electric field $E(x,t)$ can be integrated at each instant of time to obtain the terminal voltage across the device at each instant.

The boundary conditions are obtained from the assumption that perfect ohmic contacts are made to the P^+ region and the N region. One contact is at $x = 0$, the other at $x = L$. Therefore, the normalized boundary conditions

for the particle densities are as follows:

$$n(0,t) = 1/N_A \tag{22a}$$

$$p(0,t) = N_A \tag{22b}$$

$$n(L,t) = N_D \tag{22c}$$

$$p(L,t) = 1/N_D \tag{22d}$$

The electric field is chosen at the boundaries so that the total current equals the external applied current.

The initial conditions are assumed to be the thermal equilibrium distributions for $E(x,0)$, $n(x,0)$, and $p(x,0)$.

<u>Type of equations</u>

Before discussing the numerical methods used to solve the three coupled non-linear differential equations, we first discuss the type of equations. The general form of a second order linear partial differential equation in two independent variables x and t may be written as follows:

$$A \frac{\partial^2 Z}{\partial x^2} + 2B \frac{\partial^2 Z}{\partial t \partial x} + C \frac{\partial^2 Z}{\partial t^2} = F\left(\frac{\partial Z}{\partial t}, \frac{\partial x}{\partial t}, Z, x, t\right)$$

The type of equation is determined by the quantity:

$$\Delta = B^2 - AC$$

Where Δ is the discriminant of the partial differential equation (P.D.E.)

(a) If $\Delta > 0$, the equation is said to be hyperbolic

(b) If $\Delta = 0$, the equation is said to be parabolic

(c) If $\Delta < 0$, the equation is said to be elliptic

It is clear that equations (16) and (17) are parabolic non-linear equations since $C = B = 0$.

Therefore, the parabolic equation can be written in the following form:

$$\frac{\partial Z}{\partial t} = F\left(\frac{\partial^2 Z}{\partial x^2}, \frac{\partial Z}{\partial x}, Z, x, t\right) \tag{23}$$

To solve this equation one needs to know its open boundary conditions, i.e., the value of $Z(x,t)$ has to be known on three sides of a rectangle described as follows:

$x = 0$, and $t \geq 0$
$x = L$, and $t \geq 0$
$t = 0$, and $0 \leq x \leq L$

The obtain a numerical solution, the x and t axes have to be divided into uniform or non-uniform spatial and time steps (Δx and Δt). Then the spatial and time derivatives are approximated by one of several differential equation schemes at each space and time point. This procedure reduces the partial differential equation to a set of algebraic equations to be solved simultaneously.

Convergence and stability are the two problems of major difficulty in the numerical solution. To understand what they mean, the following terms are defined:

D = exact solution of the partial differential equation

Δ = exact solution of the partial difference equation generated by the difference equation scheme

N = numerical solution achieved from the partial difference equation

D - Δ = discretization error

Δ - N = numerical error

The discretization error or the truncaton error is a result of the finite sizes of the time and spatial steps. The convergence problem deals with the conditions under which D - Δ -> 0, for Δx and Δt -> 0. The stability problem deals with the condition under which Δ - N is small throughout the entire region of solution (space and time).

Numerical Techniques Used to Solve the Equations:

The normalized set of equations to be solved are as follows:

$$\frac{\partial E(x,t)}{\partial t} = J_n(x,t) + J_P(x,t) - J(t) \quad (24)$$

$$\frac{\partial P(x,t)}{\partial t} = G(x,t) - R(x,t) + \frac{\partial JP(x,t)}{\partial x} \quad (25)$$

$$\frac{\partial n(x,t)}{\partial t} = G(x,t) - R(x,t) - \frac{\partial Jn(x,t)}{\partial x} \quad (26)$$

$$\frac{\partial E(x,t)}{\partial x} = P(x,t) - N(x,t) + ND(x) \quad (27)$$

To solve the equations numerically, the x-axis and the time axis are divided into spatial and time steps (Δx and Δt). The spatial and the time derivatives are then approximated by a difference scheme. This procedure reduces the non-linear partial differential equations to a set of algebraic equations to be solved numerically.

The time-space mesh that is used to derive the difference equations is shown in Fig. 2. The one-dimensional semiconductor device is divided into JW partitions. At both ends of each partition, there are space charge

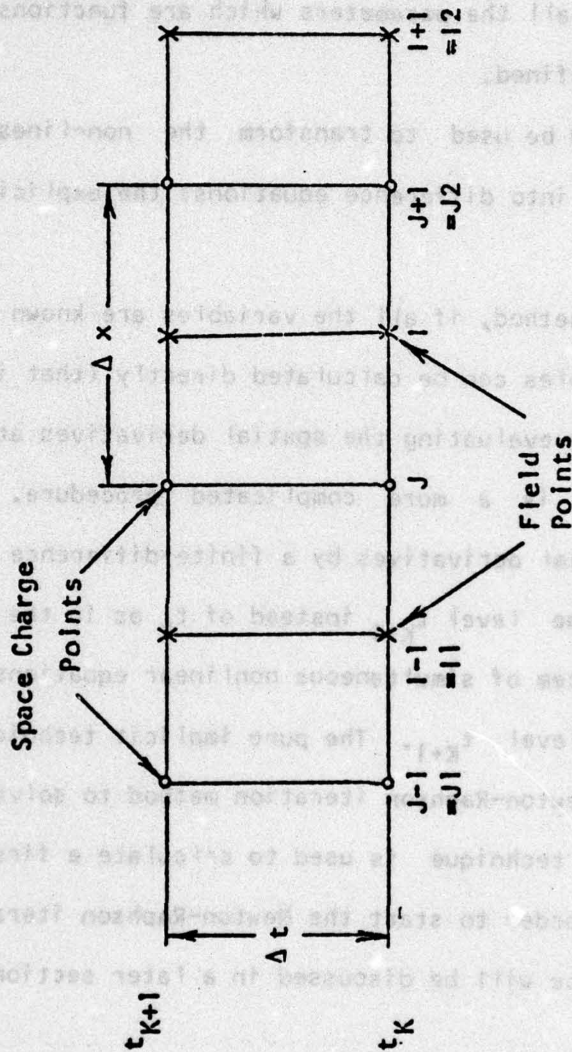

Figure 2. Time-space mesh for the implicit method

points where the hole density, electron density, and doping density are defined. In the middle of the two space-charge points there are field points I, where the electric field intensity, hole current density, and electron current density, and all the parameters which are functions of the electric field intensity are defined.

Two methods could be used to transform the non-linear partial differential equations into difference equations: the explicit method and the implicit method.

In the explicit method, if all the variables are known at any time level t_K, then the variables can be calculated directly (that is explicitly) at the time level t_{K+1} by evaluating the spatial derivatives at time level t_K. The implicit method is a more complicated procedure. It consists of representing the spatial derivatives by a finite-difference form evaluated at the advanced time level t_{K+1} instead of t_K as in the explicit method. This results in a system of simultaneous nonlinear equations in the unknown variables at time level t_{K+1}. The pure implicit technique is used here, with the aid of the Newton-Raphson iteration method to solve the equations, while the explicit technique is used to calculate a first guess for the unknown variables in order to start the Newton-Raphson iteration. The basic reasons for this choice will be discussed in a later section of the report.

The pure implicit technique:

The time-space mesh of Fig. 2 is used to convert the partial differentials into algebraic equations in a difference equation form. It is assumed that the three variables of interest, (the electric field, the hole density, and the electron density) are known at time level t_K and at all the previous time levels. In the rest of this chapter, the time index is assumed to be K + 1, unless otherwise specified. For example, E(I) means the electric

field at point (I, K + 1), while $E^K(I)$ means the electric field at point (I,K). Keeping this notation in mind, the different quantities in equations (24), (25), and (26) are evaluated at points (J, K + 1) and (I, K + 1) as follows:

$$\frac{\partial E(I)}{\partial t} = \frac{E(I) - E^K(I)}{\Delta t} \tag{28}$$

$$\frac{\partial P(J)}{\partial t} = \frac{P(J) - P^K(J)}{\Delta t}$$

$$\frac{\partial N(J)}{\partial t} = \frac{N(J) - N^K(J)}{\Delta t}$$

The drift components of the hole and electron current densities at point (I) depend on *whether the electric field is positive or negative* as explained in Fig. 3.

For negative electric field, the drift current components depend on N(J) and P(J2), while in the case of a positive electric field they depend on P(J) and N(J2). Using a central difference for the diffusion current density terms, the difference equations for the current densities become:

For $E(I) \geq 0$

$$JN(I) = -VN(I)\cdot N(J2) - \left|\frac{VN(I)}{E(I)}\right| \frac{1}{\Delta x} [N(J2) - N(J)]$$

$$JP(I) = -VP(I)\cdot P(J) + \left|\frac{VP(I)}{E(I)}\right| \frac{1}{\Delta x} [P(J2) - P(J)] \tag{29}$$

For $E(I) < 0$

$$JN(I) = -VN(I)\cdot N(J) - \left|\frac{VN(I)}{E(I)}\right| \frac{1}{\Delta x} [N(J2) - N(J)]$$

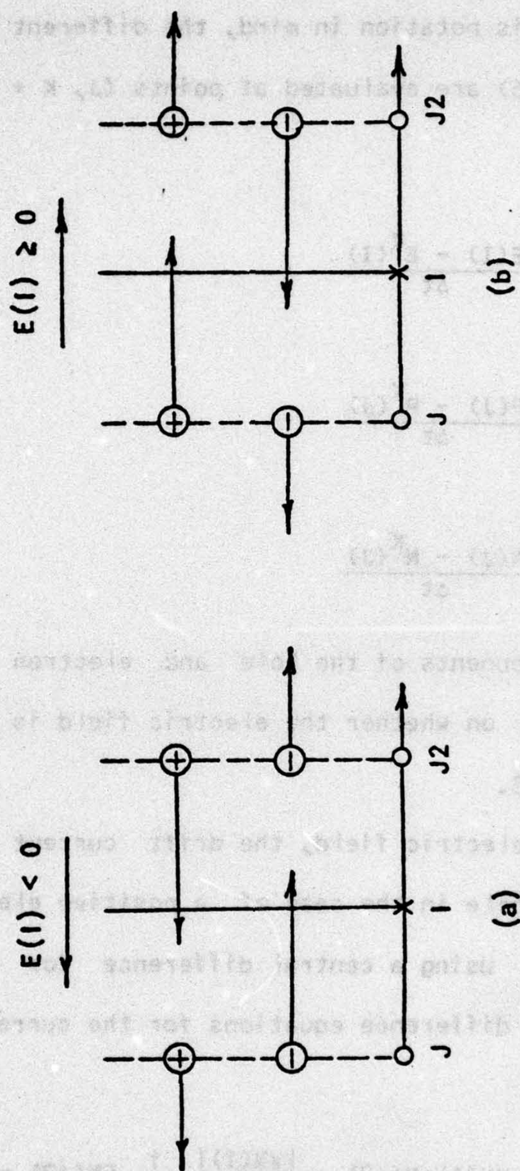

Figure 3. Electron and hole movements
(a) For negative electric field
(b) For positive electric field

$$JP(I) = -VP(I)\cdot P(J2) - \left|\frac{VP(I)}{E(I)}\right| \frac{1}{\Delta x} [P(J2) - P(J)] \quad (30)$$

The generation term at the Jth point is approximated by its average value between the Ith and the (I - 1)th point (I and I1) as shown in Figure 2.

$$G(J) = \frac{1}{2} (G(I1) + G(I))$$

$$= \frac{1}{2} [\alpha(I1)\cdot|JN(I1)| + \beta(I1)\cdot|JP(I1)|]$$

$$+ \frac{1}{2} [\alpha(I)\cdot|JN(I)| + \beta(I)\cdot|JP(I)|] \quad (31)$$

While

$$R(J) = \frac{N(J)\cdot P(J)-1}{\tau_0[2+N(J) + P(J)]} \quad (32)$$

$$\frac{\partial JP(J)}{\partial x} = \frac{1}{\Delta x}[JP(I) - JP(I1)] \quad (33)$$

$$\frac{\partial JN(J)}{\partial x} = \frac{1}{\Delta x} [JN(I) - JN(I1)] \quad (34)$$

It is clear that the quantities in equations (28) through (34) depend directly or indirectly on the electric field, the electron, and the hole densities, all of which are defined at points J1, I1, J, I, J2, and I2. Therefore, the vector of unknowns in equations (24), (25), and (26) at points I and J is defined as follows:

$$[X] = [E(I1),N(J1),P(J1),E(I),N(J),P(J),E(I2),N(J2),P(J2)]^T \quad (35)$$

By writing equations (24) to (26) in a difference form, and by moving all terms in the three discrete equations to the right hand side, and by using equations (28) through (30) to show the dependency of each term on the vec-

tor $[\underset{\sim}{X}]$, we obtain the following three discrete functions:

$$F1I = \frac{E(I)^K - E(I)}{\Delta t} + JN(I)\ [E(I),N(J),N(J2)]$$

$$+ JP(I)\ [E(I),P(J),P(J2)] - J(t) = 0 \qquad (36)$$

$$F2J = \frac{P^K(J) - P(J)}{\Delta t} + \frac{1}{2}\ G(I1)[E(I1),N(J1),P(J1),N(J),P(J)]$$

$$+ \frac{1}{2}\ G(I)[E(I),N(J),P(J),N(J2),P(J2)] - R(J)[N(J),P(J)]$$

$$+ \frac{1}{\Delta x}\ \{JP(I)[E(I),P(J),P(J2)] - JP(I1)[E(I1),P(J1),P(J)]\} \qquad (37)$$

$$F3J = \frac{N^K(J) - N(J)}{\Delta t} + \frac{1}{2}\ G(I1)[E(I1),N(J1),P(J1),N(J),P(J)]$$

$$+ \frac{1}{2}\ G(I)[E(I),N(J),P(J),N(J2),P(J2)] - R(J)[N(J),P(J)]$$

$$- \frac{1}{\Delta x}\ \{JN(I)[E(I),N(J),N(J2)] - JN(I1)[E(I1),N(J1),N(J)]\} \qquad (38)$$

The one-dimensional semiconductor device contains a total number of "M" spage-charge points, and "M-1" field points, including the boundaries J = 1 and J = M.

At time level K + 1, equation (36) will be written once for each point $2 \le I \le M-1$, while equations (37) and (38) will be written for each point $2 \le J \le M-1$, resulting in a system of 3(M-1) simultaneous equations in the 3(M-2) unknowns,

E(I),N(J),P(J), where $2 \leq I, J \leq M-1$.

The boundary conditions for the particle densities are obtained from the assumption that perfect ohmic contacts are made to the device terminals. One contact is at $x = 0$, the other is at $x = L$. Therefore, the normalized particle densities at the boundary are:

$$
\begin{aligned}
N(0,t) &= N(1) = 1/NA^{-} \\
P(0,t) &= P(1) = NA^{-} \\
N(L,t) &= N(M) = N_D^{+} \\
P(L,t) &= P(M) = 1/ND^{+}
\end{aligned} \qquad (39)
$$

The electric field is obtained iteratively through the solution of equations (36) to insure a constant total current at the boundaries, and throughout the whole device.

<u>Newton-Raphson Iteration Method</u>

To solve the system of nonlinear 3(M-1) simultaneous equations, the Newton-Raphson iteration method was used. In order to have a better understanding of this procedure, Newton's Method for solving a single non-linear equation is discussed first.

This method is illustrated graphically in Fig. 4. If this figure, if $F(x) = 0$, then $x = \alpha$ is the required solution. If an initial approximation x_i to the root α is provided, a sequence $x_{i+1}, x_{i+2}, \ldots$ may be defined by the recursion relation

$$\frac{\partial F(x)}{\partial x}\Big|_{x=x_i} = \frac{F(x_i)}{x_i - x_{i+1}}$$

or

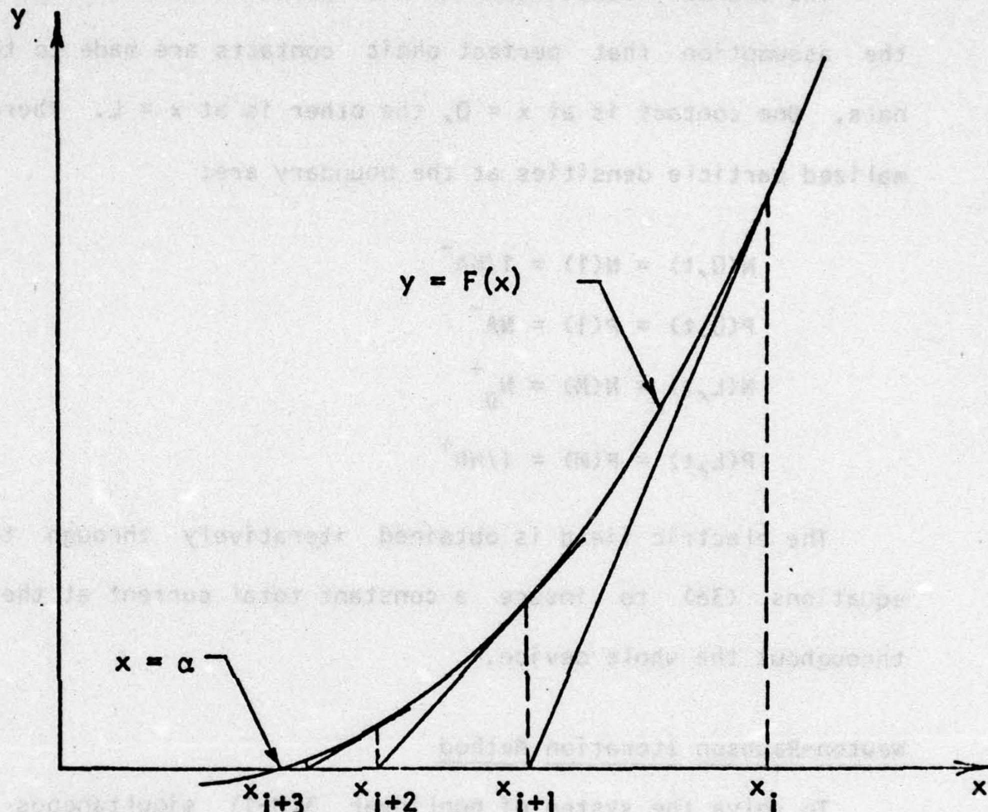

Figure 4. Newton's Method to solve F(x) = 0

$$F'(x_i) \cdot [x_{i+1} - x_i] = -F(x_i) \tag{40}$$

We draw a tangent to the curve $y = F(x)$ at the point $(x_i, F(x_i))$. This tangent meets the x-axis at the point $(x_{i+1}, 0)$. If, then, the curve crosses the x-axis at a point $(\alpha, 0)$ sufficiently near $(x_i, F(x_i))$, it may easily be seen that the number x_{i+1} is nearer α than x_i. A criterion for terminating the iterative procedure of (40) is:

$$\left| \frac{x_{i+1} - x_i}{x_{i+1}} \right| \leq \varepsilon$$

Here ε is a small positive number. For $\varepsilon = 10^{-N}$, the final value of x_{i+1} should be accurate to approximately N significant figures. It should also be noted that Newton's method may fail to converge to a root, if given a bad starting value.

The concept behind the Newton-Raphson Method is identical except that it applies to solving a set of simultaneous nonlinear equations. Therefore, equation (40) will take the form of a matrix equation as follows:

$$\frac{\partial [\underset{\sim}{F}]^{i-1}}{\partial \underset{\sim}{x}} (\underset{\sim}{x}^{(i)} - \underset{\sim}{x}^{(i-1)}) = -\underset{\sim}{F}(\underset{\sim}{x}^{(i-1)}) \tag{41}$$

where $\underset{\sim}{x}^{(i-1)}$ is the old approximation of the 3(M-2) arrays of unknowns, while $\underset{\sim}{x}^{(i)}$ is the better approximation.

$\underset{\sim}{F}(\underset{\sim}{x}^{(i-1)})$ is an array of 3(M-2) functions similar to equations (36), (37), and (38) evaluated according to the old approximation $\underset{\sim}{x}^{(i-1)}$.

$\dfrac{\partial [\underset{\sim}{F}]^{i-1}}{\partial \underset{\sim}{x}}$ is a square matrix of 3(M-2) dimension, whose elements are described by equation (42).

$$F_{LK}(\underset{\sim}{X}) = \frac{\partial F_L(\underset{\sim}{X})}{\partial X_k} \quad \text{where } 2 \leq L \leq M-1 \text{ and } 2 \leq K \leq M-1 \tag{42}$$

With the above notation im mind, equation (41) is applied to equations (36), (37), and (38) to evaluate the corrections in the array $[\underset{\sim}{X}]$ of equation (35). Therefore, the discretized equations at points I and J yield the following matrix equations:

$$\begin{bmatrix} a_1 & a_2 & a_3 & b_1 & b_2 & b_3 & c_1 & c_2 & c_3 \\ a_4 & a_5 & a_6 & b_4 & b_5 & b_6 & c_4 & c_5 & c_6 \\ a_7 & a_8 & a_9 & b_7 & b_8 & b_9 & c_7 & c_8 & c_9 \end{bmatrix} \begin{bmatrix} \Delta E(I1) \\ \Delta N(J1) \\ \Delta P(J1) \\ \Delta E(I) \\ \Delta N(J) \\ \Delta P(J) \\ \Delta E(I2) \\ \Delta N(J2) \\ \Delta P(J2) \end{bmatrix} = \begin{bmatrix} -F1I(\underset{\sim}{X}^{i-1}) \\ -F2J(\underset{\sim}{X}^{i-1}) \\ -F3J(\underset{\sim}{X}^{i-1}) \end{bmatrix} \tag{43}$$

Equations (36), (37), and (38) show the dependency of F1I, F2J, and F3J on the elements of the $\underset{\sim}{X}$ array. Therefore, the Matrix elements in equation (43) are defined as follows:

$$a_1 = \frac{\partial F1I}{\partial E(I1)} = 0 \tag{44a}$$

$$a_2 = \frac{\partial F1I}{\partial N(J1)} = 0 \tag{44b}$$

$$a_3 = \frac{\partial F1I}{\partial P(J1)} = 0 \tag{44c}$$

$$a_4 = \frac{\partial F2J}{\partial E(I1)} = \frac{1}{2}\frac{\partial G(I1)}{\partial E(I1)} - \frac{1}{\Delta x}\frac{\partial JP(I1)}{\partial E(I1)} \tag{44d}$$

$$a_5 = \frac{\partial F2J}{\partial N(J1)} = \frac{1}{2}\frac{\partial G(I1)}{\partial N(J1)} \tag{44e}$$

$$a_6 = \frac{\partial F2J}{\partial P(J1)} = \frac{1}{2}\frac{\partial G(I1)}{\partial P(J1)} - \frac{1}{\Delta x}\frac{\partial JP(I1)}{\partial P(J1)} \tag{44f}$$

$$a_7 = \frac{\partial F3J}{\partial E(I1)} = \frac{1}{2}\frac{\partial G(I1)}{\partial E(I1)} - \frac{1}{\Delta x}\frac{\partial JN(I1)}{\partial E(I1)} \tag{44g}$$

$$a_8 = \frac{\partial F3J}{\partial N(J1)} = \frac{1}{2}\frac{\partial G(I1)}{\partial N(J1)} - \frac{1}{\Delta x}\frac{\partial JN(I1)}{\partial N(J1)} \tag{44h}$$

$$a_9 = \frac{\partial F3J}{\partial P(J1)} = \frac{1}{2}\frac{\partial G(I1)}{\partial P(J1)} \tag{44i}$$

$$b_1 = \frac{\partial F1I}{\partial E(I)} = \frac{-1}{\Delta t} + \frac{\partial JN(I)}{\partial E(I)} + \frac{\partial JP(I)}{\partial E(I)} \tag{45a}$$

$$b_2 = \frac{\partial F1I}{\partial N(J)} = \frac{\partial JN(I)}{\partial N(J)} \tag{45b}$$

$$b_3 = \frac{\partial F1I}{\partial P(J)} = \frac{\partial JP(I)}{\partial P(J)} \tag{45c}$$

$$b_4 = \frac{\partial F2J}{\partial E(I)} = \frac{1}{2}\frac{\partial G(I)}{\partial E(I)} + \frac{1}{\Delta x}\frac{\partial JP(I)}{\partial E(I)} \tag{45d}$$

$$b_5 = \frac{\partial F2J}{\partial N(J)} = \frac{1}{2}\frac{\partial G(I1)}{\partial N(J)} + \frac{1}{2}\frac{\partial G(I)}{\partial N(J)} - \frac{\partial R(J)}{\partial N(J)} \tag{45e}$$

$$b_6 = \frac{\partial F2J}{\partial P(J)} = \frac{-1}{\Delta t} + \frac{1}{2}\frac{\partial G(I1)}{\partial P(J)} + \frac{1}{2}\frac{\partial G(I)}{\partial P(J)} - \frac{\partial R(J)}{\partial P(J)} \tag{45f}$$

$$+ \frac{1}{\Delta x}\frac{\partial JP(I)}{\partial P(J)} - \frac{1}{\Delta x}\frac{\partial JP(I1)}{\partial P(J)}$$

$$b_7 = \frac{\partial F3J}{\partial E(I)} = \frac{1}{2}\frac{\partial G(I)}{\partial E(I)} - \frac{1}{\Delta x}\frac{\partial JN(I)}{\partial E(I)} \tag{45g}$$

$$b_8 = \frac{\partial F3J}{\partial N(J)} = \frac{-1}{\Delta t} + \frac{1}{2}\frac{\partial G(I1)}{\partial N(J)} + \frac{1}{2}\frac{\partial G(I)}{\partial N(J)} - \frac{\partial R(J)}{\partial N(J)} \tag{45h}$$

$$- \frac{1}{\Delta x} \frac{\partial JN(I)}{\partial N(J)} + \frac{1}{\Delta x} \frac{\partial JN(I1)}{\partial N(J)}$$

$$b_9 = \frac{\partial F3J}{\partial P(J)} = \frac{1}{2} \frac{\partial G(I1)}{\partial P(J)} + \frac{1}{2} \frac{\partial G(I)}{\partial P(J)} - \frac{\partial R(J)}{\partial P(J)} \quad (45i)$$

$$c_1 = \frac{\partial F1I}{\partial E(I2)} = 0 \quad (46a)$$

$$c_2 = \frac{\partial F1I}{\partial N(J2)} = \frac{\partial JN(I)}{\partial N(J2)} \quad (46b)$$

$$c_3 = \frac{\partial F1I}{\partial P(J2)} = \frac{\partial JP(I)}{\partial P(J2)} \quad (46c)$$

$$c_4 = \frac{\partial F2J}{\partial E(I2)} = 0 \quad (46d)$$

$$c_5 = \frac{\partial F2J}{\partial N(J2)} = \frac{1}{2} \frac{\partial G(I)}{\partial N(J2)} \quad (46e)$$

$$c_6 = \frac{\partial F2J}{\partial P(J2)} = \frac{1}{2} \frac{\partial G(I)}{\partial P(J2)} + \frac{1}{\Delta x} \frac{\partial JP(I)}{\partial P(J2)} \quad (46f)$$

$$c_7 = \frac{\partial F3J}{\partial E(I2)} = 0 \quad (46g)$$

$$c_8 = \frac{\partial F3J}{\partial N(J2)} = \frac{1}{2} \frac{\partial G(I)}{\partial N(J2)} - \frac{1}{\Delta x} \frac{\partial JN(I)}{\partial N(J2)} \quad (46h)$$

$$c_9 = \frac{\partial F3J}{\partial P(J2)} = \frac{1}{2} \frac{\partial G(I)}{\partial P(J2)} \quad (46i)$$

A detailed calculation of these elements is found in Appendix A. Poisson's [equation (27)] is used to eliminate the $\Delta E(I1)$ coefficients, a_1, a_4, and a_7.

The discretized form of Poissons's equation is:

$$\frac{E(I) - E(I1)}{\Delta x} = P(J) - N(J) + N_B(J) \tag{47}$$

If for any reason, the values of N(J) and P(J) were changed by ΔN(J) and ΔP(J), the changes of ΔE(I) and ΔE(I1) will be related by equation (48)

$$\Delta E(I1) = \Delta E(I) - \Delta x\ [\Delta P(J) - \Delta N(J)] \tag{48}$$

Therefore, the coefficient ΔE(I1) will be distributed to the coefficients of ΔE(I), ΔP(J), and ΔN(J) as follows:

$$a_4 \Delta E(I1) = a_4 \Delta E(I) - (a_4 \Delta x)\ [\Delta P(J) - \Delta N(J)]$$

$$a_7\ \Delta E(I1)\quad a_7 \Delta E(I) - (a_7 \Delta x)\ [\Delta P(J) - \Delta N(J)]$$

This will change the elements, a_4, a_7, b_1, b_5, b_6, b_7, b_8, b_9 as follows:

$$a_4 \rightarrow 0 \tag{49a}$$

$$a_7 \rightarrow 0 \tag{49b}$$

$$b_4 \rightarrow b_4 + a_4 \tag{49c}$$

$$b_5 \rightarrow b_5 + (a_4 \Delta x) \tag{49d}$$

$$b_6 \rightarrow b_6 - (a_4 \Delta x) \tag{49e}$$

$$b_7 \rightarrow b_7 + a_7 \tag{49f}$$

$$b_8 \leftarrow b_8 + (a_7 \Delta x) \tag{49g}$$

$$b_9 \leftarrow b_9 - (a_7 \Delta x) \tag{49h}$$

Rewriting equation (43) using equations (44), (45), (46), and (49) results in equation (50).

$$\left[\begin{array}{ccc|ccc|ccc} 0 & 0 & 0 & b_1 & b_2 & b_3 & 0 & c_2 & c_3 \\ 0 & a_5 & a_6 & b_4 & b_5 & b_6 & 0 & c_5 & c_6 \\ 0 & a_8 & a_9 & b_7 & b_8 & b_9 & 0 & c_8 & c_9 \end{array}\right] \begin{bmatrix} \Delta E(I1) \\ \Delta N(J1) \\ \Delta P(J1) \\ \Delta E(I) \\ \Delta N(J) \\ \Delta P(J) \\ \Delta E(I2) \\ \Delta N(J2) \\ \Delta P(J2) \end{bmatrix} = \begin{bmatrix} -F1I(\underset{\sim}{X}^{i-1}) \\ -F2J(\underset{\sim}{X}^{i-1}) \\ -F3J(\underset{\sim}{X}^{i-1}) \end{bmatrix} \tag{50}$$

By defining the submatrix $[A_i]$, $[B_i]$, and $[C_i]$, as follows,

$$[A_i] = \begin{bmatrix} 0 & 0 & 0 \\ 0 & a_5 & a_6 \\ 0 & a_8 & a_9 \end{bmatrix}, \quad [B_i] = \begin{bmatrix} b_1 & b_2 & b_3 \\ b_4 & b_5 & b_6 \\ b_7 & b_8 & b_9 \end{bmatrix}, \quad [C_i] = \begin{bmatrix} 0 & c_2 & c_3 \\ 0 & c_5 & c_6 \\ 0 & c_8 & c_9 \end{bmatrix} \tag{51}$$

and by repeating equation (50) for all the spatial points $2 \leq I \leq M-1$, and

$2 \leq J \leq M-1$, at time level of $K + 1$, we obtain the following equation:

$$
\begin{bmatrix}
[B_2] & [C_2] & & & & & & \\
[A_3] & [B_3] & [C_3] & & & & & \\
 & [A_4] & [B_4] & [C_4] & & & & \\
 & & [A_i] & [B_i] & [C_i] & & & \\
 & & & [A_{M-2}] & [B_{M-2}] & [C_{M-2}] & & \\
 & & & & [A_{M-1}] & [B_{M-1}] & &
\end{bmatrix}
\begin{bmatrix}
\Delta E(2) \\ \Delta N(2) \\ \Delta P(2) \\ \cdot \\ \cdot \\ \cdot \\ \cdot \\ \cdot \\ \Delta E(I) \\ \Delta N(J) \\ \Delta P(J) \\ \cdot \\ \cdot \\ \Delta E(M-1) \\ \Delta N(M-1) \\ \Delta P(M-1)
\end{bmatrix}
=
\begin{bmatrix}
-F12 \\ -F22 \\ -F32 \\ -F13 \\ -F23 \\ -F33 \\ \cdot \\ \cdot \\ -F1I \\ -F2J \\ -F3J \\ \cdot \\ \cdot \\ -F1(M-1) \\ -F2(M-1) \\ -F3(M-1)
\end{bmatrix}
\qquad (52)
$$

or

$$[J]\,[\Delta x^{(i)}] = [F^{(i-1)}] \qquad (53)$$

where $[J]$ is a Tri-tridiagonal Matrix with a dimension of $3(M-2)$. Also $[A_2]$ and $[C_{M-1}]$ were eliminated due to a knowledge of boundary conditions.

Equation (52) is solved at each Newton-Raphson iteration. The algorithm of solving this equation is included in Appendix B [9].

The solution of equation (52) gives $[\Delta x^{(i)}]$, which is the difference between the two iterations i and i-1. When this difference reaches a very small number, we consider that the solution for the instant of time t_{k+1} is satisfactory. Using this solution, we proceed to solve for the next instant of time.

To start the iteration procedure at any instant of time, a first estimate for the array of unknowns is calculated using the explicit technique.

The explicit technique.

The space-time mesh used for the explicit technique is shown in Fig. 5. In this method, the right hand side of equations (24) to (26) are evaluated at the time level t_K. The definitions of JN, JP, G, and R are the same as in the implicit method. This allows us to directly calculate the different variables at time level t_{K+1}, from a knowledge of their values at the previous time level t_K. Therefore, Maxwell's equation and the two continuity equations for points I and J, can be written as:

$$E^{K+1}(I) = E^K(I) + \Delta t[JN^K(I) + JP^K(I) - J^K(t)] \quad (54)$$

$$P^{K+1}(J) = P^K(J) + \Delta t[G^K(J) - R^K(J) + \frac{1}{\Delta x}(JP^K(I) - JP^K(I1))] \quad (55)$$

$$N^{K+1}(J) = N^K(J) + \Delta t[G^K(J) - R^K(J) + \frac{1}{\Delta x}(JN^K(I) - JN^K(I1))] \quad (56)$$

It is clear that the value of E(I) at time level t_{K+1} depends only on the values of N(J), P(J), E(I), N(J2), and P(J2) at the level t_K, while the values of N(J) and P(J) at the level t_{K+1} depends on N(J1), P(J1), E(I1), N(J), P(J), E(I), N(J2), and P(J2) at time level t_K.

Referring to Fig. 6, only those variables within the pyramid-shaped area A can have any influence on the value of E(I), P(J), N(J) at time level t_{K+1}, whereas it is known that the solution of the partial differential equations depends also on the variable values in B for times earlier than t_{K+1}. Therefore, this method is used here only to calculate a first guess of the variables to start the Newton-Raphson iteration at time level t_{K+1}.

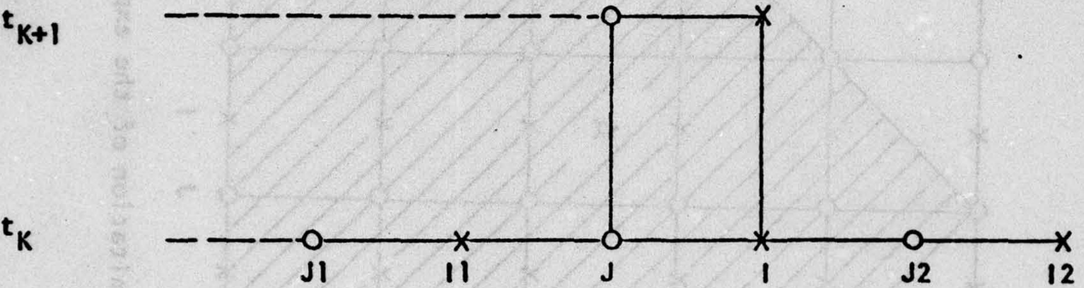

Figure 5. Time-space mesh for the explicit method

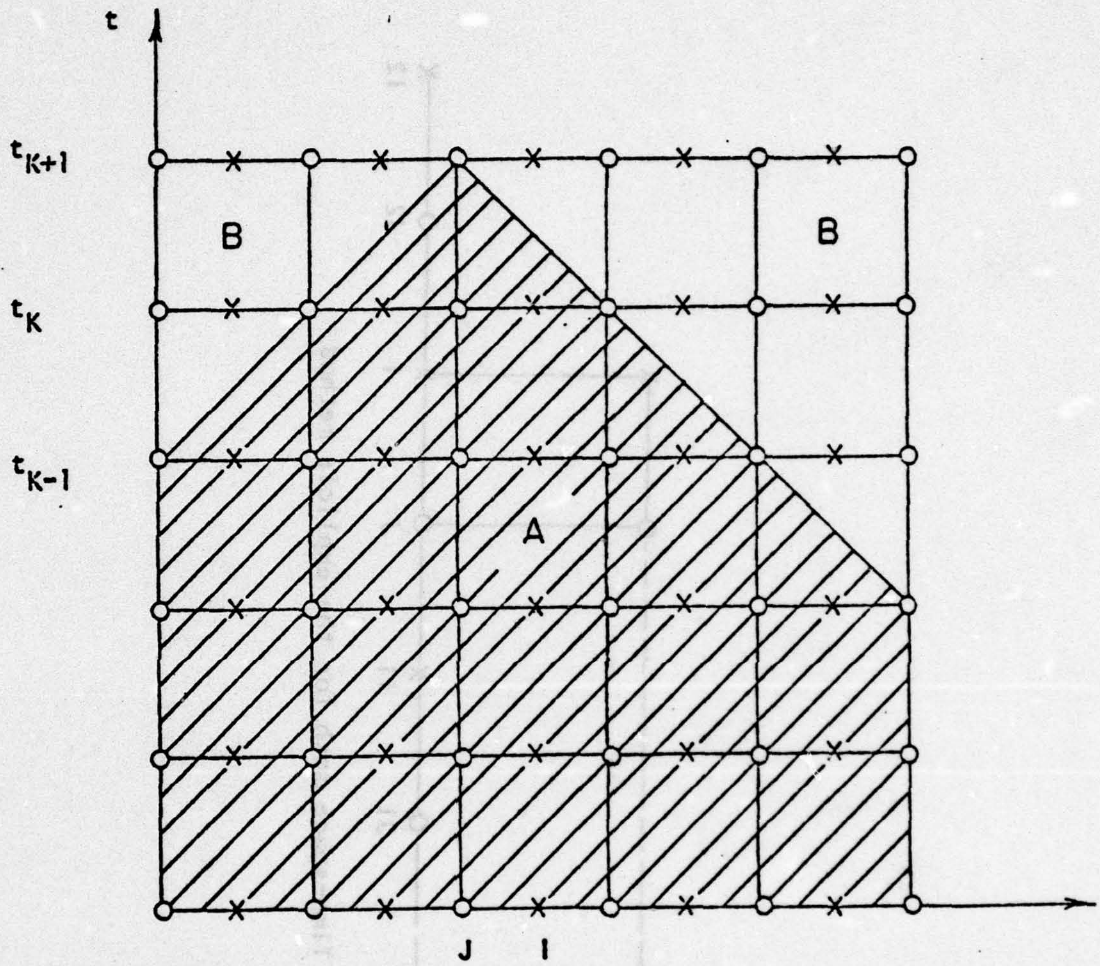

Figure 6. Limitation of the explicit method

To start the transient solution, an accurate initial condition is also required as a boundary condition, which describes the spatial distribution of the electric field, the hole density, and the electron density at time $t = 0$. The initial conditions used here are the thermal equilibrium conditions. Chapter III explains in detail the method used to obtain the thermal equilibrium conditions along with some computer generated results.

Literature review for different numerical techniques

A. De Mari [1] solved a similar set of coupled non-linear differential equations using the following assumptions:

(i) constant hole and electron mobilities, i.e., the region where the hole and electron velocities are linearly dependent on the electric field, was considered.

(ii) the absence of the recombination-generation term.

(iii) external current excitation in the form of a current step with a maximum value of current density smaller than what is considered for this research.

Using the generalized pure implicit scheme, equation (23) was represented by the following difference equation:

$$\frac{{}_k z_i - {}_{k-1} z_i}{{}_k \Delta t} = {}_k F_i = F\{{}_k t[\frac{\partial^2 z(x,t)}{\partial x^2}]x_i, {}_k t[\frac{\partial z(x,t)}{\partial x}]x_i, z(x,t_k)\}$$

where

K is the index identifying the instant of time t_K

i is the index identifying the spatial point x

${}_K\Delta t = t_K - t_{K-1}$ is the magnitude of the time step at the instant K.

In DeMari's work a non-uniform two-dimensional mesh in the position and time coordinates, as shown in Fig. 7, was used. The assigned boundary and initial conditions specify all the quantities at i = 1, i = L, and K = 0.

The boundary conditions used for the particle density were the same as presented in equation (22). As for the electric field, charge neutrality was assumed at the ohmic contacts. This boundary condition can be derived from equation (5) to give the following equation:

$$\frac{\partial E(0,t)}{\partial x} = \frac{\partial E(L,t)}{\partial x} = 0 \tag{57}$$

The initial conditions for n, p and E were either the thermal equilibrium distributions or an arbitrary steady state distribution. Therefore, the three non-linear equations generate the following system of difference equations:

$$\frac{{}_K E_i - {}_{k-1}E_i}{{}_k\Delta t} = {}_k(FI)_i \tag{58}$$

$$\frac{{}_k n_i - {}_{k-1}n_i}{{}_k\Delta t} = {}_k(FII)_i \tag{59}$$

$$\frac{{}_k p_i - {}_{k-1}p_i}{{}_k\Delta t} = {}_k(FIII)_i \tag{60}$$

Quantities at instant of time $t \leq t_{K-1}$ at any spatial point $0 \leq x_i \leq L$ are assumed known. An iterative procedure is employed at each instant of time to determine the unknown quantities. Therefore, a third index j was introduced to identify the cycle of iteration, while the correction for the elec-

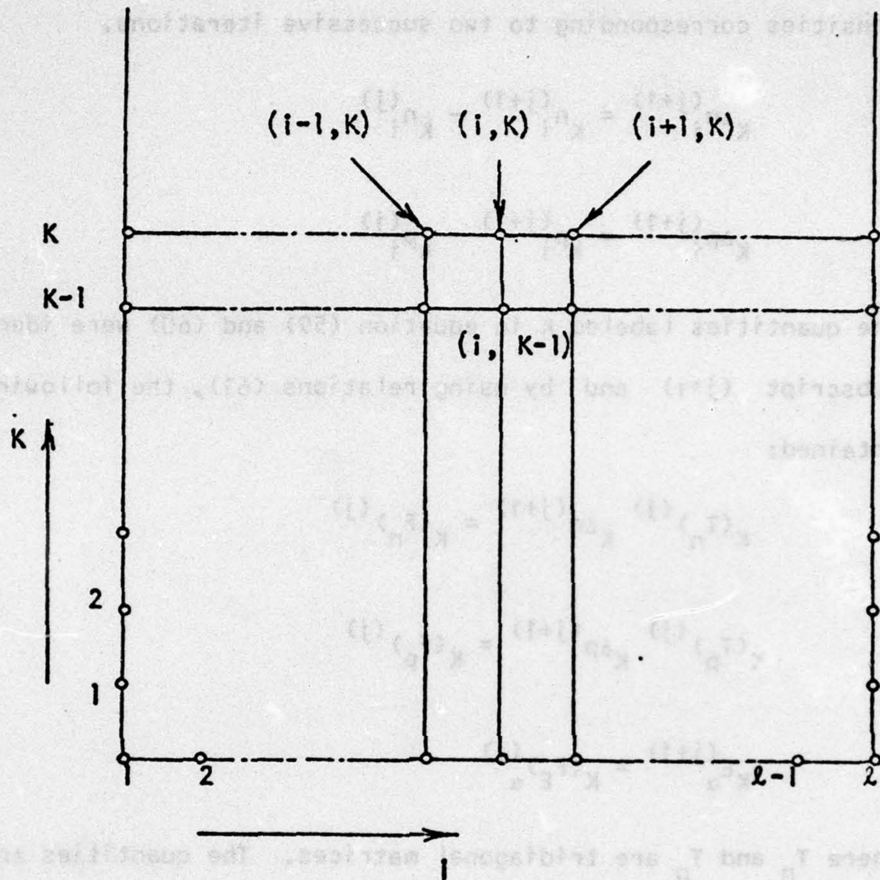

Figure 7. Time-space mesh for the generalized pure implicit scheme

tron and hole densities Δn and Δp were defined as the difference between densities corresponding to two successive iterations.

$$_K\Delta n_i^{(j+1)} = {_K}n_i^{(j+1)} - {_K}n_i^{(j)} \tag{61a}$$

$$_K\Delta p_i^{(j+1)} = {_K}p_i^{(j+1)} - {_K}p_i^{(j)} \tag{61b}$$

The quantities labeled K in equation (59) and (60) were identified with the subscript (j+1) and by using relations (61), the following equations were obtained:

$$_K(T_n)^{(j)} \; {_K}\Delta n^{(j+1)} = {_K}(F_n)^{(j)} \tag{62}$$

$$_K(T_p)^{(j)} \; {_K}\Delta p^{(j+1)} = {_K}(F_p)^{(j)} \tag{63}$$

$$_K E_\alpha^{(j+1)} = {_K}(F_E)_\alpha^{(j)} \tag{64}$$

where T_n and T_p are tridiagonal matrices. The quantities Δn, Δp, F_n, and F_p are the vectors:

$$\Delta n = \begin{bmatrix} \Delta n_2 \\ \Delta n_3 \\ \cdot \\ \cdot \\ \cdot \\ \Delta n_{\ell-1} \end{bmatrix} \qquad \Delta p = \begin{bmatrix} \Delta p_2 \\ \Delta p_3 \\ \cdot \\ \cdot \\ \cdot \\ \Delta p_{\ell-1} \end{bmatrix}$$

$$F_n = \begin{bmatrix} (F_n)_2 \\ (F_n)_3 \\ \cdot \\ \cdot \\ \cdot \\ (F_n)_{\ell-1} \end{bmatrix} , \quad F_p = \begin{bmatrix} (F_p)_2 \\ (F_p)_3 \\ \cdot \\ \cdot \\ \cdot \\ (F_p)_{\ell-1} \end{bmatrix}$$

Since the iterative procedure is repeated at each instant t, the index j was set to zero each time consistency was reached at one instant. Quantities labeled with the subscript j = 0 are then the trial distribution required to initiate the iterative procedure at the next instant of time.

Scharfetter and Gummel [2] solved a similar set of equations for a silicon Read diode oscillator. Their equations did not directly contain a displacement current component. Therefore, after using the difference approximation in Poisson's equation and the continuity equations, the following set of equations were obtained:

$$\frac{dp(N)}{dt} = g(N) - [J_p(M) - J_p(M-1)]/\Delta x \tag{65}$$

$$\frac{dn(N)}{dt} = g(N) + [J_n(M) - J_n(M-1)]/\Delta x \tag{66}$$

$$\frac{E(M) - E(M-1)}{\Delta x} = \frac{q}{\epsilon} [p(N) - n(N) + N_D(N) - N_A(N)] \tag{67}$$

where the Mth point is located midway between the major mesh points N + 1 and N. The current equations were taken as:

$$J_p = q\, \mu_p pE - KT\, \mu_p \frac{\partial p}{\partial x} \tag{68a}$$

$$J_n = q\, \mu_n nE + KT\, \mu_n \frac{\partial n}{\partial x} \tag{68b}$$

It was noted that substituting expressions (68a) and (68b) in (65) and (66)

leads to a numerical instability whenever the voltage change between mesh points exceeds 2KT/q. Therefore, equations (68a) and (68b) were treated as differential equations in p and n with J_n, J_p, μ_n, μ_p, and E assumed constant between mesh points. The solution of these then relates J_n and J_p to the other variables as follows:

$$J_p(M) = E(M)\left[\frac{P(N)\mu_p(M)}{(1-\exp(-E(M)\Delta x))} + \frac{P(N+1)\mu_p(M)}{(1-\exp(E(M)\Delta x))}\right] \tag{69a}$$

$$J_n(M) = E(M)\,\frac{n(N+1)\mu_n(M)}{(1-\exp(-E(M)\Delta x))} + \frac{n(N)\mu_n(M)}{(1-\exp(E(M)\Delta x))} \tag{69b}$$

The hole and electron concentrations were presented by the two component vector Y; where,

$$\dot{Y} = f(Y)$$

i.e., the time derivative of Y equals some nonlinear function of Y. If Y_0 is the initial value of Y, and ∂Y is the deviation from this value as time increases; and,

$$y(t) = y_0 + \partial y(t) \tag{70}$$

$$\dot{\delta y} = f(y_0) + M\delta y = \left.\frac{\partial y}{\partial t}\right|_{t=0} + \frac{\partial f}{\partial y}\,\delta y$$

If M, f, and δY were ordinary numbers, the solution of (44) is:

$$\delta y(t) = (e^{Mt}-1)\ f/M$$

or

$$\delta y(t) = f \cdot t(1 + Mt/2 + (Mt)^2/6 + \ldots)$$

For small but finite time step this can be written in the following form:

$$\delta y(t) = \frac{ft}{1 - \frac{Mt}{2}}$$

or

$$(1 - \frac{Mt}{2})\ \delta y = ft \qquad (71)$$

The vector Y_n was defined as: $Y_N = \begin{vmatrix} y_1 \\ y_2 \\ y_3 \end{vmatrix}$ where y_1, y_2, y_3 are deviations in the hole concentration, electron concentration, and electric field. The right hand side of the continuity equation is defined as the vector f_N as follows: $f_N = \begin{vmatrix} f_1 \\ f_2 \end{vmatrix}$ The vector equation that was solved for each increment of time is:

$$[\frac{2}{t} - M_N]\ (y_N) = 2(f_0)_N \qquad (72)$$

where

$$M_N = \frac{\partial f_N}{\partial y_N}$$

The matrix elements of M are defined by the expanded form of (72) shown below:

$$[XL]_N \begin{pmatrix} y_1 \\ y_2 \end{pmatrix}_{N-1} + [XM]_N \begin{vmatrix} y_1 \\ y_2 \end{vmatrix}_N + [XR] \begin{vmatrix} y_1 \\ y_2 \end{vmatrix}_{N+1} + \qquad (73)$$

$$+ (FL)_M\, y_{3_M} + (FR)_M\, y_{3_M} = (RH)_N$$

where: $(RH)_N = 2(f_0)_N$, the 2 x 2 matrices XL, XM, and XR are obtained by taking the partial derivatives of f_N with respect to y_1 and y_2 at mesh points N-1, N, and N+1 respectively, while the two component vectors FL and FR are obtained by taking the partial derivatives of f_N with respect to y_3 at mesh points M and M-1.

The boundary conditions were introduced by requiring that J_n in equation (68b) is equal to the terminal current density at the N-contact and that J_p in equation (68a) is equal to the terminal current density at the P-contact. In addition, the electric field at the two end metallic contacts is assumed to be zero.

Lee, Lomax, and Haddad [3] also solved a similar set of equations for Si avalanche-diode oscilltors, using the implicit and explicit techniques. The recombination term was ignored in using the implicit technique. In the explicit method, the time space mesh shown in Fig. 5 was used to derive the difference equations. The unknown parameters at the instant $t = t_{K+1}$ were obtained as follows:

$$P_j^{K+1} = P_j^K + \Delta t \cdot [\frac{\partial P}{\partial t}]_{t = K}$$

$$N_j^{K+1} = N_j^K + \Delta t \cdot [\frac{\partial N}{\partial t}]_{t = K}$$

$$E_I^{K+1} = E_{I-1}^{K+1} + \Delta x \; [\frac{\partial E}{\partial x}]_{t = K+1}$$

For each time advancement, the time step Δt is not a constant. It has to be determined at each time step to satisfy certain numerical stability conditions in order to insure that the numerical model does not result in oscillatory behavior and diverge.

In the implicit method, the time space mesh shown in Fig. 2 was used. The vector Q and the vector F were defined by:

$$[Q] = \begin{vmatrix} P \\ N \end{vmatrix}$$

$$[F] = \begin{vmatrix} FP \\ FN \end{vmatrix} = \begin{vmatrix} \partial P/\partial t \\ \partial N/\partial t \end{vmatrix}$$

The objective was to find a difference equation to approximate the continuity equation evaluated at the instant of time halfway between the Kth time step and the (K+1)th time step or:

$$[\frac{\partial Q}{\partial t}]^{K+1/2} = [F]^{K+1/2} = [F]^{K} + \frac{\partial}{\partial Q}[F]^{K} \cdot \frac{\Delta Q}{2} \tag{74}$$

$$+ \frac{\partial}{\partial E}[F]^{K} \cdot \frac{\Delta E}{2}$$

$$\frac{2}{\Delta t} - \frac{\partial}{\partial Q}[F]^{K} \cdot [\Delta Q] - \frac{\partial}{\partial E}[F]^{K} \cdot [\Delta E] = 2[F]^{K} \tag{75}$$

Equation (75) is identical to equation (73) of Scharfetter and Gummel, although the argument used in deriving equation (75) was different. The above equation is solved for each instant of time.

At the boundaries, it was assumed that the surface state density is high enough so that surface recombination velocity is infinite and the semiconductor is extrinsic; hence the particle densities at the boundaries assumed their thermal equilibrium values. For D. C. solutions with constant current, the value of the electric field at the boundaries was chosen iteratively such that the space average of particle density over the active region of the device was equal to the specified D. C. current.

As a conclusion, the explicit method is very inexpensive for each advancement of Δt but because the size of Δt is limited by the stability con-

ditions, it may become expensive when the particle densities are high, the mobilities are high, or when the simulation is to be carried over a long time duration. The implicit method is complicated and is more expensive for each Δt, but it is more stable numerically. Also, the time step Δt can usually be made very large. It has been observed that if the initial guess is not good the implicit method sometimes becomes unstable when Δt equals infinity, i.e. for steady state calculations.

CHAPTER III

THERMAL EQUILIBRIUM CONDITION

This chapter describes a numerical method used to obtain an accurate distribution for the electric field, the hole density, and the electron density at thermal equilibrium. The thermal equilibrium solution is used as a boundary condition for the transient problem as discussed previously in Chapter II.

In this formulation one has complete freedom of choosing the semiconductor device structure between the two ohmic contacts. This is accomplished by specifying the acceptor and the donor impurity distribution. Although the formulation presented could easily be modified to include degenerate semiconductors, Boltzmann statistics are assumed.

The thermal equilibrium condition is, by definition, with no applied voltage and no net current flow. The solution is obtained by accurately solving Poisson's equation:

$$- \frac{\partial^2 V(x)}{\partial x^2} = \frac{q}{\varepsilon} [P(x) - N(x) + N_D^+(x) - N_A^-(x)] \qquad (76)$$

A semiconductor device consists of bulk regions and transition regions. As an example, Figure 8 shows the electron energy band diagram, and the potential variations with distance for a P^+-N structure. By using the following definitions:

$$\phi_r(x) = V(x) = E_F(x) - E_i(x) \qquad (77a)$$

and,

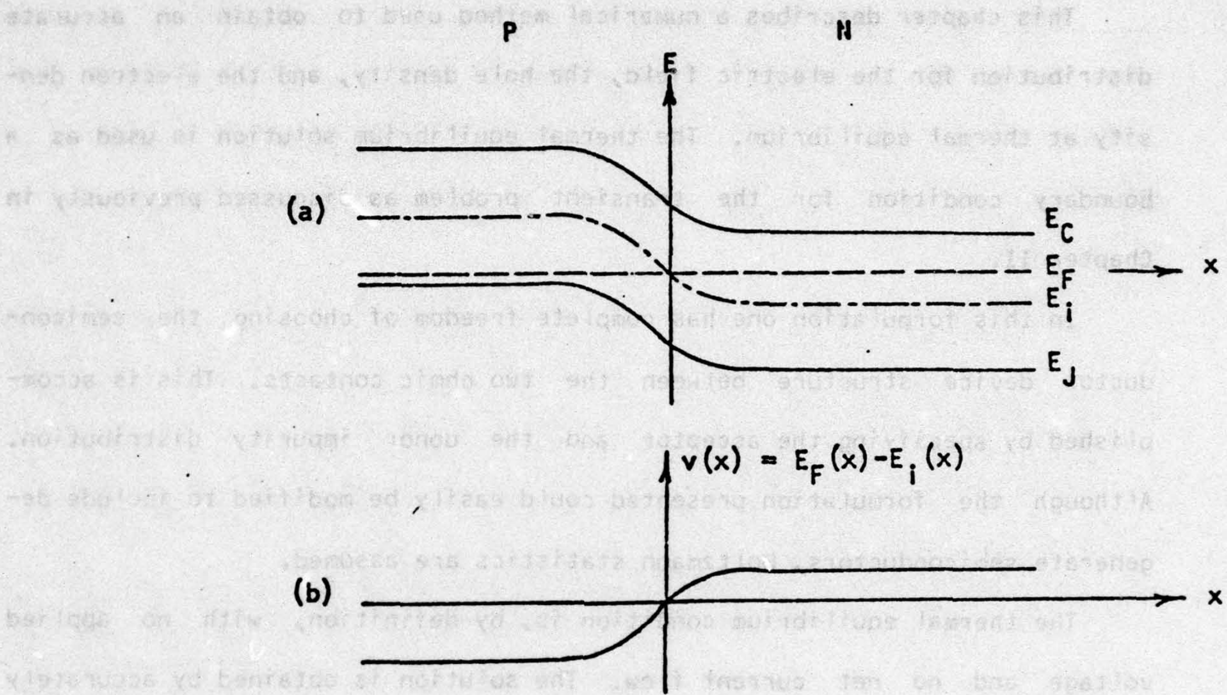

Figure 8. Band diagram and potential variation for P^+-N structure
(a) electron band diagram
(b) potential variation with distance

$$\phi(x) = \frac{1}{VT} = \phi_r(x) \tag{77b}$$

$$VT = KT/q \tag{77c}$$

Each term of equation (76) is written as a function of $\phi(x)$ as follows:

$$-\frac{\partial^2 V(x)}{\partial x^2} = -\frac{\partial^2 \phi_r(x)}{\partial x^2} = -VT\left[\frac{\partial^2 \phi(x)}{\partial x^2}\right] \tag{78}$$

$$P(x) = n_i\, e^{-\phi(x)} \tag{79}$$

$$N(x) = n_i\, e^{\phi(x)} \tag{80}$$

$$N_D^+(x) = N_D(x)\left[\frac{1}{1 + 2\exp\frac{(E_F - E_D)}{VT}}\right] \tag{81}$$

$$N_A^+(x) = N_A(x)\left[\frac{4}{4 + \exp\frac{(E_A - E_F)}{VT}}\right] \tag{82}$$

where E_D and E_A are the donor level and the acceptor level as shown in Fig. 9. Also,

$$E_F - E_D = (E_D' - Eg/2) + \phi(x) \tag{83a}$$

and

$$E_A - E_F = (E_A' - Eg/2) - \phi(x) \tag{83b}$$

Therefore equations (81) and (82) can be rewritten as:

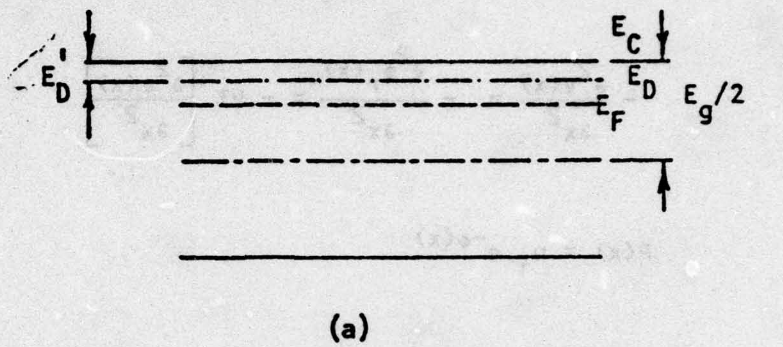

(a)

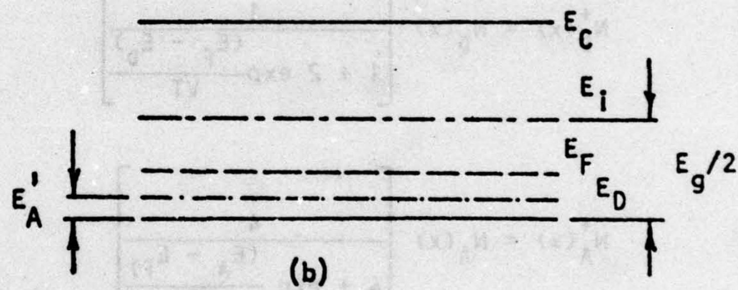

(b)

Figure 9. Donor and acceptor levels
(a) for N-type
(b) for P-type

$$N_D^+(x) = N_D(x)\left[\frac{1}{1 + 2a\ e^{\phi(x)}}\right] \quad (84)$$

$$N_A^+(x) = N_A(x)\left[\frac{4}{4 + b\ e^{-\phi(x)}}\right] \quad (85)$$

where

$$a = e^{\frac{1}{VT}(E_D' - Eg/2)}$$

and

$$b = e^{\frac{1}{VT}(E_A' - Eg/2)}$$

By substituting equations (78) to (80), and (84) and (85) into equation (76), equation (86) results:

$$-\frac{\partial^2\phi(x)}{\partial x^2} = \frac{q}{(\epsilon\cdot VT)}\cdot \quad (86)$$

$$\left[n_i e^{-\phi(x)} - n_i e^{\phi(x)} + \frac{N_D(x)}{1 + 2\ a\ e^{\phi(x)}} - \frac{4N_A(x)}{4 + b\ e^{-\phi(x)}}\right]$$

In order to solve equation (86) numerically, the device is divided into (M-1) spatial steps. The second order derivative is approximated by the three-point finite difference formula. Therefore, for point J in Fig. 10, equation (86) reduces to the following:

$$\frac{\dfrac{\phi(J2) - \phi(J)}{H(J)} - \dfrac{\phi(J) - \phi(J1)}{H(J1)}}{\dfrac{H(J) + H(J1)}{2}} = \frac{q}{(\epsilon . VT)}\cdot$$

$$\left[n_i e^{-\phi(J)} - n_i e^{\phi(J)} + \frac{N_D(J)}{1+2ae^{\phi(J)}} - \frac{4N_A(J)}{4+be^{-\phi(J)}}\right]$$

or

$$G[\phi(J1),\phi(J),\phi(J2)] = 0$$

$$= H(J)\phi(J1) - (H(J)+H(J1))\phi(J)+H(J1)\phi(J2)$$

$$+ \frac{qH(J)H(J1)(H(J)+H(J1))}{2.\varepsilon.VT}$$

$$X \left[n_i e^{-\phi(J)} - n_i e^{\phi(J)} + \frac{N_D(J)}{1+2ae^{\phi(J)}} - \frac{4N_A(J)}{4+be^{-\phi(J)}}\right] \qquad (87)$$

Equation (87), for all points $2 \leq J \leq M-1$, is solved using a Newton-Raphson iteration method. To start the iteration procedure, a first guess for $\phi(J)$ is required at each spatial point. This guess is obtained by assuming charge neutrality throughout the whole device. Although this assumption is not valid outside the bulk regions, the solution of $\phi(J)$ in the transition regions will be corrected after a few iterations.

Therefore at each spatial point the following non-linear equation is solved using Newton's Method.

$$F[\phi(J)] = n_i e^{-\phi(J)} - n_i e^{\phi(J)} + \frac{N_D(J)}{1+2ae^{\phi(J)}} - \frac{4N_A(J)}{4+be^{-\phi(J)}} = 0 \qquad (88)$$

A first guess for Newton's method is easily obtained as follows:

For N-type regions, $N_D(J) \approx N(J)$ and $N_A(J) = 0$

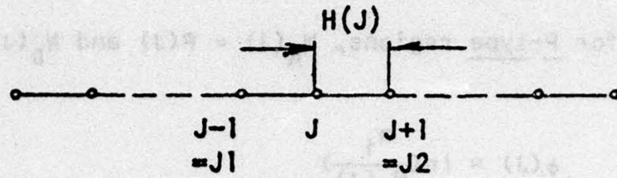

Figure 10. Spacial steps for thermal equilibrium case

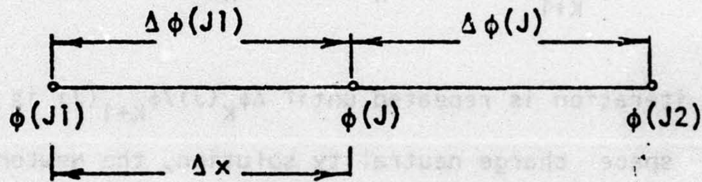

Figure 11. Using the same points as space charge points and field points

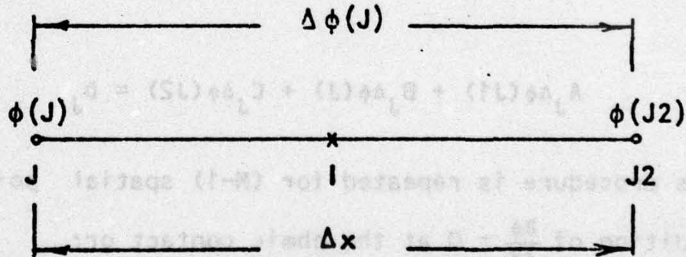

Figure 12. Different space charge points and field points

$$\phi(J) = \ln\left(\frac{N_D(J)}{n_i}\right) \tag{89a}$$

while for P-type regions, $N_A(J) \simeq P(J)$ and $N_D(J) = 0$

$$\phi(J) = \ln\left(\frac{n_i}{N_A(J)}\right) \tag{89b}$$

Starting with either equation (89a), or (89b) the correction in $\phi(J)$, for each iteration is:

$$\Delta\phi_{K+1}(J) = -F[\phi_K(J)]/F'[\phi_K(J)]$$

The iteration is repeated until $\Delta\phi_K(J)/\phi_{K+1}(J)$ is very small. Then having the space charge neutrality solution, the Newton-Raphson method is applied to solve equation (87) as follows:

$$\frac{\partial G}{\partial\phi(J1)}\Delta\phi(J1) + \frac{\partial G}{\partial\phi(J)}\Delta\phi(J) + \frac{\partial G}{\partial\phi(J2)}\Delta\phi(J2) = -G \tag{90}$$

or

$$A_J\Delta\phi(J1) + B_J\Delta\phi(J) + C_J\Delta\phi(J2) = D_J \tag{91}$$

This procedure is repeated for (M-1) spatial points. Using the boundary condition of $\frac{\partial\phi}{\partial x} = 0$ at the ohmic contact or:

$$\Delta\phi(1) = \Delta\phi(2) \tag{92a}$$

$$\Delta\phi(M) = \Delta\phi(M-1) \tag{92b}$$

The following matrix equation results:

$$\begin{bmatrix} B_2 & C_2 & & & & & \\ A_3 & B_3 & C_3 & & & & \\ & \ddots & \ddots & \ddots & & & \\ & & A_J & B_J & C_J & & \\ & & & \ddots & \ddots & \ddots & \\ & & & & A_{M-1} & B_{M-1} & \end{bmatrix} \begin{bmatrix} \Delta\phi(2) \\ \Delta\phi(3) \\ \cdot \\ \cdot \\ \Delta\phi(J) \\ \cdot \\ \cdot \\ \Delta\phi(M-1) \end{bmatrix} = \begin{bmatrix} D_1 \\ D_2 \\ \cdot \\ \cdot \\ D_J \\ \cdot \\ \cdot \\ D_{M-1} \end{bmatrix} \tag{93}$$

Equation (93) is solved for each iteration by using the algorithm of Appendix B. The iteration is continued until $\Delta\phi(J)/\phi(J)$ reaches a very small number for $2 \leq J \leq M-1$. Knowing the exact spatial distribution of $\phi(x)$, the electron and hole distributions are easily obtained from equations (79) and (80).

To calculate the electric field, one has to keep in mind that the zero electron and hole currents are the main numerical constraint for thermal equilibrium. At this point we have to make a decision on whether to use different space-charge points and field points, or to consider all points as space charge and field points. Also a decision has to be made on whether to calculate the electric field directly from Poisson's equation, or to calculate it from $J_n = 0$ and $J_p = 0$. In the following discussion, these four possibilities are investigated and compared with each other.

(a) <u>Using the same points as space charge points and field points:</u>

The following quantities are defined according to Fig. 11.

$\phi(J) = \phi_r(J)/VT$

$$\Delta\phi(J1) = \phi(J) - \phi(J1)$$

$$\Delta\phi(J) = \phi(J2) - \phi(J)$$

$$\frac{\partial N(J)}{\partial x} = \frac{N(J2) - N(J1)}{2\Delta x} = \frac{n_i}{2\Delta x}\left[e^{\phi(J) + \Delta\phi(J)} - e^{\phi(J) - \Delta\phi(J1)}\right]$$

$$= \frac{N(J)}{2\Delta x}\left[e^{\Delta\phi(J)} - e^{-\Delta\phi(J1)}\right] \quad (94)$$

$$\frac{\partial P(J)}{\partial x} = \frac{n_i}{2\Delta x}\left[e^{-\phi(J) - \Delta\phi(J)} - e^{-\phi(J) + \Delta\phi(J1)}\right]$$

$$= \frac{P(J)}{2\Delta x}\left[e^{-\Delta\phi(J)} - e^{\Delta\phi(J1)}\right] \quad (95)$$

$$JN(J) = q\mu_n[E(J)\cdot N(J) + \frac{VT\cdot N(J)}{2\Delta x}(e^{\Delta\phi(J)} - e^{-\Delta\phi(J1)})] \quad (96)$$

$$JP(J) = q\mu_p[E(J)\cdot P(J) + \frac{VT\cdot P(J)}{2\Delta x}(e^{\Delta\phi(J1)} - e^{-\Delta\phi(J)})] \quad (97)$$

(i) Using Poisson's Equation:

$$E(J) = \frac{\partial\phi_r}{\partial x} = -VT\frac{(\Delta\phi(J1) + \Delta\phi(J))}{2\Delta x} \quad (98)$$

If $\Delta\phi(J)$ and $\Delta\phi(J1) << 1$, the exponential terms of equations (96) and (97) can be approximated by a linear term and only then JN and JP will have a zero value.

The total potential variation across a typical transition region, as shown in Fig. 8, is about 0.8 volts. If this region is divided into a 100 spatial points, the average value of $\Delta\phi(J)$ will be given by:

$$\Delta\phi(J) \approx \frac{0.8}{VT} \cdot \frac{1}{100} = 0.3 \text{ which is not} << 1$$

Therefore, this method requires a very large number of spatial points, which makes it difficult to use.

(ii) Using the current equations:

In order to calculate the electric field from equations (96) and (97) so that JN = JP = 0, $\Delta\phi(J)$ has to be equal to $\Delta\phi(J1)$, which is not the case, expecially if a non-uniform mesh is used.

(b) Different space-charge points and field points:

Following the same argument as in (a) and using Fig. 12, we get:

$$\frac{\partial N(I)}{\partial x} = \frac{n_i}{\Delta x}[e^{\phi(J) + \Delta\phi(J)} - e^{\phi(J)}] \tag{99}$$

$$= \frac{N(J)}{\Delta x}[e^{\Delta\phi(J)} - 1]$$

$$\frac{\partial P(I)}{\partial x} = \frac{n_i}{\Delta x}[e^{-\phi(J2)} - e^{-\phi(J2) + \Delta\phi(J)}] \tag{100}$$

$$= \frac{P(J2)}{\Delta x}[1 - e^{\Delta\phi(J)}]$$

for E < 0:

$$JN(I) = q\mu_n[E(I)\cdot N(J) + \frac{VT\cdot N(J)}{\Delta x}(e^{\Delta\phi(J)}-1)] \tag{101}$$

$$JP(I) = q\mu_p[E(I)\cdot P(J2) + \frac{VT\cdot P(J2)}{\Delta x}(e^{\Delta\phi(J)}-1)] \tag{102}$$

(i) Using Poisson's Equation:

$$E(I) = \frac{VT}{\Delta x}\Delta\phi(J) \tag{103}$$

As in case (a-i), the use of Poisson's equation requires a very large number of spatial points to insure that JN = JP = 0.

(ii) Using the current equations:

From equations (101) and (102), one can easily obtain a value for the electric field to satisfy the zero current requirement

$$E(I) = \frac{VT}{\Delta x}(1 - e^{\Delta\phi(J)}) \tag{104}$$

Therefore the electric field is calculated using equation (104).

It should be noted that for small values of $\Delta\phi(J)$, equation (104) can be approximated by equation (103). Therefore, in order to satisfy both the zero current condition and Poisson's equation, $\Delta\phi(J)$ should have a small value inside the P^+-N transition region. As a result, a uniform space-mesh is safe to use in the case of a low doped N-region, while for high doping where the potential variation in the P^+-N transition region is large, a nonuniform space-mesh is necessary.

Although all the formulations and numerical methods apply for any two terminal one-dimensional semiconductor device, from now on we will be concerned with discussing and presenting the results for the P^+-N-N^+ diode structure.

Device under consideration:

The typical construction of a semiconductor P^+-N-N^+ diode is illustrated in Fig. 13. The junction may be circular with a diameter of 3 mils to 5 mils. The lightly doped N^- bulk semiconductor may be doped from $10^{14}/cm^3$ to $10^{16}/cm^3$ and has a thickness (w) from 10 microns to 300 microns. The P^+-region is heavily doped from $10^{18}/cm^3$ to $10^{20}/cm^3$. The N^+-region is

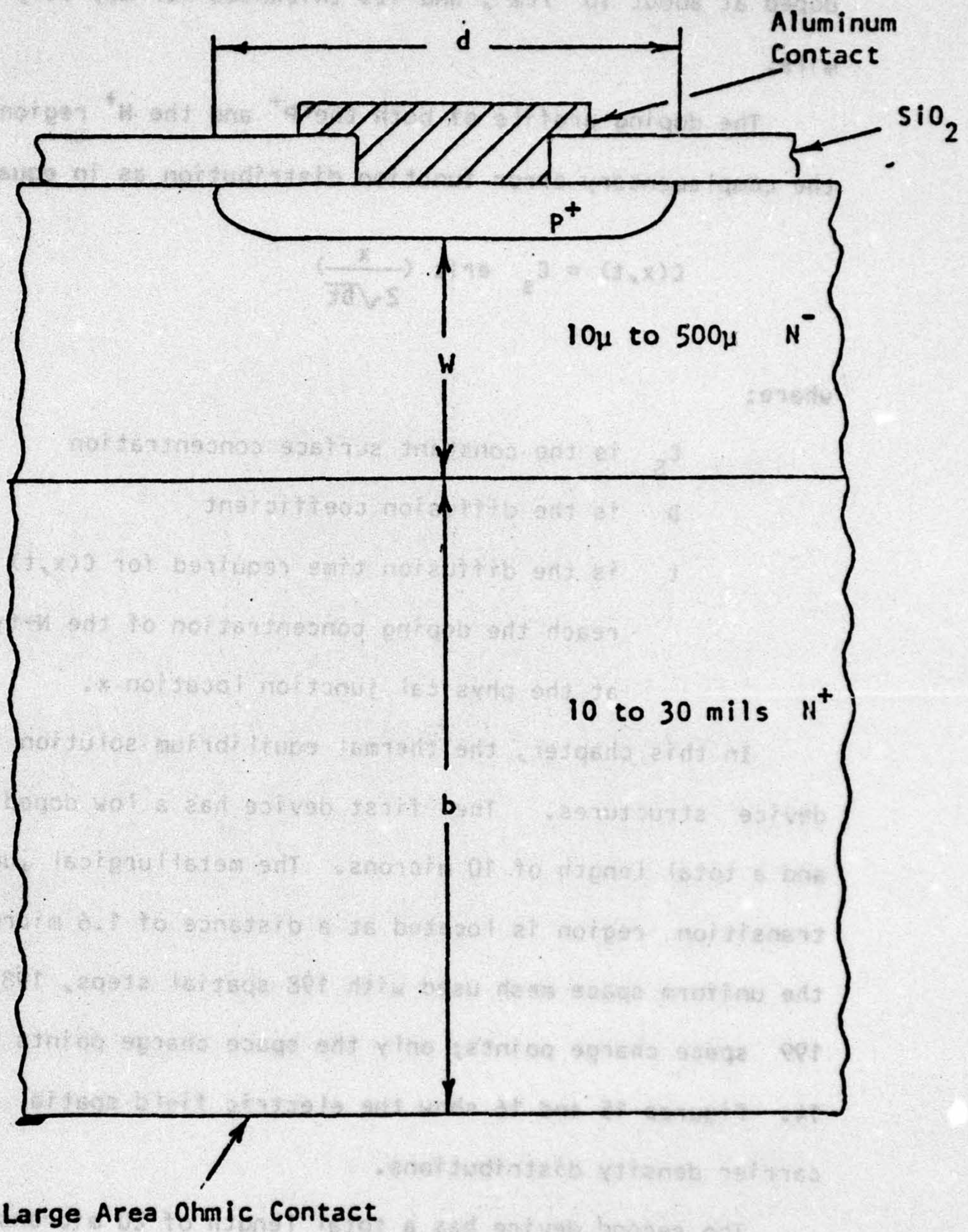

Figure 13. Cross section of a typical $P^+N^-P^+$ junction.

doped at about $10^{19}/cm^3$, and its thickness (b) may vary between 10 and 25 mils.

The doping profile of both the P^+ and the N^+ regions is approximated by the complementary error function distribution as in equation (105).

$$C(x,t) = C_s \ \text{erfc}\left(\frac{x}{2\sqrt{Dt}}\right) \tag{105}$$

where:

C_S is the constant surface concentration

D is the diffusion coefficient

t is the diffusion time required for C(x,t) to reach the doping concentration of the N-type at the physical junction location x.

In this chapter, the thermal equilibrium solution is presented for two device structures. The first device has a low doped N region of $10^{14}/cm^3$ and a total length of 10 microns. The metallurgical junction of the P^+-N transition region is located at a distance of 1.6 microns. Figure 14 shows the uniform space mesh used with 198 spatial steps, 198 field points, and 199 space charge points; only the space charge points are indicated in Fig. 14. Figures 15 and 16 show the electric field spatial distribution and the carrier density distributions.

The second device has a total length of 20 microns. The doping density of the N-region is chosen to be equal to $2.64 \times 10^{15}/cm^3$ in order to match the fabricated device discussed in Chapter VI. A non-uniform space-mesh is used with 239 spatial steps, 239 field points, and 240 space charge points. As discussed before, the point density is highest inside the P^+-N transition region, to insure a small potential variation "$\Delta\phi_r(J)$". Figures 17 and 18 show the electric field distribution and the carrier density distributions

of the second device.

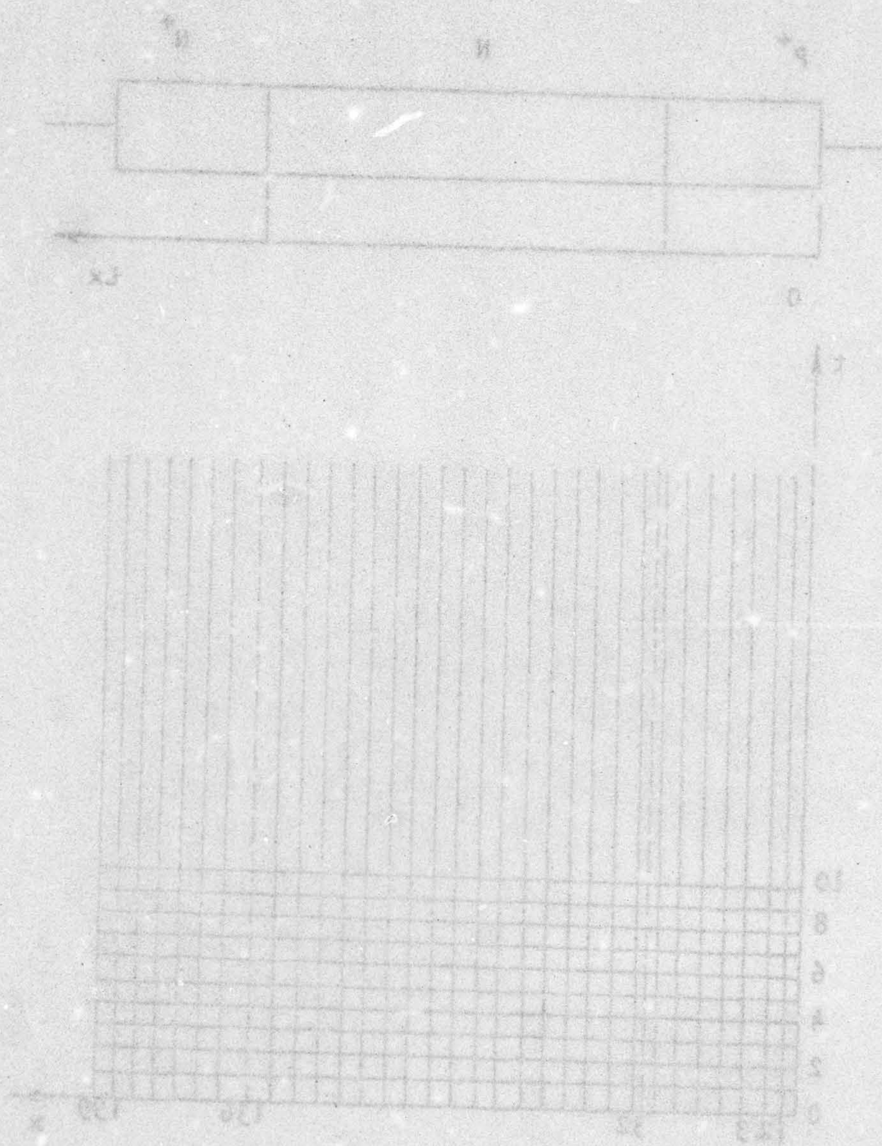

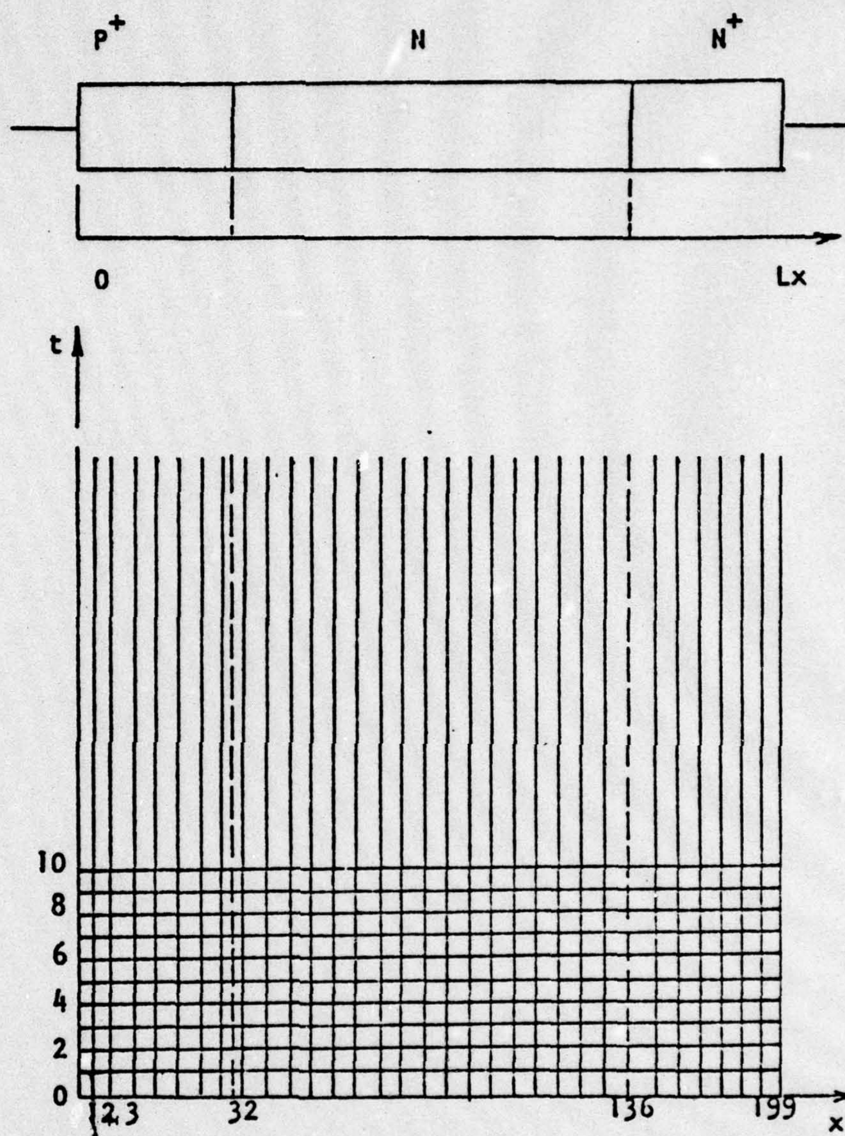

Figure 14. Uniform time-space mesh

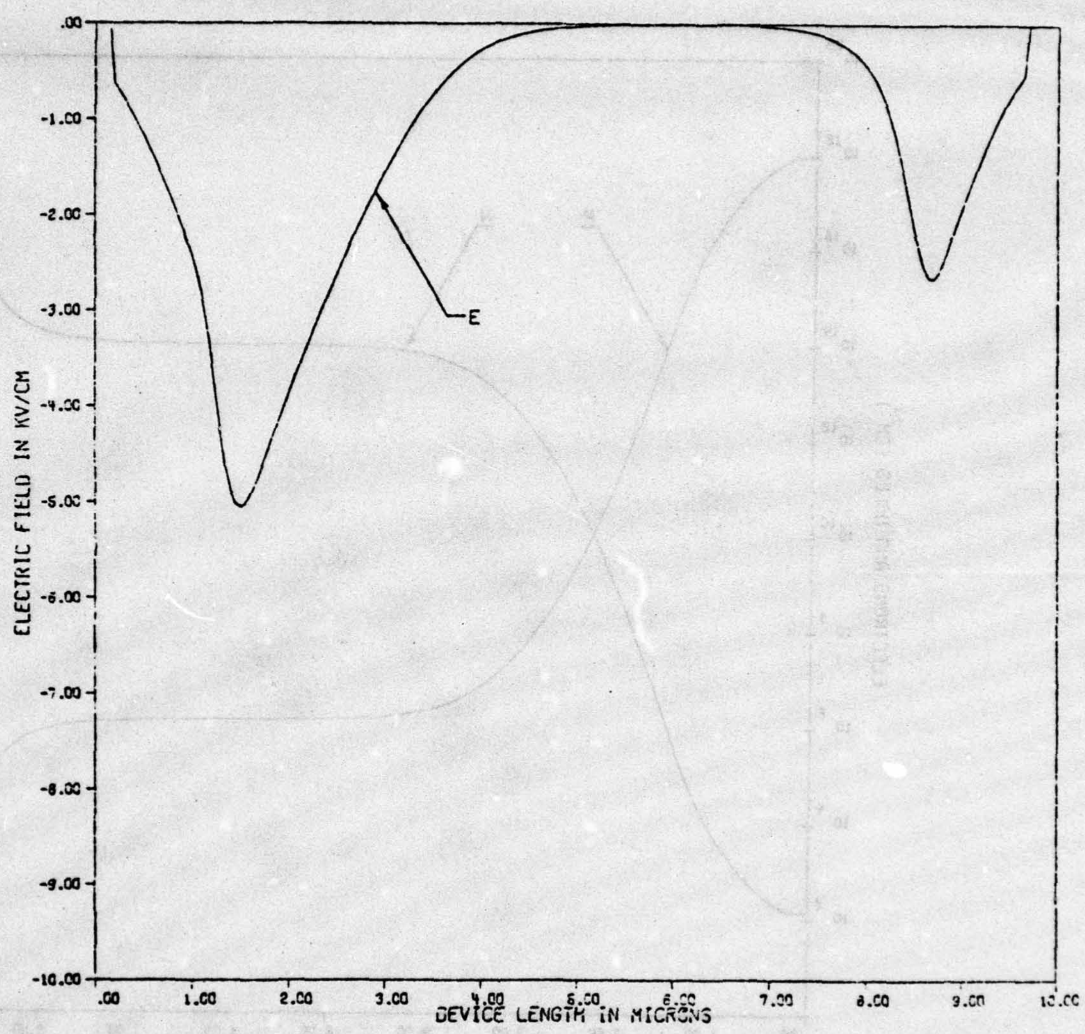

Figure 15. Electric field distribution at thermal equilibrium for diode #1

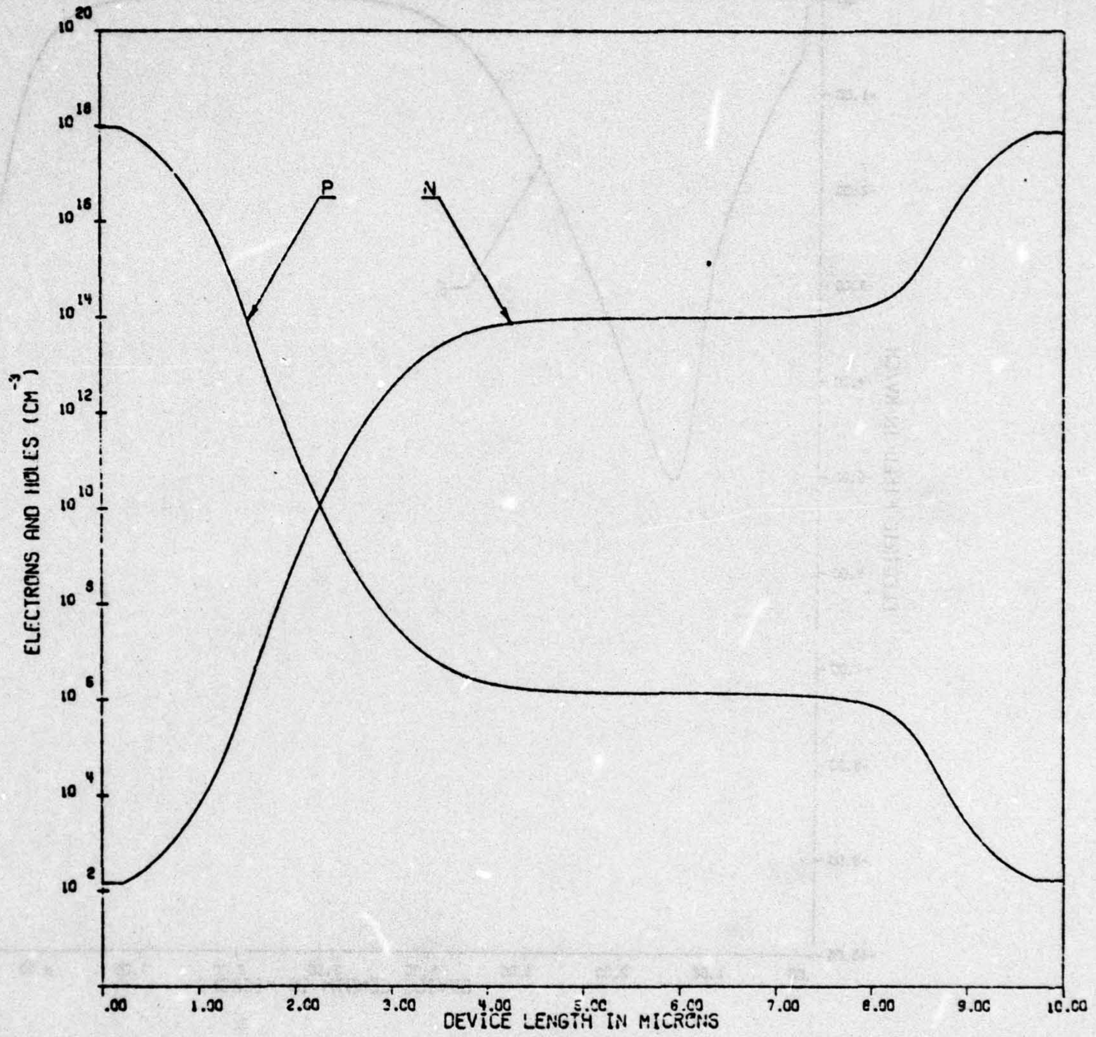

Figure 16. Electron and hole density distribution of thermal equilibrium for diode #1

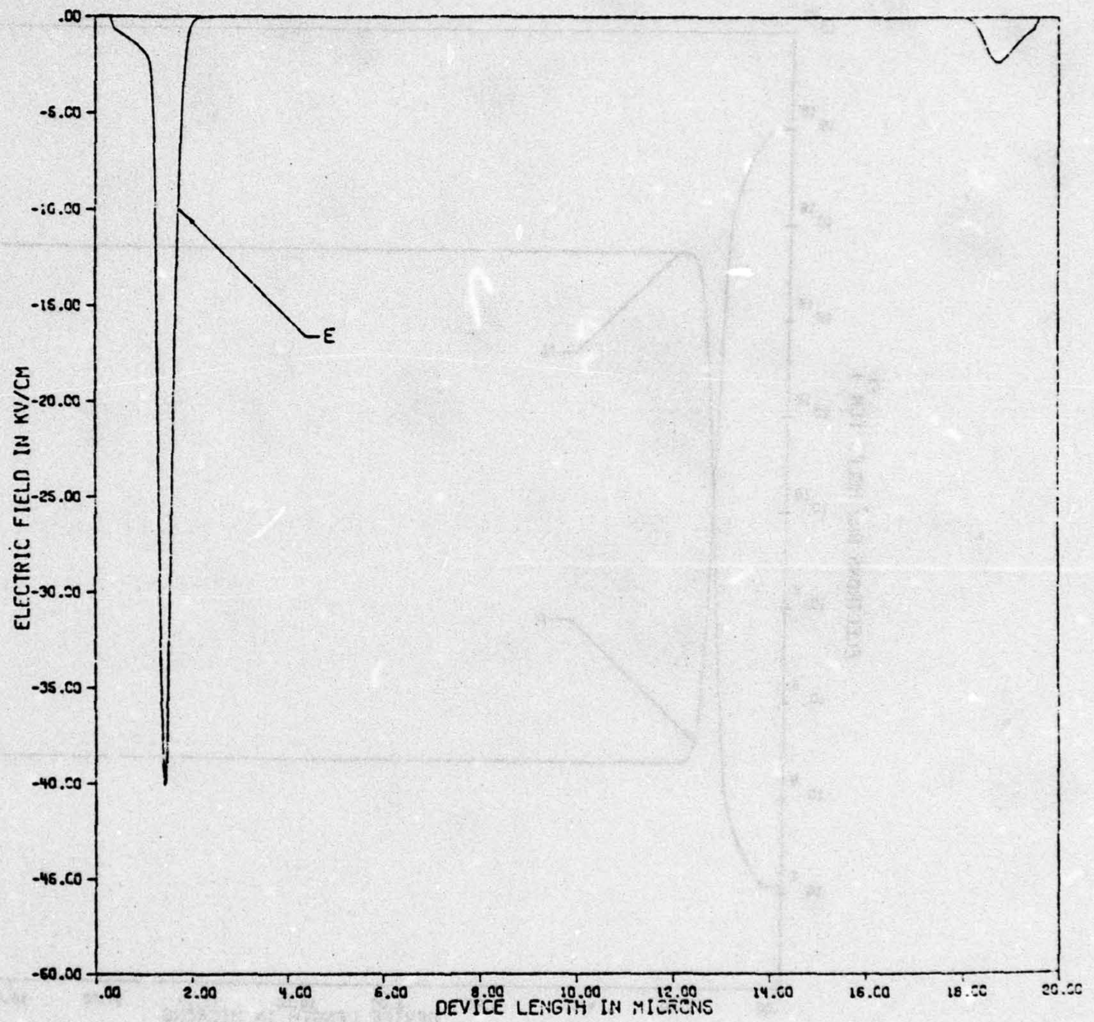

Figure 17. Electric field distribution at thermal equilibrium for diode #2

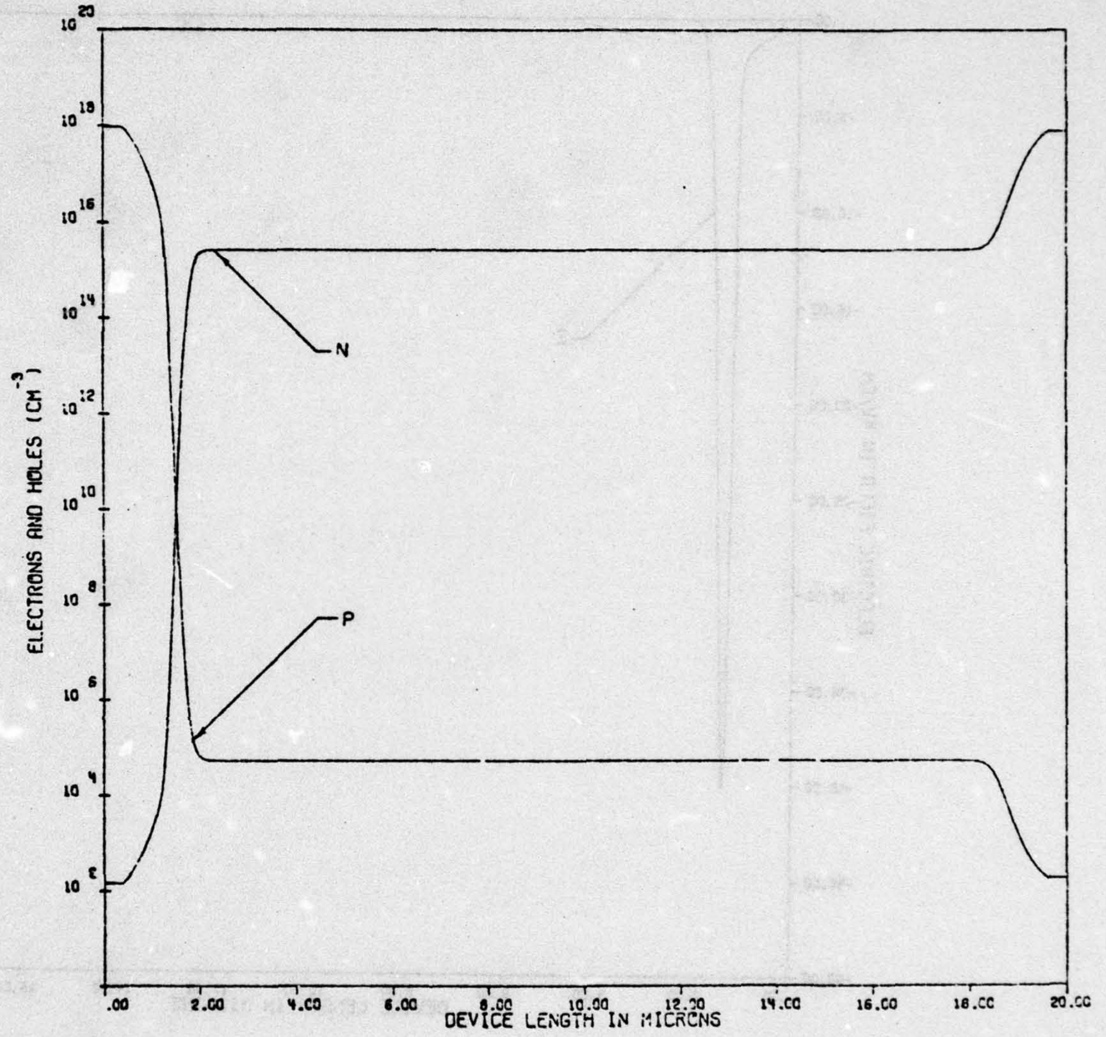

Figure 18. Electron and hole density distributions at thermal equilibrium for diode #2

CHAPTER IV

REVERSE PULSED CASE

In this chapter, the numerical technique and the formulations of Chapter II are used to solve for the transient behavior of the two P^+-N-N^+ structures previously considered in Chapter III.

The device of 10 microns length and $10^{14}/cm^3$ doping density is considered first. The thermal equilibrium conditions of Figs. 15 and 16 in Chapter III are used here as the initial conditions. The external excitation is in the form of a negative current step, of -10 amp/cm^2 amplitude, and 0.1 nanosecond rise time. The numerical solution simulates the device transient behavior, between the thermal equilibrium and the steady state. The time step "Δ t" is chosen, when implementing the computer program, in such a way that a converged solution is obtained after a maximum of five iterations for each instant of time. If not, a new Δt is chosen.

Fig. 19 shows the applied current density vs. time, along with the ouput voltage vs. time. The time axis is divided into three regions, A, B, and C. Region A describes the behavior between thermal equilibrium and punch through of the N^--region. Region B is the period between punch through and the beginning of impact ionization. Region C describes the avalanching period unitl a steady state solution is reached.

The spatial distributions of the electrons and holes, displacement current density, carrier current densities, and electric field for the instants of time indicated in Fig. 19 are shown in Figs. 20 through 38.

The transient solution of region A is shown in Figs. 20 to 23. Immediately after the current step application, the electric field will change in a short period of time in order to support the total current. Therefore,

the displacement current component will be equal to the total current throughout the whole device according to the following equation:

$$J(T=0^+) = \dot{\varepsilon}\frac{\partial E}{\partial t}$$

Shortly after the step application, the build-up of ohmic voltage across the heavily doped P^+-region causes the total current to be carried by the majority carriers (holes) instead of being carried by the displacement current. Similarly, in the N^--N^+ region, the total current will be carried by majority carriers (electrons). In the P^+-N depletion region, the carrier densities are very small, too small to support any current. Therefore, the total current will still be carried by the displacement current component as shown in Fig. 21. At this stage, the $\frac{1}{q}\left|\frac{\partial J_n}{\partial x}\right|$ term of the electron continuity equation near the depletion region is negative in the N^-- region. Also, the $-\frac{1}{q}\left|\frac{\partial J_p}{\partial x}\right|$ term of the hole continuity equation is negative between the P^+ -region and the depletion region as shown in Fig. 20 for times t_1 to t_6. Mathematically this causes recombination of majority carriers near the depletion region. Physically it represents extraction of majority carriers, or in other words, depletion. This carrier depletion is shown in Fig. 22 for region A. As the N^--region continues to deplete, the displacement current component replaces the electron current component. Therefore, the electric field increases negatively in the depletion region until punch-through at time t6. These electric field distributions are shown in Fig. 23 for region A.

In Region B, the current is mainly carried by the displacement current in the N^--depleted region as shown in Fig. 25. The carrier depletion continues at a much slower rate as shown in Fig. 25. The electric field continues to increase negatively until it approaches the avalanching value of

time in nanoseconds

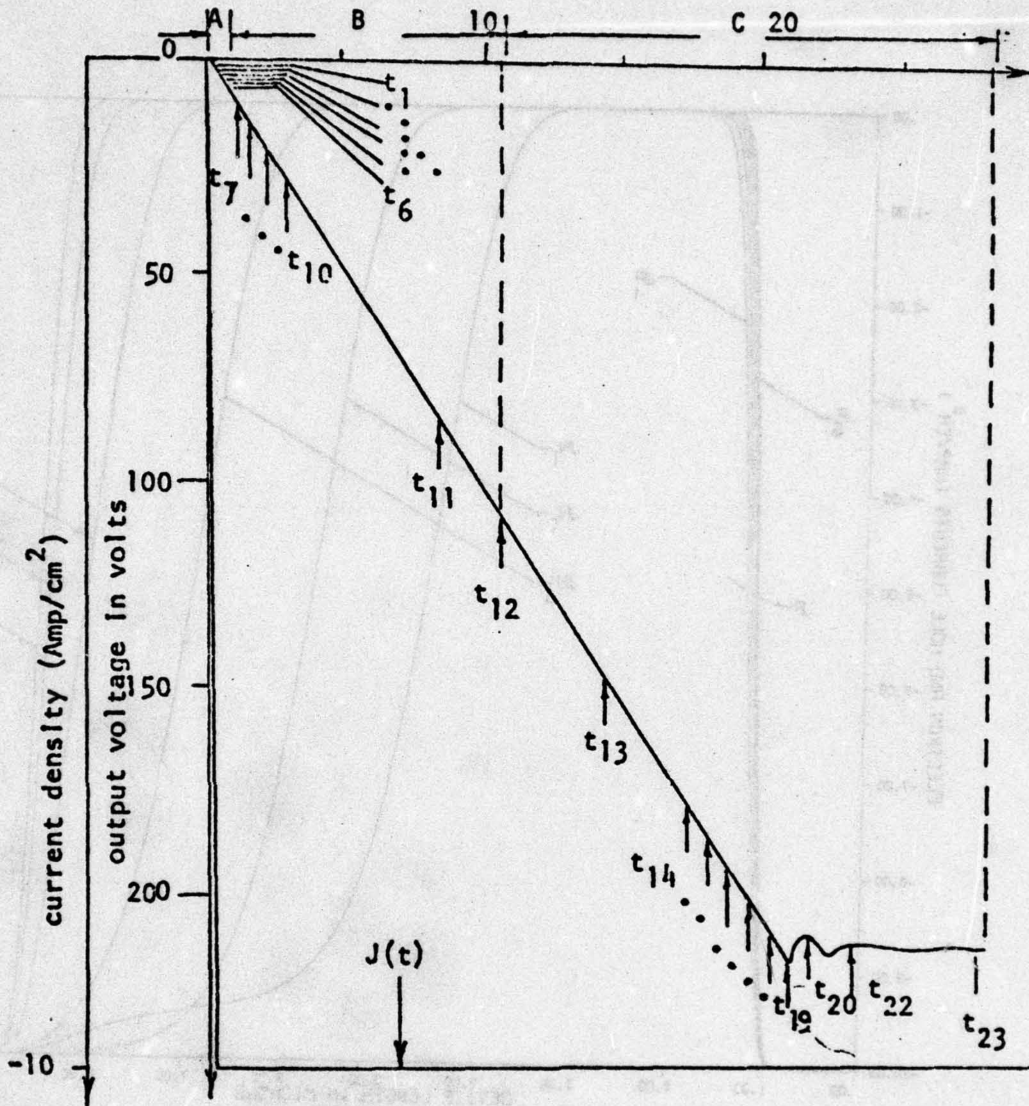

Figure 19. Output voltage for the reverse biased case (first device)

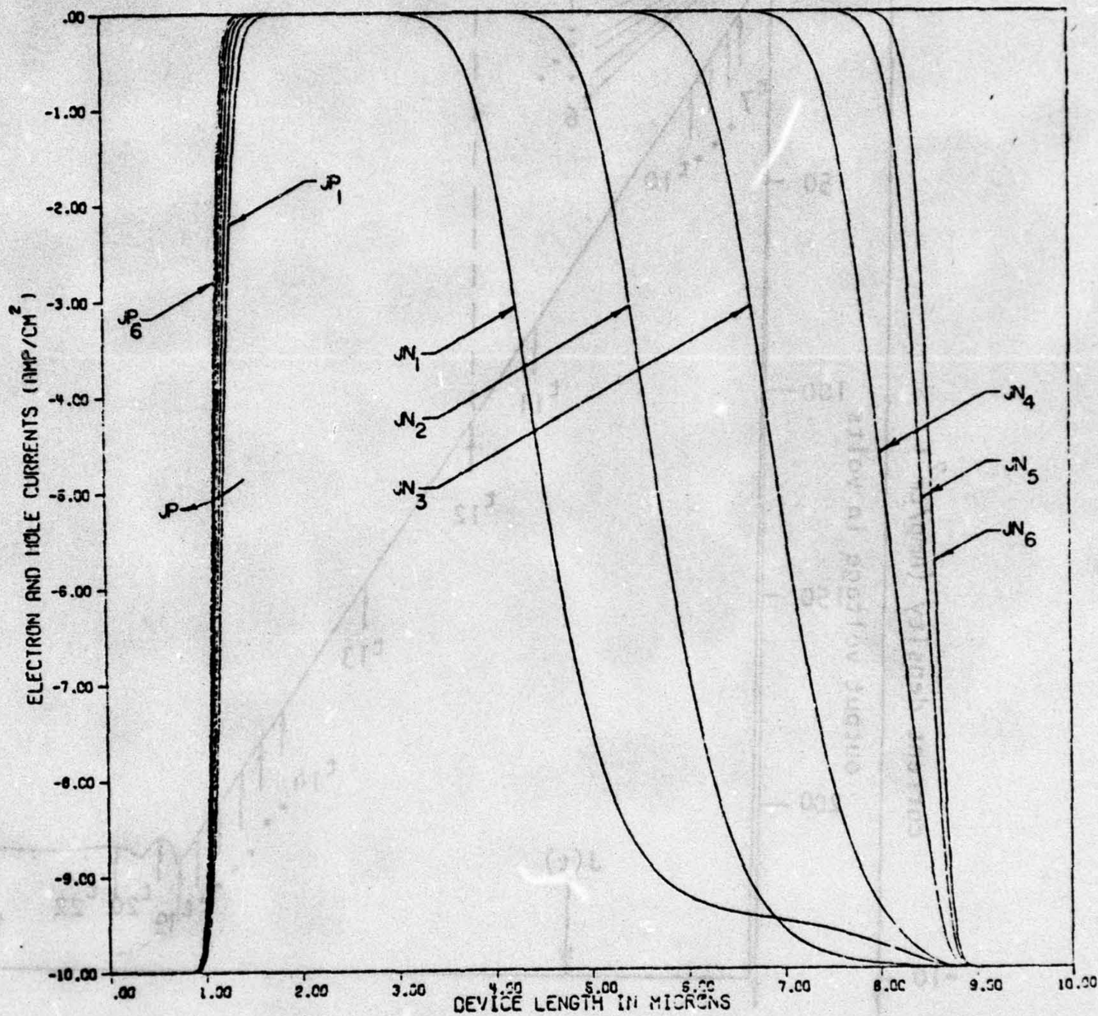

Figure 20. Electron and hole current density distributions for time instants t_1 to t_6 as shown in Figure 19

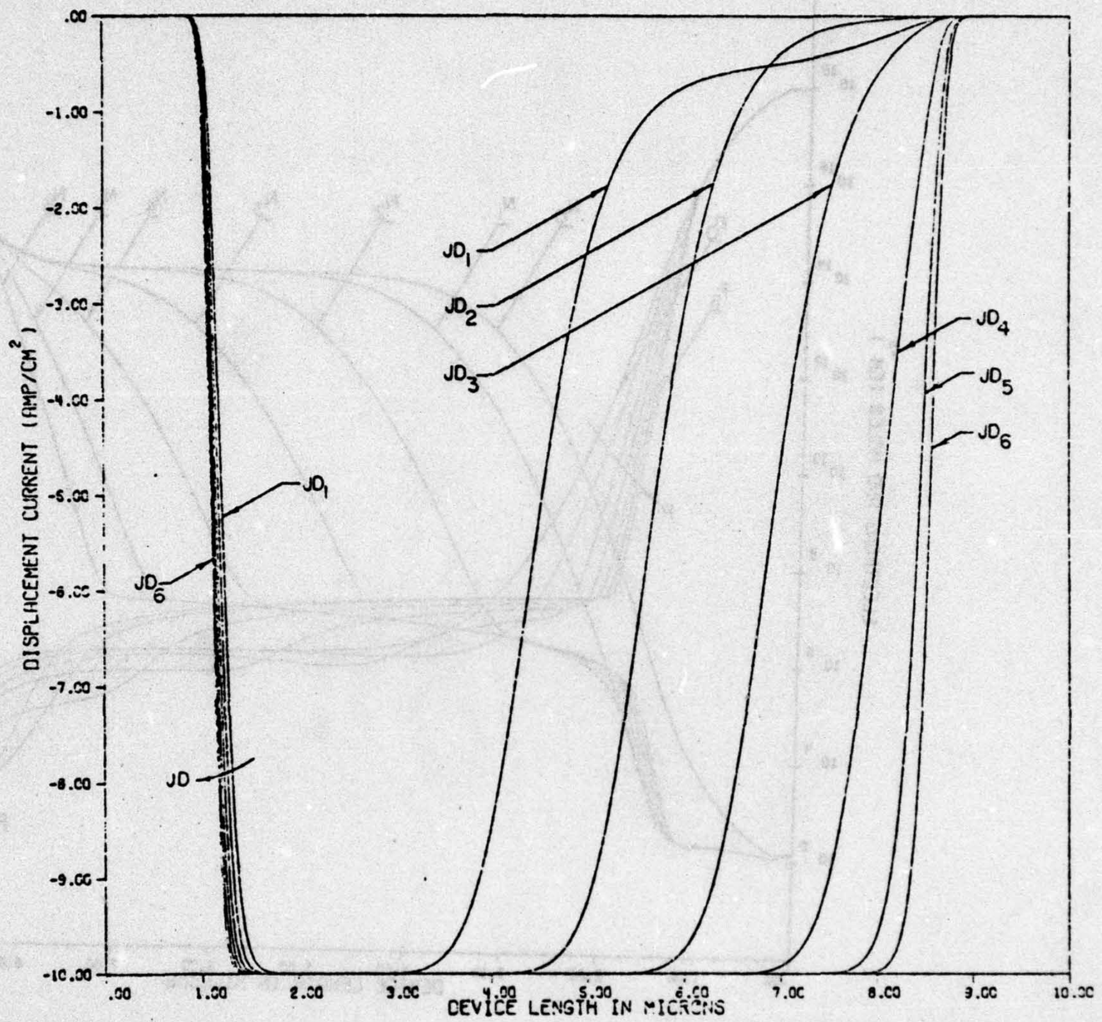

Figure 21. Displacement current density distribution for time instants t_1 to t_6 as shown in Figure 19

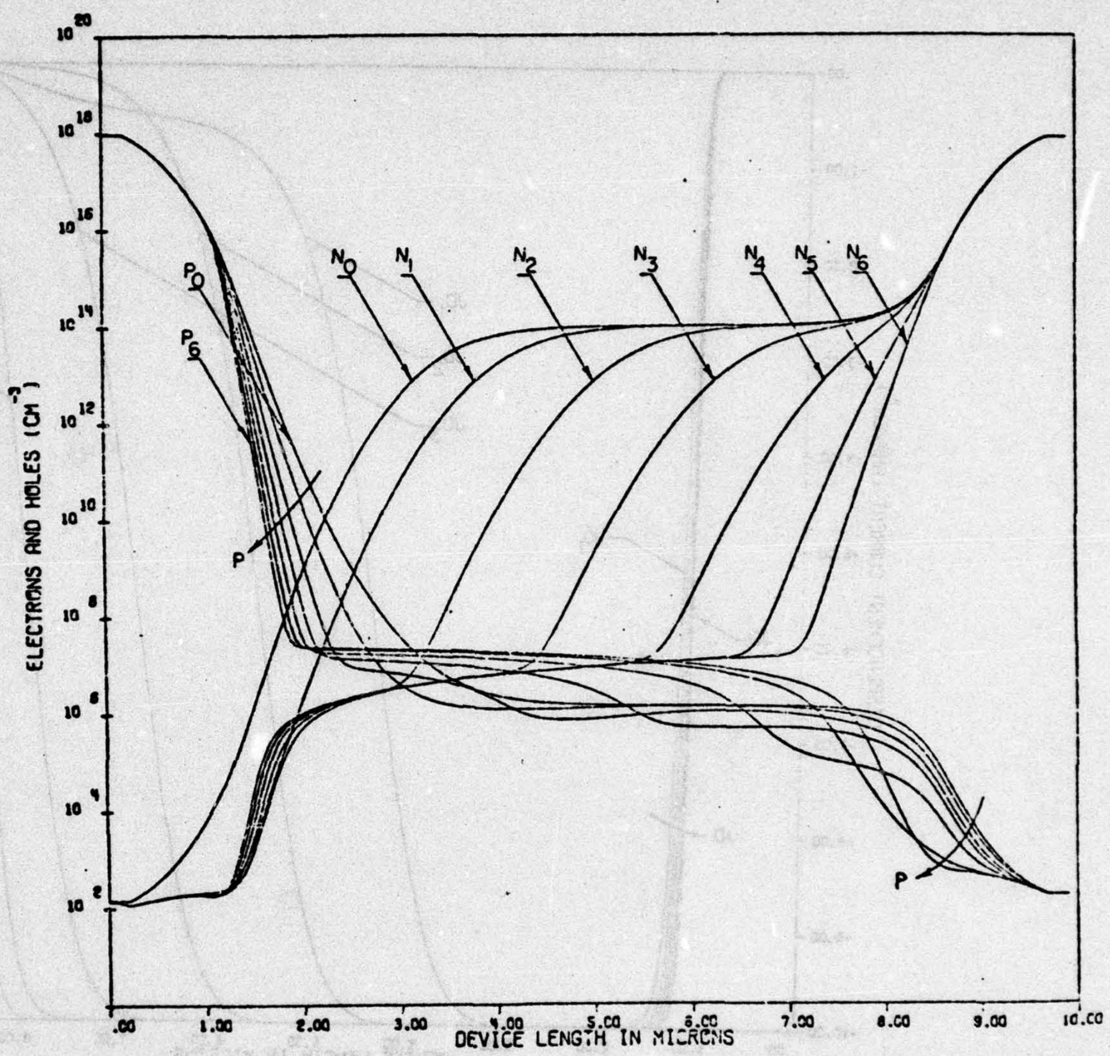

Figure 22. Electron and hole densities for time instants t_1 to t_6 as shown in Figure 19

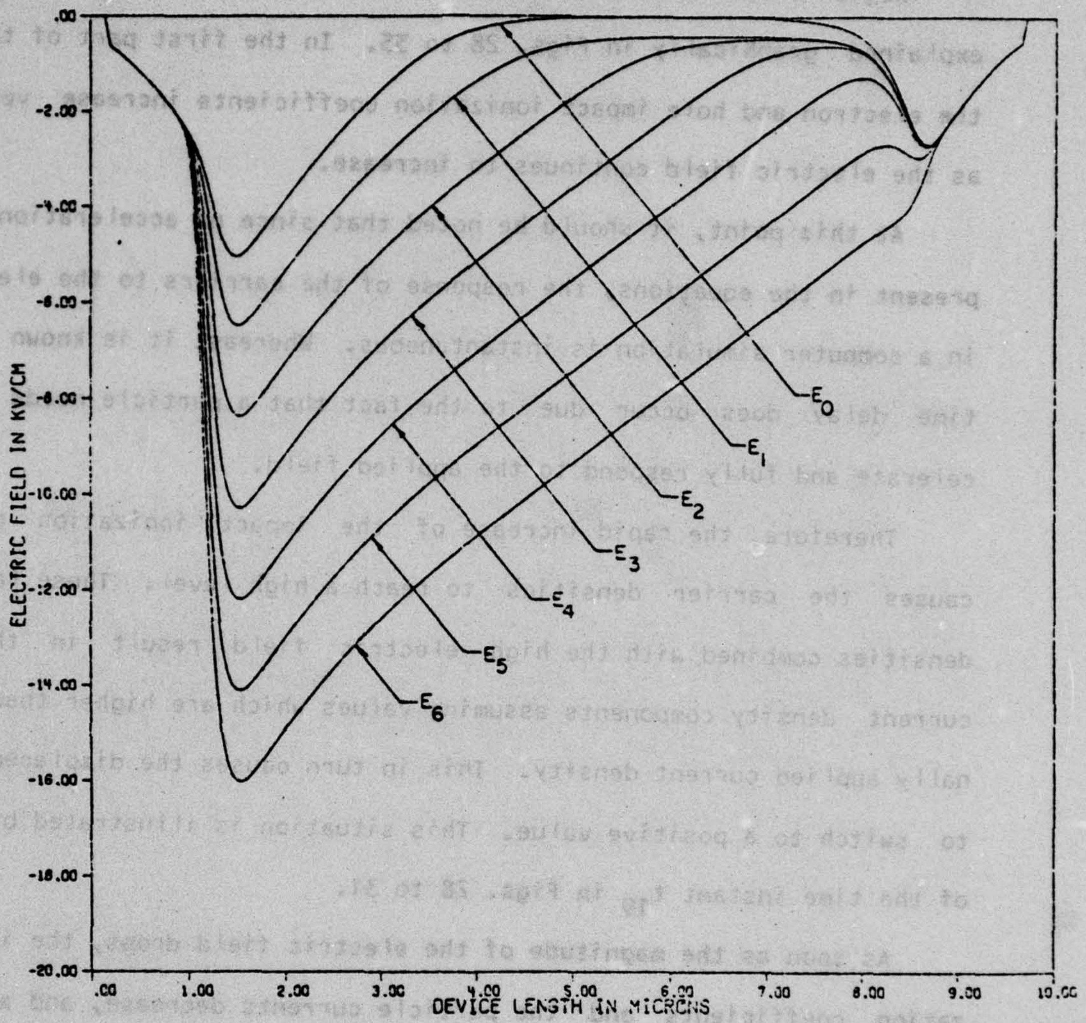

Figure 23. Electric field distribution for time densities t_1 to t_6 as shown in Figure 19

about $-2x10^5$ volt/cm at time t_{13} as shown in Fig. 27.

Region C describes the avalanching part of the transient behavior as explained graphically in Figs. 28 to 35. In the first part of this region, the electron and hole impact ionization coefficients increase very rapidly as the electric field continues to increase.

At this point, it should be noted that since no acceleration terms are present in the equations, the response of the carriers to the electric field in a computer simulation is instantaneous. Whereas, it is known that some time delay does occur due to the fact that a particle needs time to accelerate and fully respond to the applied field.

Therefore, the rapid increase of the impact ionization coefficients causes the carrier densities to reach a high level. These large carrier densities combined with the high electric field result in the particle current density components assuming values which are higher than the externally applied current density. This in turn causes the displacement current to switch to a positive value. This situation is illustrated by the curves of the time instant t_{19} in Figs. 28 to 31.

As soon as the magnitude of the electric field drops, the impact ionization coefficients and the particle currents decrease, and again a large portion of the total current is carried by the displacement current component as illustrated by the curves of the time instant t_{20} in Figs. 32 to 35. This trade-off between the particle currents and the displacement current causes the output voltage to fluctuate around an average value as shown in Fig. 19 until near steady state where the particle current densities replace the displacement current component as shown in Figs. 32 and 33. At steady state, the displacement current component vanishes throughout the whole device. Also, the generation rate due to the avalanching mechanism is

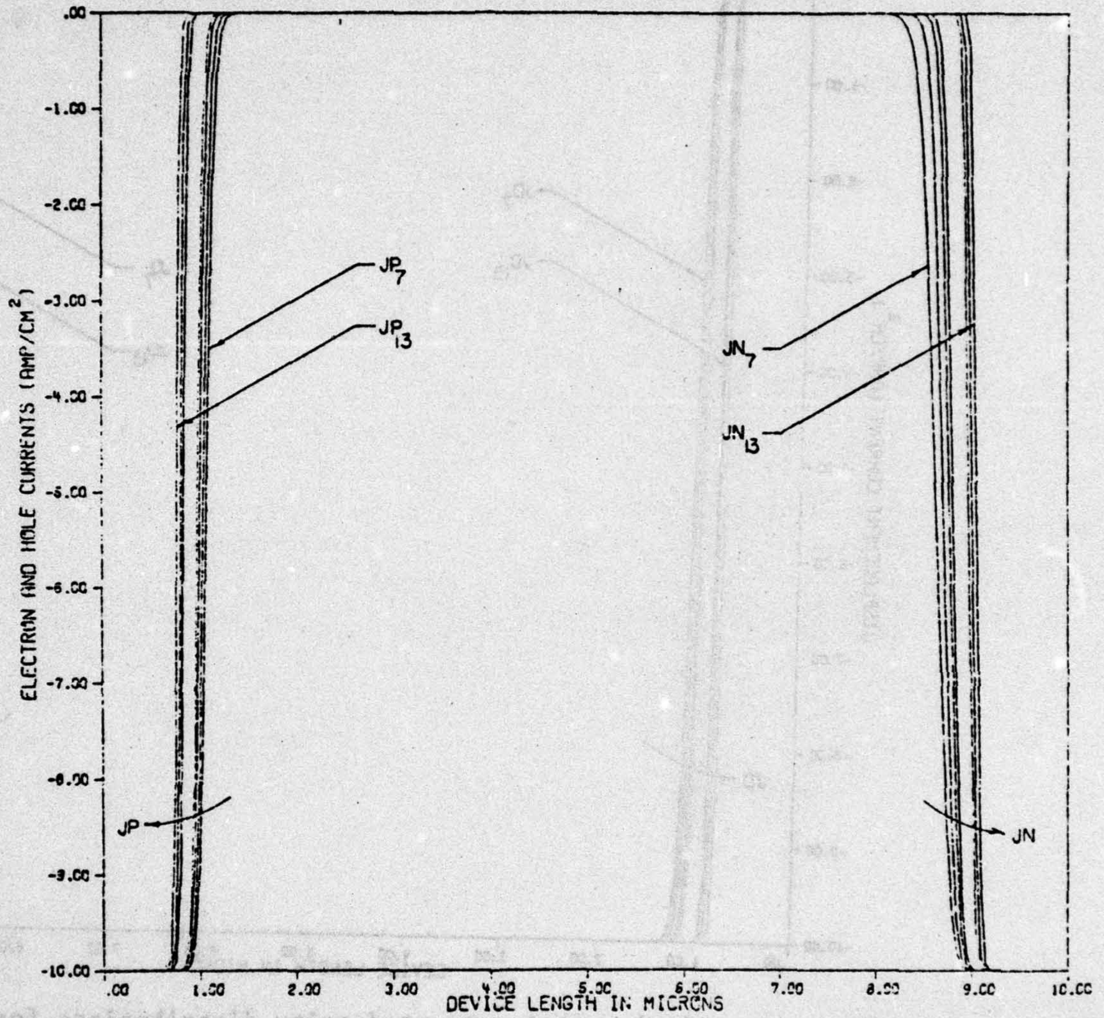

Figure 24. Electron and hole current density distribution for time instants t_7 to t_{13} as shown in Figure 19

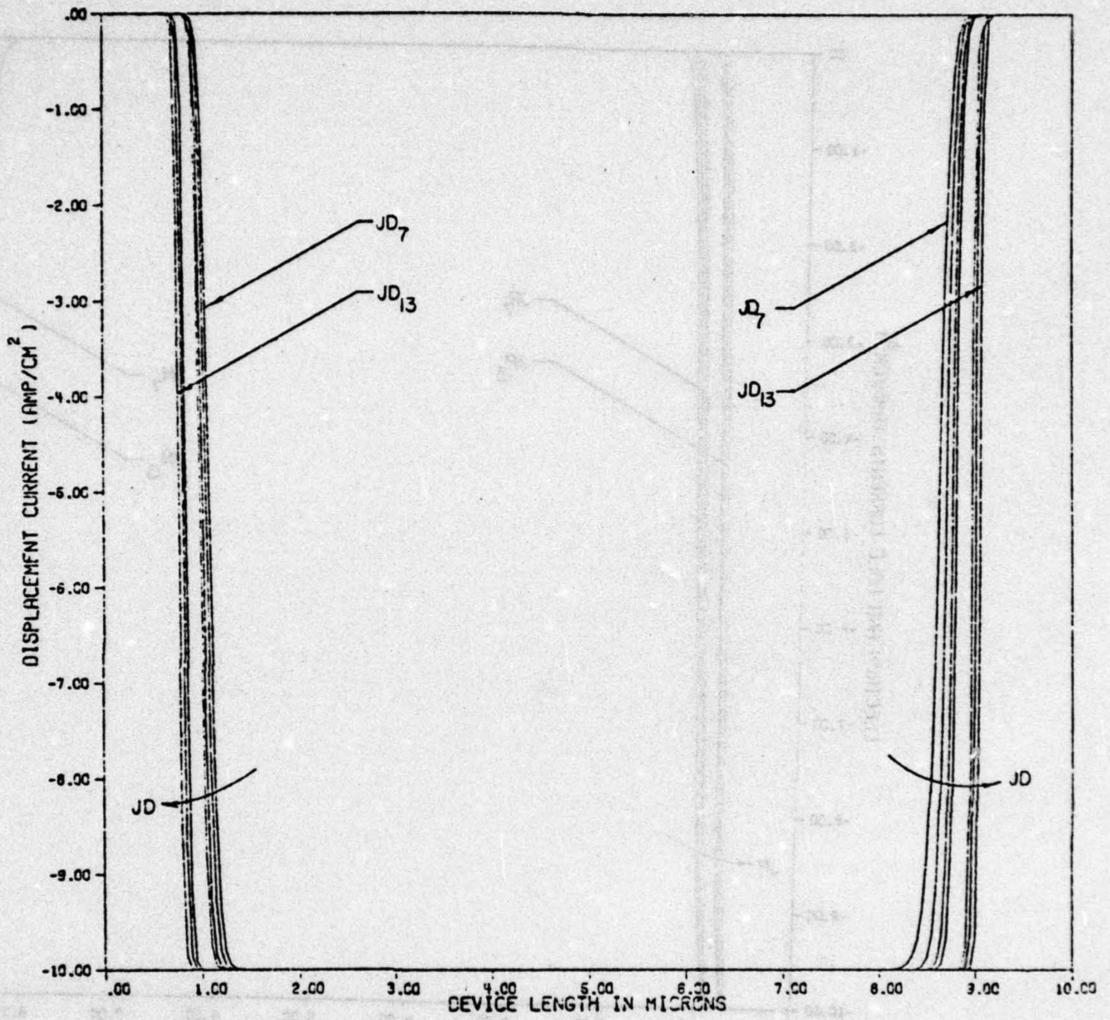

Figure 25. Displacement current density distributions for time instants t_7 to t_{13} as shown in Figure 19

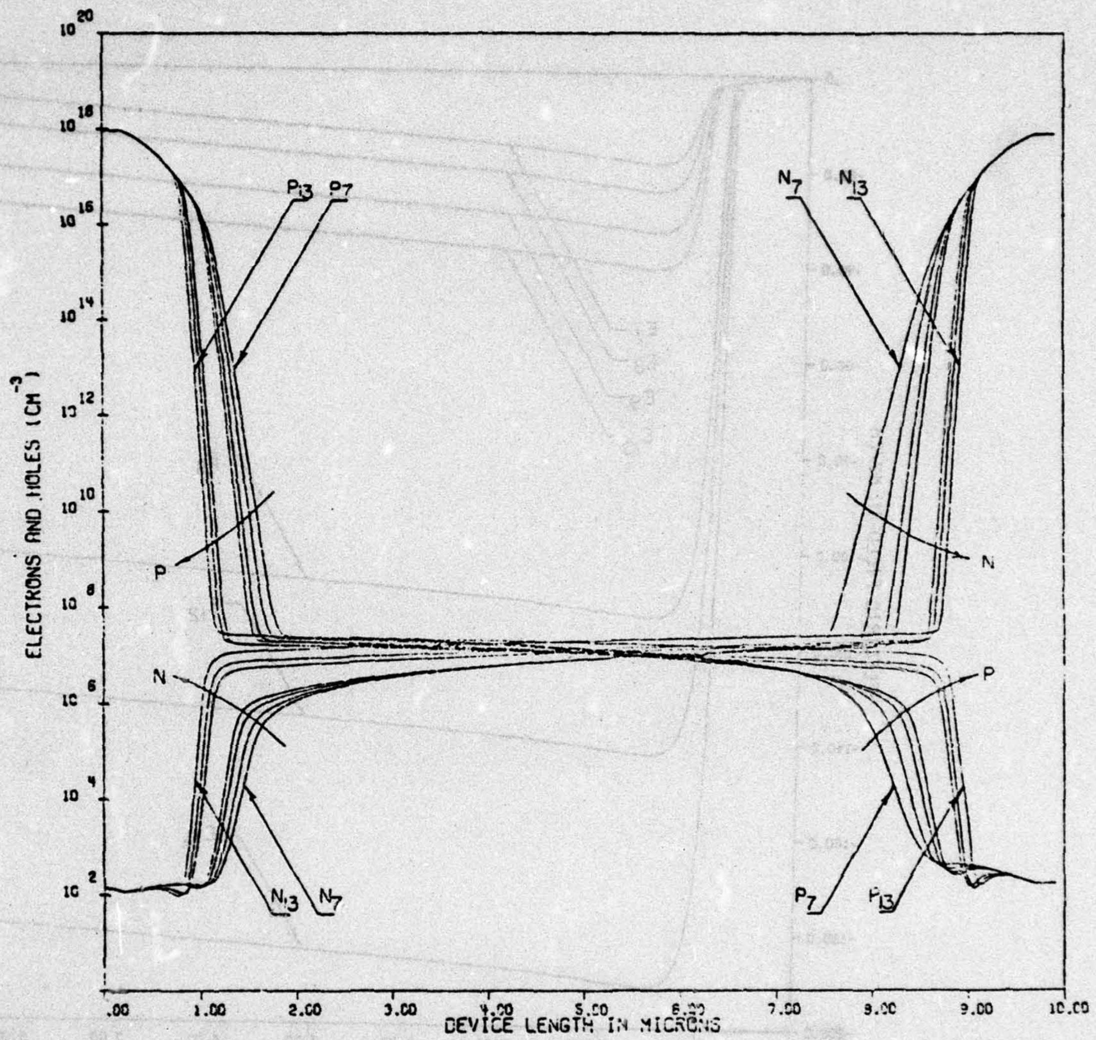

Figure 26. Electron and hole density distributions at time instants t_7 to t_{13} as shown in Figure 19

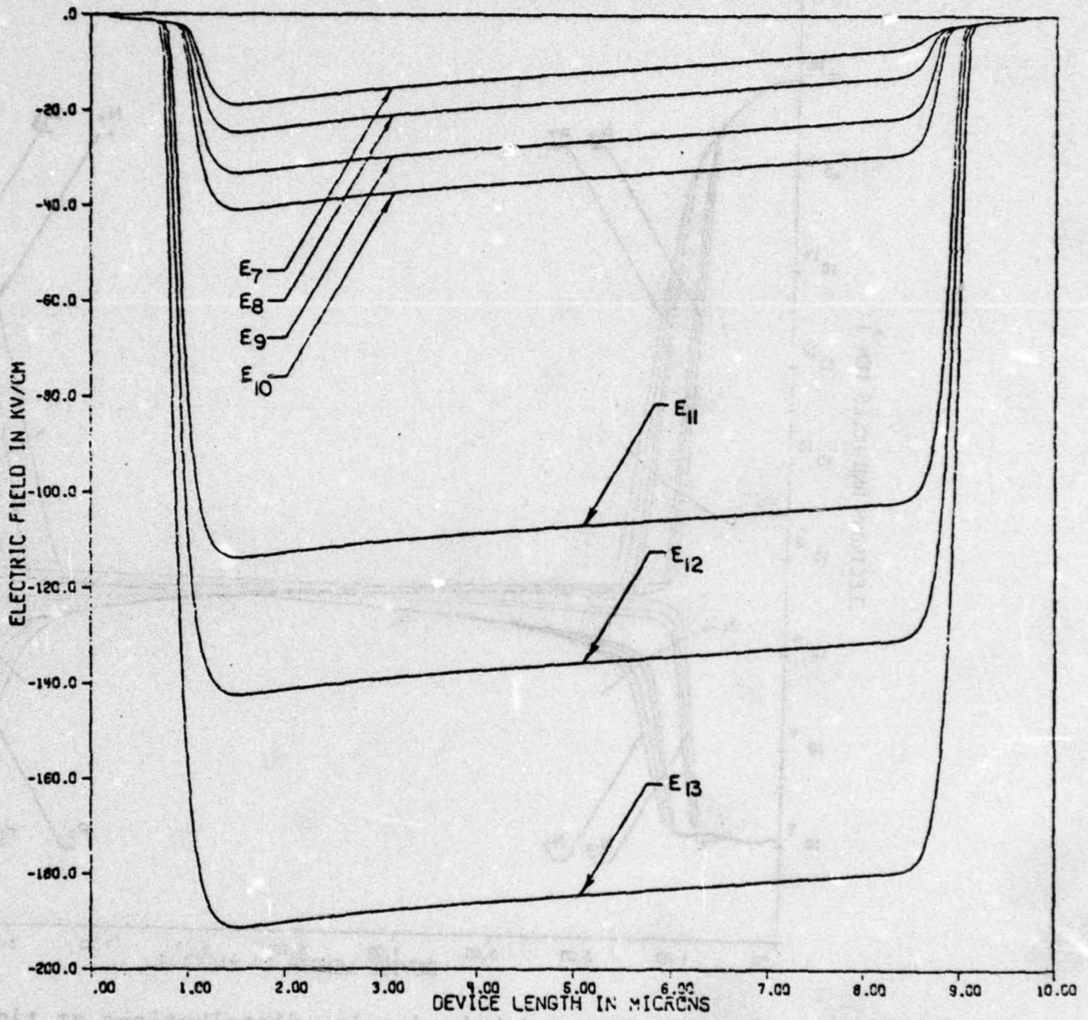

Figure 27. Electric field distribution at time instants t_7 to t_{13} as shown in Figure 19

balanced by the rate of carriers extraction, and the Shockley-Read-Hall recombination rate. In other words, the two continuity equations reduce to the following two equations.

$$G = -R + \frac{1}{q}\left|\frac{\partial J_n}{\partial x}\right| \tag{106}$$

$$G = -R - \frac{1}{q}\left|\frac{\partial J_p}{\partial x}\right| \tag{107}$$

where:

$$G = \alpha|J_n| + \beta|J_p|$$

$$R = \frac{pn - n_i^2}{T_0(p+n+2n_i)}$$

From equations (106) and (107), it is clear that at steady state the following condition has to be satisfied

$$\frac{1}{q}\left|\frac{\partial J_n}{\partial x}\right| = -\frac{1}{q}\left|\frac{\partial J_p}{\partial x}\right| \tag{108}$$

The steady state solution is shown in Figs. 36 to 38. The solution in Fig. 19 is obtained by dividing the time axis into a thousand non-uniformly spaced time steps. The time steps have relatively small values in region A, where the time variations of all the physical quantities are changing very rapidly. In region B, the time steps are made larger since the electric field is mainly the variable quantity. In region C, the time step is reduced again in the avalanching period. As the steady state approaches, the

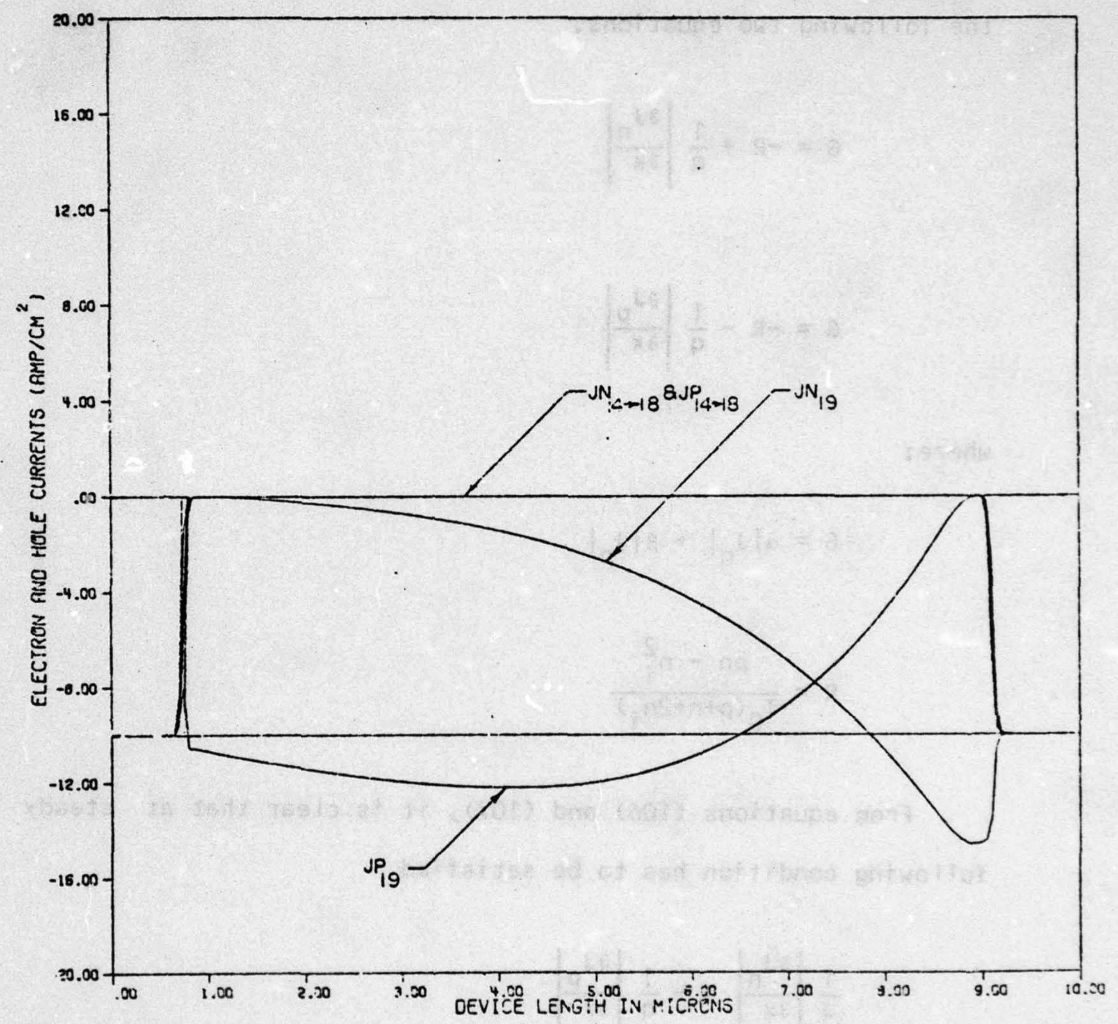

Figure 28. Electron and hole current density distributions for time instants t_{14} to t_{19} as shown in Figure 19

AD-A053 539 PURDUE UNIV LAFAYETTE IND SCHOOL OF ELECTRICAL ENGI--ETC F/G 9/1
THE ANOMALOUS VOLTAGE RESPONSE OF THE P(+)N-N(+) DEVICE AND ITS--ETC(U)
DEC 77 G W NEUDECK, L R RAZOUK DAAG29-77-G-0191
UNCLASSIFIED TR-EE-77-40 ARO-15322.1-A-EL NL

2 OF 3
AD
A053539

2 OF 3
AD
A053539

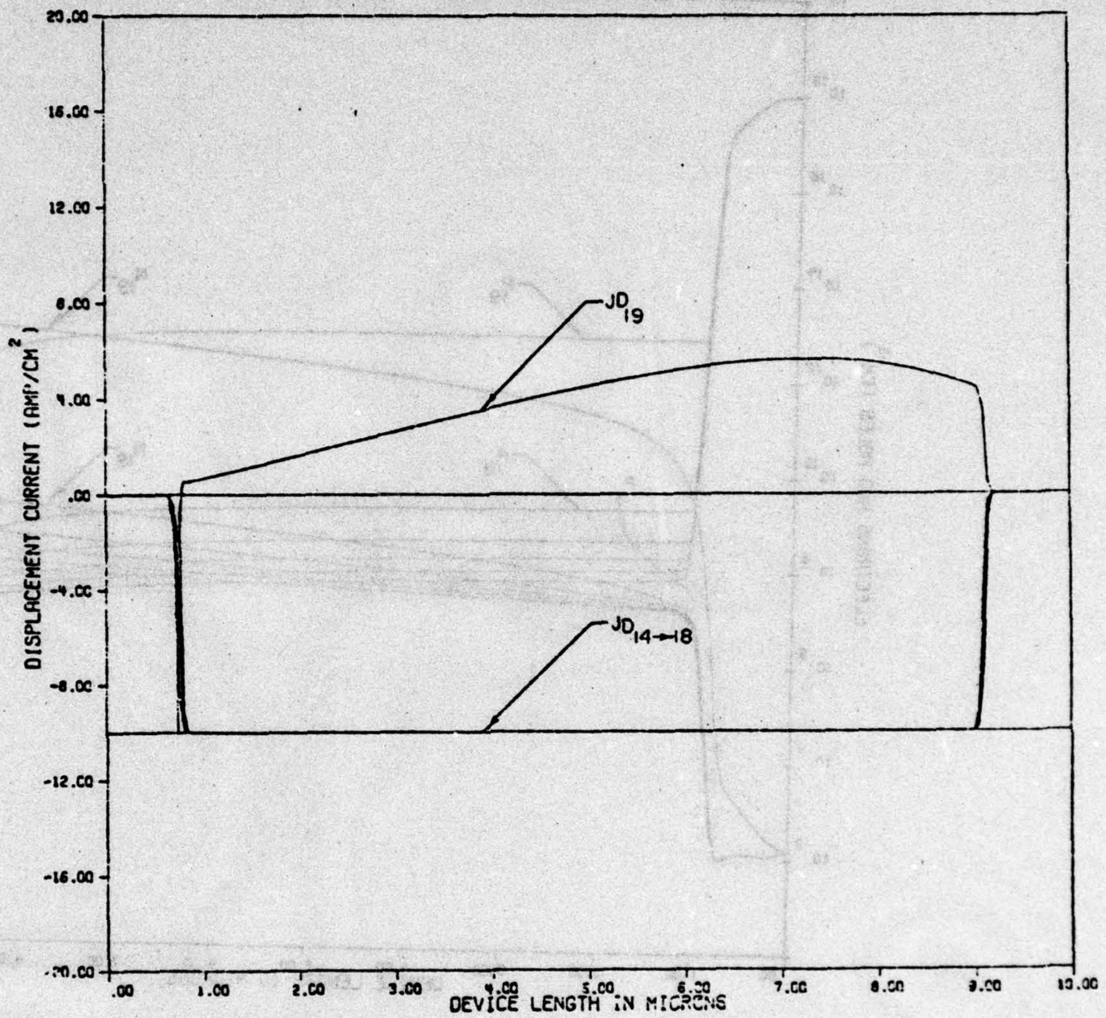

Figure 29. Displacement current density distribution for time instants t_{14} to t_{19} as shown in Figure 19

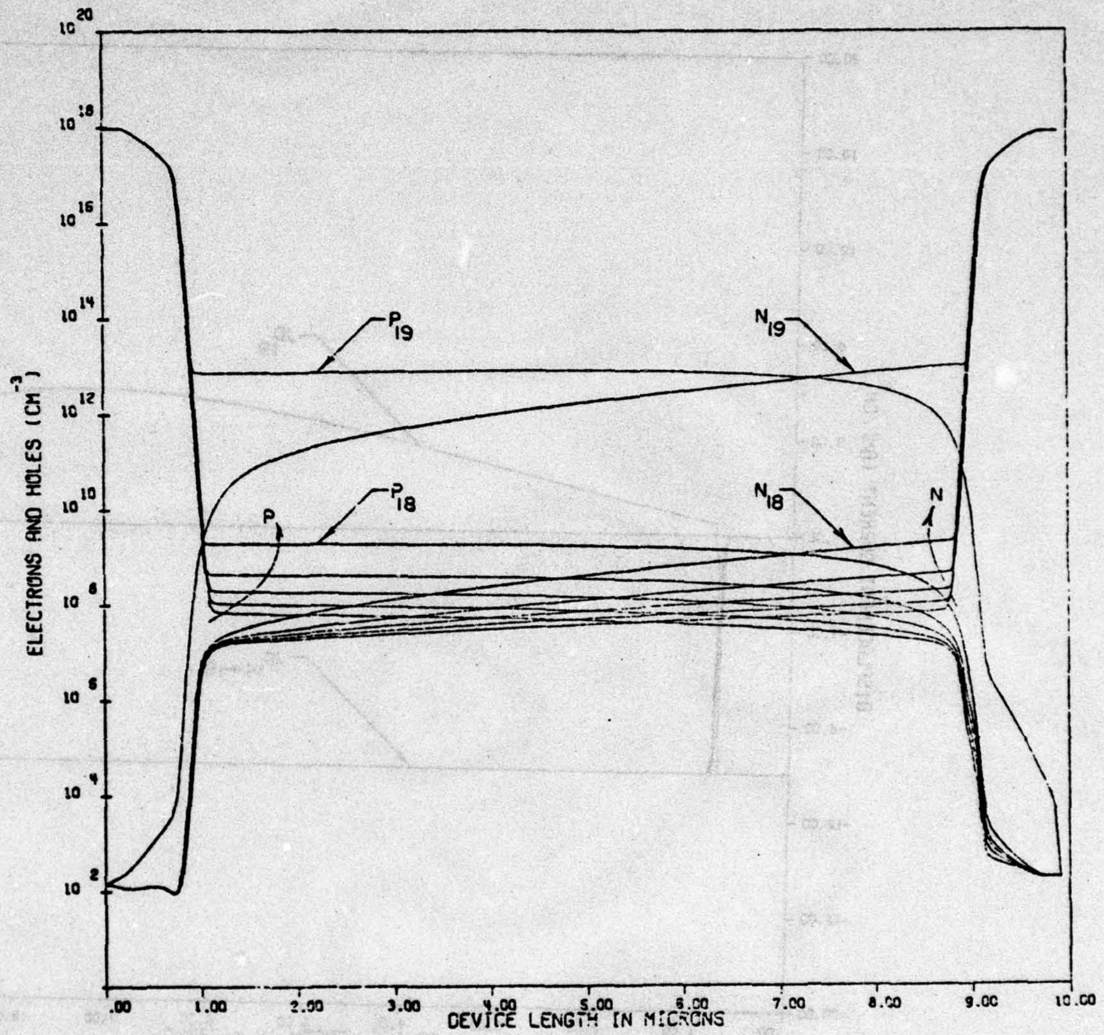

Figure 30. Electron and hole density distributions for time instants t_{14} to t_{19} as shown in Figure 19

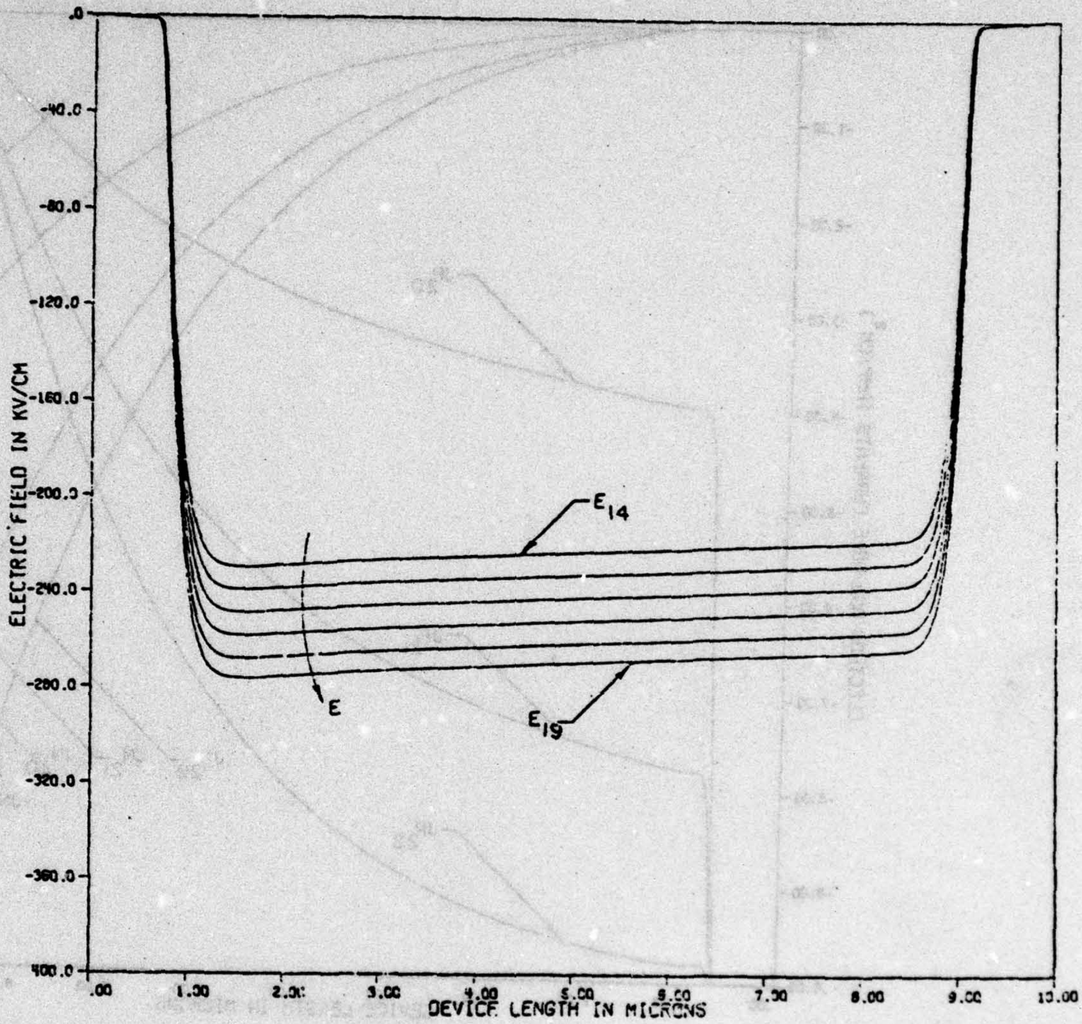

Figure 31. Electric field distribution for time instants t_{14} to t_{19} as shown in Figure 19

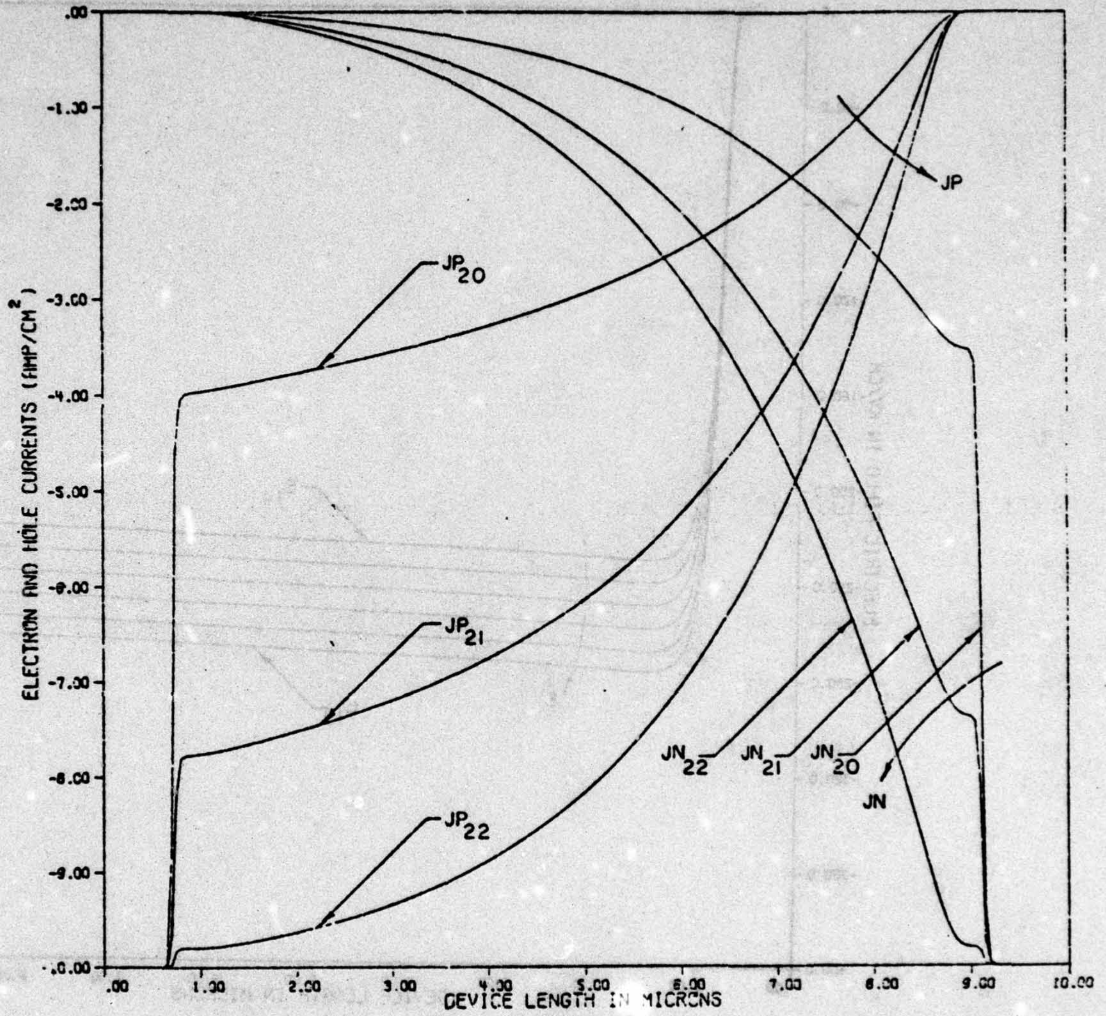

Figure 32. Electron and hole current density distributions for time instants t_{20} to t_{22} as shown in Figure 19

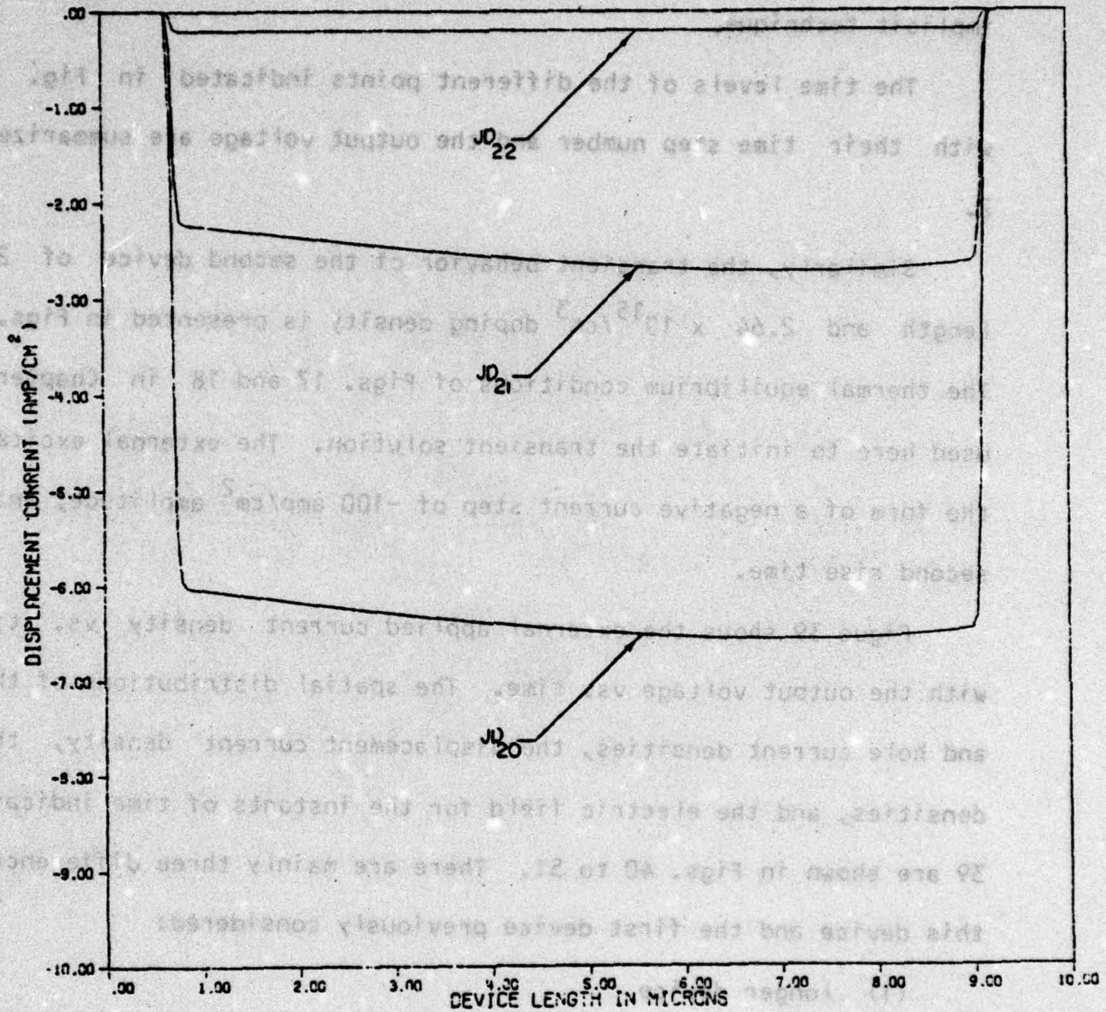

Figure 33. Displacement current density distribution for time instants t_{20} to t_{22} as shown in Figure 19

time step could be adjusted to a very large value without any loss of accuracy. This is one of the very important advantages of using the iterative implicit technique.

The time levels of the different points indicated in Fig. 19, along with their time step number and the output voltage are summarized in Table 2.

Similarly, the transient behavior of the second device of 20 microns length and 2.64 x $10^{15}/cm^3$ doping density is presented in Figs. 39 to 51. The thermal equilibrium conditions of Figs. 17 and 18 in Chapter III are used here to initiate the transient solution. The external excitation is in the form of a negative current step of -100 amp/cm^2 amplitude, and 0.1 nano second rise time.

Figue 39 shows the external applied current density vs. time, along with the output voltage vs. time. The spatial distributions of the electron and hole current densities, the displacement current density, the carrier densities, and the electric field for the instants of time indicated in Fig. 39 are shown in Figs. 40 to 51. There are mainly three differences between this device and the first device previously considered:

(1) longer device

(2) higher doping in the N^--region

(3) larger amplitude of the externally applied current step.

The second difference causes a slower rate of the N^--region depletion, which is combined with the first difference result in a partial depletion of the N^--region at steady state. The second and third differences are responsible for the higher electric field, and for more voltage fluctuation near steady state.

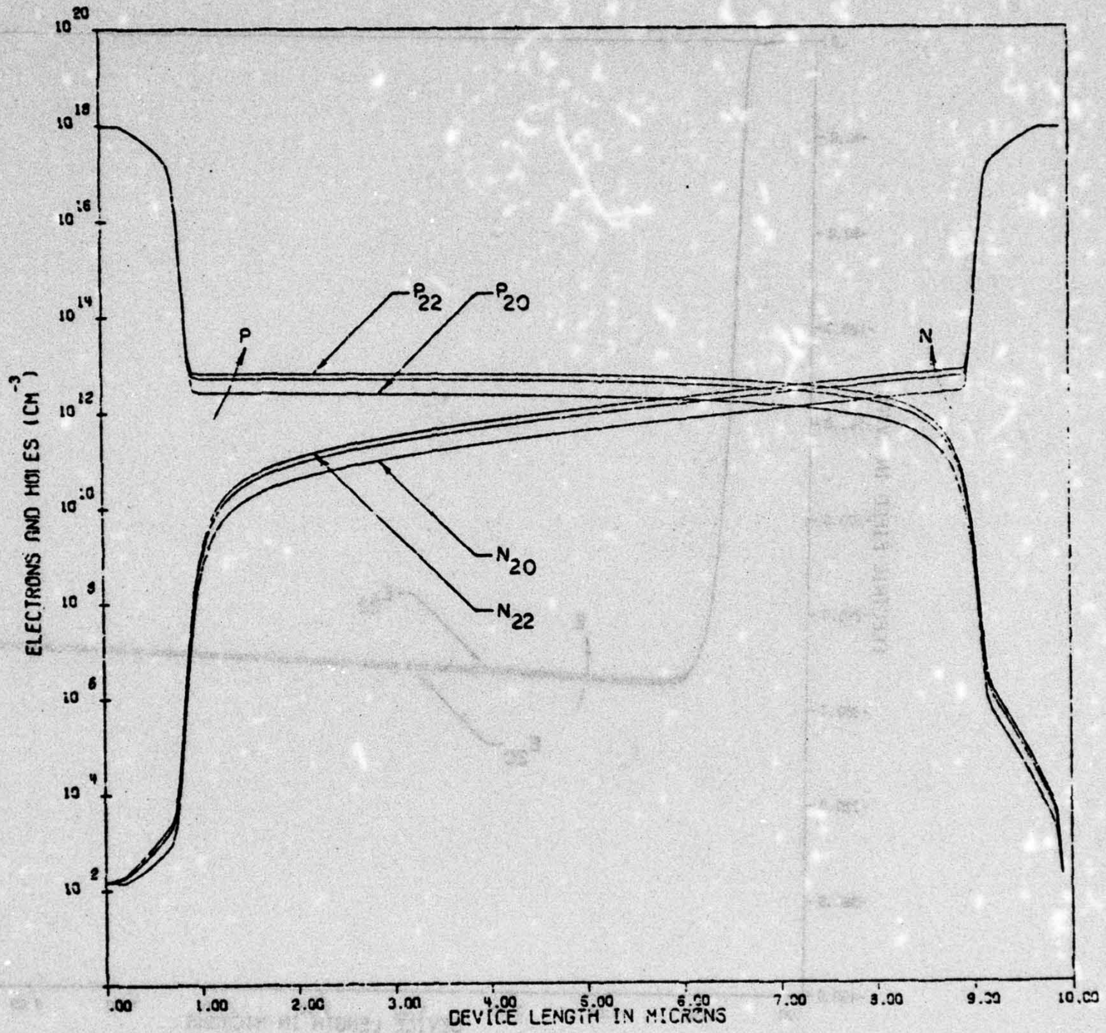

Figure 34. Electron and hole density distributions for time instants t_{20} to t_{22} as shown in Figure 19

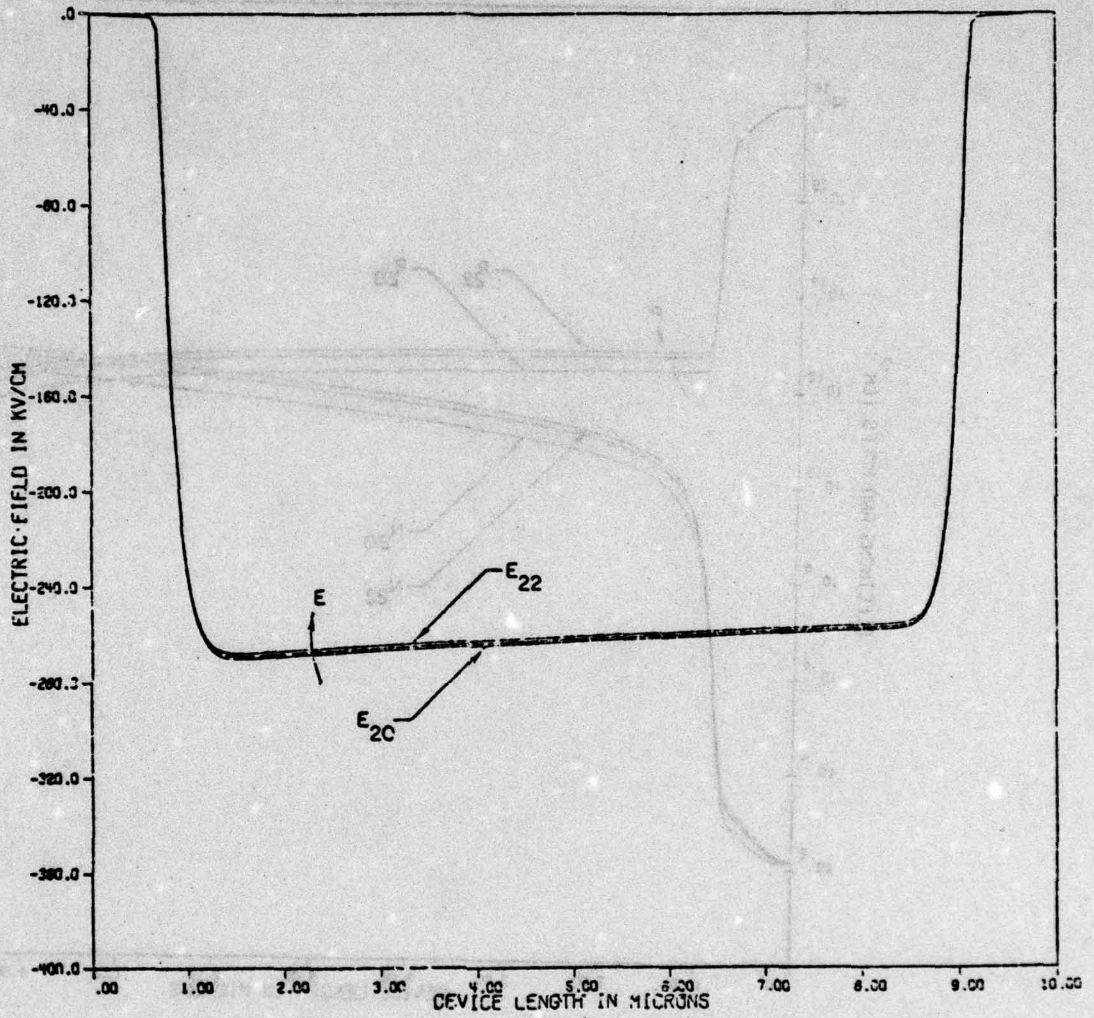

Figure 35. Electric field distribution for time instants t_{20} to t_{22} as shown in Figure 19

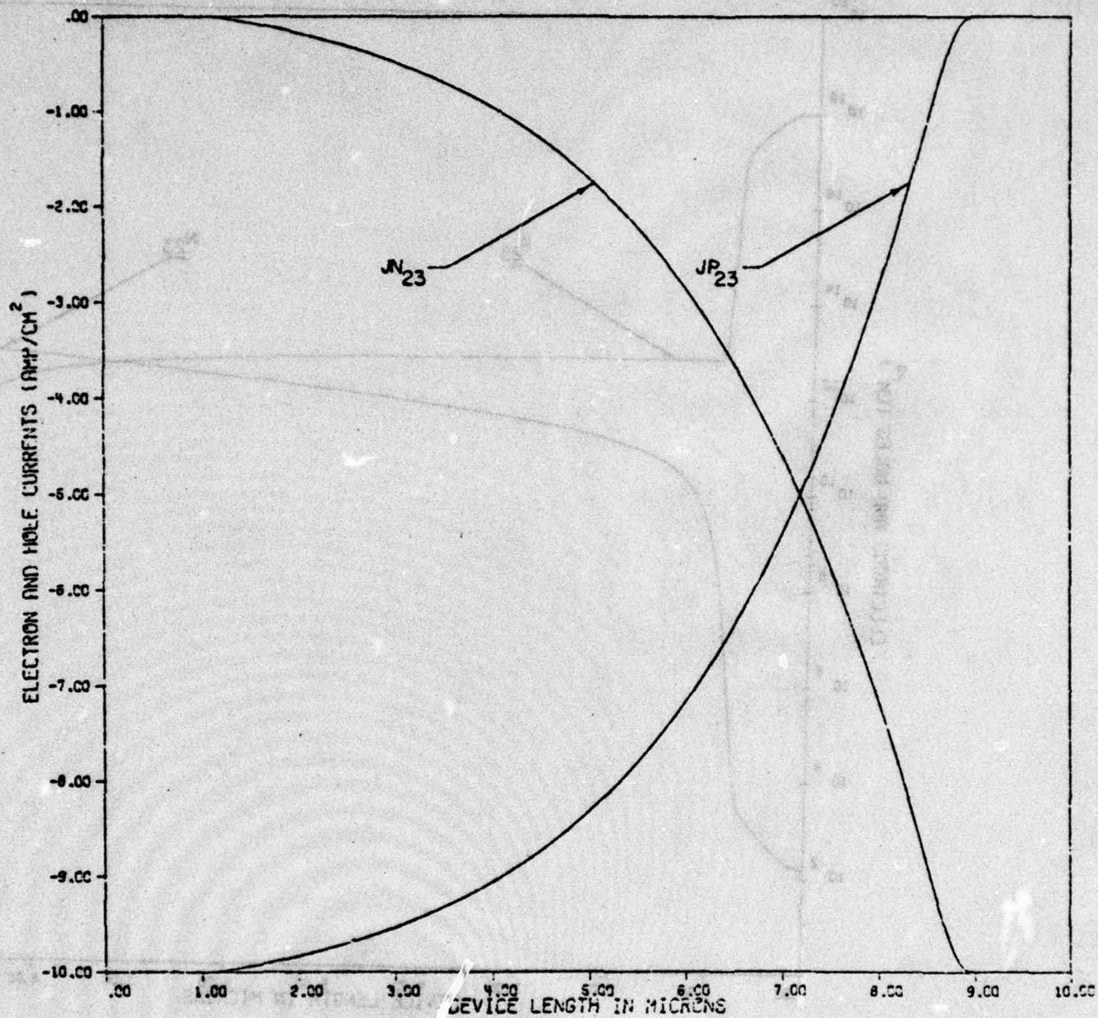

Figure 36. Electron and hole current density distributions for time instant t_{23} as shown in Figure 19

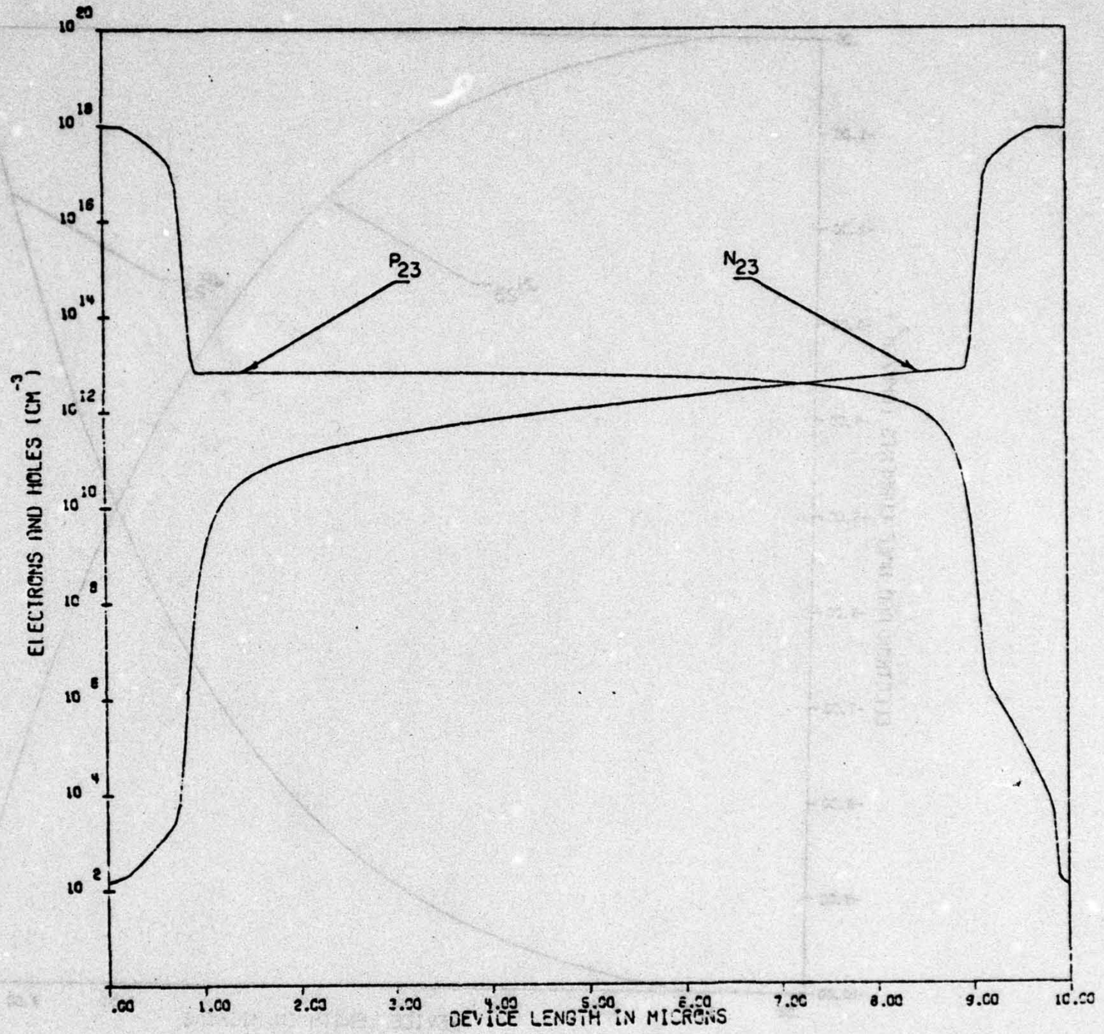

Figure 37. Electron and hole density distributions for time instant t_{23} as shown in Figure 19

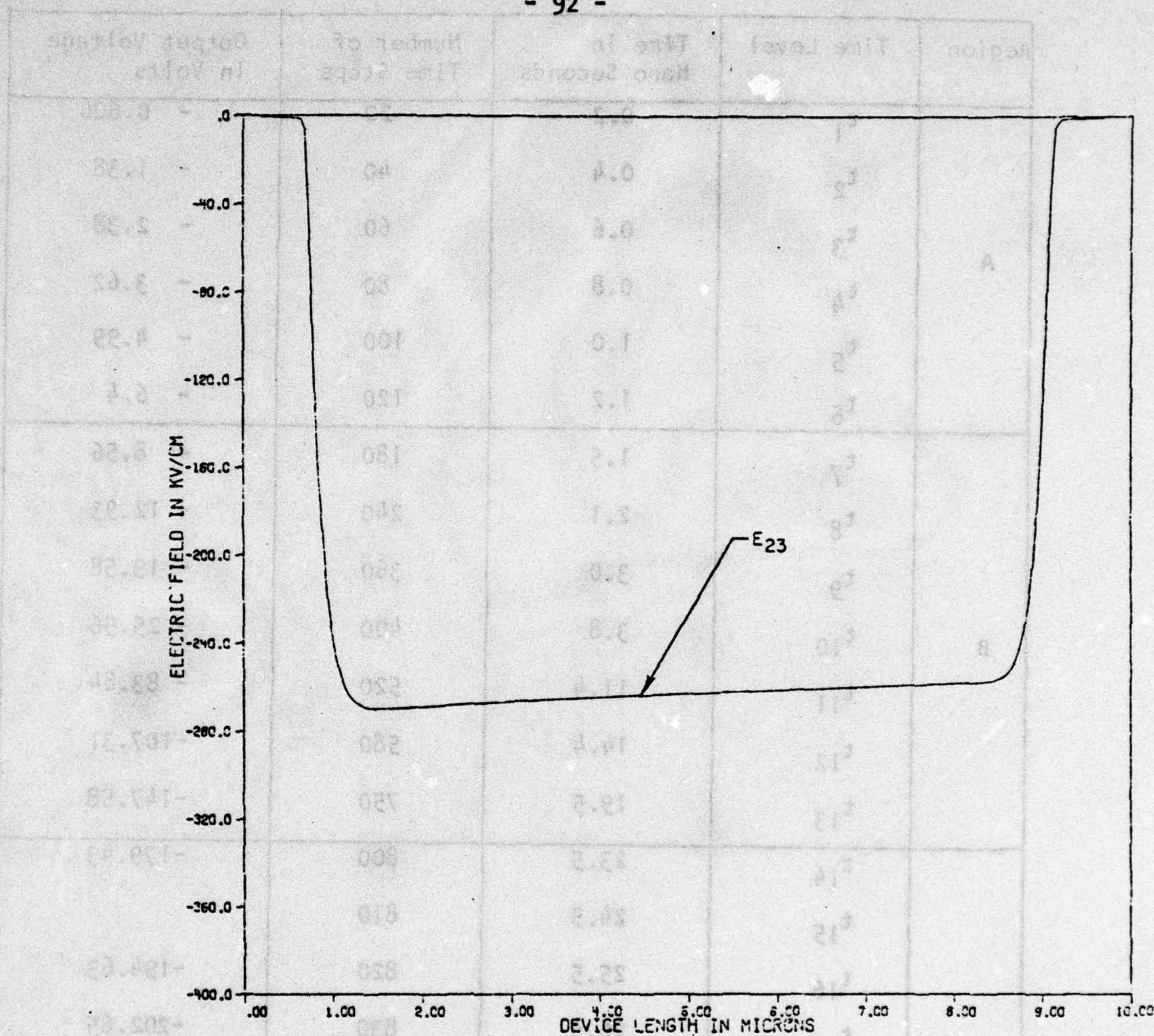

Figure 38. Electric field distribution for time instant t_{23} as shown in Figure 19

Table 2. Output voltage as a function of time

Region	Time Level	Time in Nano Seconds	Number of Time Steps	Output Voltage in Volts
A	t_1	0.2	20	- 0.606
	t_2	0.4	40	- 1.38
	t_3	0.6	60	- 2.38
	t_4	0.8	80	- 3.62
	t_5	1.0	100	- 4.99
	t_6	1.2	120	- 6.4
B	t_7	1.5	180	- 8.56
	t_8	2.1	240	- 12.93
	t_9	3.0	360	- 19.58
	t_{10}	3.8	400	- 25.56
	t_{11}	11.4	520	- 83.84
	t_{12}	14.4	580	-107.31
	t_{13}	19.5	750	-147.58
C	t_{14}	23.5	800	-179.43
	t_{15}	24.5	810	
	t_{16}	25.5	820	-194.63
	t_{17}	26.5	830	-202.65
	t_{18}	27.5	840	-210.68
	t_{19}	28.5	850	-218.44
	t_{20}	29.5	860	-210.68
	t_{21}	31.5	880	-212.24
	t_{22}	37.5	940	-213.05
steady state	t_{23}	38.0	945	-213.04
	t_{24}	43.5	1000	-213.04

Figures 40 to 43 demonstrate a very interesting phenomena in the sense that after time t_3 (=1.8 nanoseconds) both carrier depletion and avalanche multiplication are simultaneously present. This is due to the triangular shape of the electric field. Therefore, the high electric field near the metallurgical junction causes avalanche multiplication, while the negative terms of $\frac{1}{q}\left|\frac{\partial J_n}{\partial x}\right|$ and $-\frac{1}{q}\left|\frac{\partial J_p}{\partial x}\right|$ in the low field regions, away from the junction, cause carrier depletion. This is very clearly illustrated in the curves of the time instant t_5. Figs. 44 to 47 show the spatial distributions of the different quantities at one of the voltage fluctuating time instants t_6 (= 4.8 nanoseconds), while Figs. 48 to 51 show the steady state solution at time instant t_7 (=8 nanoseconds). The time levels of the different points indicated in Fig. 39, along with their time step number and the output voltage, are summarized in Table 3.

To summarize the reverse pulsed conditions, the device with low doping density and short N^--region depletes at a relatively fast rate until punch through is reached. The electric field increases uniformly in the N^--region, until the onset of avalanche by impact ionization. On the other hand, the device with high doping density and long N^--region does not fully deplete. In this case the electric field increases while keeping its triangular shape in the depletion region until it reaches avalanche. In both cases, the steady state condition is satisfied when the rate of generated carriers via avalanche multiplication is balanced by the recombination and depletion rates as shown in equations (106) and (107).

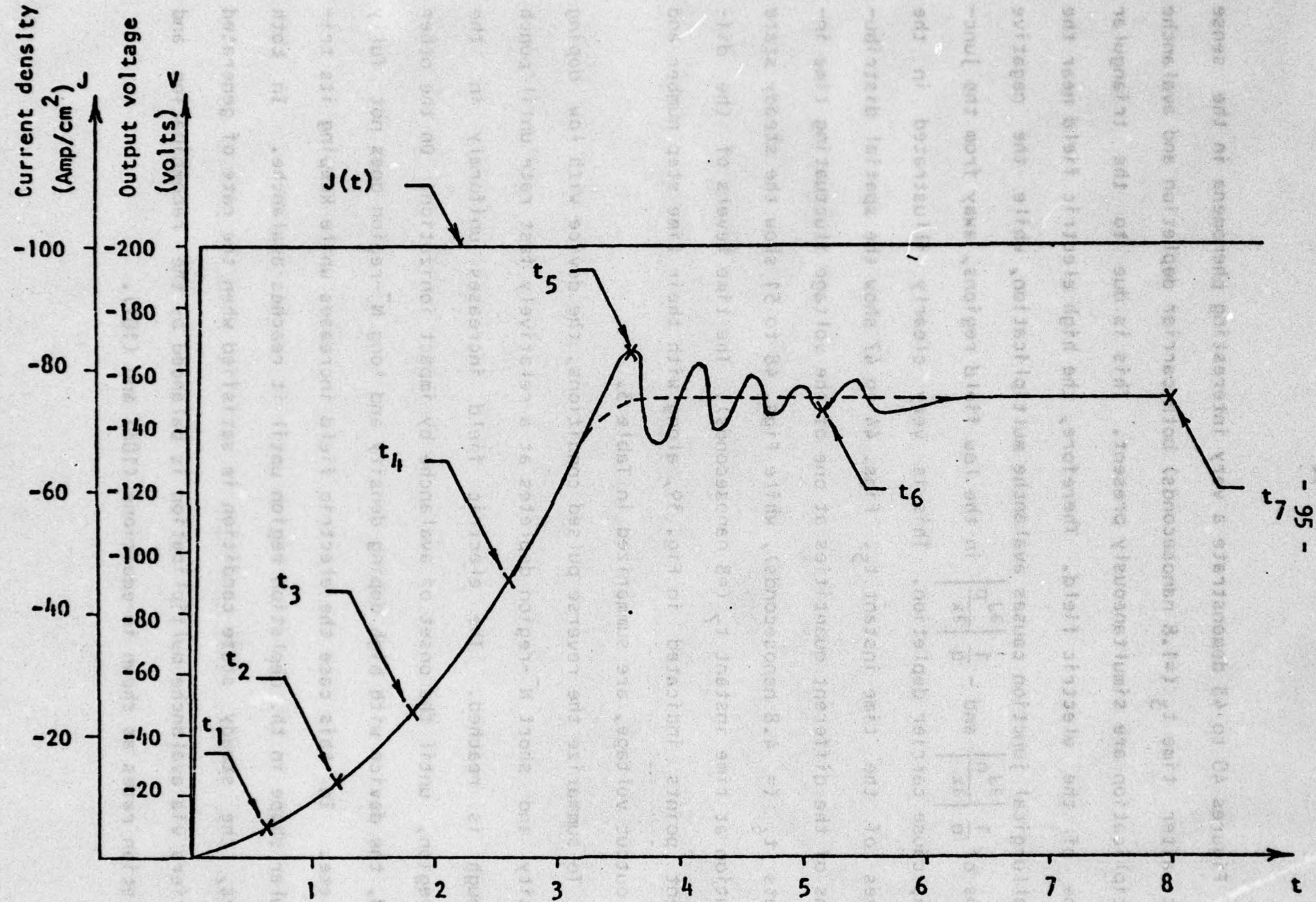

Figure 39. Current density and output voltage for the reverse biased case (second device)

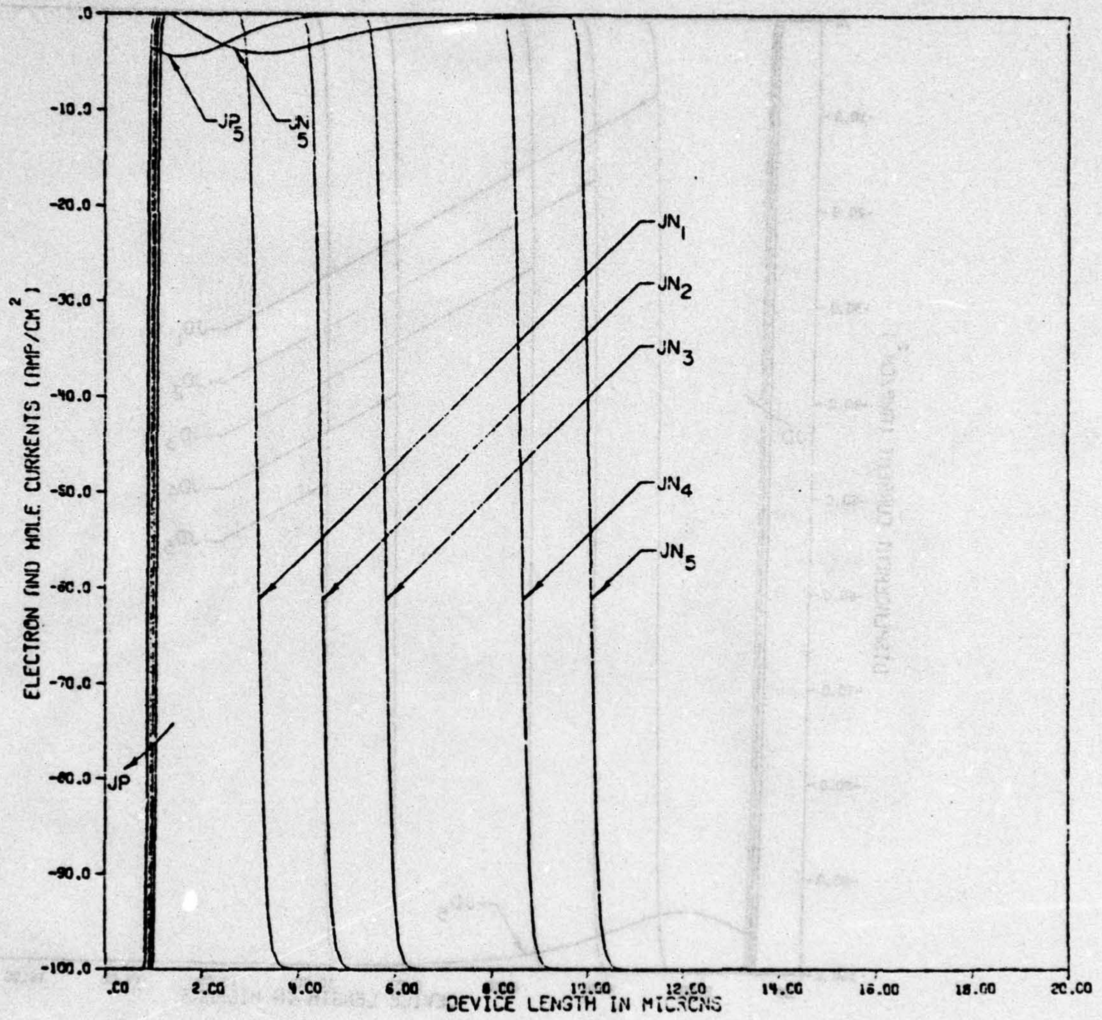

Figure 40. Electron and hole current density distributions for time instants t_1 to t_5 as shown in Figure 39

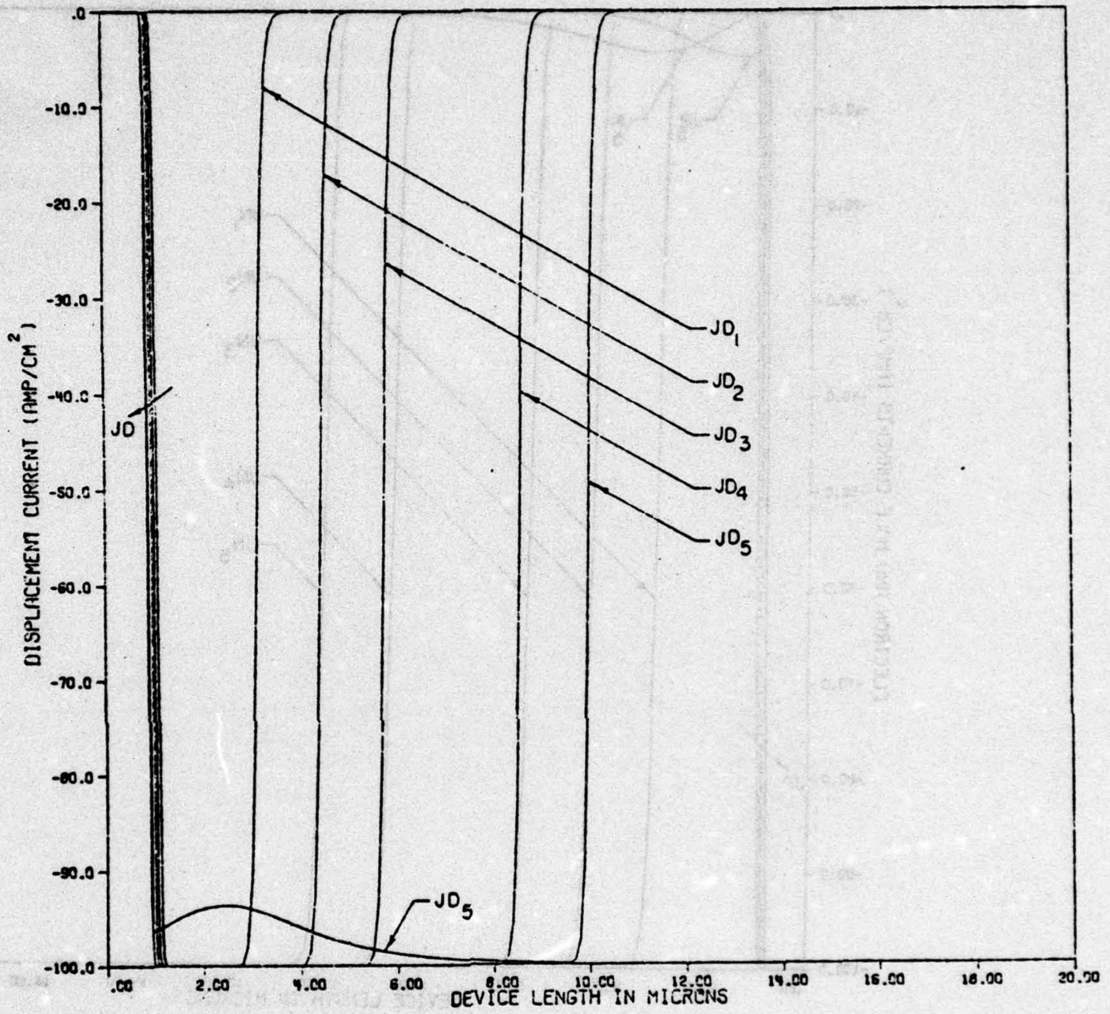

Figure 41. Displacement current density distribution for time instant t_1 to t_5 as shown in Figure 39

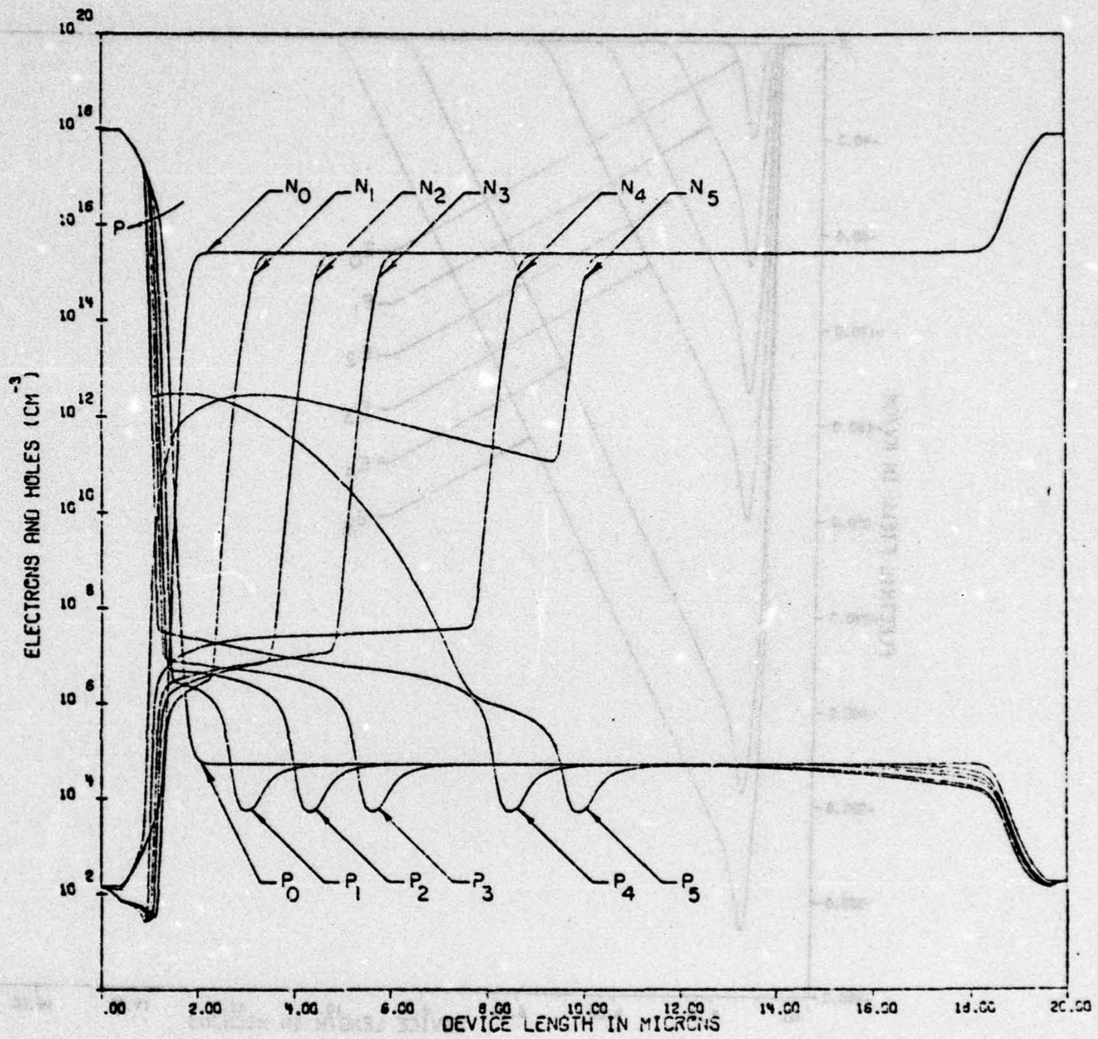

Figure 42. Electron and hole density distributions for time instants $t = 0$ to t_5 as shown in Figure 39

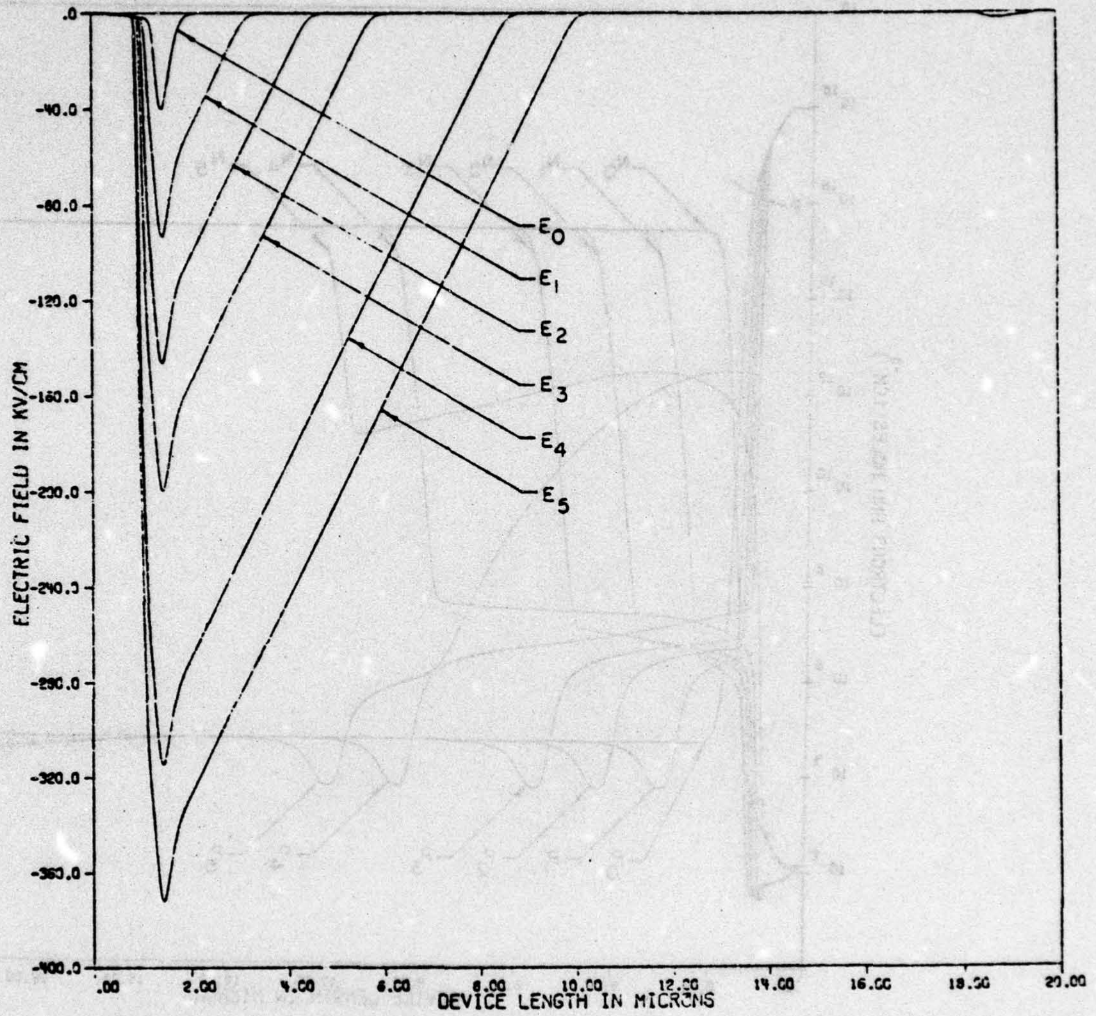

Figure 43. Electric field distribution for time instants $t = 0$ to t_5 as shown in Figure 39

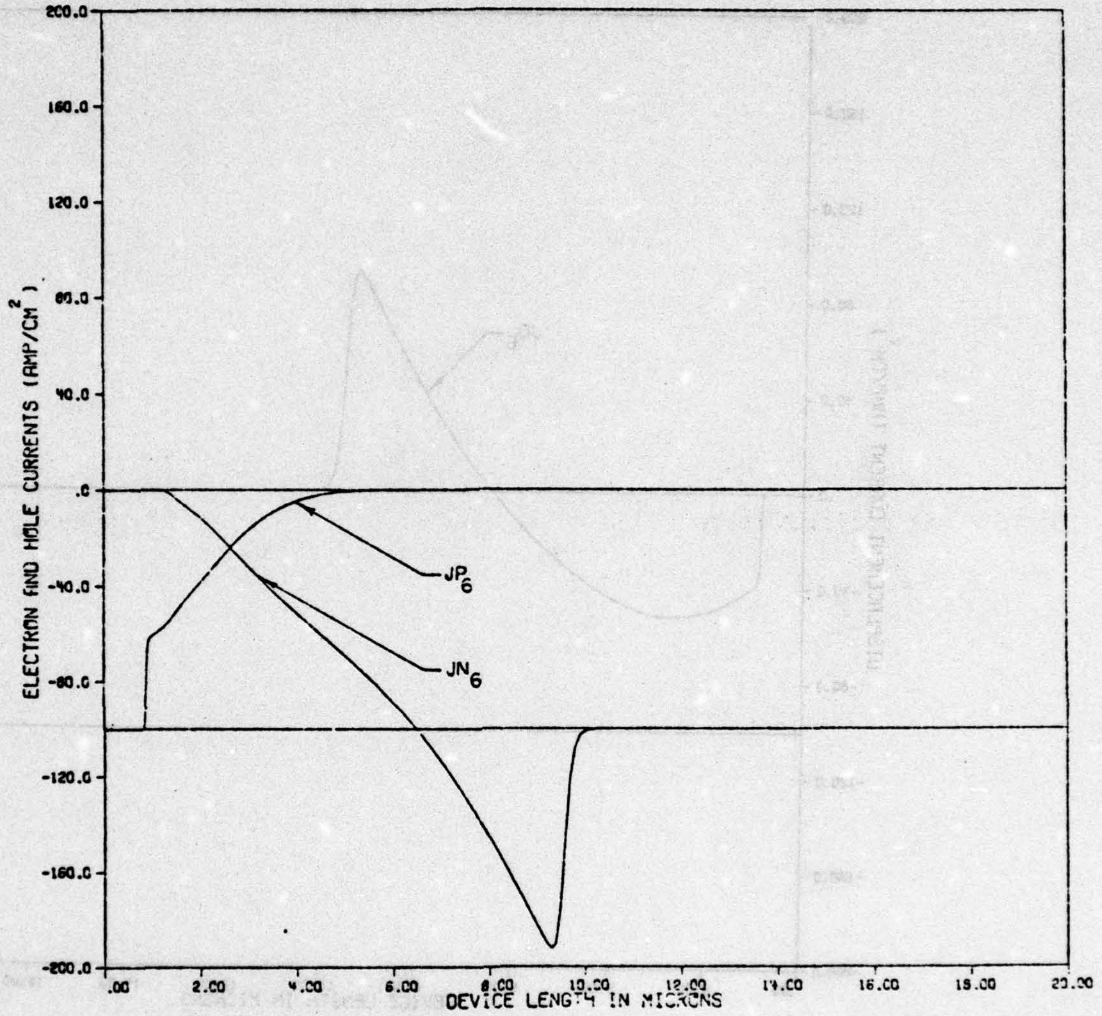

Figure 44. Electron and hole current density distributions for time instant t_6 as shown in Figure 39

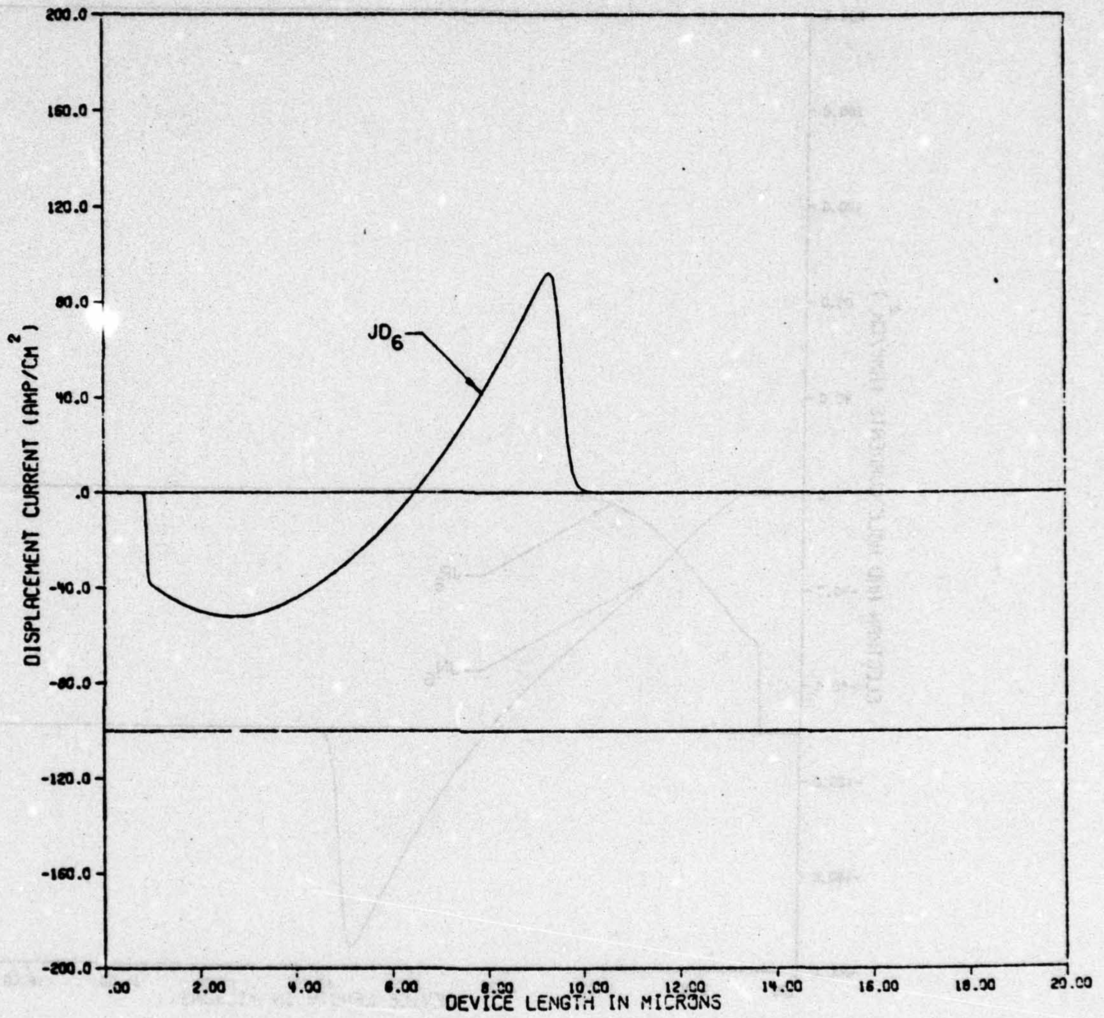

Figure 45. Displacement current density distribution for time instant t_6 as shown in Figure 39

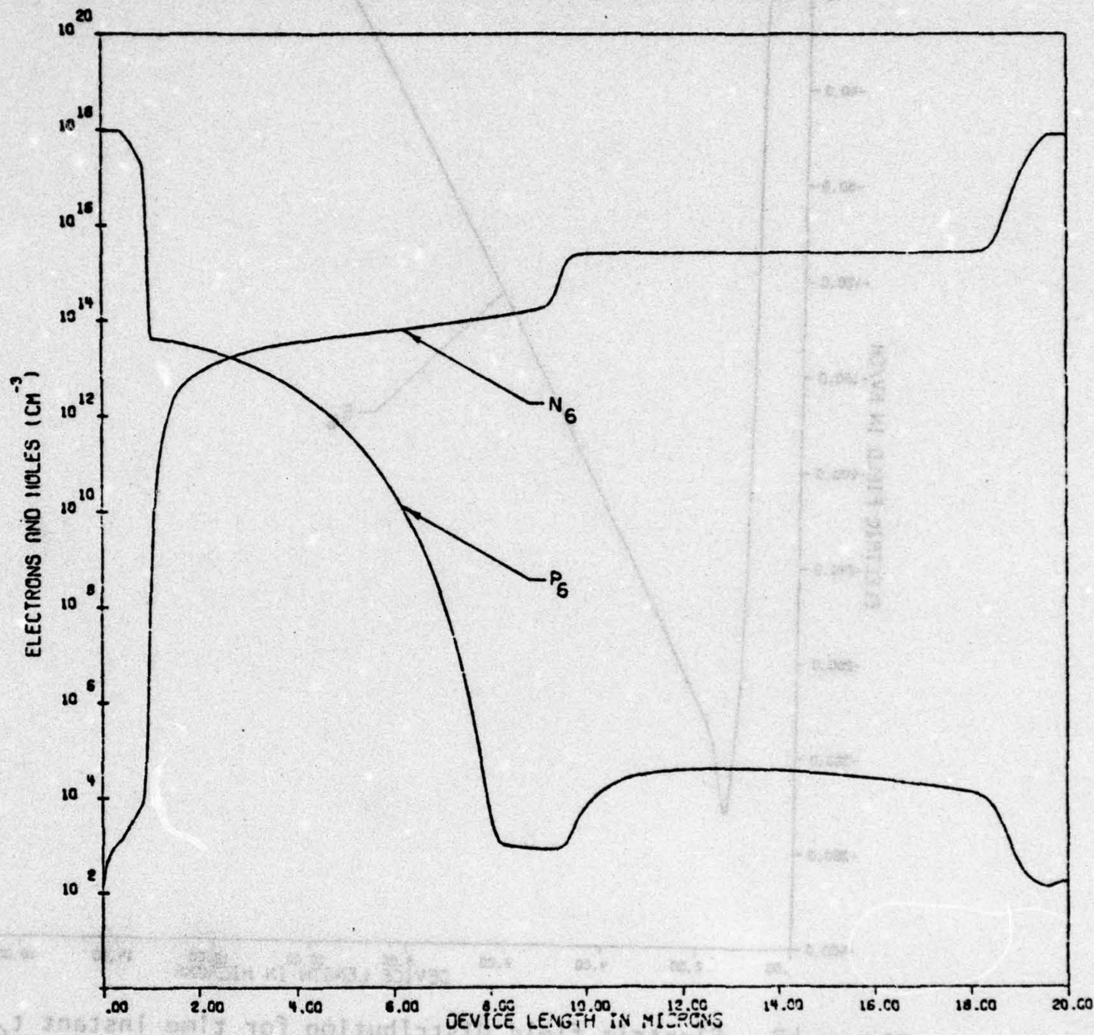

Figure 46. Electron and hole density distributions for time instant t_6 as shown in Figure 39

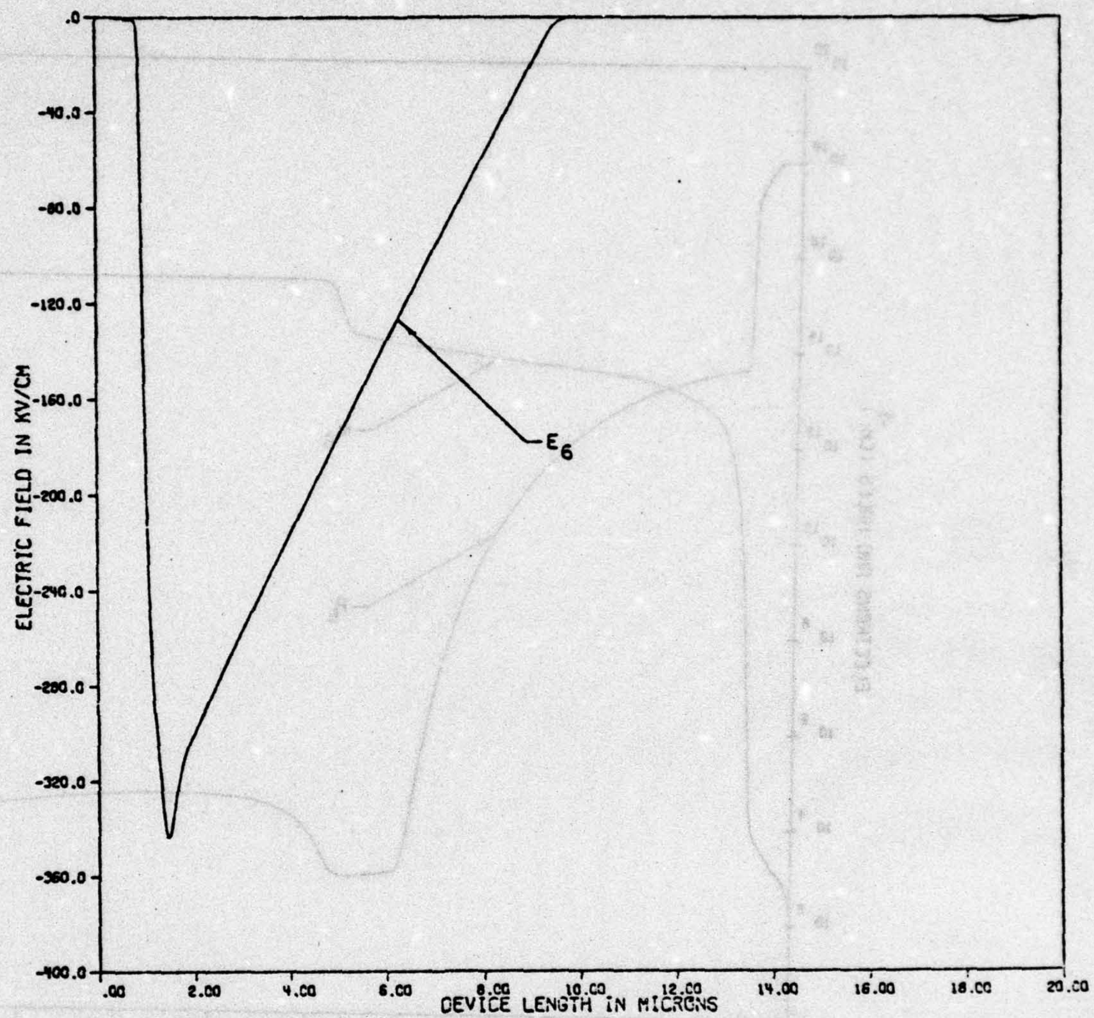

Figure 47. Electric field distribution for time instant t_6 as shown in Figure 39

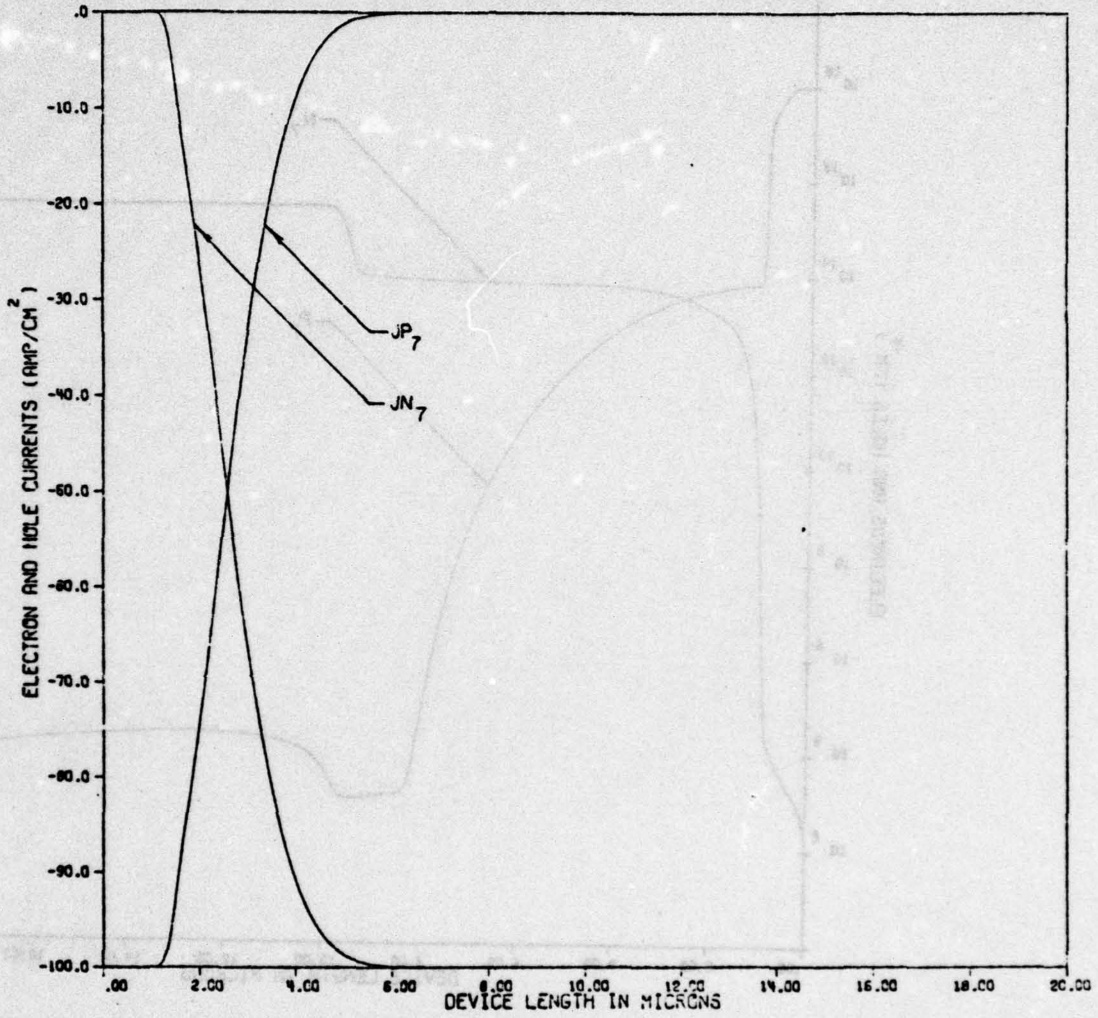

Figure 48. Electron and hole current density distributions for time instant t_7 as shown in Figure 39

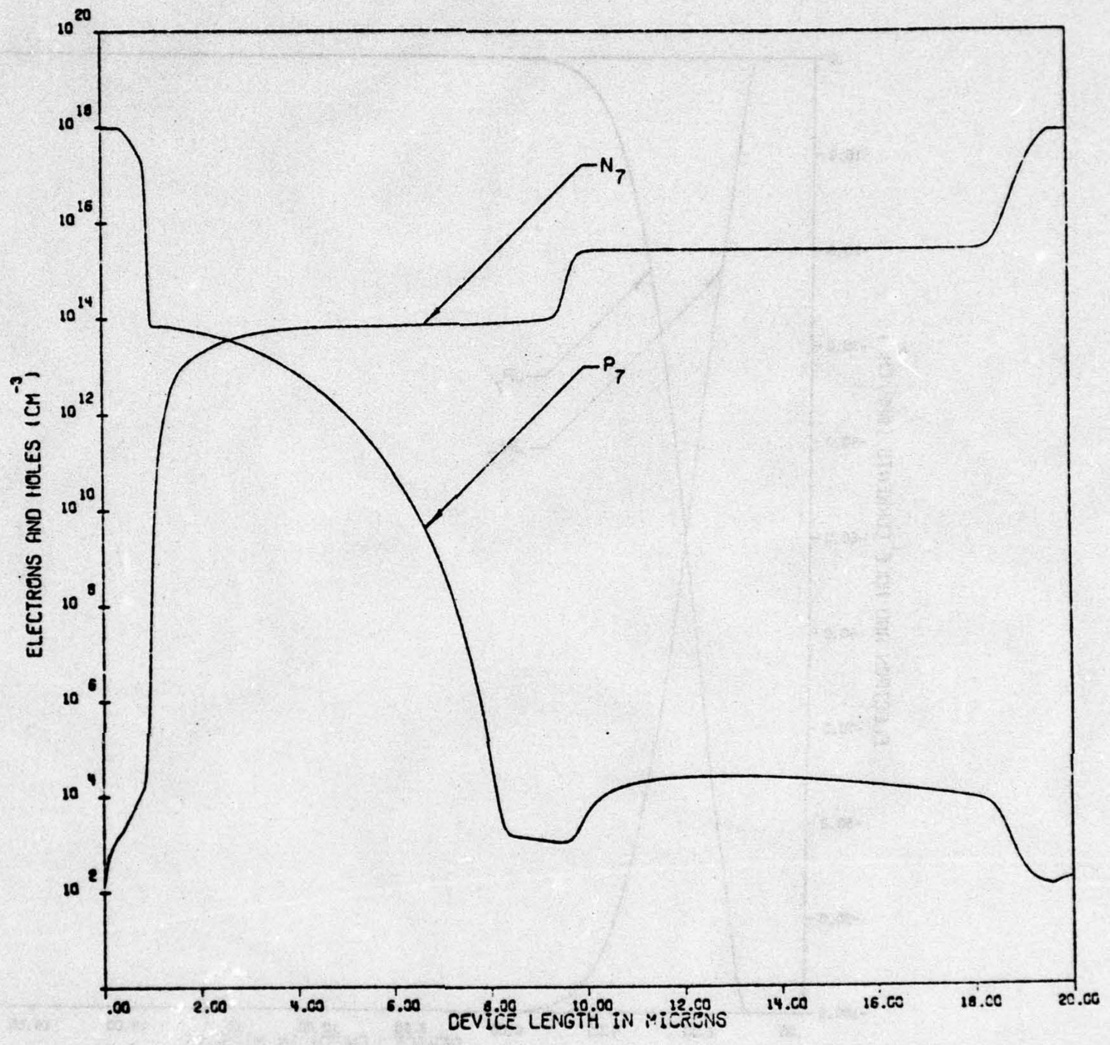

Figure 49. Electron and hole density distributions for time instant t_7 as shown in Figure 39

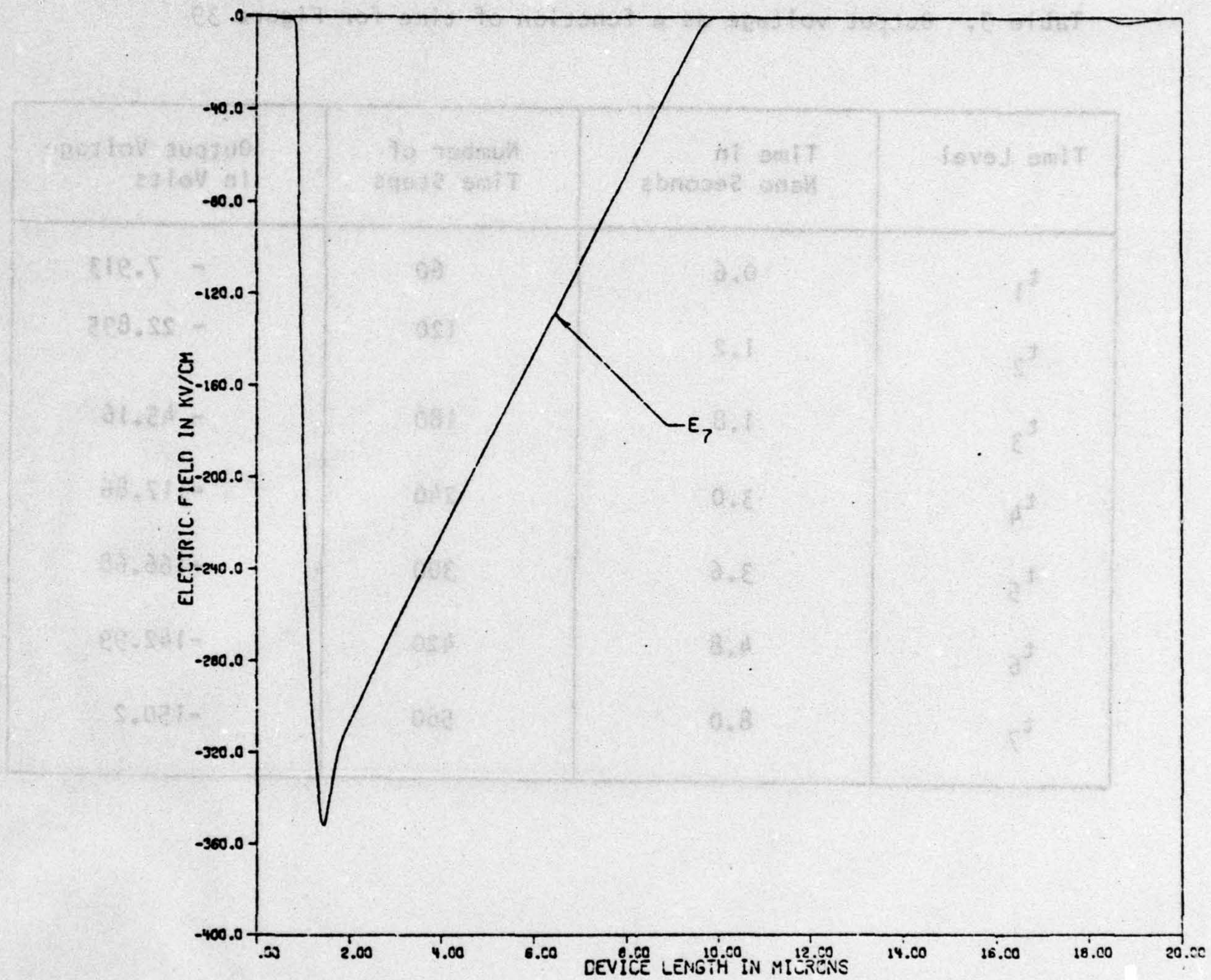

Figure 50. Electric field distribution for time instant t_7 as shown in Figure 39

Table 3. Output voltage as a function of time for Figure 39

Time Level	Time in Nano Seconds	Number of Time Steps	Output Voltage In Volts
t_1	0.6	60	- 7.913
t_2	1.2	120	- 22.895
t_3	1.8	180	- 45.16
t_4	3.0	240	-117.86
t_5	3.6	300	-166.68
t_6	4.8	420	-142.99
t_7	8.0	560	-150.2

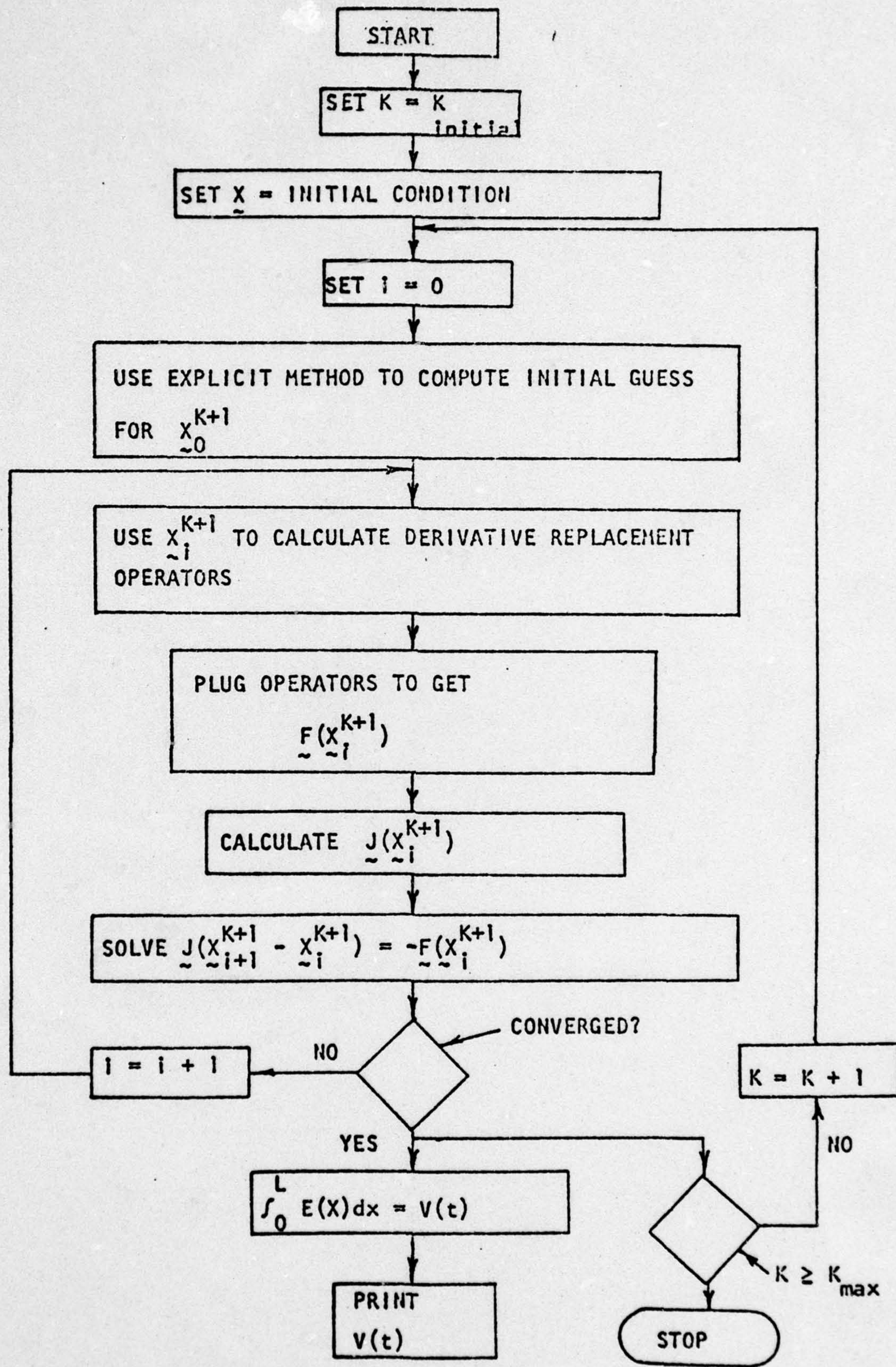

Figure 51. Pure implicit technique flow chart

CHAPTER V

FORWARD PULSED CASE

The main purpose of this chapter is to explain the unexpectedly high voltage which appears across the P^+-N^--N^+ structure when pulsed with extreme current densities in the forward pulsed direction. A qualitative discussion is presented first, followed by the computer simulation results using the conventional Shockley-Read-Hall recombination term in the two continuity equations. Discussion of the results leads to the prediction of an effective transient lifetime which varies with time and reduces to its equilibrium value near the steady state condition.

In the P^+-N^--N^+ structure, there are four regions which may give rise to the unexpected high voltage across the device, the heavily doped P^+ and N^+ regions, the P^+-N^- transition region, and the N^- region. The heavily doped regions operate under low level injection conditions; therefore, their ohmic voltage drop is almost nonexistent. The voltage across the P^+-N^- transition layer is very small due to the forward biased condition. Therefore, the low-doped N^- region must be considered the cause of the large voltage. This can be explained by considering the behavior of an N-type semiconductor at an extreme current density. At relatively low current densities bulk silicon will obey Ohm's Law and the current density is given by equation (109) and (110).

$$\vec{J} = q\mu_n N\vec{E} \tag{109}$$

$$\vec{J} = qN\vec{v}_d \tag{110}$$

where,

N = electron concentration, $\#/cm^3$

$q = 1.602 \times 10^{-19}$, coulomb

μ_n = mobility, $cm^2/v\text{-}sec$

$\vec{E}$ = electric field, v/cm

$\vec{v}_d$ = average drift velocity of the carriers, cm/sec

This relationship is valid at low values of electric field. At larger electric fields (or current density) the mobility will become field dependent [5] as shown in Fig. 52.

At electric fields below the critical value for avalanche breakdown, the electron concentration is constant. The resistance of the bulk region, therefore, increases as the electric field increases. Since Fig. 52 is for very pure material, for doped material one would expect the slope to be smaller at low values of the electric field. However, in both cases at an electric field of about 2×10^4 v/cm the electron velocity approaches a scattering-limited value of about 10^7 cm/sec. Much higher electric fields are required for holes in silicon, 2×10^5 v/cm before the scattering limited velocity is obtained. For N-type silicon an applied field in excess of 10^4 v/cm, the velocity being scattering-limited, implies a large resistivity. Or, looking at it from the current standpoint, by using equation (110),

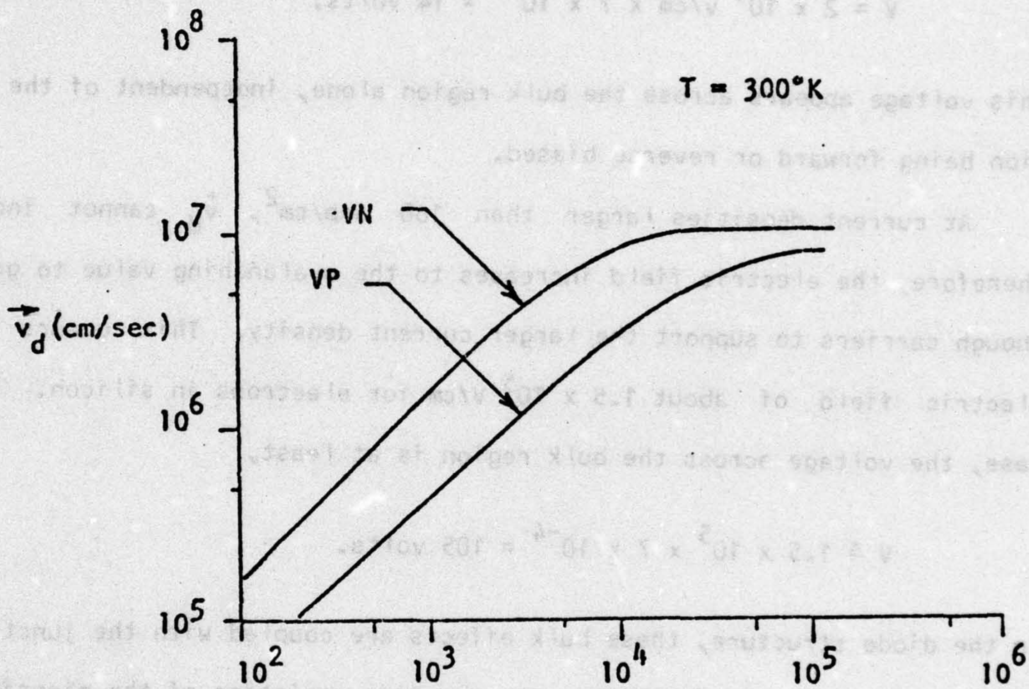

Figure 52. Electron and hole drift velocity vs. electric field for pure samples of Si.

$$\vec{J} = qN\vec{v}_d = 10^{14} \times 1.602 \times 10^{-19} \times 10^7 = 160 \text{ Amp/cm}^2$$

in the high resistance region, for an N-region doped at $10^{14}/cm^3$, where $N \doteq N_D$, below avalanche. This implies that the larger the N-region is doped, the larger the current density needed to place it in the high resistance region. If the bulk N-region is 7 microns, then,

$$V = 2 \times 10^4 \text{ v/cm} \times 7 \times 10^{-4} = 14 \text{ volts.}$$

This voltage appears across the bulk region alone, independent of the junction being forward or reverse biased.

At current densities larger than 160 Amp/cm^2, $\vec{v}_d$ cannot increase; therefore, the electric field increases to the avalanching value to generate enough carriers to support the larger current density. This occurs at an electric field of about 1.5×10^5 V/cm for electrons in silicon. In this case, the voltage across the bulk region is at least,

$$V \doteq 1.5 \times 10^5 \times 7 \times 10^{-4} = 105 \text{ volts.}$$

In the diode structure, these bulk effects are coupled with the junction effects. As discussed in Chapter II, the time variation of the minority carries follows the time variation of the electric field due to the relaxation time constant being shorter than the transit time.

To study the behavior of a P^+-N-N^+ diode following the application of a low level current pulse, we assume that the diode is initially at thermal equilibrium. To insure that the device will reach a final steady state before the pulse end, we assume that the pulse width is greater than five times the transit time of the N^- region. Immediately after the pulse application, the electric field will change in a short period of time in order to support the total current. Hence, the displacement current component will

be equal to the total current throughout the device according to the following equation:

$$J(t = 0^+) = \epsilon \frac{\partial E}{\partial t} \qquad (111)$$

As time proceeds, one can investigate four separate regions. After a time of the order of the dielectric relaxation time constant in the two heavily doped regions, the build-up of ohmic voltages causes the total current to be carried by the majority carriers (holes in the P^+ region and electrons in the N^+ region).

Similarly, in the low doped region, the majority carrier current will replace the displacement current after a period of time of the order of the dielectric relaxation time constant in the N^--region. In the P^+-N^- transition layer, the minority carriers start to diffuse and charge the transition layer capacitance. This phenomena needs a period of time in the order of the transit time, during which the hole and electron currents replace the displacement current in the transition layer.

If a large current pulse is applied to the P^+-N^--N^+ diode, initially the voltage that would appear across the diode will be the sum of the voltage across the transition region and the ohmic voltage drop across the N^- region, as discussed in the low current pulse case, except that the ohmic drop in this case is much larger due to lower mobility of the carriers at the higher electric field. As the minority carriers start to diffuse, the N^- region will operate under high injection conditions, conductivity modulation will start, and the voltage across the N^--region will begin to decay with a time constant approximately equal to the transit time.

If an extremely intense current pulse is applied, the large current density will initially be carried by the displacement current component.

The majority carriers in the N^- region will not be sufficient to replace the displacement current; therefore, the electric field increases very rapidly to create avalanche, which in turn generates enough majority and minority carriers to replace the displacement current. In this case the N^- region is under high level injection, and yet the voltage appearing across the device is very high. As the injection and diffusion process has time to take place, the electric field necessary to support the current decreases.

In the remainder of this chapter the numerical method of Chapter II is used to solve for the transient behavior of the P^+-N-N^+ structure, with external excitations in the form of current steps with different amplitudes and rise times.

The device under consideration is the first device presented in Chapter III with a low doping region of $10^{14}/cm^3$, and 7 microns width. The total device length is 10 microns. The N^--region "lifetime" is 4×10^{-8} seconds.

<u>External excitation in the form of a low current step</u>

A relatively low current step is first applied to the device initially under thermal equilibrium. The thermal equilibrium solution is described by Figs. 15 and 16 in Chapter III. The current step has a rise time of 1.25 nanoseconds, and an amplitude of 1 ampere/cm^2. The response of the device is illustrated in Figs. 53 to 57. The terminal voltage v(t) as a function of time is shown in Fig. 53 along with the external excitation J(t). Figs. 54 to 57 show the electron and hole current density components, the displacement current density component, the carrier densities, and the electric field as functions of position for various instants of time.

Immediately after the current step application, the current will be totally carried by the displacement current component according to equation (111). As soon as any electric field is established in the heavily doped

regions, the current will be carried by the majority current component. This situation is illustrated in Figs. 54 and 55 for the time instant t_1 where the total current is equal to 0.2 amp/cm^2. At this time level, the current is partially carried by the majority carrier component, and partially by the displacement current component in the low doped region, while it is totally carried by the displacement current component in the depletion region. A positive displacement current means an increase in the electric field, or less negative value as shown in Fig. 57. After a short time, the current in the N^--region will be totally carried by the majority carrier component. This occurs within a period approximately equal to the dielectric relaxation constant of the N^--region. This is illustrated by the curves of the time instant t_2, where the displacement current is still equal to the total current in the depletion region. At time level t_3, the depletion region becomes narrower due to the increase in the electric field, and to some carrier diffusion across the junction. This causes the electron current component to further replace the displacement current component on the right side of the depletion region. At this point, it should be noted that one of the main differences between a forward biased junction and a reverse biased one, is the sign of the spatial derivatives of the electron and hole currents near the depletion region. In Chapter IV it was shown that these two terms cause carrier recombination or in other words carrier depletion near the reverse biased junction. From Fig. 54, it is clear that the $\frac{1}{q}\left|\frac{\partial JN}{\partial x}\right|$ and $-\frac{1}{q}\left|\frac{\partial JP}{\partial x}\right|$ terms of the particle continuity equations are positive near the depletion region. This causes electron diffusion from the N^--region to the P^+-region, and hole diffusion from the P^+-region to the N^--region. As time proceeds, these carrier diffusions increase and cause the electric field to decrease in the N^--region and also cause the displace-

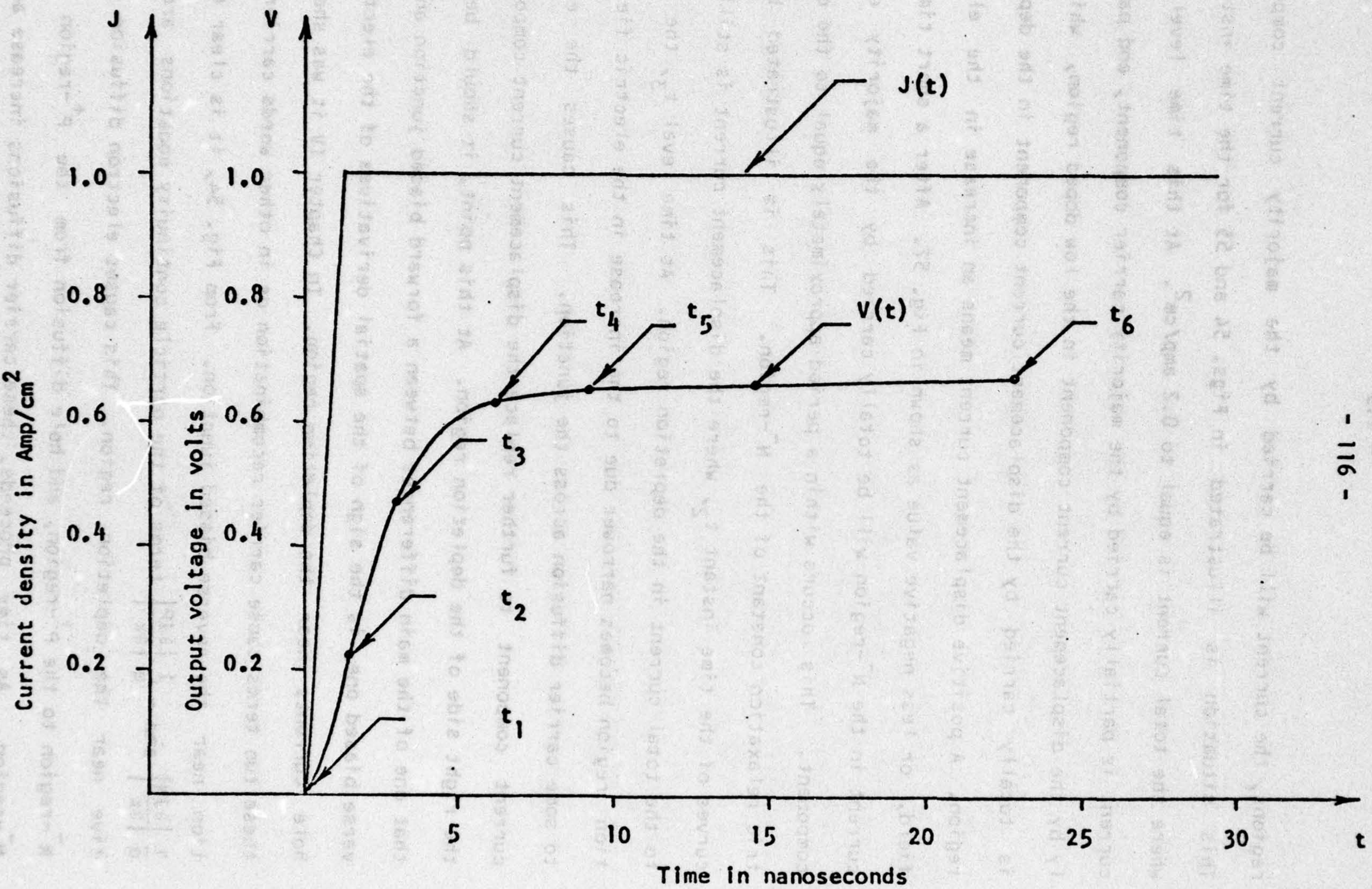

Figure 53. J(t) and V(t) for a relatively low current step in the forward direction

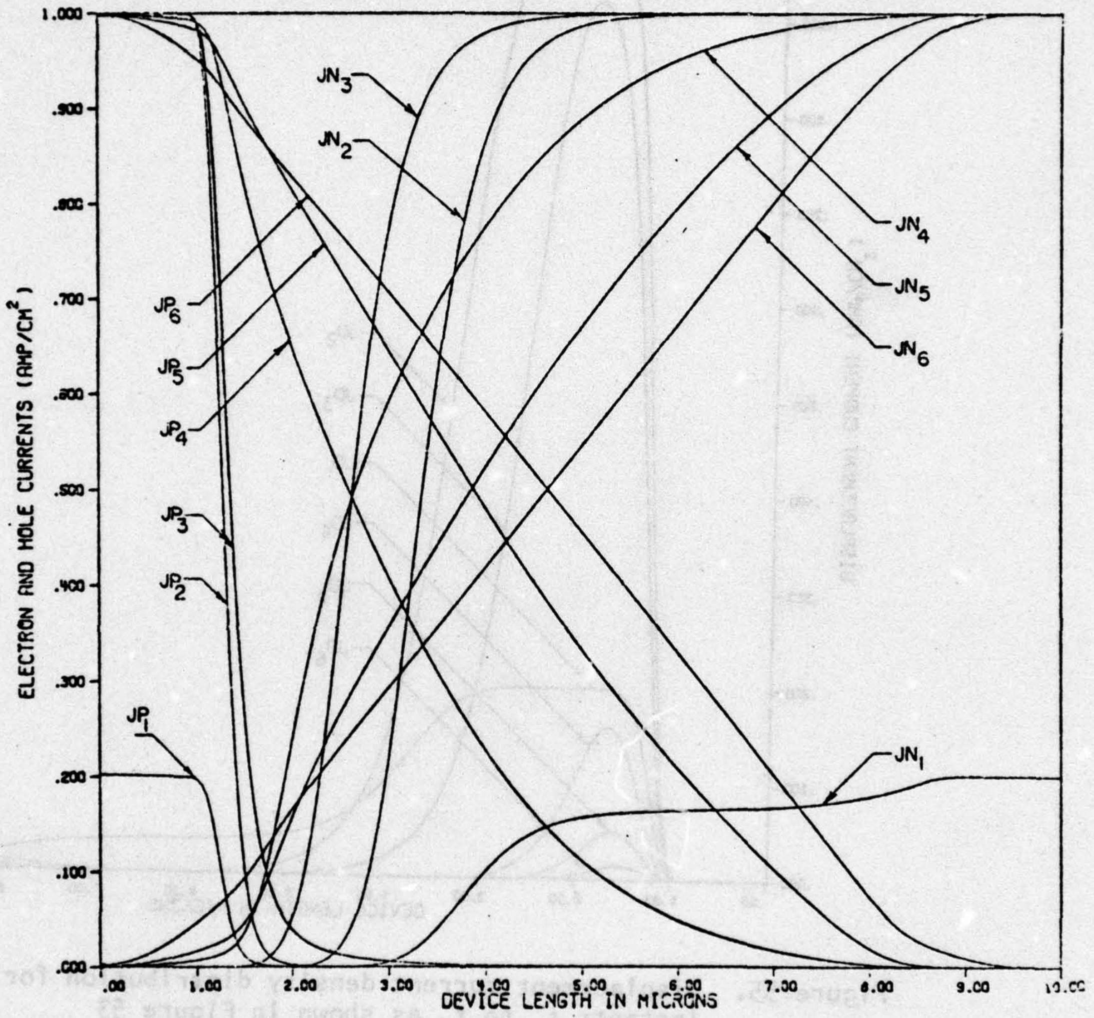

Figure 54. Electron and hole current density distributions for time instants t_1 to t_6 as shown in Figure 53

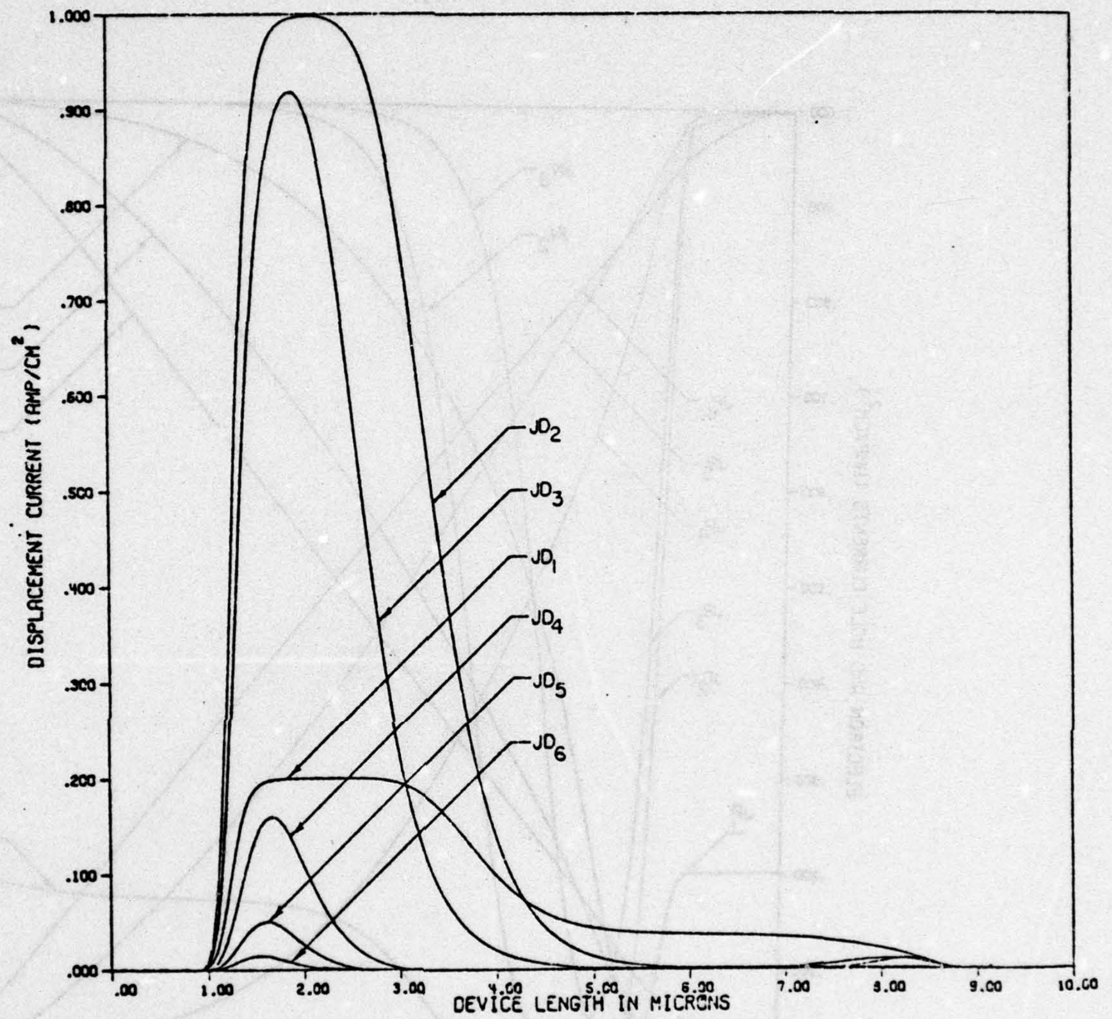

Figure 55. Displacement current density distribution for time instants t_1 to t_6 as shown in Figure 53

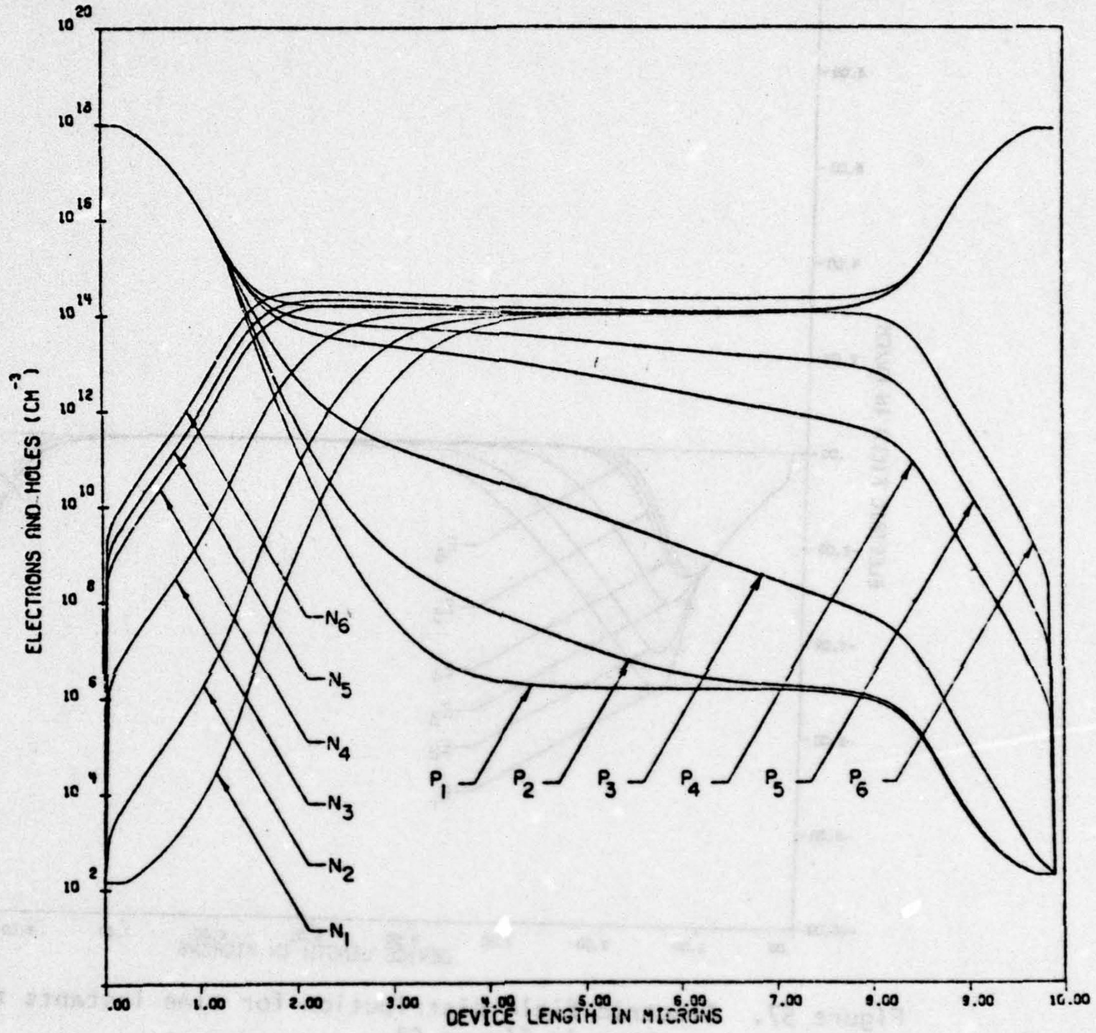

Figure 56. Electron and hole density distributions for time instants t_1 to t_6 as shown in Figure 53

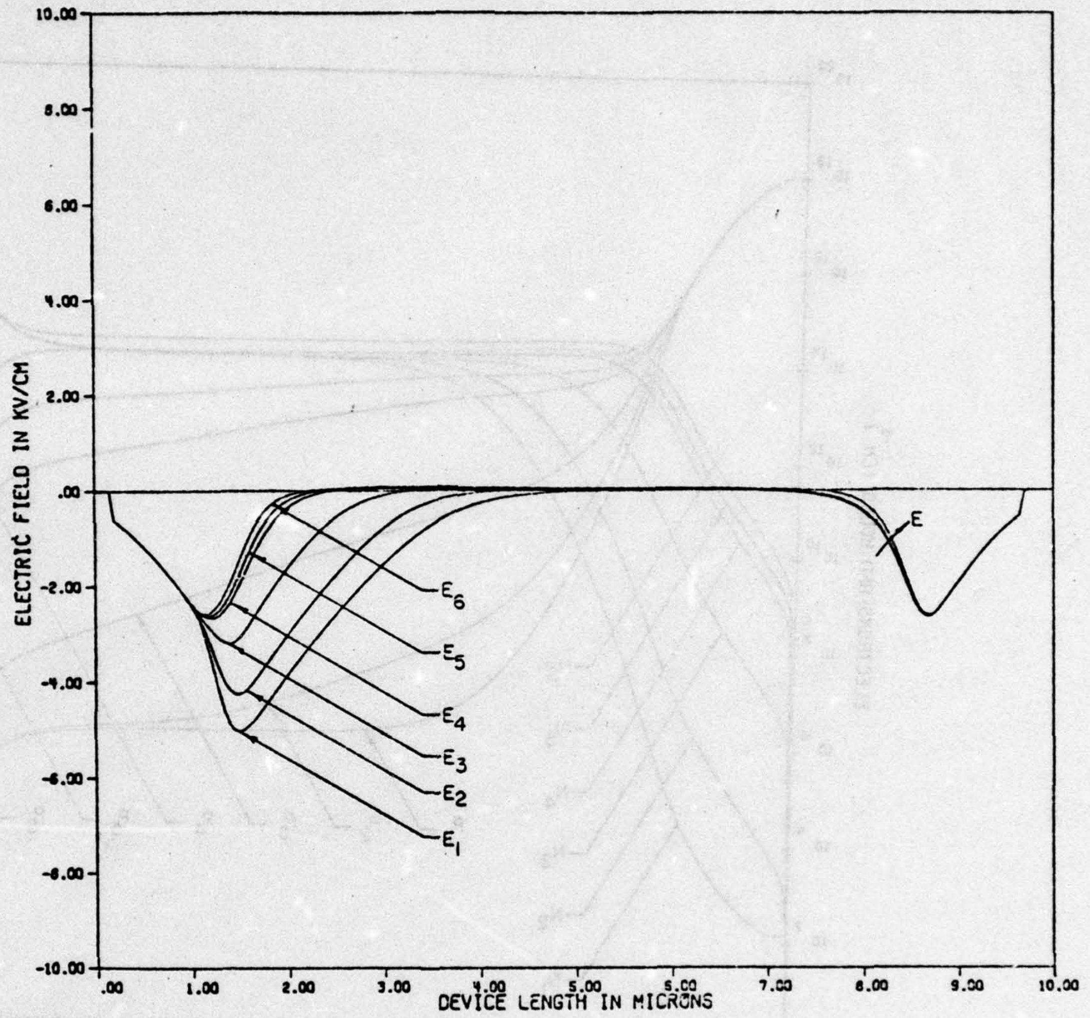

Figure 57. Electric field distribution for time instants t_1 to t_6 as shown in Figure 53

ment current to decrease in the depletion region. This process continues until steady state, where the displacement current goes to zero throughout the entire device, and the total current is carried by both electrons and holes as illustrated by the curves of the time instant t_6 (which is near steady state). It should be noticed that after a time of the order of t_2, the displacement current in the N-region is almost non-existent compared to that in the depletion region. Therefore, any time variation of electric field inside the N^--region does not affect the output voltage for this level of injection.

<u>External excitation in the form of extremely high current step</u>

An extremely high current step of 10^4 Amp/cm^2 amplitude and two pico seconds rise time is applied to the P^+-N^--N^+ structure. The computer simulation results are illustrated in Figs. 58 to 69 for nine instants of time. Shortly after the step application (t_1 and t_2), the current in the heavily doped regions is carried by the majority carrier components, while the displacement current equals the total current in the low doped and the depletion regions. As shown in Fig. 59, both quantities $-\frac{1}{q}\left|\frac{\partial JP}{\partial x}\right|$ near the P^+-region, and $\frac{1}{q}\left|\frac{\partial JN}{\partial x}\right|$ near the N^+-region are positive and have very large values due to the high current level. On the other hand, the quantities $-\frac{1}{q}\left|\frac{\partial JP}{\partial x}\right|$ near the N^+-region and $\frac{1}{q}\left|\frac{\partial JN}{\partial x}\right|$ near the P^+-region are very small. This causes a very large number of holes to diffuse from the P^+-region to the N^--region, and a similar amount of electrons to diffuse from the N^+-region to the N^--region. In other words, the P^+-N^- and the N^+-N^- transition regions show identical behavior. This increase of the diffused carriers causes the hole current to replace the displacement current in the left side of the N^--region, while the electron current replaces it in the right side. Also it is clear from Fig. 62 that the electric field increases

very rapidly with time, due to the large displacement current value, until it reaches an avalanching value. At first (t_1 and t_2) the avalanche multiplication effect is noticeable in the hole increment. As the electric field, the electron current, and the hole current increase, the avalanche multiplication gets larger. As a result, the avalanched carriers start to play a role in current transport as shown for time instant t_3. This process continues in Figs. 62 and 64. The carrier levels increase due to diffusion and avalanche multiplication, the particle currents increase, and as a result, the displacement current decreases, then switches to a negative value as the particle currents become larger than the external applied current. This causes the electric field to decrease in the N^--region, and consequently, the output voltage decreases as shown in Fig. 58.

To reach a steady state, the displacement current and the time variation of both holes and electrons should go to zero values or,

$$JN + JP = Jt \tag{112}$$

$$\frac{PN - n_i^2}{\tau_0 (P+N+2n_i)} = -\frac{1}{q}\left|\frac{\partial JP}{\partial x}\right| = \frac{1}{q}\left|\frac{\partial JN}{\partial x}\right| \tag{113}$$

equation (112) is satisfied for time instants t_8 and t_9 as shown in Fig. 67, but the condition of the following equation is also satisfied,

$$\frac{1}{q}\left|\frac{\partial JP}{\partial x}\right| = \frac{1}{q}\left|\frac{\partial JN}{\partial x}\right| >> \frac{PN - n_i^2}{\tau_0 (P+N+2n_i)} \tag{114}$$

This is again due to the high current values. Equation (114) causes the carrier levels to keep rising throughout the entire device until the minority carriers in the heavily doped regions become comparable to the dop-

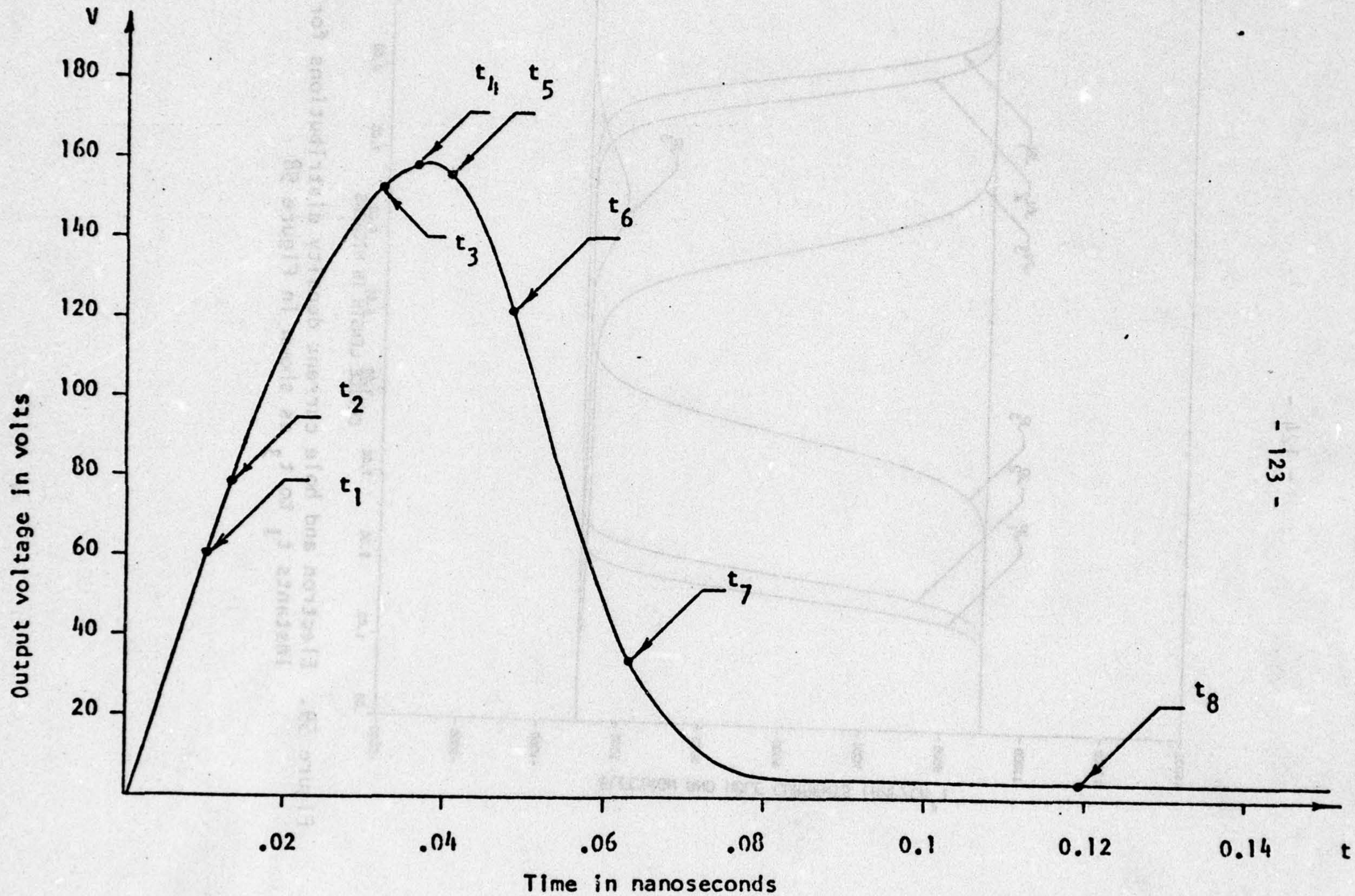

Figure 58. V(t) for an extremely high current step using the equilibrium lifetime

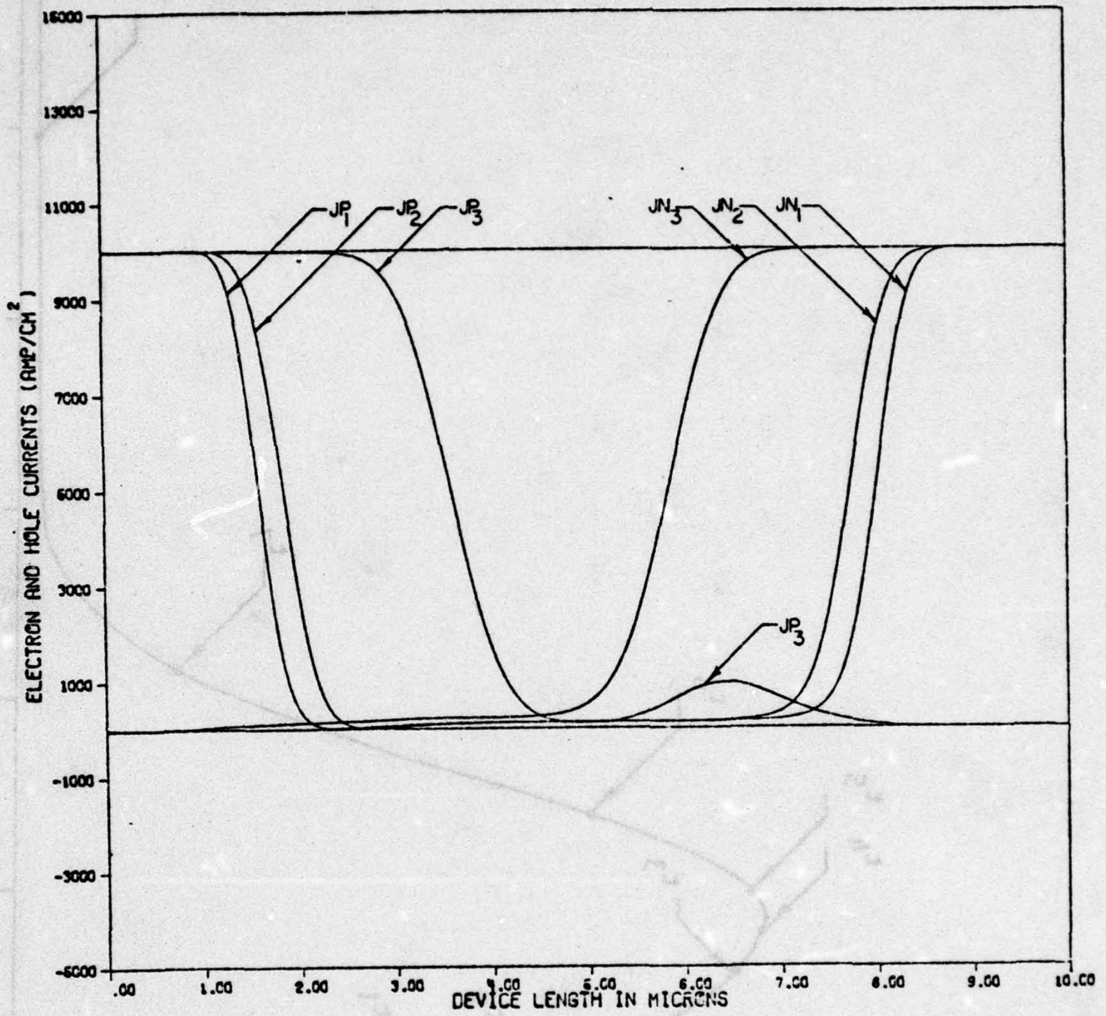

Figure 59. Electron and hole current density distributions for time instants t_1 to t_3 as shown in Figure 58

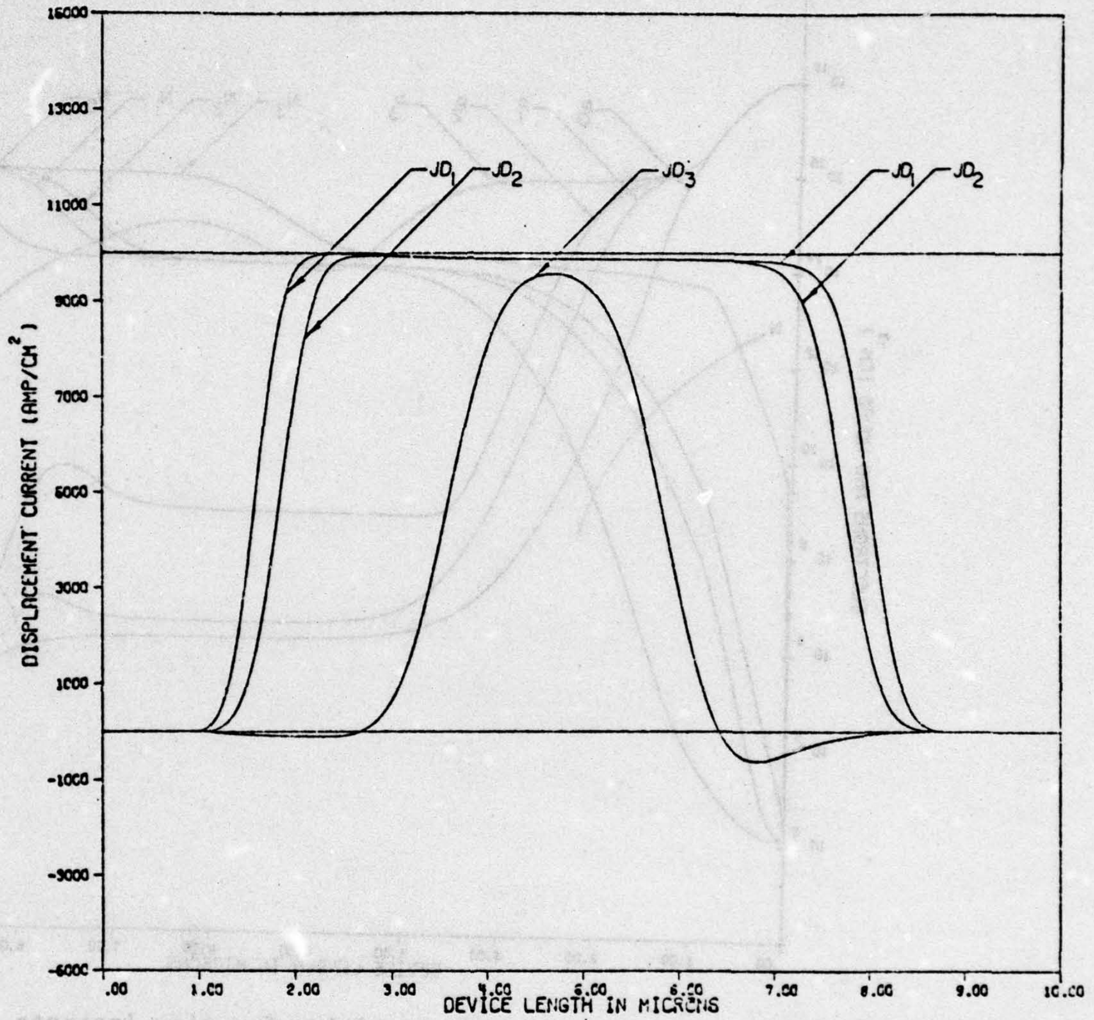

Figure 60. Displacement current density distribution for time instants t_1 to t_3 as shown in Figure 58

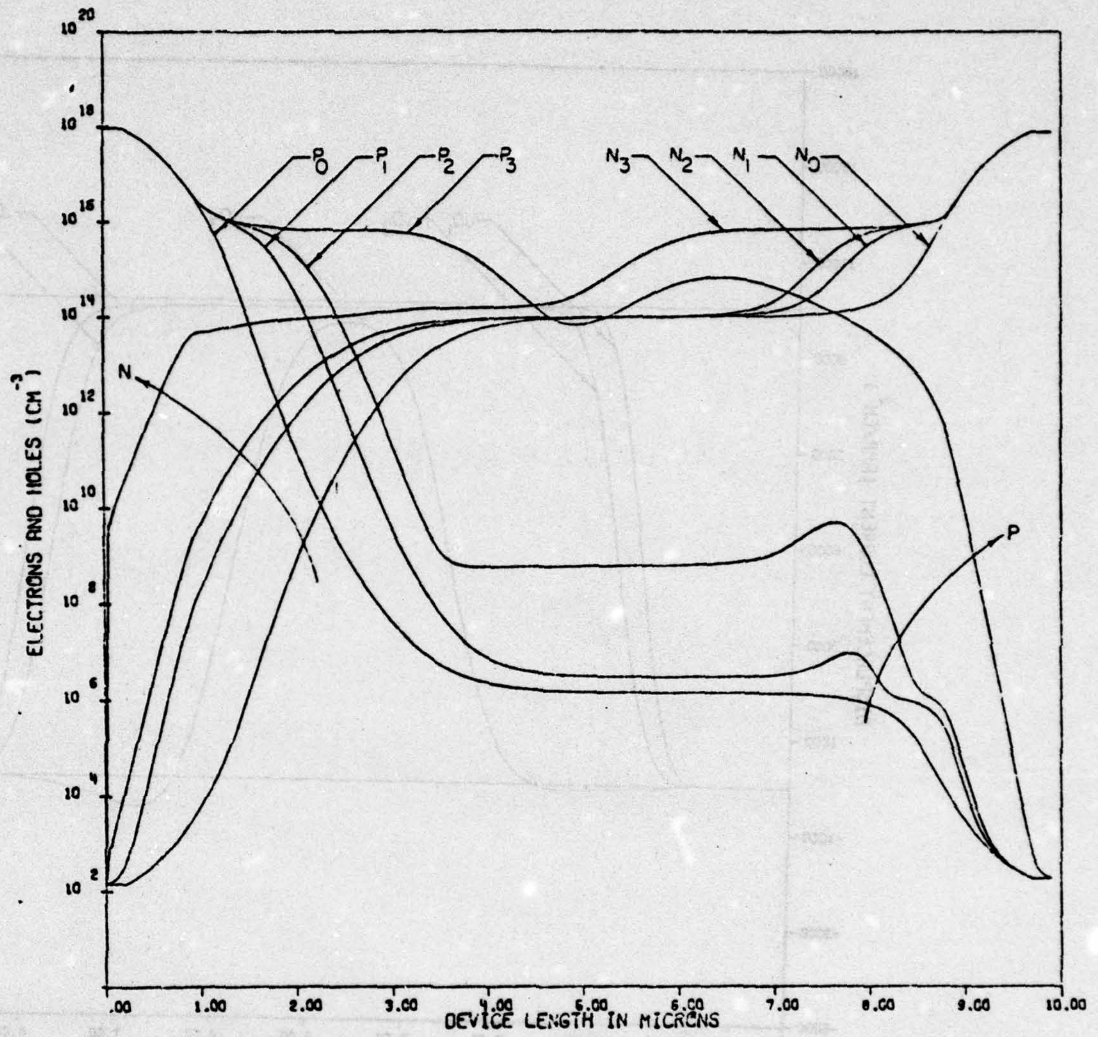

Figure 61. Electron and hole densities for time instants $t = 0$ to t_3 as shown in Figure 58

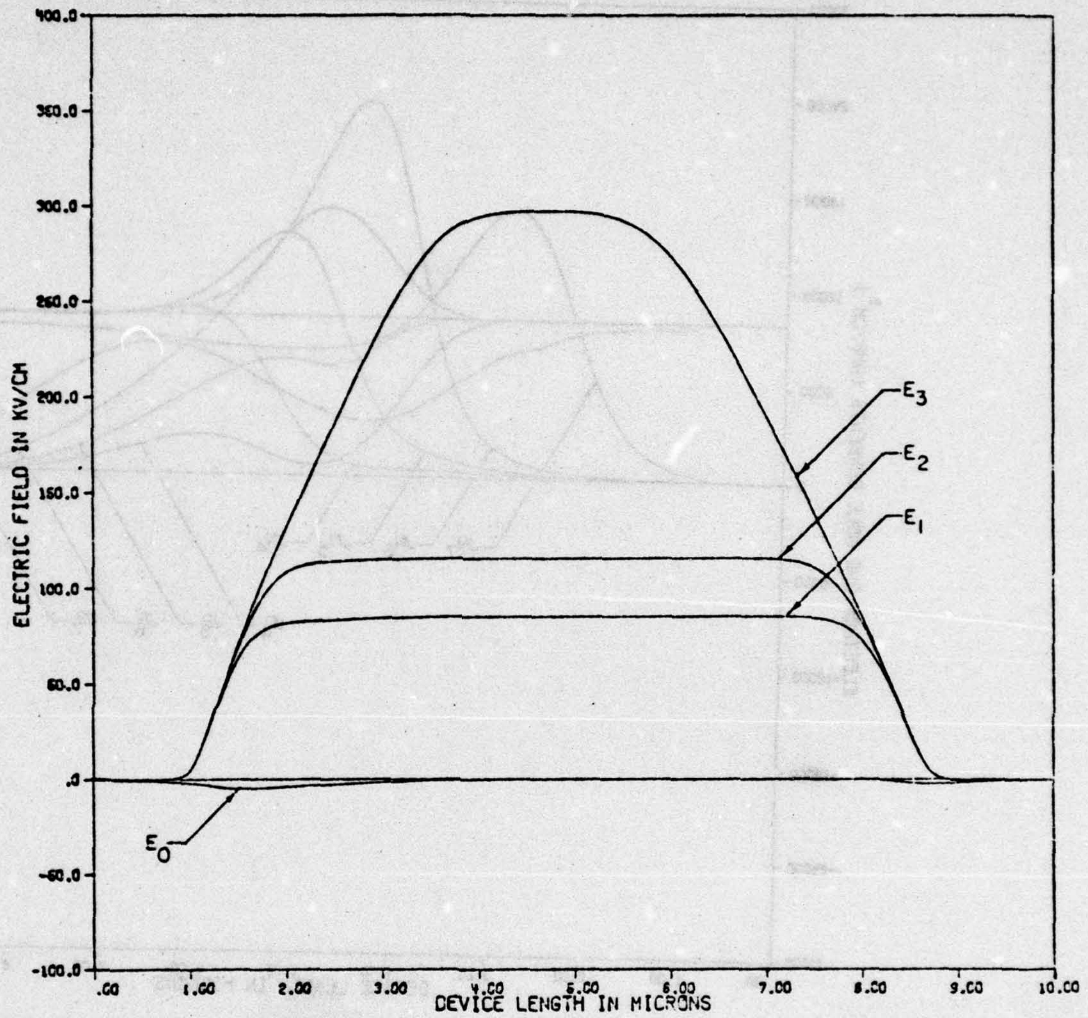

Figure 62. Electric field distribution for time instants t = 0 to t_3 as shown in Figure 58

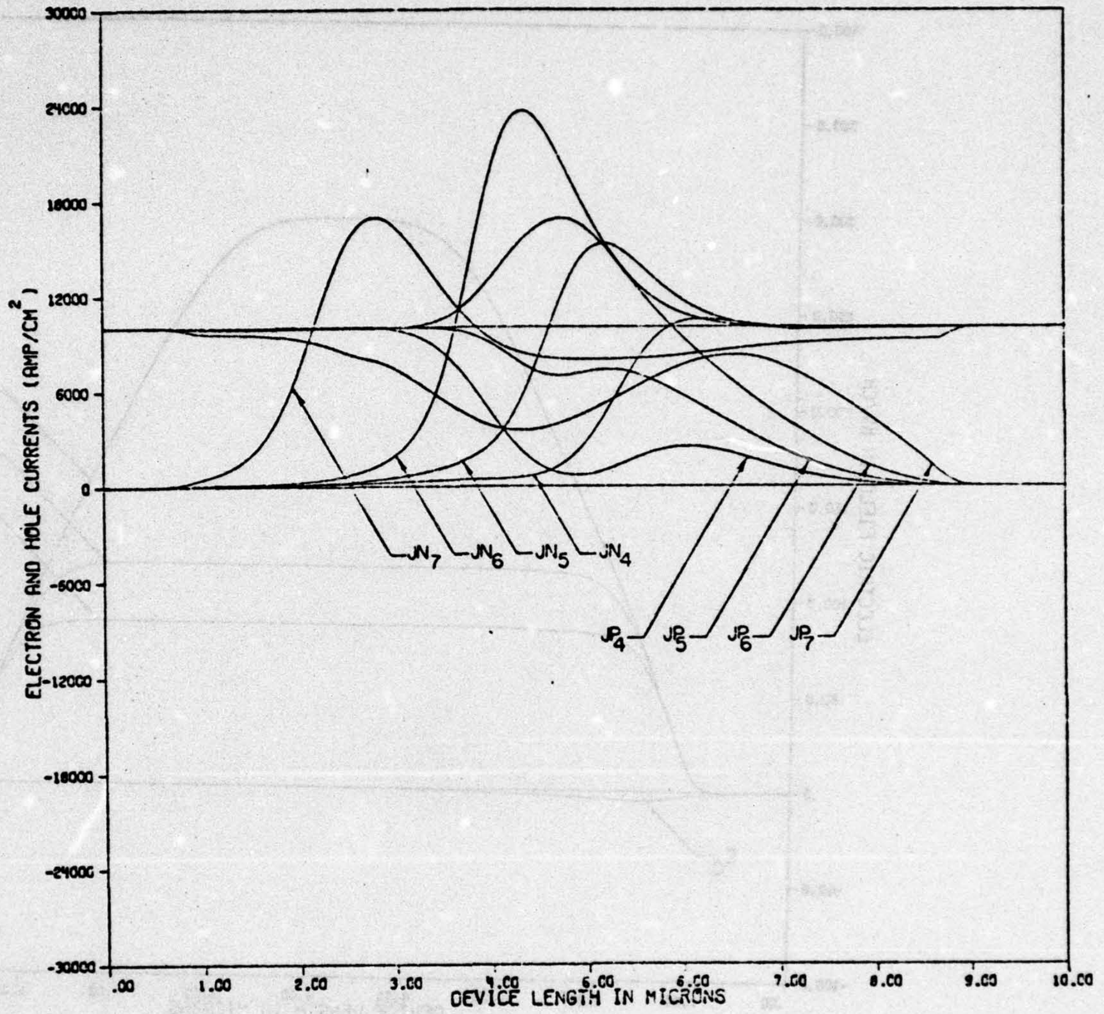

Figure 63. Electron and hole current density distributions for time instants t_4 to t_7 as shown in Figure 58

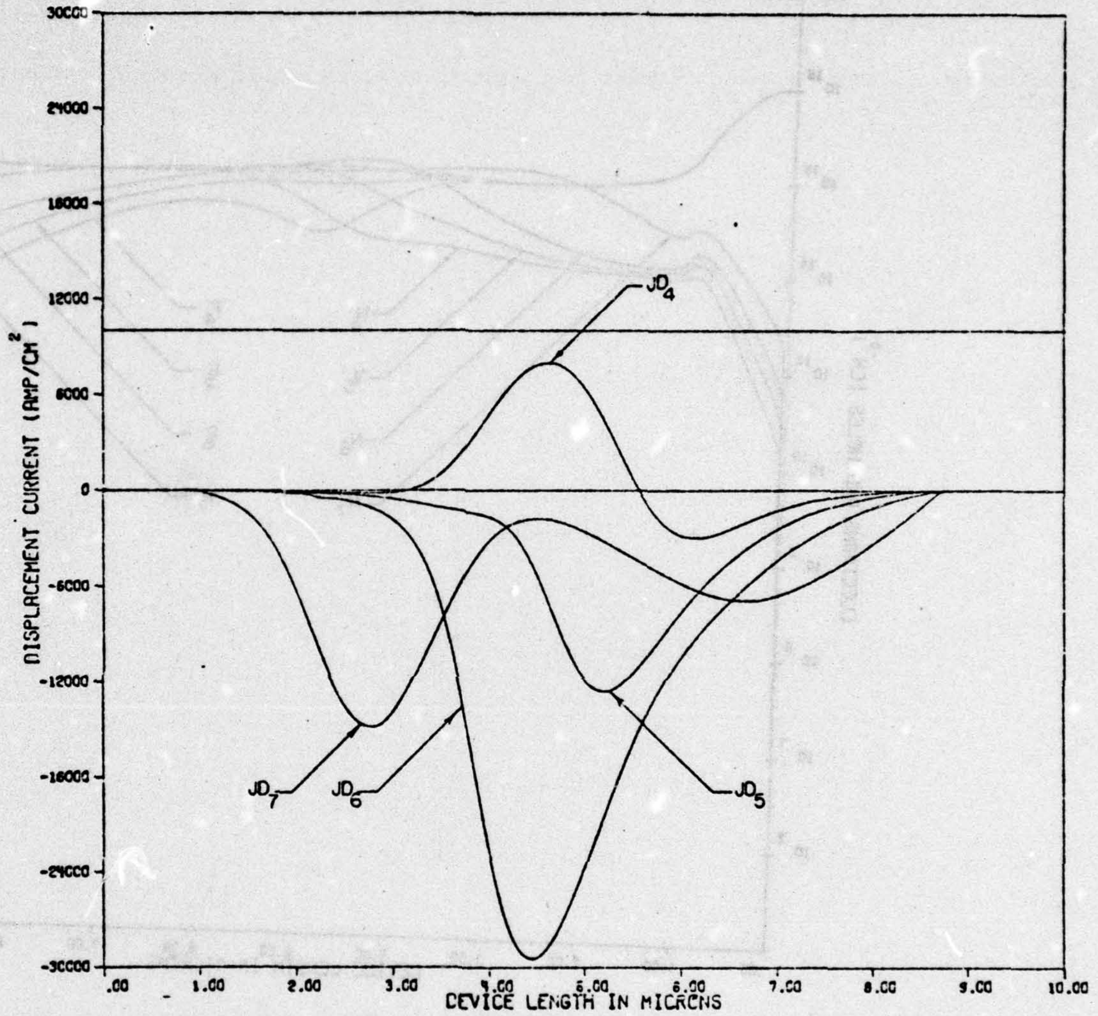

Figure 64. Displacement current density distribution for time instants t_4 to t_7 as shown in Figure 58

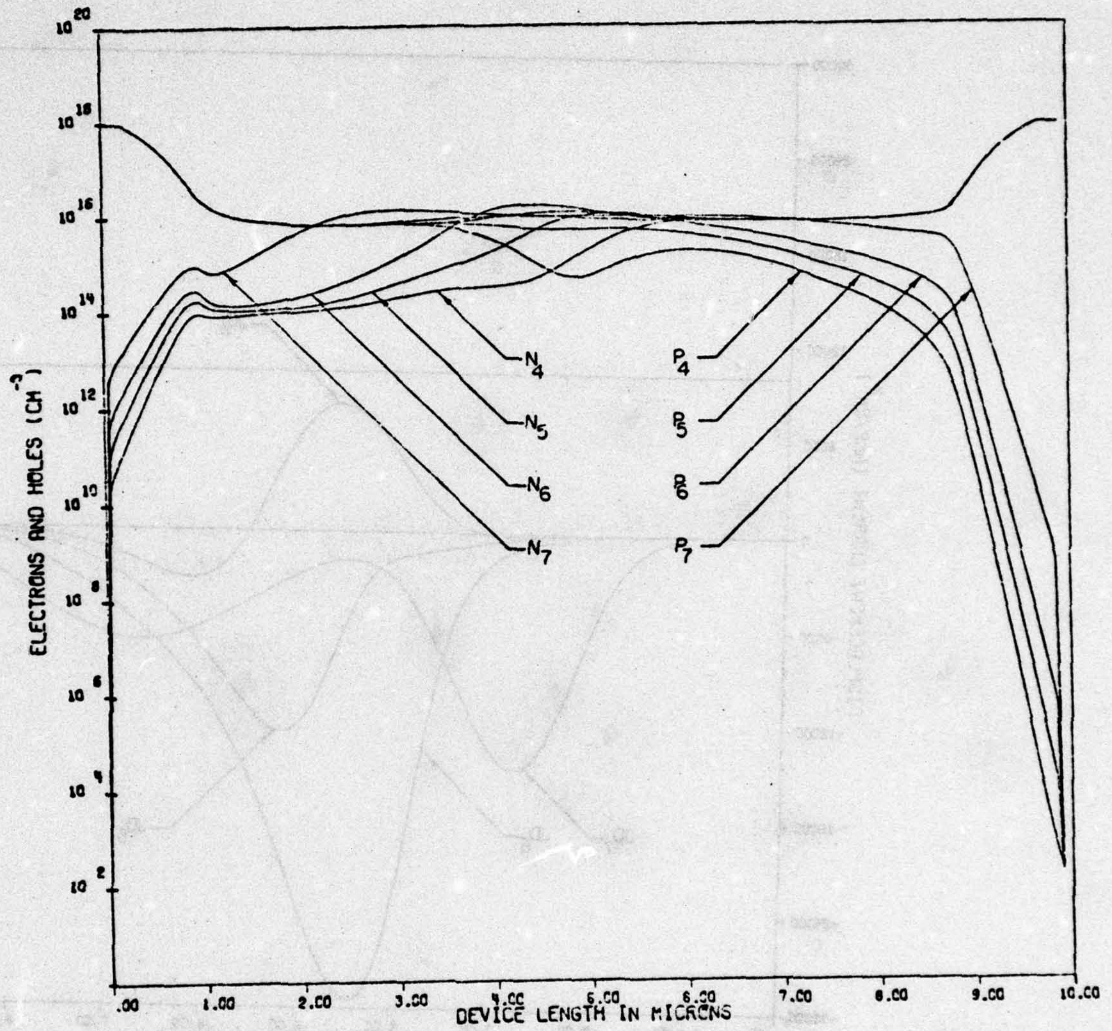

Figure 65. Electron and hole density distributions at time instants t_4 to t_7 as shown in Figure 58

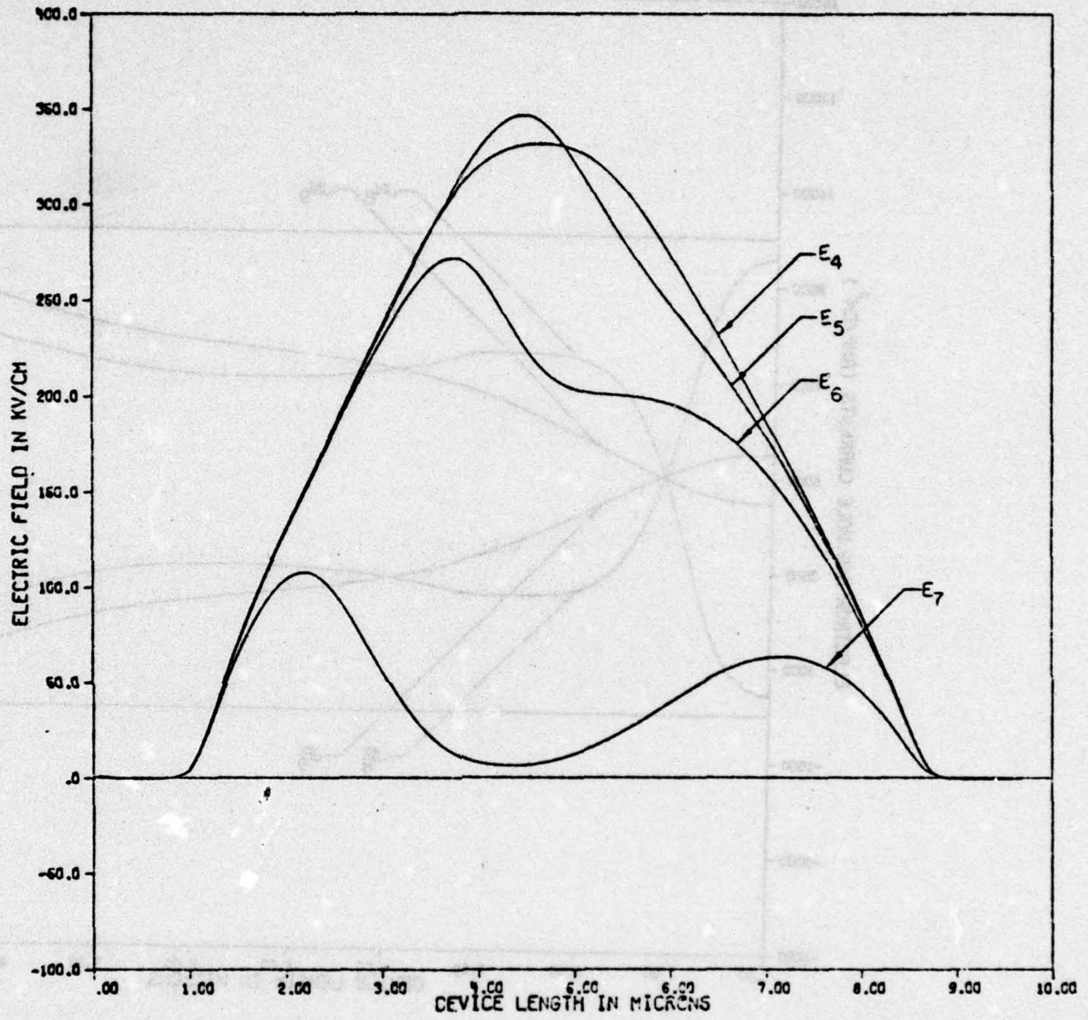

Figure 66. Electric field distribution for time instants t_4 to t_7 as shown in Figure 58

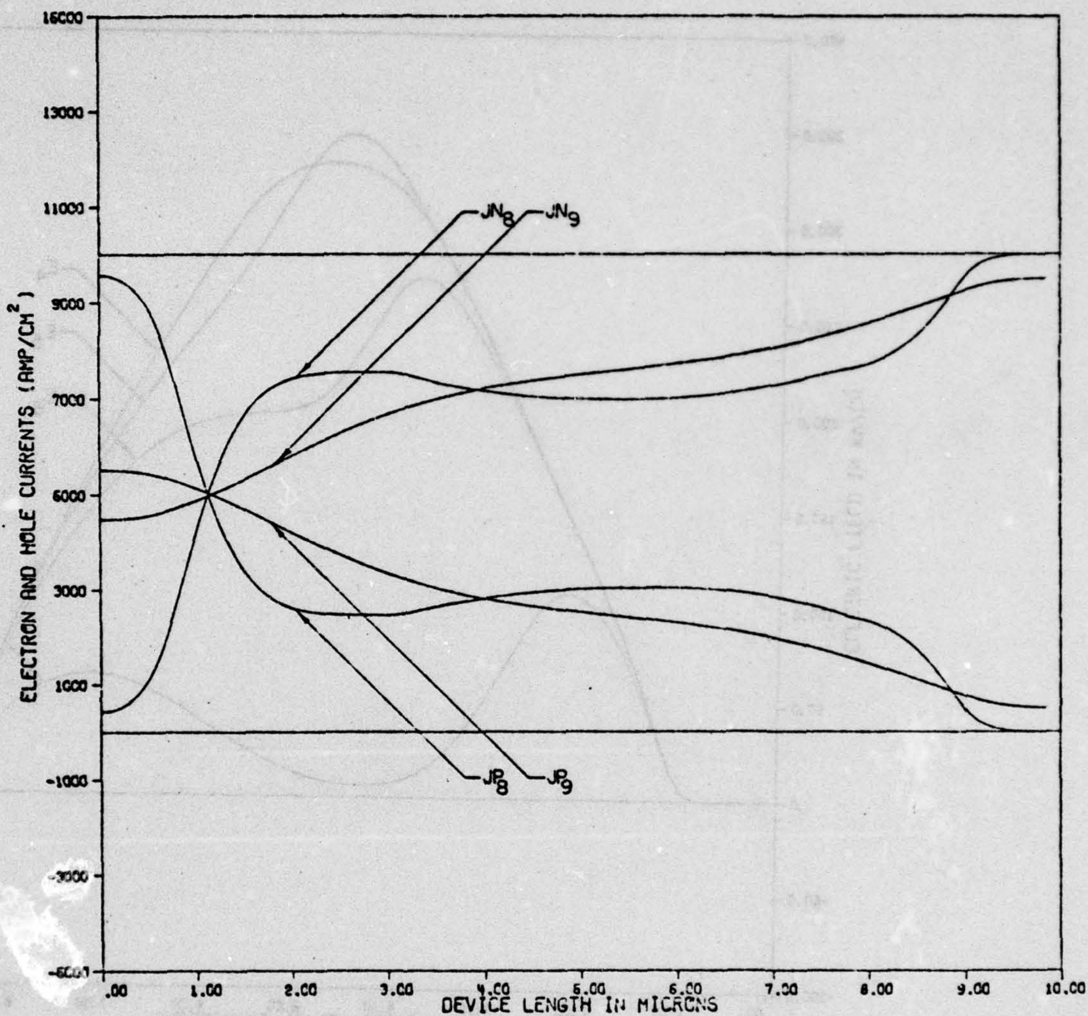

Figure 67. Electron and hole current density distributions for time instants t_8 and t_9 as shown in Figure 58

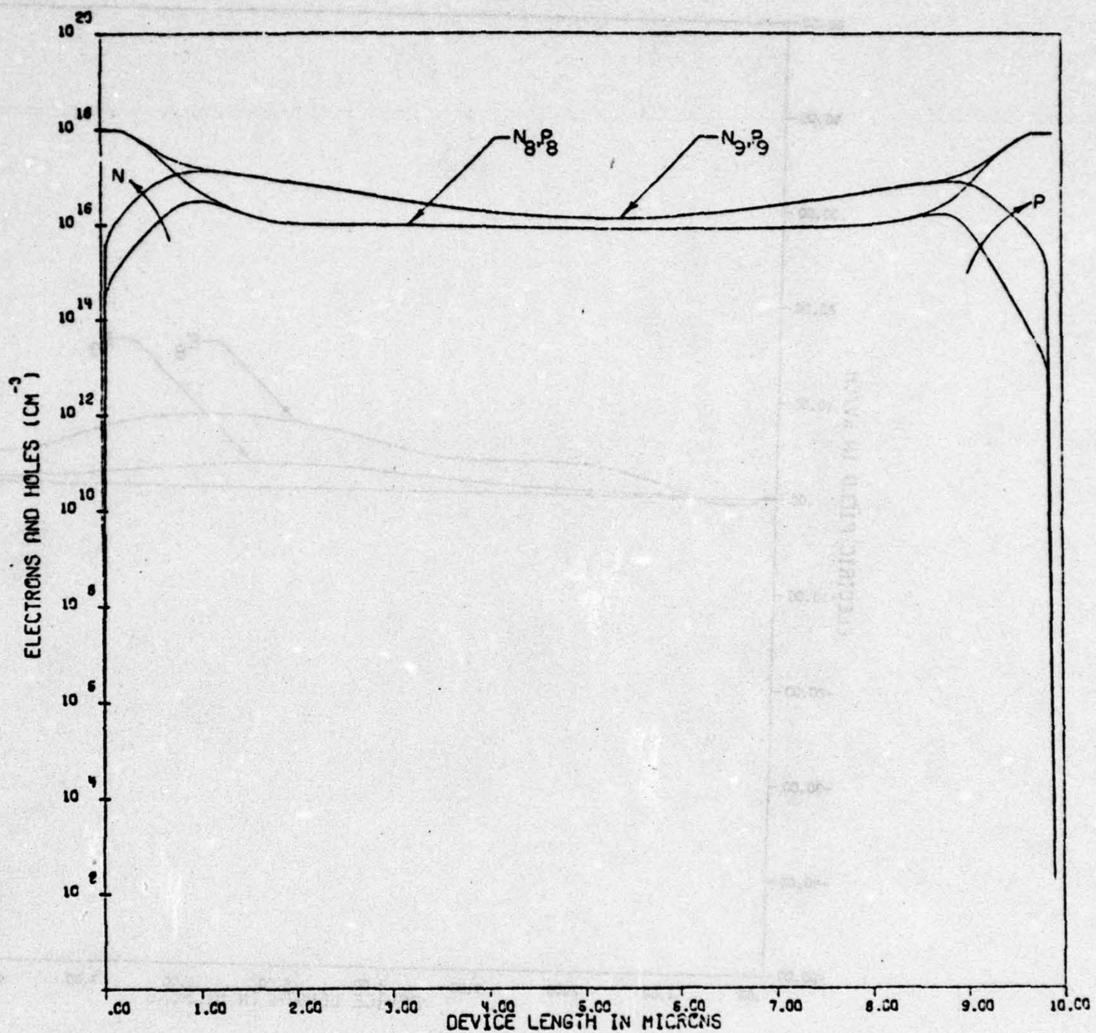

Figure 68. Electron and hole density distributions for time instants t_8 and t_9 as shown in Figure 58

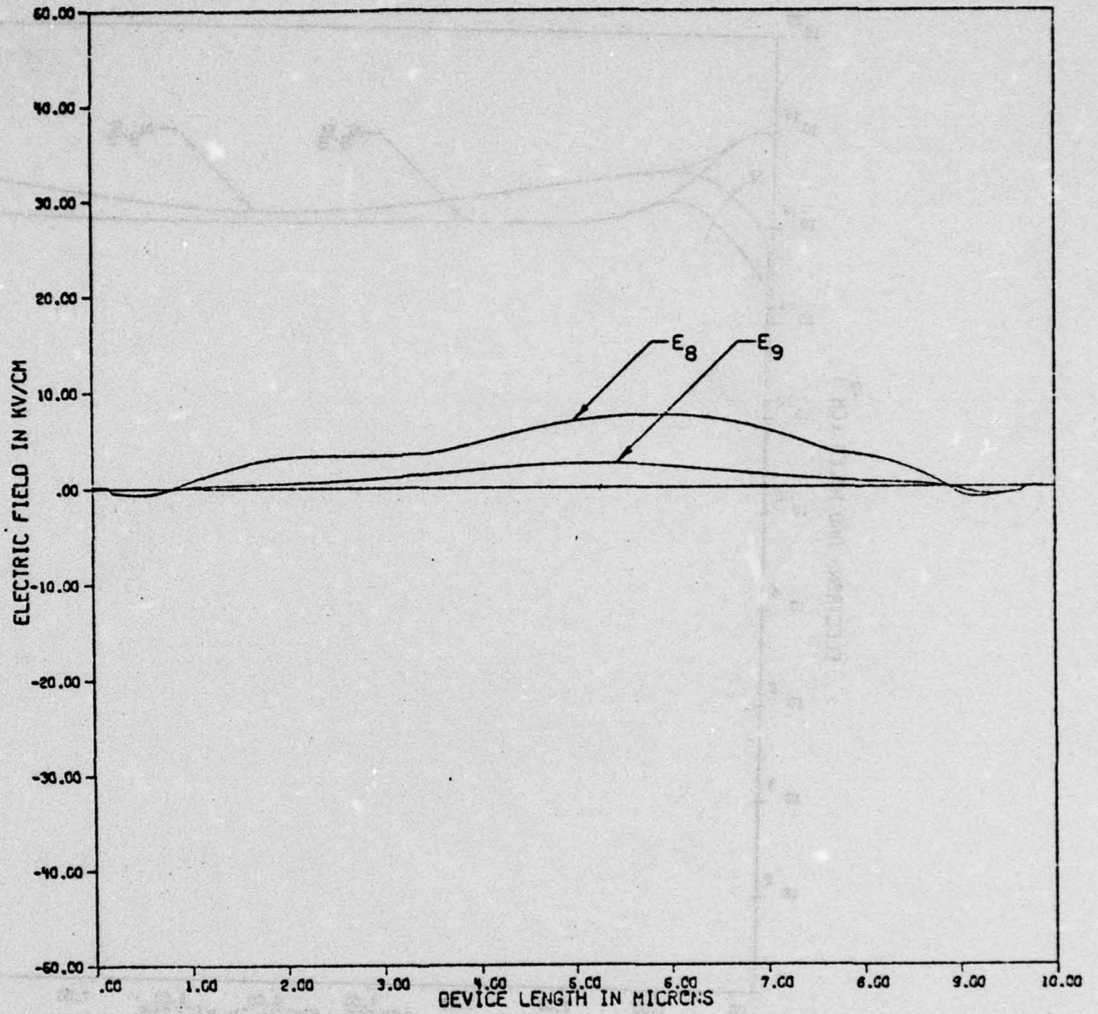

Figure 69. Electric field distribution for time instants t_8 and t_9 as shown in Figure 58

ing density, which causes the current at the ohmic contacts to be carried by both the minority and the majority carriers, in such a way as to reduce the particle current derivatives and to satisfy equation (113). This situation continues until t_9 where the output voltage drops to a value of 2.1 volts without reaching a steady state.

From the results presented previously, it is clear that although the present formulations are adequate in explaining the transient response for relatively low current densities, it fails to give a physical explanation for extreme current levels, where the device is too far from the equilibrium condition. This is mainly because in the forward bias case, the present formulation does not provide a means of extracting any plasma formation in the N^--region. Having that in mind, the transient response of the previous section is reanalysed during three stages, the excess diffusion stage near t=0, the impact ionization stage, and near steady state where the displacement current is very small.

The excess diffusion stage and the transient lifetime prediction

The transient behavior near t = 0, for example time instants t_1 and t_2, is shown in Figs. 59 to 62. The time rates controlling the electron and hole changes are described by the two continuity equations:

$$\frac{\partial N}{\partial t} = - R + G + \frac{1}{q} \left|\frac{\partial JN}{\partial x}\right| \qquad (115)$$

and

$$\frac{\partial P}{\partial t} = - R + G - \frac{1}{q} \left|\frac{\partial JP}{\partial x}\right| \qquad (116)$$

where

$$R = \frac{PN - n_i^2}{\tau_0 (P+N+2n_i)}$$

and G assumes a small value at this stage.

The extremely high value of $\left|\frac{\partial JP}{\partial x}\right|$ compared to $\left|\frac{\partial JN}{\partial x}\right|$ in the P^+-N^- transition region causes the number of holes to increase at a much higher rate compared to the increase in electrons. A similar situation develops in the N^+-N^- transition region causing a large increase of electrons compared to holes. Whereas, it is known that in a neutral or in a quasi-neutral region, there is the restraint on the system that the net change in negative charge is balanced by a change in the positive charge [7]. It is also known that in case of low level injection, due to the complicated nature of the two continuity equations, it is customary to solve a simplified continuity equation which controls the time variation of the minority carriers. Then the assumption of $\Delta N = \Delta P$ is usually used.

The above discussion suggests that the two recombination terms in equations (115) and (116) may not be equal, especially when the device is too far away from equilibrium, as in the present case. Blakemore [8] pointed out that these two recombination terms can be different in the two continuity equations, and that there is a hope of finding equal terms only in carefully purified semiconductors of small intrinsic band gap width at high temperatures, when band-to-band processes dominate the recombination behavior. Therefore, the two continuity equations are rewritten with different recombination terms as follows:

$$\frac{\partial N}{\partial t} = - \frac{PN - n_i^2}{\tau_n (P+N+2n_i)} + G + \frac{1}{q}\left|\frac{\partial JN}{\partial x}\right| \quad (117)$$

$$\frac{\partial P}{\partial t} = -\frac{PN - n_i^2}{\tau_p(P+N+2n_i)} + G - \frac{1}{q}\left|\frac{\partial JP}{\partial x}\right| \quad (118)$$

The transient lifetimes τ_n and τ_p are adjusted in such a way to limit the increase of majority cas to that of minority carriers in the two heavily doped regions, which normally operate under low level injection. The heavily doped regions are defined according to the difference between the two quantities $\left|\frac{\partial JP}{\partial x}\right|$ and $\left|\frac{\partial JN}{\partial x}\right|$ near the ohmic contacts as follows:

$$P^+\text{-region where, } \left|\frac{\partial JP}{\partial x}\right| > \left|\frac{\partial JN}{\partial x}\right| \quad (119)$$

and

$$N^+\text{-region where, } \left|\frac{\partial JN}{\partial x}\right| > \left|\frac{\partial JP}{\partial x}\right| \quad (120)$$

Throughout the entire device the minority carrier continuity equation assumes the normal lifetime "τ_0", while the transient lifetime in the majority carrier continuity equation is adjusted to satisfy equation (121) in both the N^+, and the P^+ regions.

$$\Delta P = \Delta N \quad (121)$$

Therefore, in the heavily doped reqions, equations (117) and (118) are equated to give the following transient lifetimes:

In the P^+ region,

$$\tau_P = \frac{Z}{\frac{Z}{\tau_0} - \frac{1}{q}\left[\left|\frac{\partial JP}{\partial x}\right| + \left|\frac{\partial JN}{\partial x}\right|\right]} \qquad (122)$$

and, in the N^+-region,

$$\tau_n = \frac{Z}{\frac{Z}{\tau_0} + \frac{1}{q}\left[\left|\frac{\partial JP}{\partial x}\right| + \left|\frac{\partial JN}{\partial x}\right|\right]} \qquad (123)$$

where

$$Z = \frac{PN - n_i^2}{P+N+2n_i}$$

and

τ_0 = equilibrium lifetime.

The lifetime variation inside the device is shown in Fig. 70. At the start of the transient solution, the transient lifetime is very short, and it depends on the level of injection. As time proceeds, the value of $\left|\frac{\partial JP}{\partial x}\right|$ approaches $\left|\frac{\partial JN}{\partial x}\right|$, and the transient lifetime reduces to the equilibrium lifetime "τ_0" throughout the entire device.

The impact ionization stage

As soon as the electric field reaches a value of about 2×10^5 volt/cm, the electron and hole levels start to increase in the N^--region, which causes an increase in electron and hole currents. The particle currents increase, combined with the electric field increase result in a higher rate of carrier generation. Since in the present formulation there is no means to extract the excess carriers, the electron and hole currents continue to increase until they exceed the external applied current. This causes the dis-

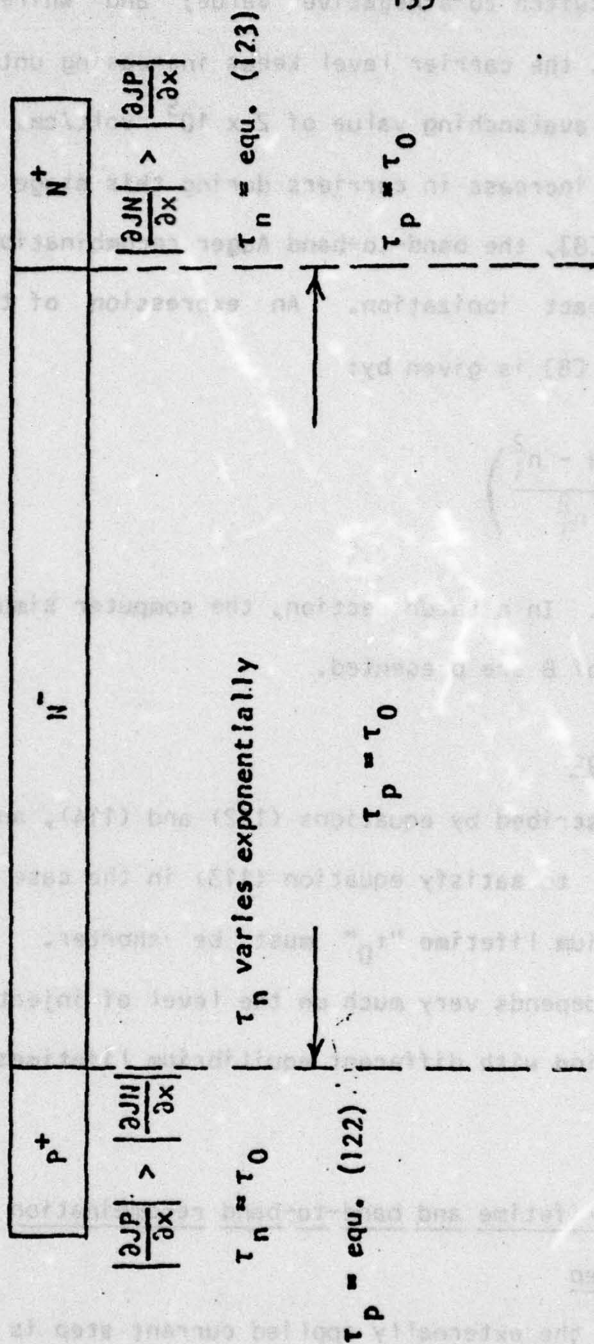

Figure 70. The lifetime variation inside the p^+-N^--N^+ structure

placement current to switch to a negative value; and while the electric field is decreasing, the carrier level keeps increasing until the electric field drops below the avalanching value of 2 x 10^5 volt/cm. Therefore, a way of limiting the increase in carriers during this stage is needed. According to Blakemore [8], the band-to-band Auger recombination is a process complementary to impact ionization. An expression of the band-to-band recombination [7] and [8] is given by:

$$R_{BB} = B \left(\frac{PN - n_i^2}{n_i^2} \right) \tag{122}$$

where B is a constant. In a later section, the computer simulation results for different values of B are presented.

Near steady state stage

This stage is described by equations (112) and (114), and is shown in Fig. 67. In order to satisfy equation (113) in the case of high current density, the equilibrium lifetime "τ_0" must be shorter. Therefore, the equilibrium lifetime depends very much on the level of injection. An investigation of the solution with different equilibrium lifetimes is also found in a later section.

The use of transient lifetime and band-to-band recombination in the case of an extreme current step

In this section, the externally applied current step is the same as the one described before, with 10^4 Amp/cm^2 amplitude and 2 nanoseconds rise time. The transient lifetime adjustment described previously is first used without any band-to-band recombination during the impact ionization stage. The voltage vs. time transient response is shown in Fig. 71 as the curve in-

dicated by a zero band-to-band recombination constant (B = 0). Fig. 71 also shows the transient response using both the transient lifetime adjustment and band-to-band recombination with different values of the constant B. The electron and hole currents, the displacement current, the carrier densities, and the electric field as a function of distance are shown in Figs. 72 to 75 for the first part of the transient response which is common to all curves of Fig. 71. At this stage the total current in the N^--region is mainly carried by the displacement current component as shown in Figs. 72 and 73. From Fig. 74 it is clear that the use of the transient lifetime does limit the excess diffusion of carriers near the heavily doped regions. Figures 76 to 79 demonstrate the variations of the physical quantities with no band-to-band recombination. As explained previously, the particle currents, as well as the carrier level increases to a very high value, which cause the displacement current to switch to a high negative value. This results in a fast decrease in the electric field as shown in Fig. 79 for the time instant t_9, and consequently the output voltage continues to drop to a very low value as shown in Fig. 71. Figures 80 to 83 demonstrate the spatial variation of the physical parameters using band-to-band recombination with a value of 5×10^{15} for the constant B. At time instant t_{10}, the impact ionization is taking place, the electric field and the carrier levels are high, the sum of the electron and hole currents exceeds the total applied current. Therefore, the displacement current switches to a negative value. Combining that with the band-to-band recombination, the net effect is a decrease in the carrier levels and the electric field. Consequently, the electron and hole currents decrease, while the displacement current switches back to a positive value as shown for the curves and time instant t_{11}. At the time instant t_{12} the device reaches steady state, the displacement current goes

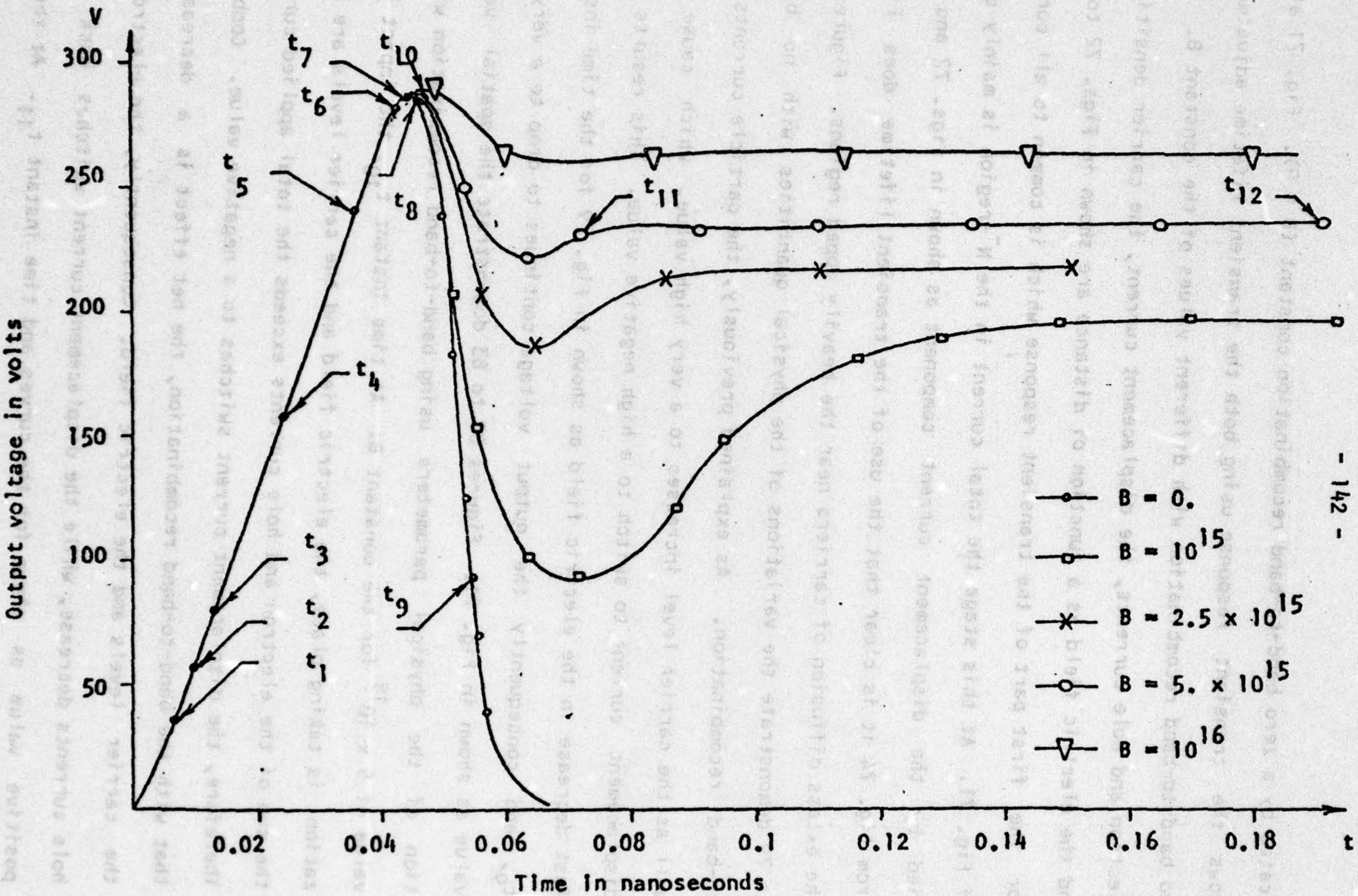

Figure 71. V(t) for an extremely high current step using the transient lifetime and band-to-band recombination

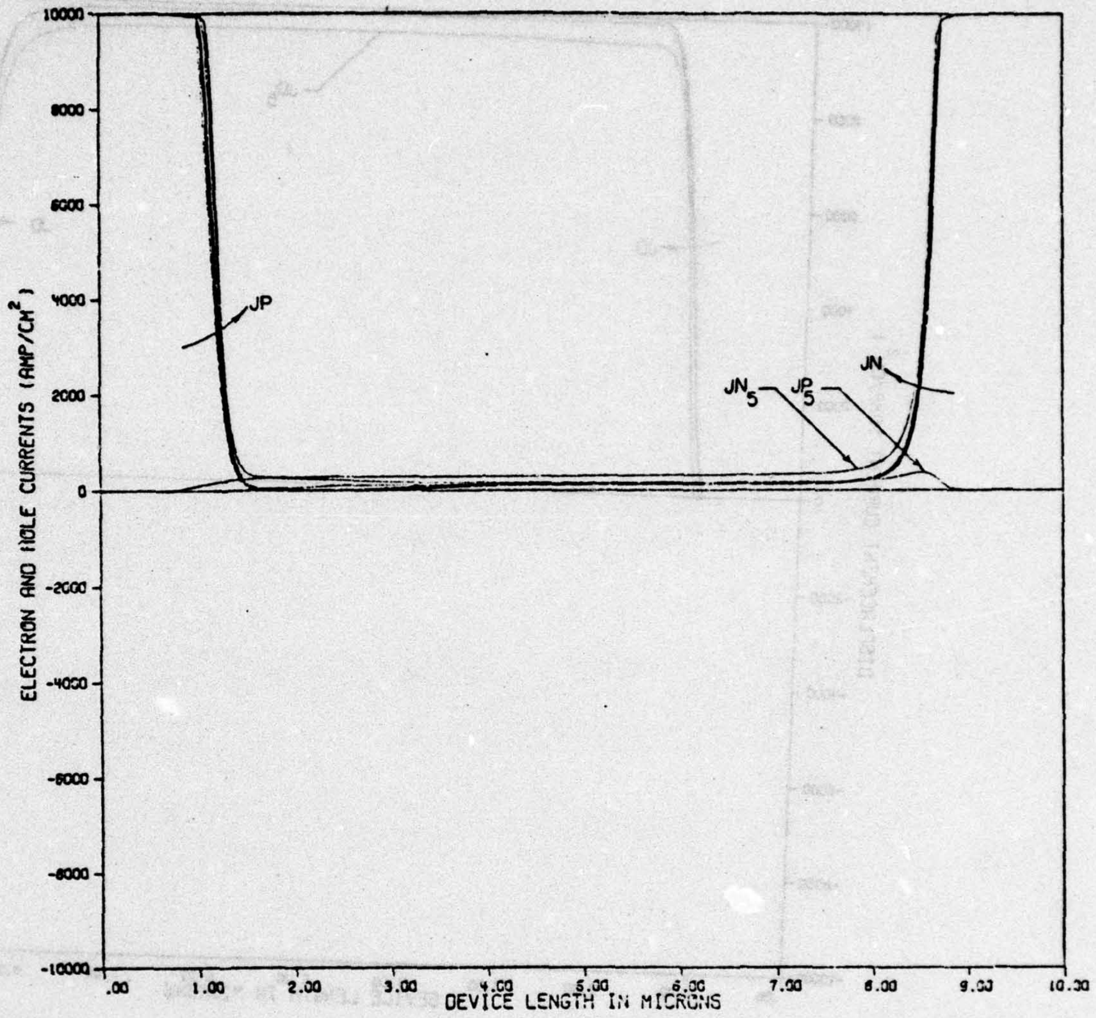

Figure 72. Electron and hole current density distributions for time instants t_1 to t_5 as shown in Figure 71

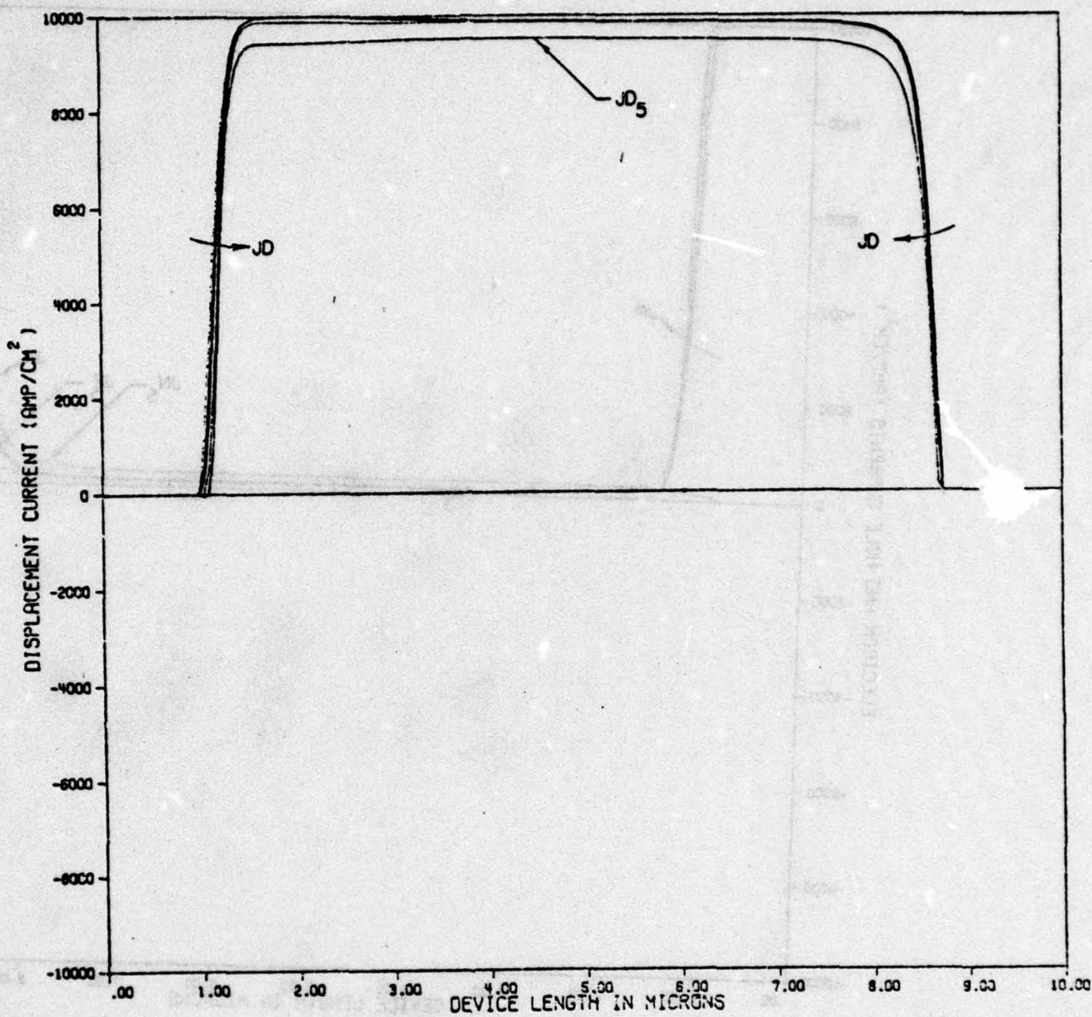

Figure 73. Displacement current density distribution for time instants t_1 to t_5 as shown in Figure 71

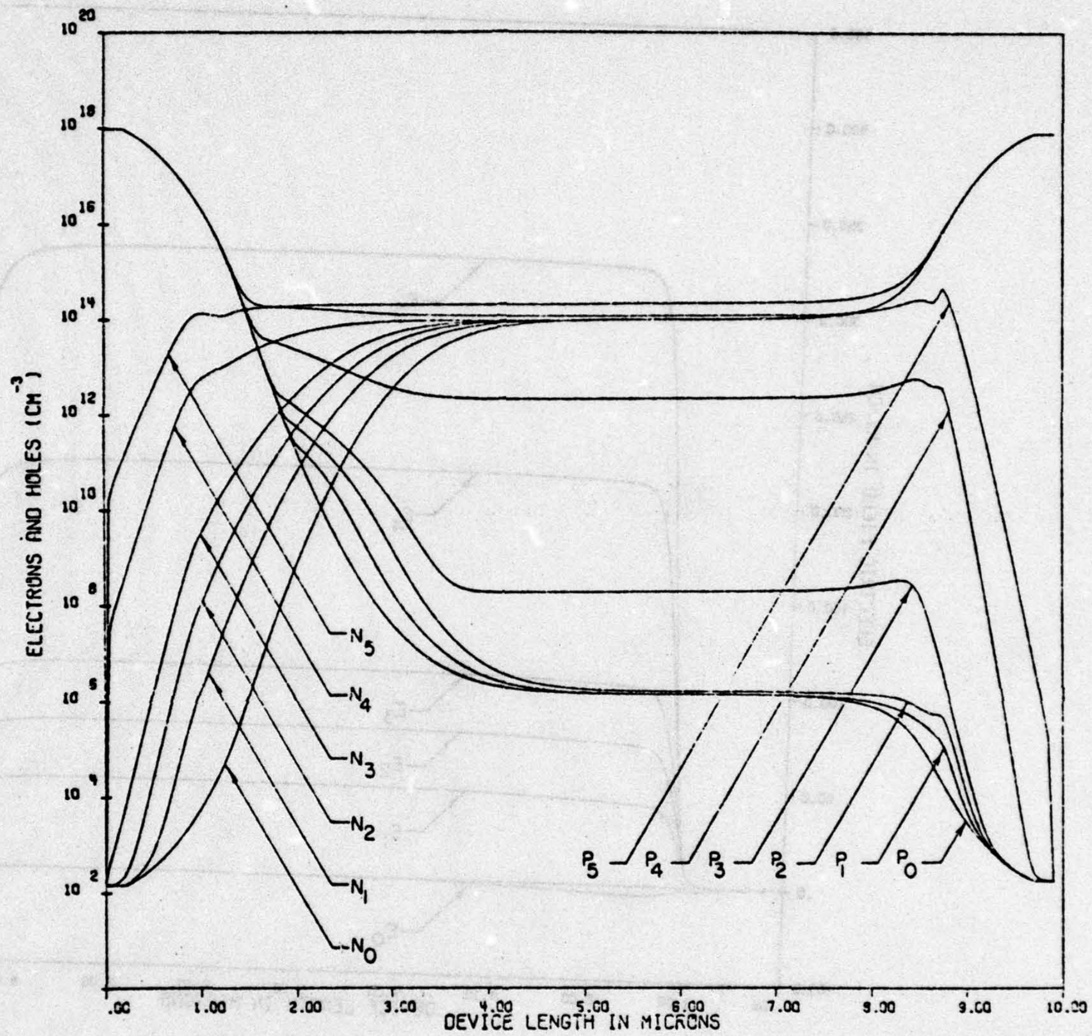

Figure 74. Electron and hole density distributions for the instants $t = 0$ to t_5 as shown in Figure 71

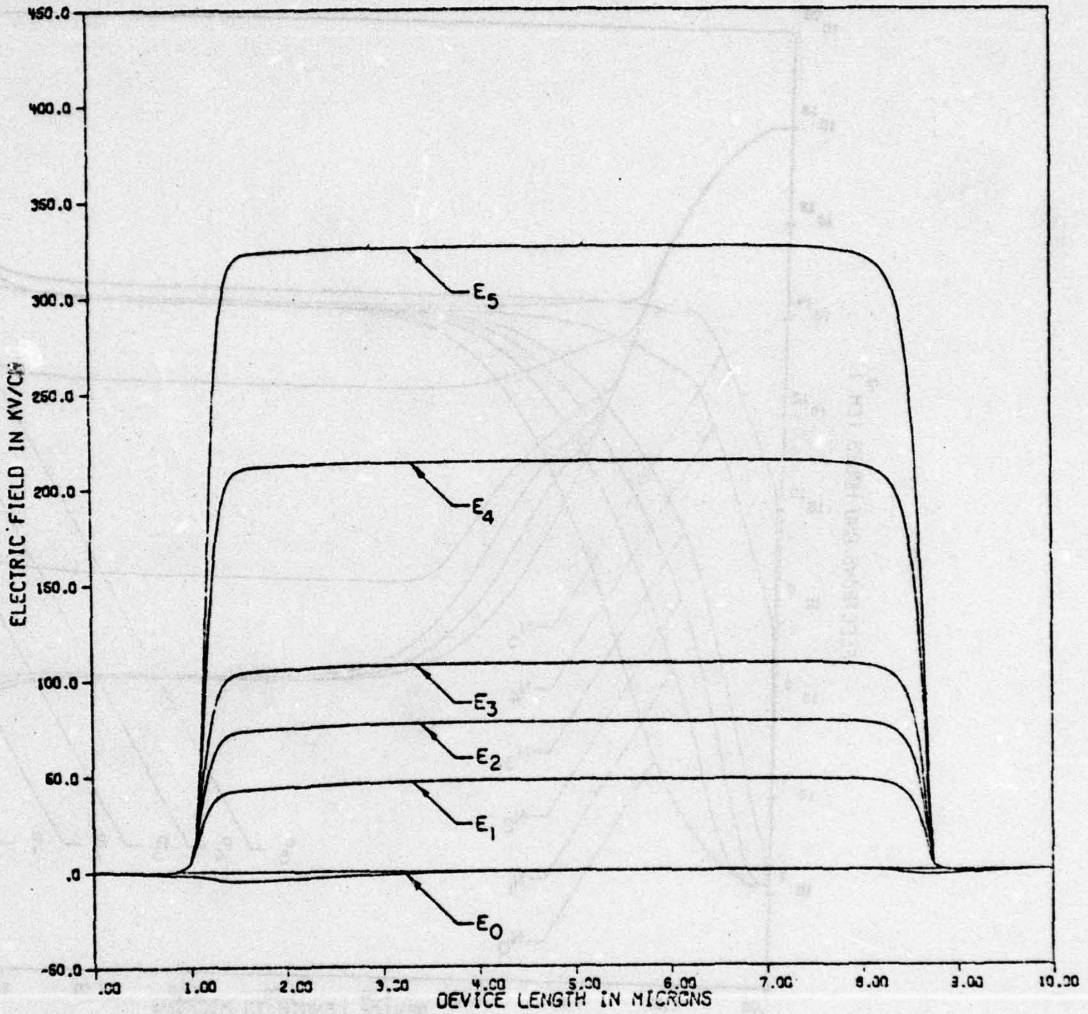

Figure 75. Electric field distribution for time instant $t = 0$ to t_5 as shown in Figure 71

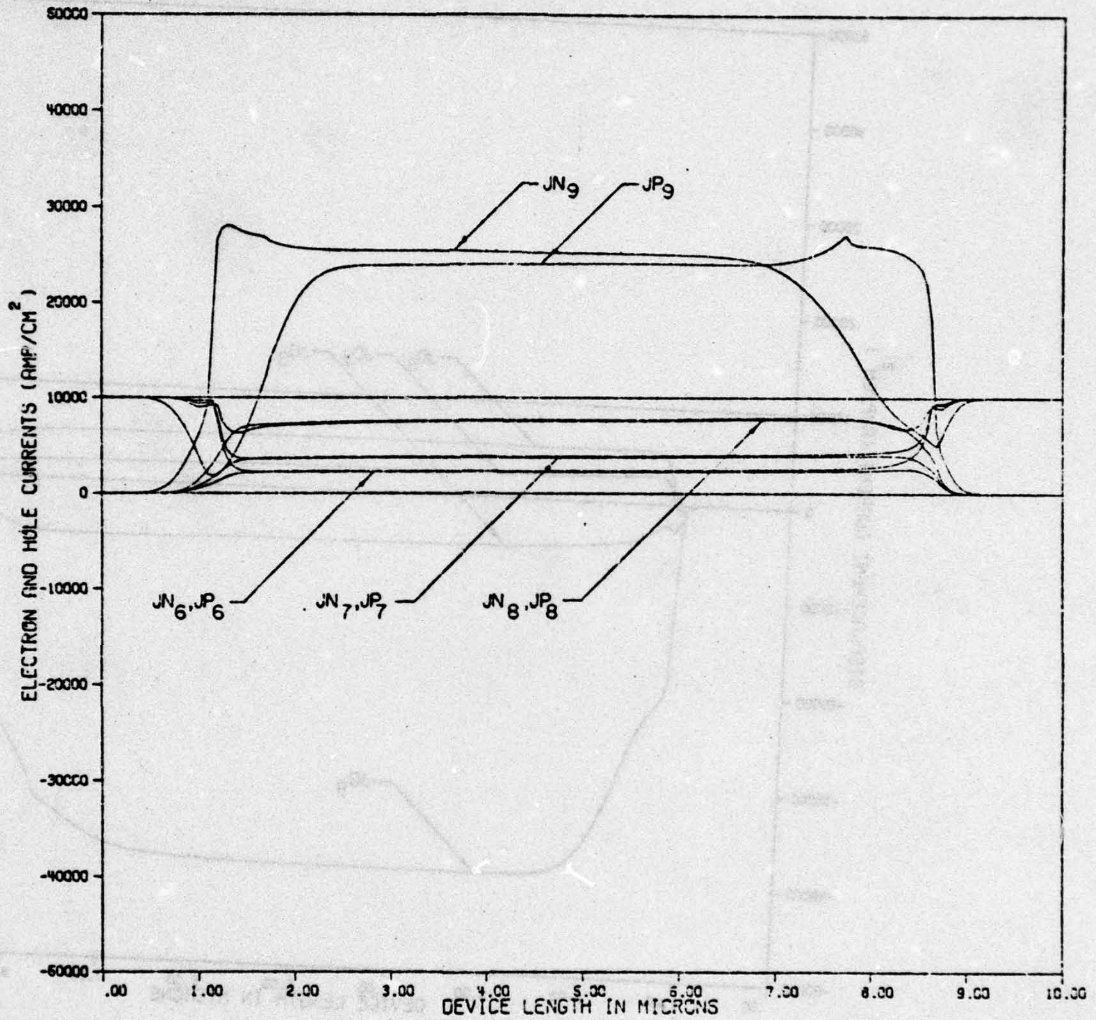

Figure 76. Electron and hole current density distributions for time instants t_6 to t_9 as shown in Figure 71

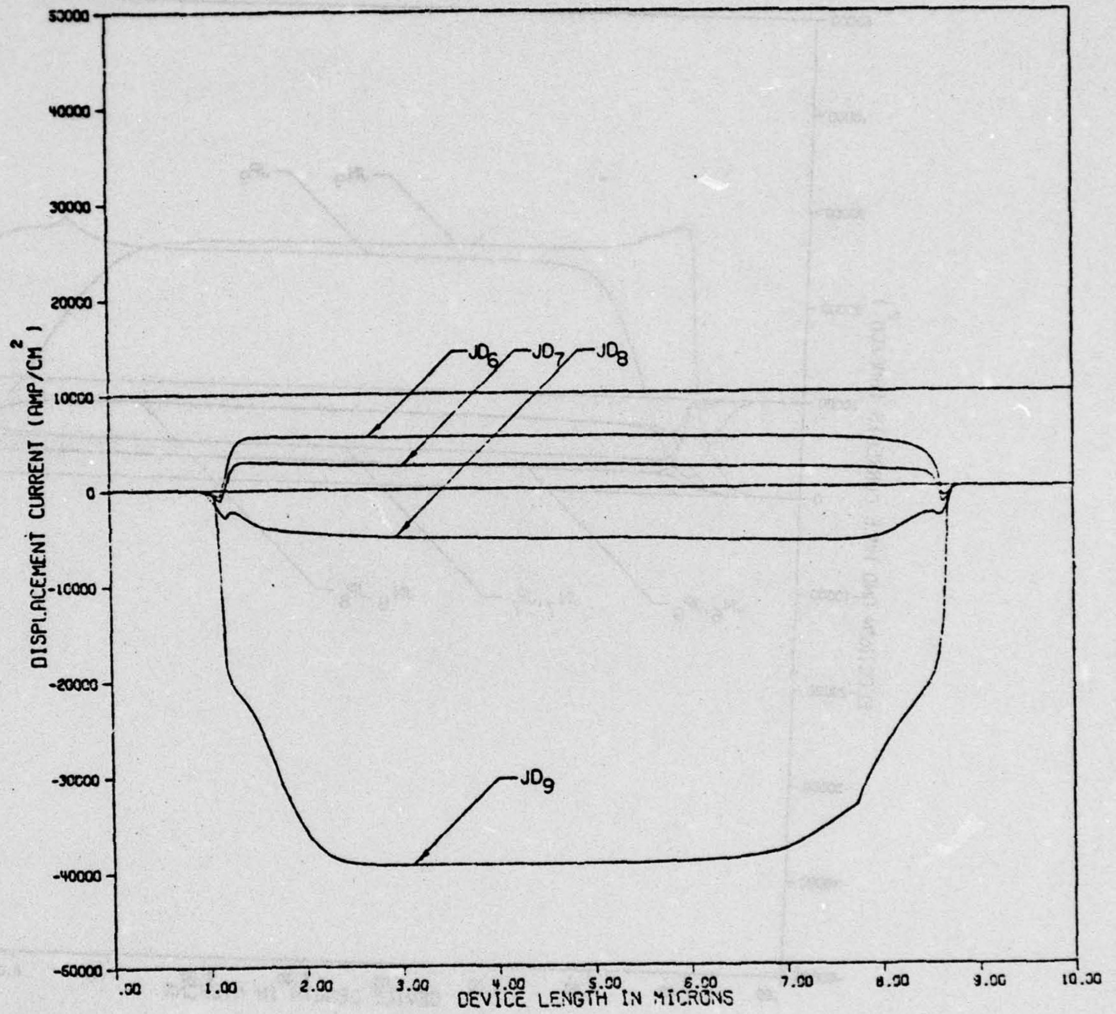

Figure 77. Displacement current density distributions for time instants t_6 to t_9 as shown in Figure 71

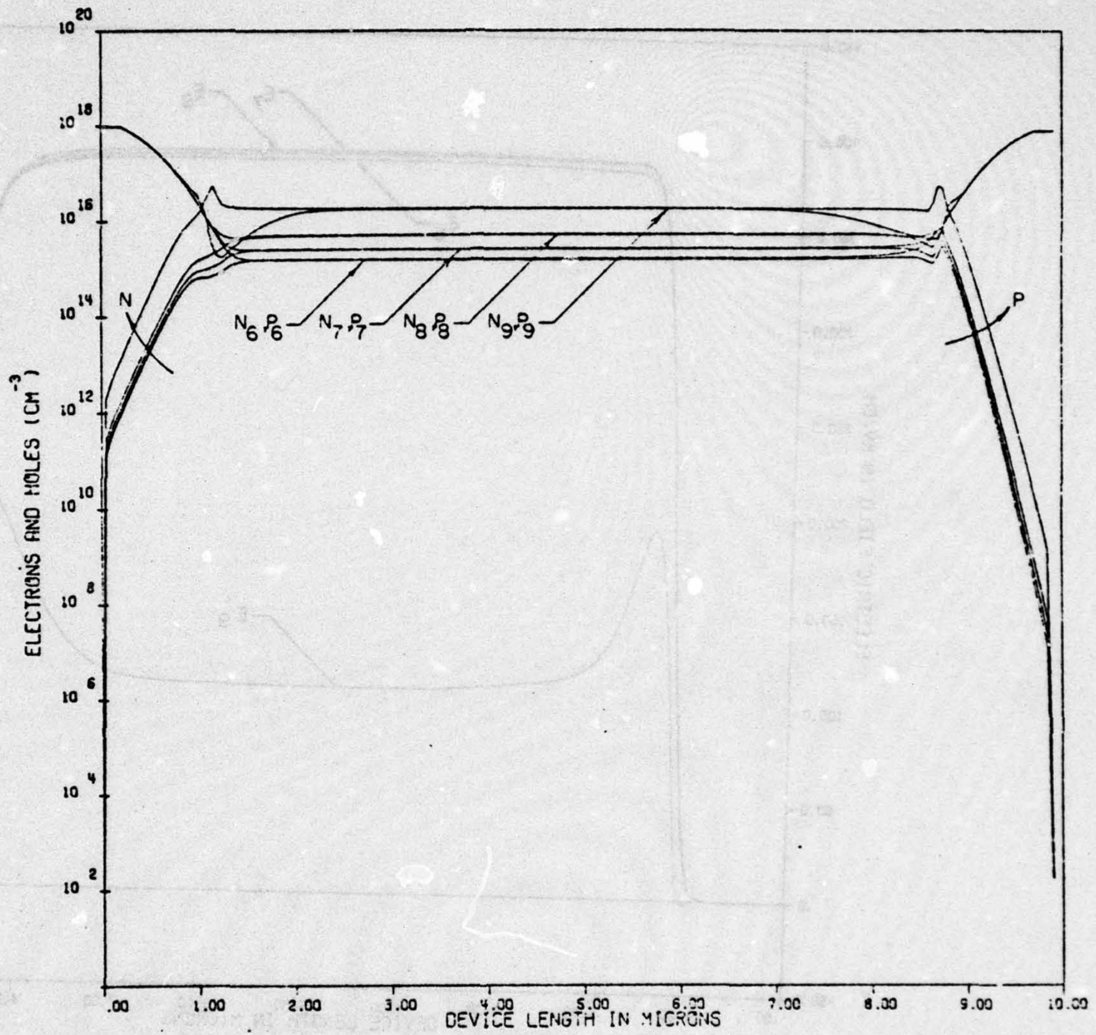

Figure 78. Electron and hole density distributions for time instants t_6 to t_9 as shown in Figure 71

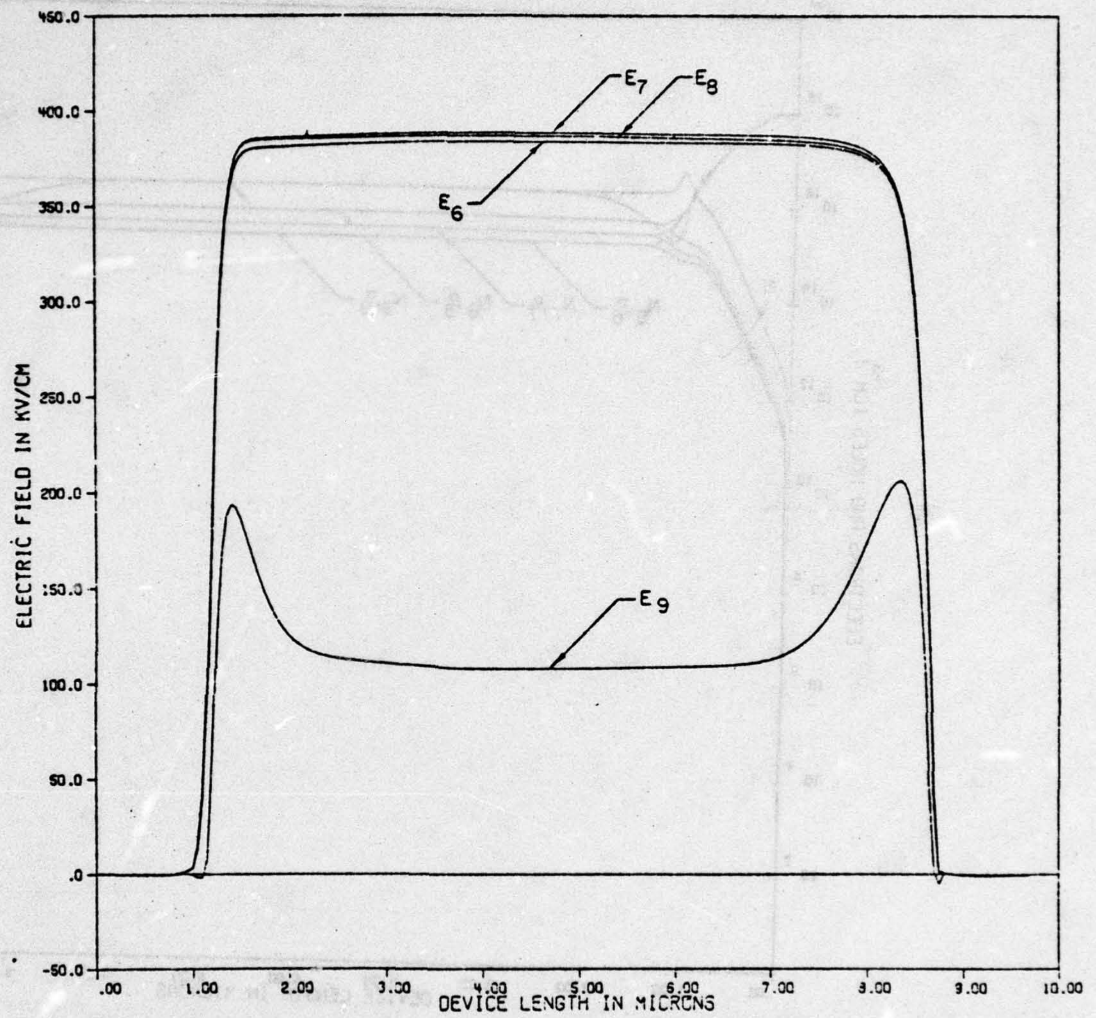

Figure 79. Electric field distributions for time instants t_6 to t_9 as shown in Figure 71

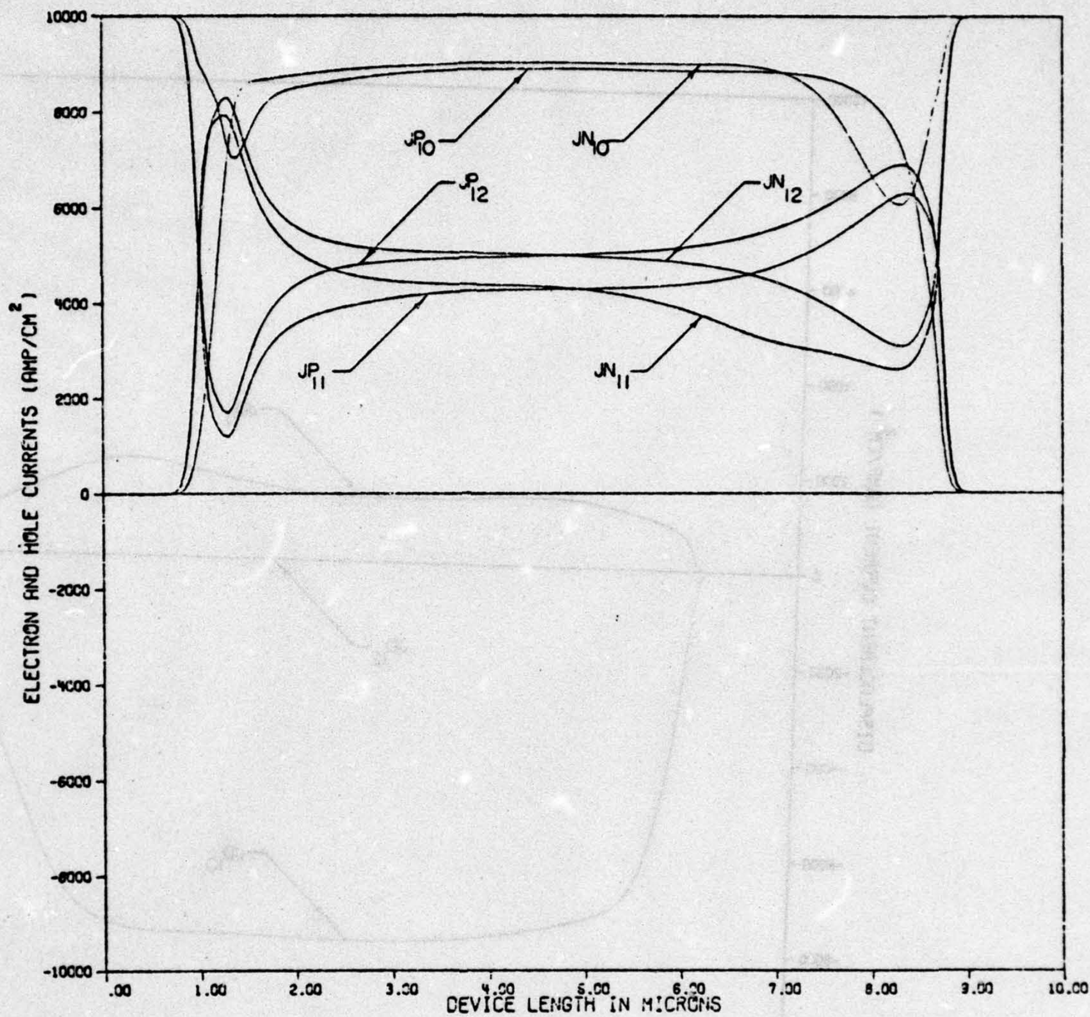

Figure 80. Electron and hole current density distributions for time instants t_{10} to t_{12} as shown in Figure 71

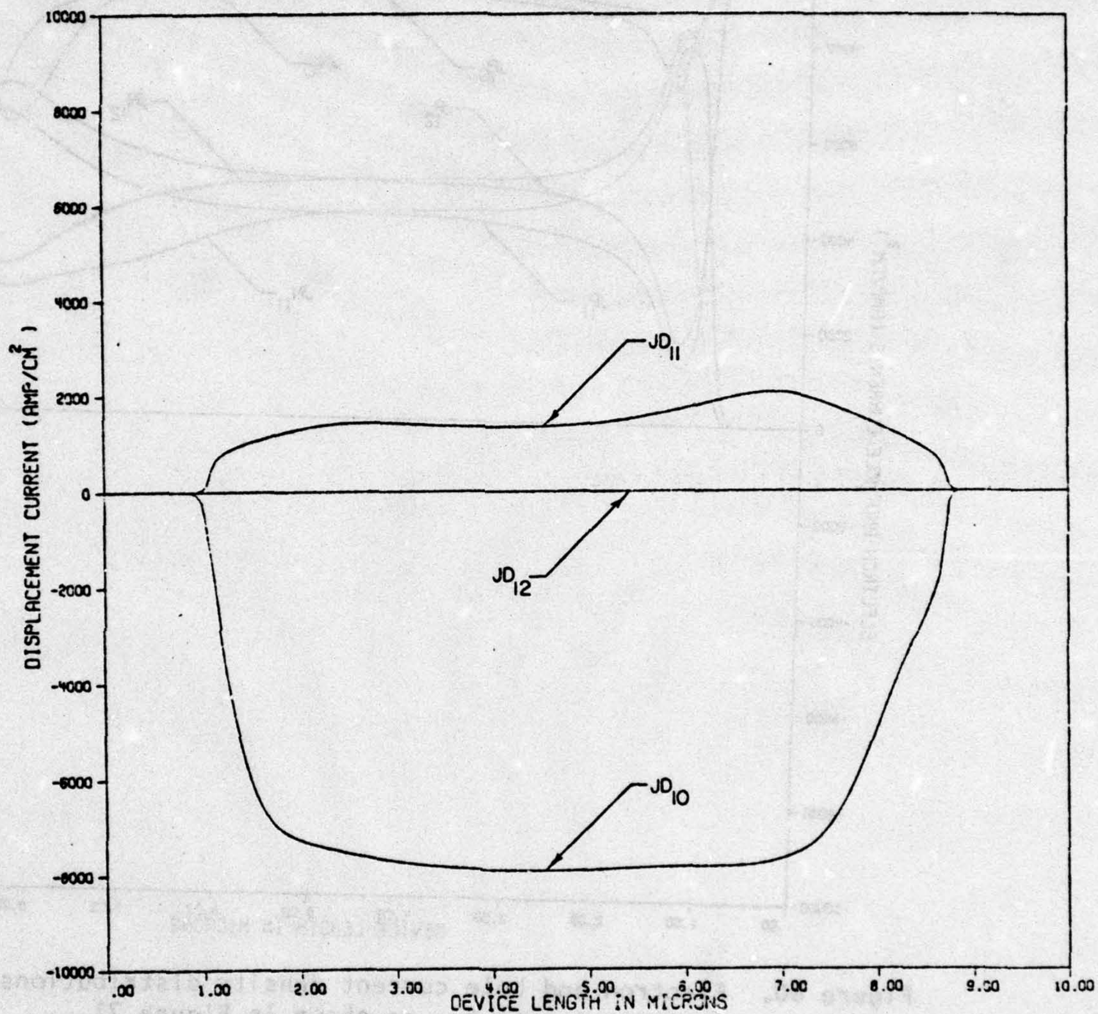

Figure 81. Displacement current density distribution for time instants t_{10} to t_{12} as shown in Figure 71

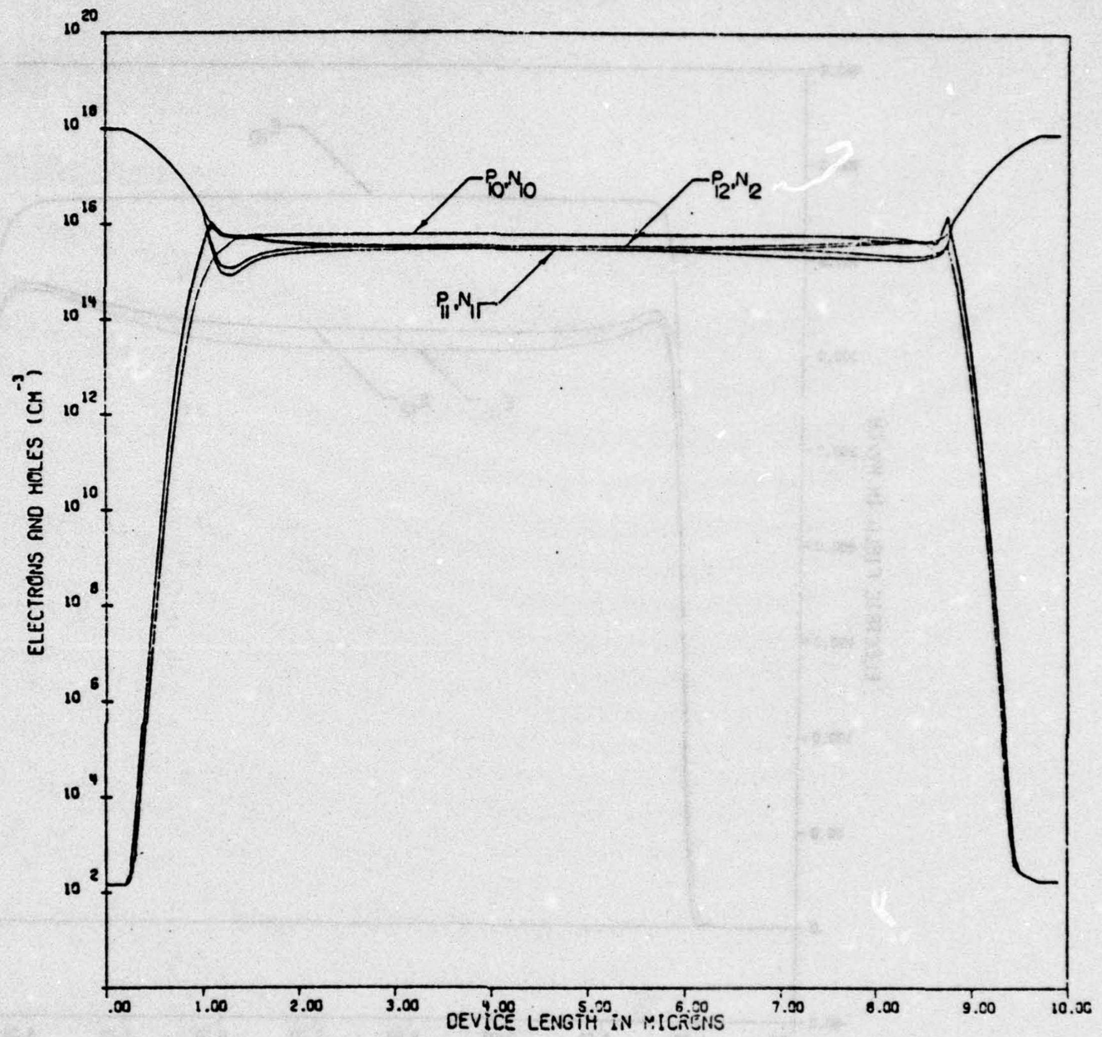

Figure 82. Electron and hole density distributions for time instants t_{10} to t_{12} as shown in Figure 71

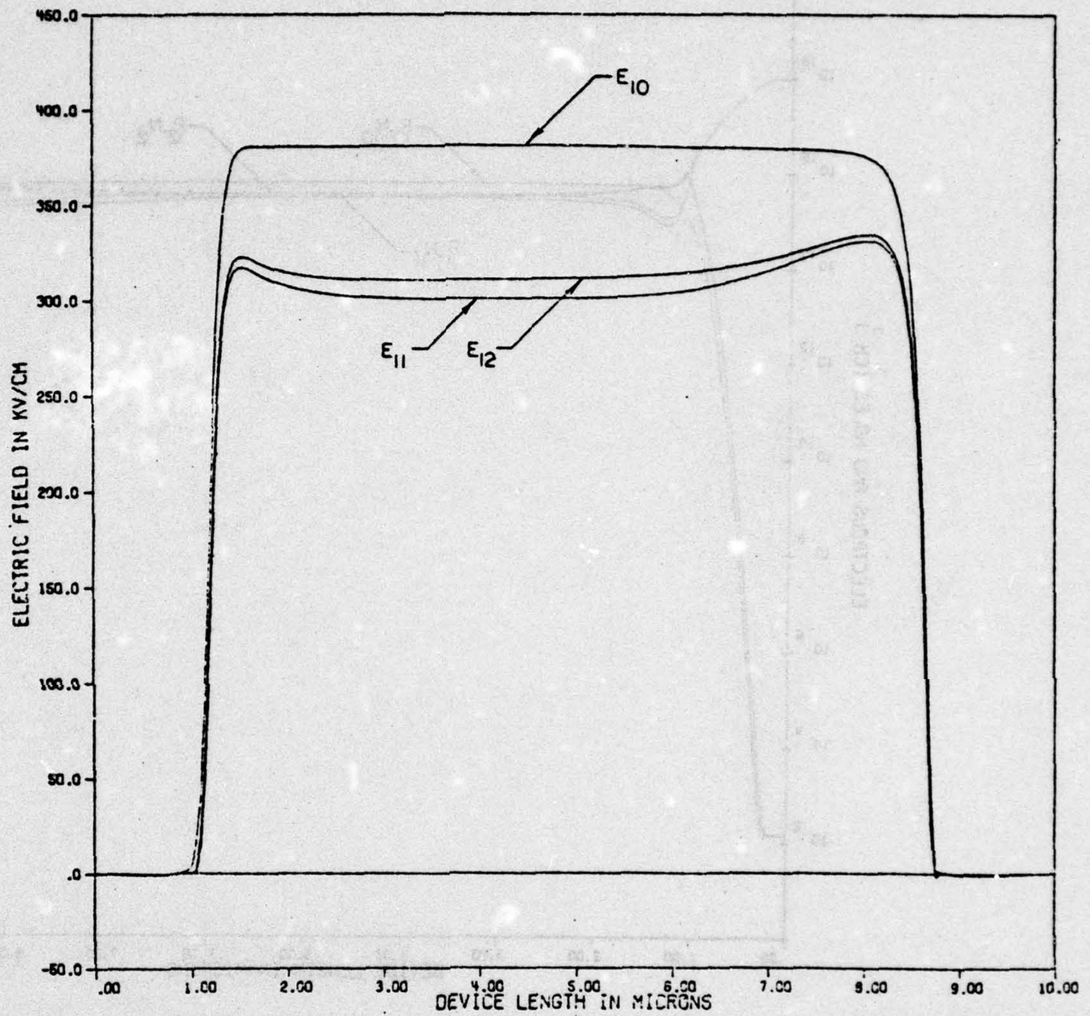

Figure 83. Electric field distribution for time instants t_{10} to t_{12} as shown in Figure 71

to zero, and the sum of the electron and hole currents is equal to the total current.

In conclusion, the use of transient lifetimes and band-to-band recombination, indeed predict a high voltage across P^+-N^--N^+ structure for extremely high current densities. The steady state high voltage depends on the strength of the band-to-band recombination. The larger the value of the constant B is, the lower the carrier level. Therefore, the electric field needed to support the current is higher. The initial decrease in the output voltage in Fig. 71, followed by an increase until steady state, is attributed to the instantaneous response of the carriers to the electric field as discussed for the reverse biased case in Chapter VI.

<u>External excitation in the form of high current step</u>

In this section, the forward current step has a 100 amp/cm^2 amplitude and 1.25 nanoseconds. The effect of varying the equilibrium lifetime on the near steady state stage, which is previously discussed, is presented here, along with the effect of using the transient lifetime. Figure 84 shows the output voltage as a function of time for three different cases. The first case, which is indicated by the triangular shaped marks, is the transient response without using the transient lifetime, and with an equilibrium lifetime in the N^--region of 4×10^{-8} seconds. The electron and hole current densities, the displacement current density, the carrier density, and the electric field as functions of distance are shown in Figs. 85 to 88 for the time instants $t = 0, t_1, \ldots,$ and t_7. It should be noticed that as steady state is approached, and the displacement current drops to a very small value, electron and hole diffusion continues in order to decrease the spatial derivatives of JN and JP to satisfy equation (113). The time instant t_7 of Fig. 85 shows that at the ohmic contact of the P^+-region, 30% of the

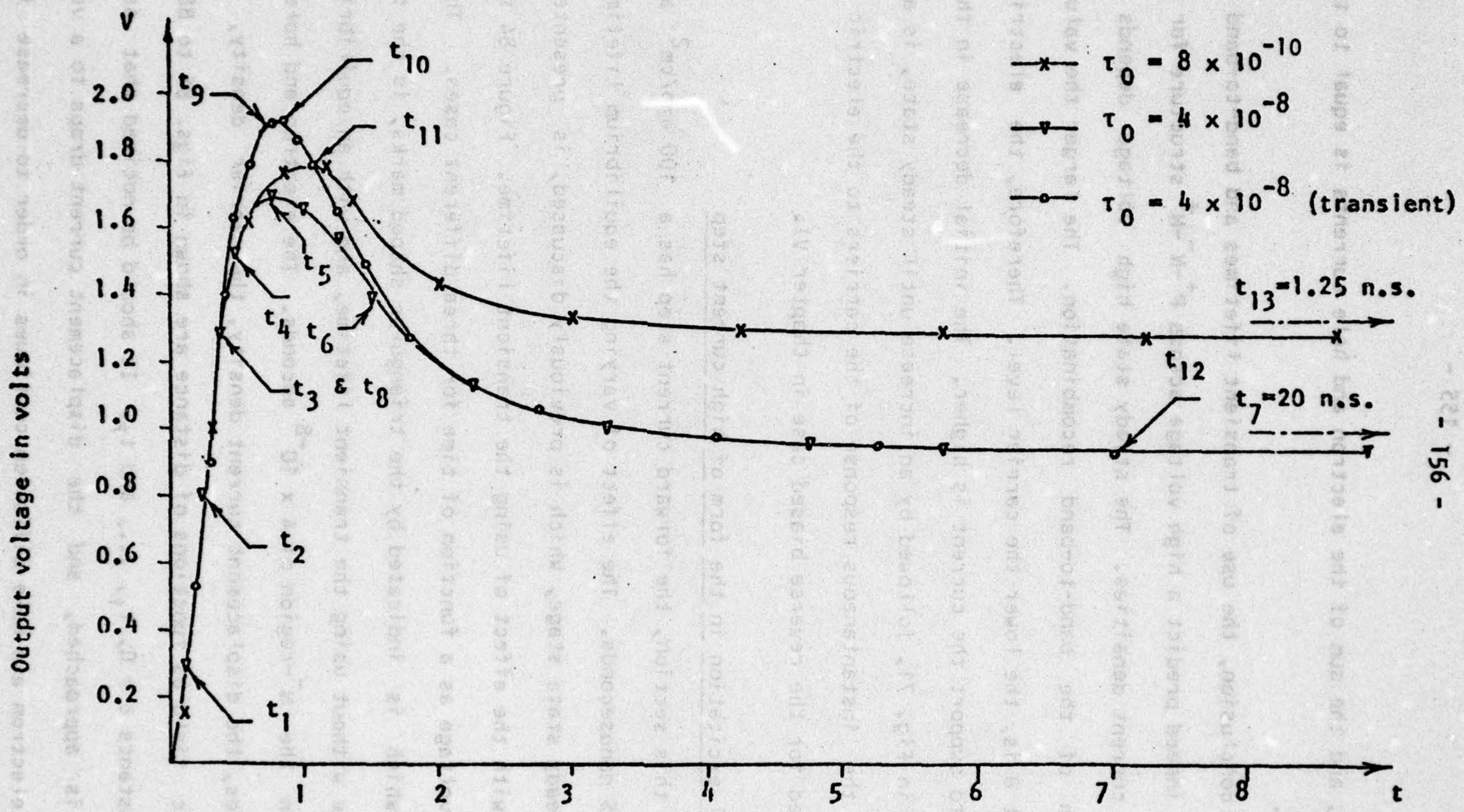

Figure 84. V(t) for a high current step with different lifetimes

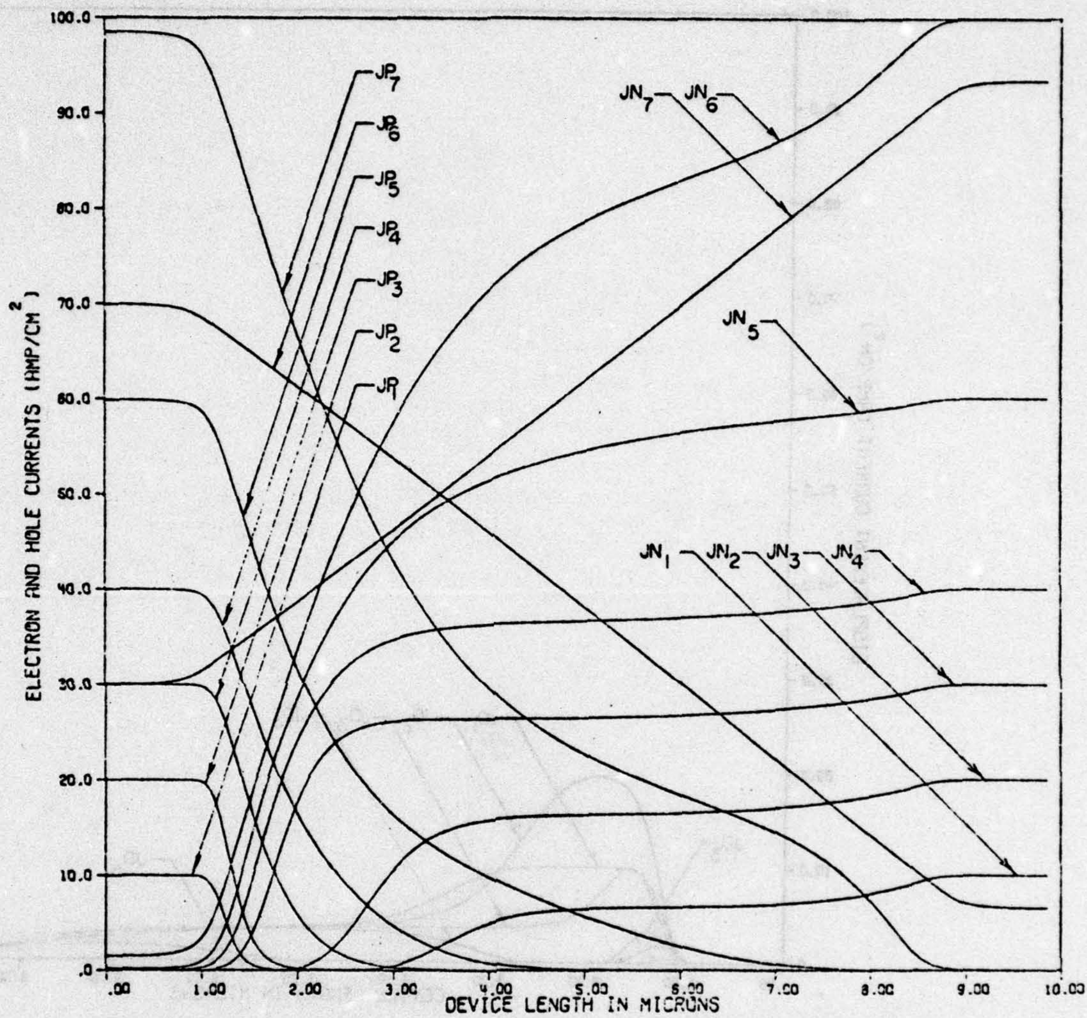

Figure 85. Electron and hole current density distributions for time instants t_1 to t_7 as shown in Figure 84

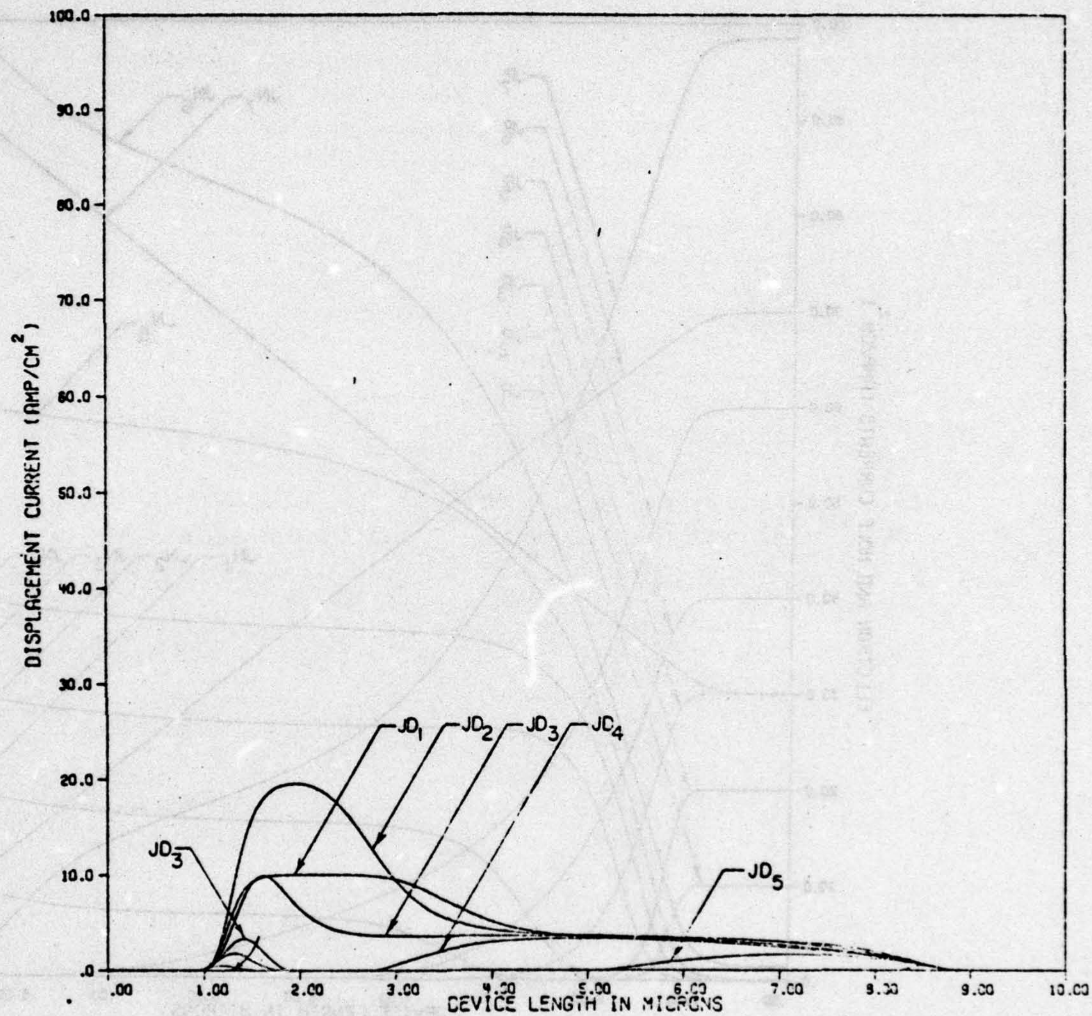

Figure 86. Displacement current density distribution for time instants t_1 to t_5 as shown in Figure 84

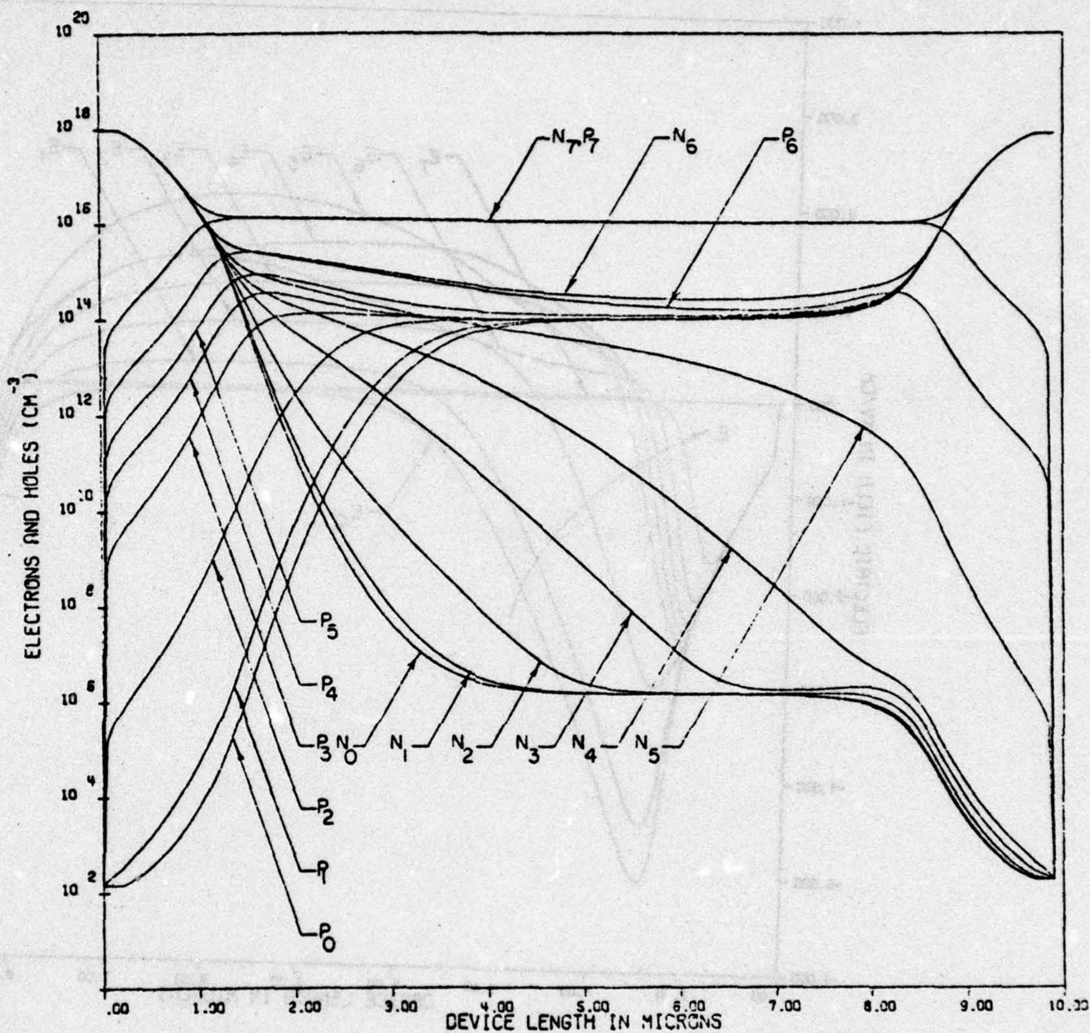

Figure 87. Electron and hole density distributions for time instants t = 0 to t_7 as shown in Figure 84

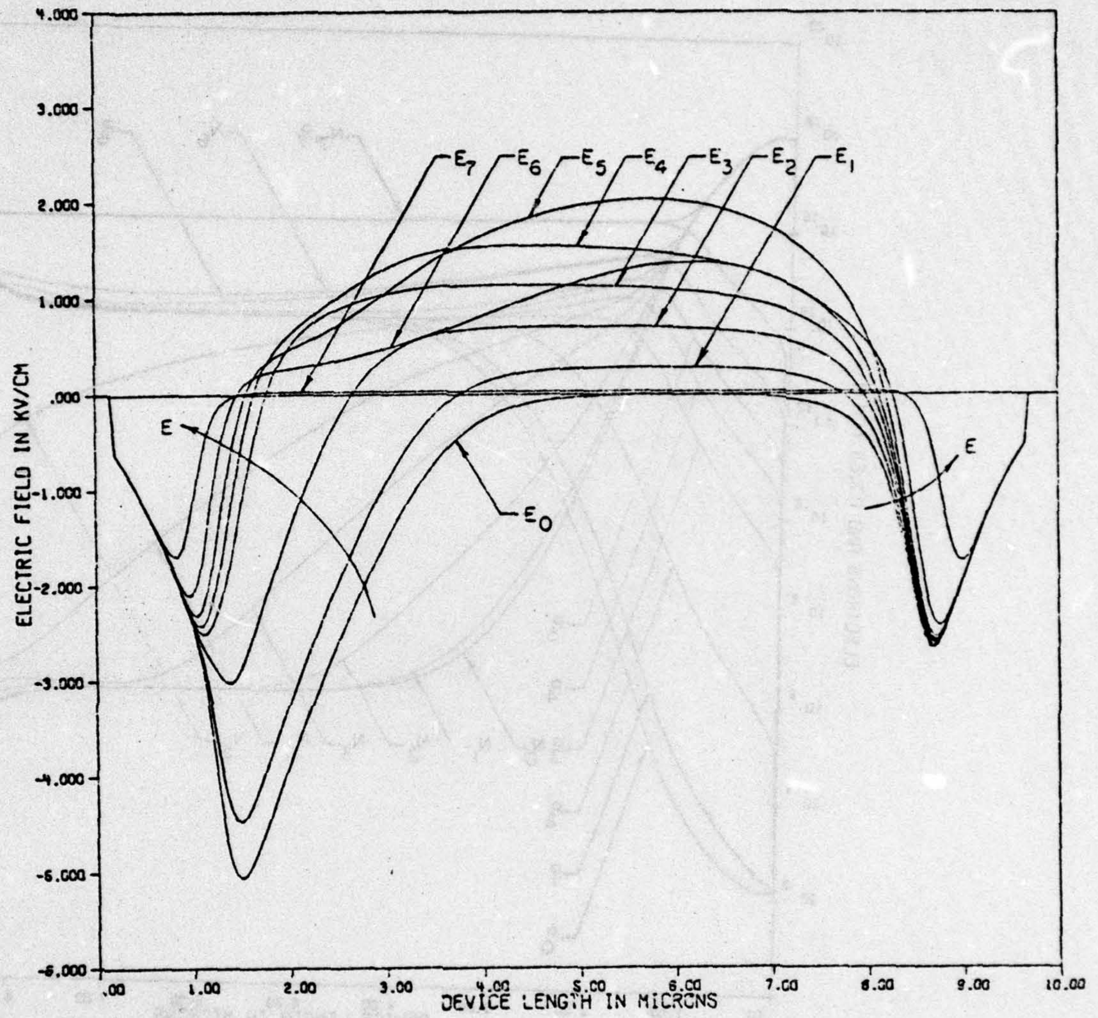

Figure 88. Electric field distribution for time instants t = 0 to t_7 as shown in Figure 84

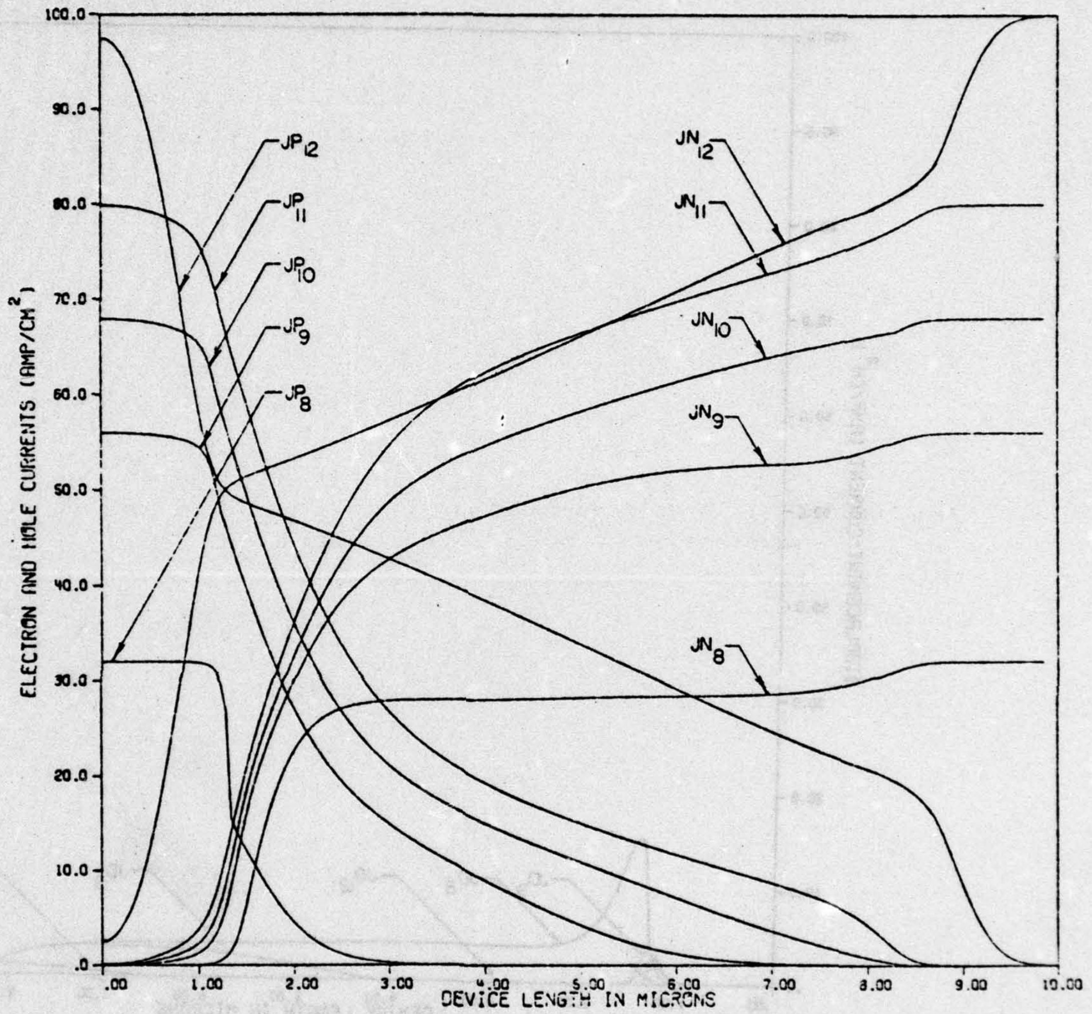

Figure 89. Electron and hole current density distributions for time instants t_8 to t_{12} as shown in Figure 84

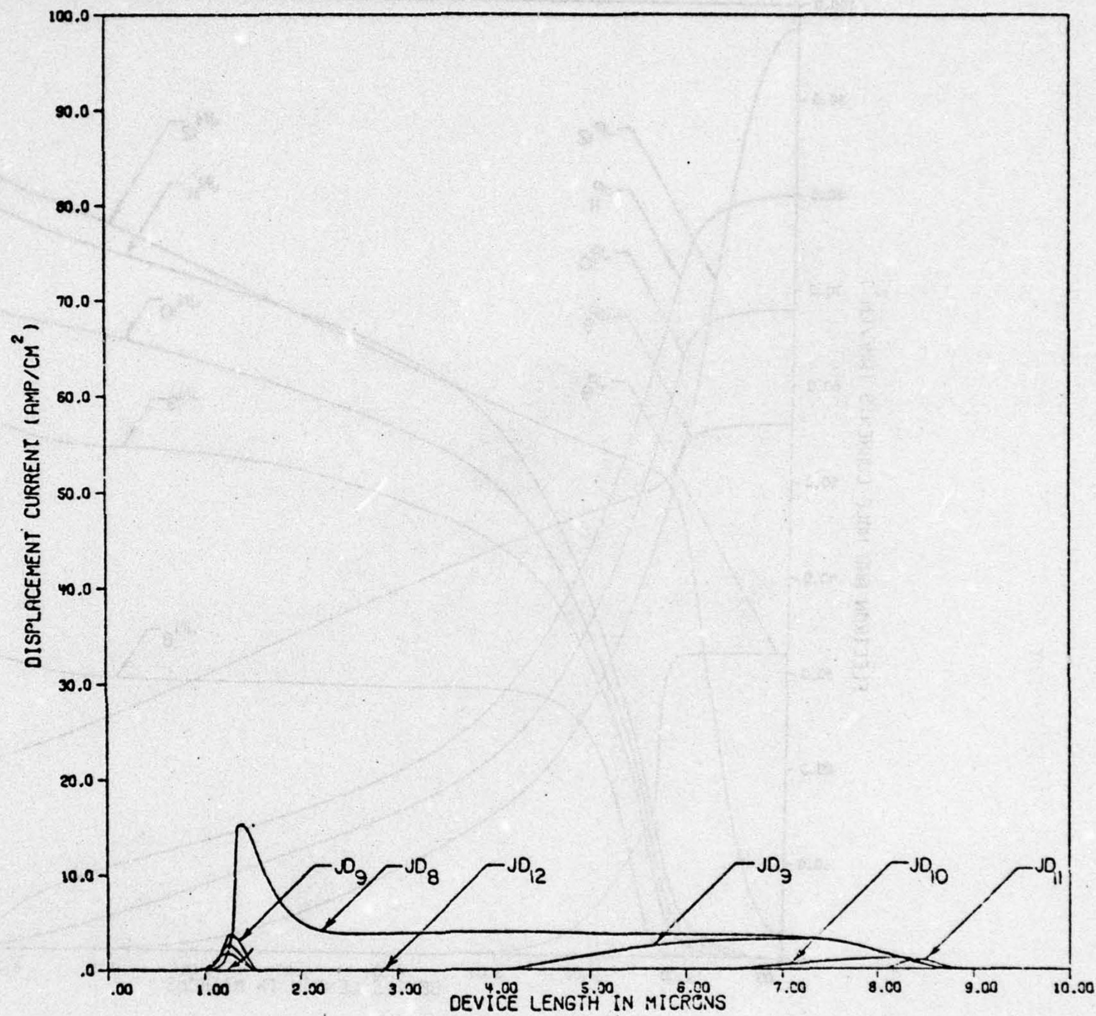

Figure 90. Displacement current density distribution for time instants t_9 to t_{11} as shown in Figure 84

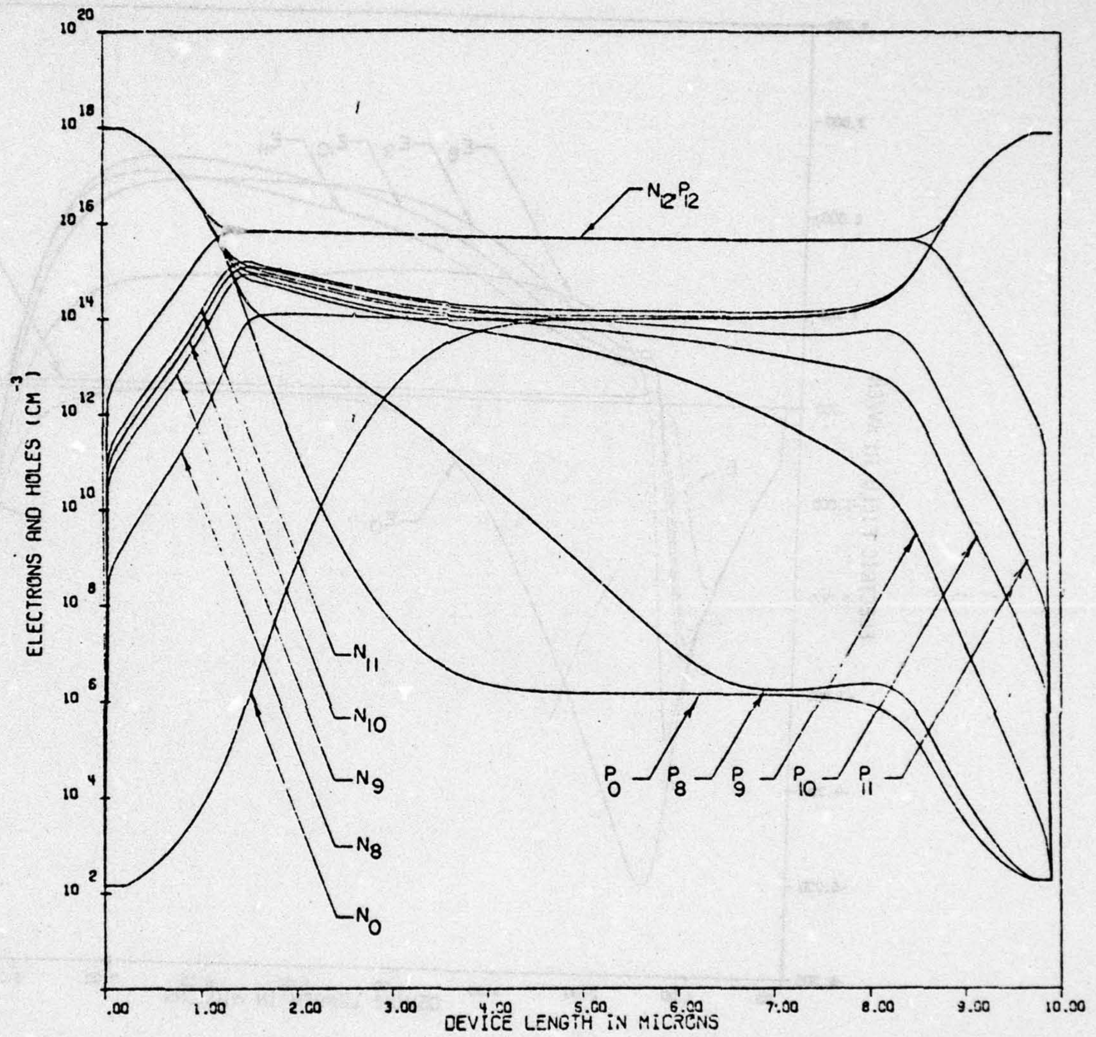

Figure 91. Electron and hole density distributions for time instants $t = 0$ to t_{12} as shown in Figure 84

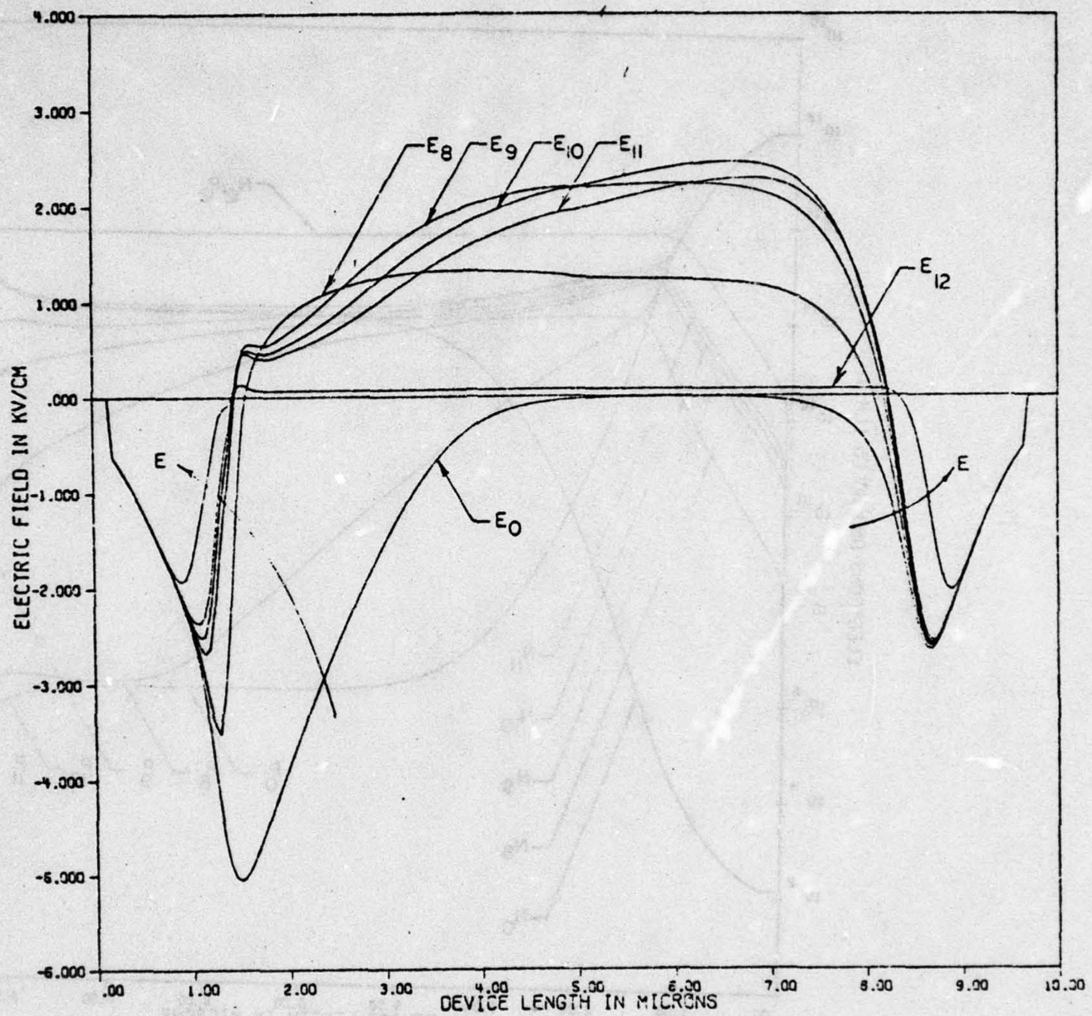

Figure 92. Electric field distribution for time instants $t = 0$ to t_{12} as shown in Figure 84

total current is carried by electrons, while the other 70% is carried by holes. A similar situation on a lower scale appears at the ohmic contact of the N^+-region. Whereas, it is known that the total current at the ohmic contact of the P^+-region is totally carried by holes, and at that of the N^+-region is totally carried by electrons. The second case which is indicated by circular shaped marks in Fig. 84 illustrates the transient response using the transient lifetime with the same value of equilibrium lifetime as before. The spatial distribution of the important parameters for the time instant $t_0, t_8, \ldots,$ and t_{12} are shown in Figs. 89 to 92. As shown in Fig. 84, the use of the transient lifetime causes an increase in the peak voltage due to the fact that it limits the excess majority carriers to that of the minority carriers in the heavily doped region, near $t = 0$, as explained previously. Due to the equal equilibrium lifetimes of these two cases, the near steady state behavior is identical, as seen by the equality of the output voltage in Fig. 84. This is also shown by the carrier diffusions continuing to decrease the spatial derivatives of JN and JP, as shown for the time instant t_{12} in Figs. 89 and 91. The third case which is indicated by the symbol "x" in Fig. 84 demonstrates the transient lifetime and with an equilibrium lifetime of 8×10^{-10} seconds. This lifetime is 50 times shorter than that of the previous two cases. The net effect of the shorter lifetime is an increase in the steady state voltage, as well as in the peak voltage.

Figures 93 to 95 illustrate the parameters of interest as a function of distance at steady state. The shorter equilibrium lifetime limits the carrier diffusion and satisfies the steady state condition of equation (113) which is repeated as follows:

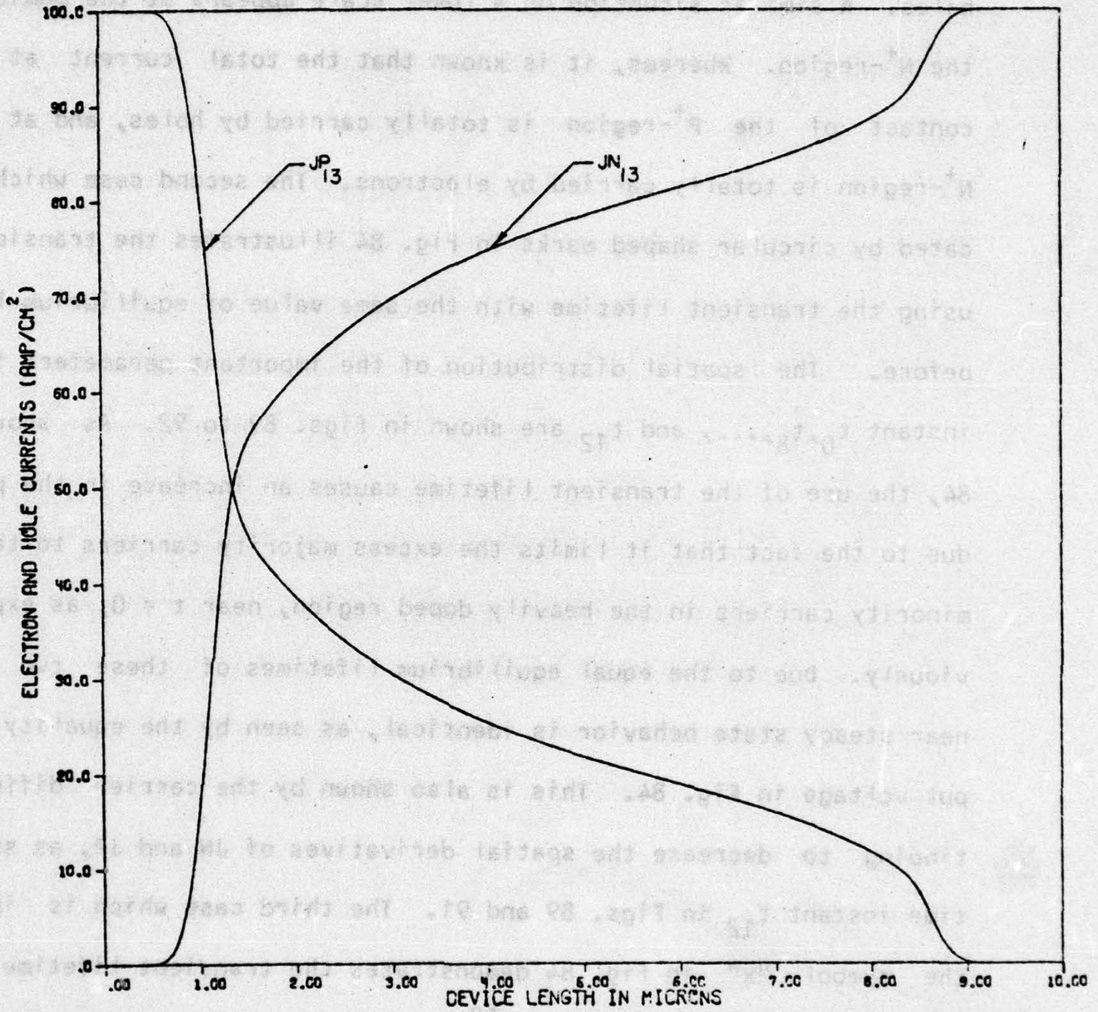

Figure 93. Electron and hole current density distributions for time instant t_{13} as shown in Figure 84

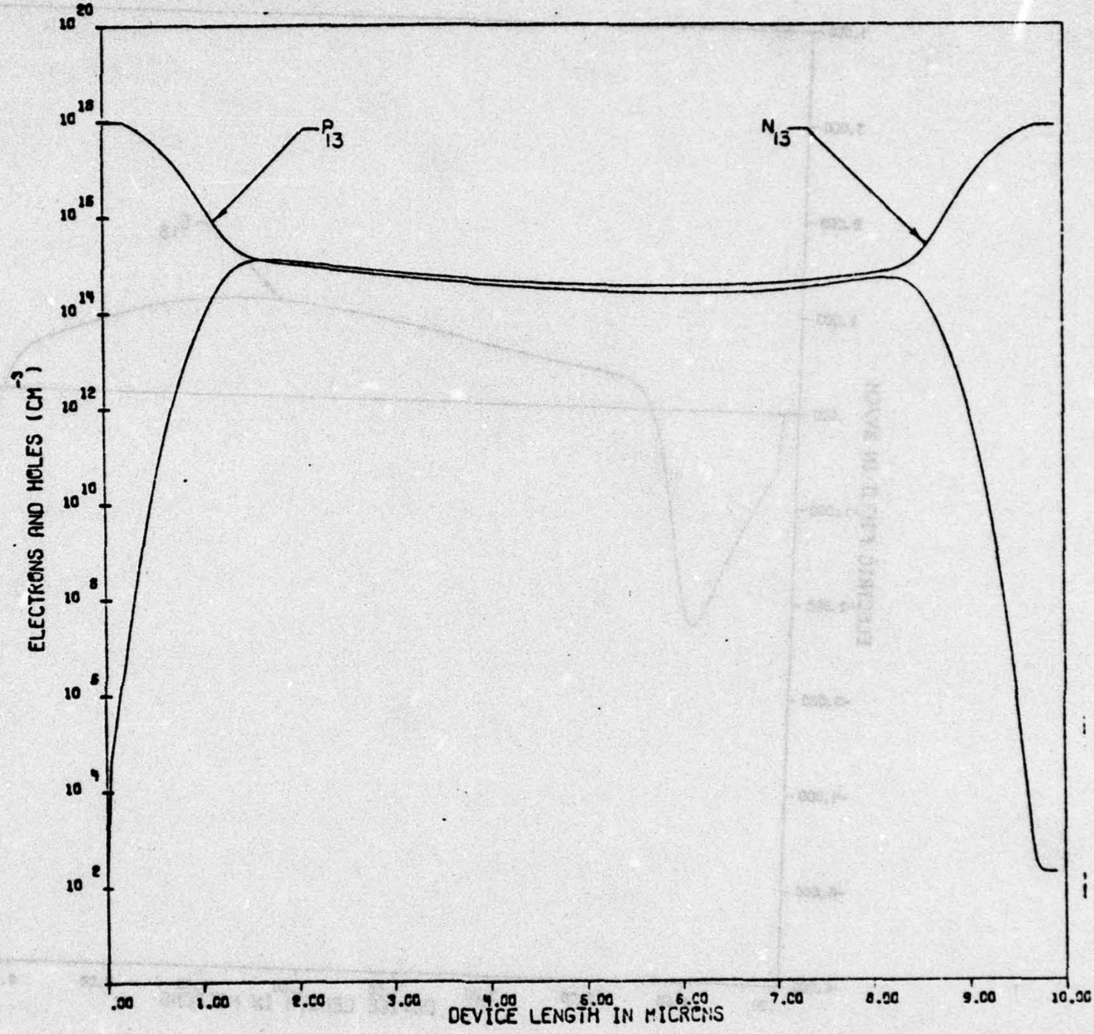

Figure 94. Electron and hole density distributions for time instant t_{13} shown in Figure 84

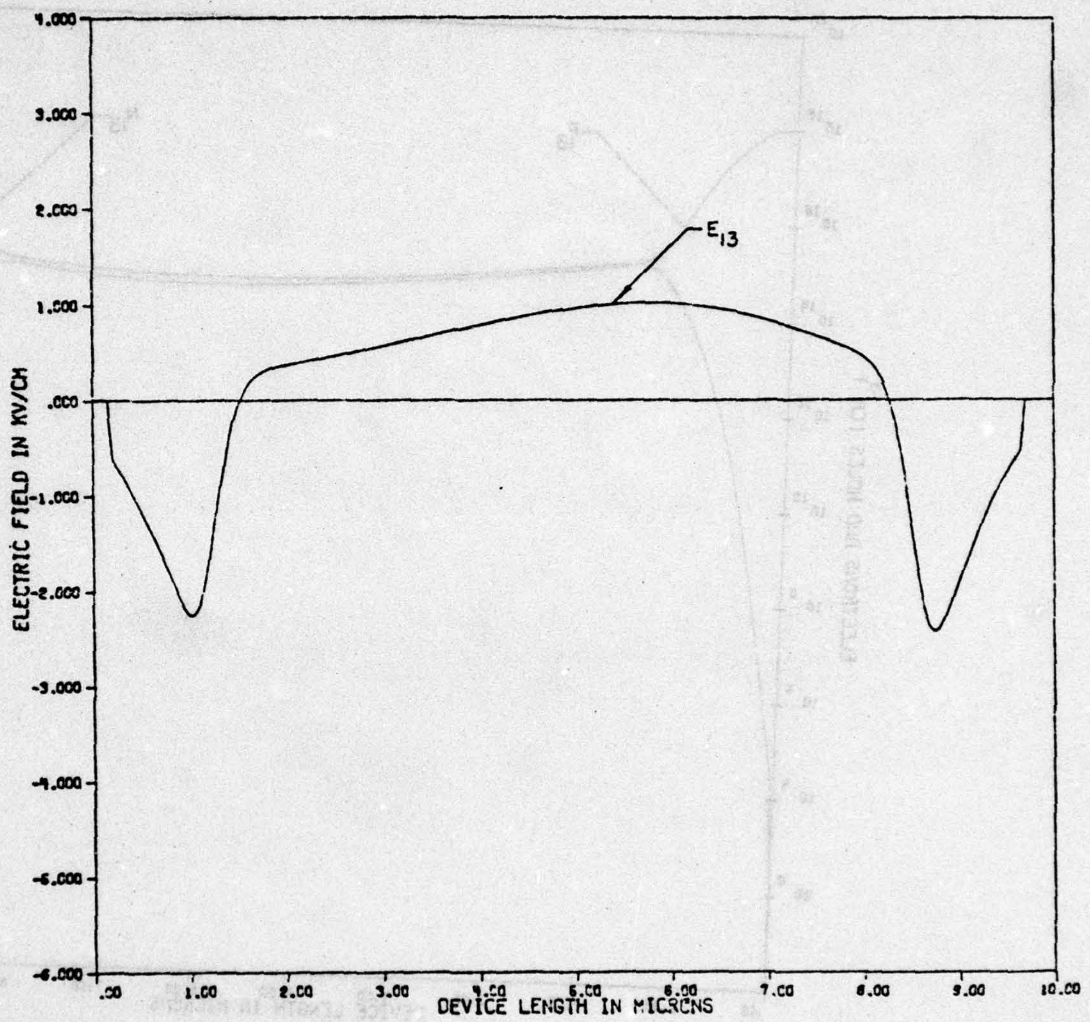

Figure 95. Electric field distribution for time instant t_3 as shown in Figure 84

$$\frac{PN - n_i^2}{\tau_0(P+N+2n_i)} = -\frac{1}{q}\left|\frac{\partial JP}{\partial x}\right| = \frac{1}{q}\left|\frac{\partial JN}{\partial x}\right|$$

As a result the total current in the P^+-region is carried by holes and by electrons in the N^+-region as shown in Fig. 95. Also the lower carrier levels causes a higher electric field, which in turn results in a higher steady state voltage.

In conclusion, the results of this chapter show that the lifetime of the Shockley-Read-Hall recombination expression depends on the level of injection in the case where the junction is forward biased. As the injection level increases, the lifetime becomes shorter in order for the device to reach a steady state where the total current is carried by majority carriers near the ohmic contacts; and as the lifetime becomes shorter, the steady state voltage, as well as the peak voltage of the transient response, increases.

In case of extreme levels of injection where the device is too far from equilibrium, the use of a transient lifetime is necessary in order to limit the excess diffusion. If the level of injection is high enough to cause avalanche multiplication, it becomes necessary to use band-to-band Auger recombination to limit the plasma in the avalanching region.

CHAPTER VI

EXPERIMENTAL RESULTS

This chapter outlines the diode fabrication procedures as well as the methods employed to determine the important diode parameters. These parameters are the diode area (A), the N^--region doping density (N_D), and its width (W). These diodes were tested in the forward direction with an external excitation in the form of a current pulse. A comparison between the experimental results and the computer simulation is also included.

As a point of comparison, N_D was first determined by calculations based on the depletion C-V characteristics of MOS capacitors, which were fabricated from the same starting wafer. Then N_D was determined from electrical measurements on fabricated diodes. The diodes are diffused and were fabricated with very short drive times (two hours at 1100°C) for the boron (P^+) diffusion. This procedure results in diodes with junctions that behave as nearly abrupt junctions. This was verified when the slope of the reverse C-V characteristics (on log-log paper) approached -0.5. Once the abrupt junction was confirmed, the theory available allowed calculation of N_D from the slope of $\frac{1}{C^2}$ versus V characteristics.

The width of the N^- region of the diode was measured directly by angle lapping and then staining with an acid solution. The wafer was scribed and broken to get a chip of the proper size for mounting on the 5° chuck for lapping. Once stained, the calibrated eye piece in the microscope allowed measurement of the width W. To get the width W from electrical measurements, a doping profile is required. This can determine the width of the lightly doped region if punch through precedes impact ionization in the re-

versed biased direction, as shown for the first device considered in Chapter IV. If avalanche occurs first, then the N^--region is not completely depleted, and W cannot be determined from the C-V measurements.

The specification for the starting wafers of single crystal silicon are listed in Table 4. All the wafers were <111> oriented epitaxial N^- on N^+. The resistivity and width values listed were from data provided by the manufacturer.

Table 4. Specifications of the Silicon Wafers

Wafer (#)	Width (μm)	Resistivity (ohm-cm)	Doping (cm^{-3})
1	12.10	8.13	6.0×10^{14}
2	52.90	28.60	1.8×10^{14}
3	21.34	2.48	2.0×10^{15}
4	54.80	29.30	1.7×10^{14}

The diode fabrication procedures as well as the MOS-C procedure are outlined below:

Diode Fabrication Procedure

1. The wafer was ultracleaned by running through a series of solvents and acids.

2. A 2000Å thick oxide was grown on the wafer in a dry oxygen atmosphere at 1100^oC for 4 hours and 30 minutes.

3. The wafer was scribed in half to be processed; one as diodes and the other as MOS-capacitors.

4. By using photoresist and masking procedures, the diffusion windows were opened in the oxide.

5. A boron deposition of 20 minutes at $1100^{\circ}C$ was followed by a 2-hour drive in a dry oxygen atmosphere at $1100^{\circ}C$.

6. The oxide stabilization step was performed in the phosphorus deposition furnace for 10 minutes.

7. A photoresist masking procedure was used to open contact windows in the oxide.

8. This was followed by an aluminum evaporation step at 10^{-6} torr, depositing a coat of 2000Å to 3000Å of aluminum.

9. The photoresist masking procedures were used to remove the excess aluminum and to form the desired aluminum pattern on the wafer.

10. An aluminum evaporation step was performed on the back of the wafer, after stripping the oxide while protecting the wafer front.

<u>MOS-C Fabrication Procedure</u>

1. A phosphorous gettering step was performed in the phosphorus deposition furnace for 20 minutes after the oxidation step.

2. The aluminum evaporation step was performed at 10^{-6} torr, depositing a coat of 2000Å to 3000Å of aluminum.

2. The wafer was annealed for 5 minutes at 500°C in a nitrogen atmosphere.

4. The last two steps of the diode fabrication were then repeated to complete the MOS-C fabrication.

N_D from MOS Measurements

To insure that the starting material was correct as labeled, MOS capacitors were fabricated so that the epitaxial layer doping density could be established before the other methods were attempted. Fig. 96 illustrates the MOS structure.

For the MOS wafers, the doping density was found by obtaining the accumulation capacitance and the minimum depletion capacitance from the C-V characteristic similar to Fig. 97. The theory for this is presented below.

$$C_{equiv.} = \frac{C_S C_O}{C_S + C_O}$$

C_O = capacitance of the SiO_2

C_S = capacitance of the semiconductor

For the geometry of Fig. 96, we have the series combination of the two capacitances.

$$C_{equiv.} = \frac{C_O}{1 + C_O/C_S} = \frac{C_O}{1 + \frac{\varepsilon_O K_O A W}{X_O \varepsilon_O K_S A}} = \frac{C_O}{1 + \frac{K_O W}{X_O K_S}}$$

$$= \frac{C_O}{\frac{K_S X_O + K_O W}{X_O K_S}}$$

$$C_O X_O K_S = C_{eq} K_S X_O + C_{eq} K_O W$$

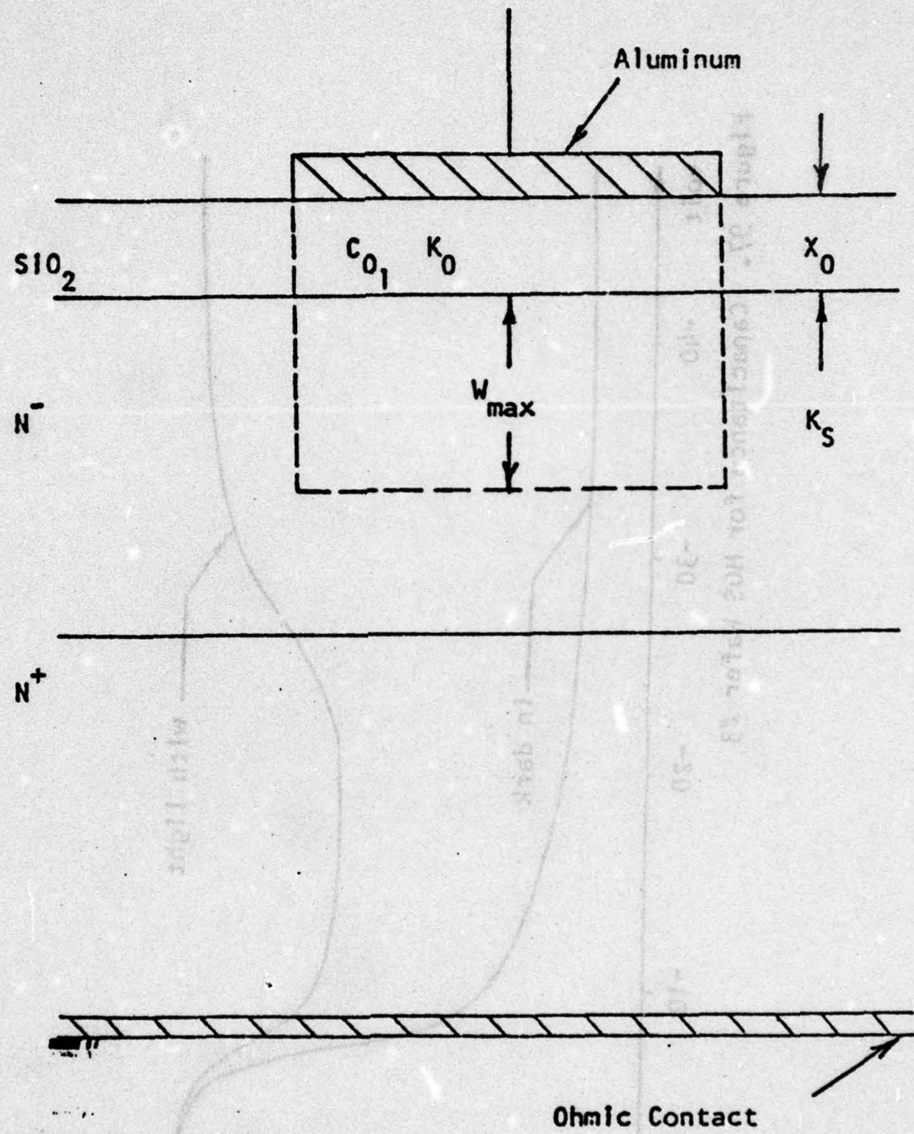

Figure 96. MOS Capacitor Geometry

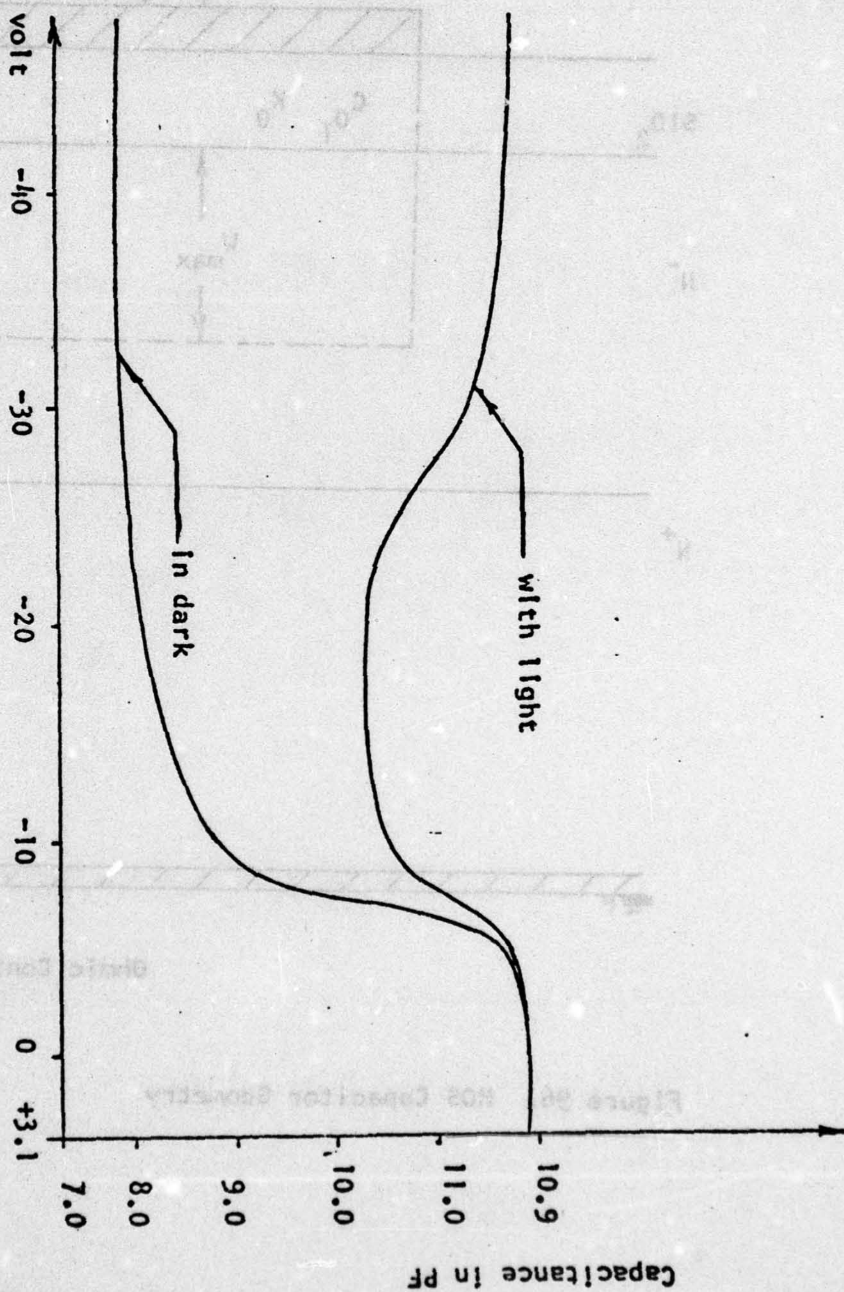

Figure 97. Capacitance for MOS Wafer #3

$$W = \frac{C_0 X_0 K_S - C_{eq} K_S X_0}{C_{eq} K_0} = \frac{K_S X_0}{K_0} \left[\frac{C_0}{C_{eq}} - 1\right]$$

and therefore

$$W_{max} = \frac{K_S X_0}{K_0} \left[\frac{C_0}{C_{min}} - 1\right] \tag{123}$$

C_0 is the maximum capacitance of accumulation where the voltage is positive. In accumulation $C_{eq} \simeq C_0$. Having C_0, the width of the oxide layer is calculated.

$$X_0 = \frac{\varepsilon_0 K_0 A}{C_0} \tag{124}$$

This value is a much more accurate method for determining X_0 than might be estimated from the color code for silicon dioxide on silicon.

Then, W_{max} was calculated, where:

$K = 1.38 \times 10^{-23}$ Joule/^oK

$T = 300^oK$

$K_S = 11.8$

$\varepsilon_0 = 8.854 \times 10^{-4}$ Fd/cm

$q = 1.602 \times 10^{-19}$ coul

$n_i = 1.18 \times 10^{10}\ cm^{-3}$

$K_0 = 3.8$

$A = 12.6 \times 10^{-4}\ cm^2$

Having W_{max}, N_D was obtained from a plot made from the following formula [6] relating N_D and W_{max}.

$$W_{max} = \sqrt{\frac{4KT\ K_S\ \varepsilon_0}{q2N_D}\ \ln \frac{N_D}{n_i}} \qquad (125)$$

Table 5 summarizes the data found for the MOS wafers.

Table 5. MOS Analysis of N_D for Starting Material

Wafer #	C_{max} (pf)	C_{min} (pf)	X_0 (A)	N_D (MOS) $(cm)^{-3}$	N_D (rated) $(cm)^{-3}$
1	12.4	1.4	3420	3.60×10^{14}	6.0×10^{14}
2	11.2	4.2	3790	1.65×10^{14}	1.8×10^{14}
3	10.9	6.8	3890	1.75×10^{15}	2.0×10^{15}
4	16.2	5.6	2620	2.60×10^{14}	1.7×10^{14}

N_D *from Diode C-V Measurements*

For the diode wafers, the reverse C-V characteristics and the log C vs. log V of these characteristics were plotted as shown in Figs. 98 and 99 for wafer #3. This was done to see if the junction can be approximated by an

AD-A053 539 PURDUE UNIV LAFAYETTE IND SCHOOL OF ELECTRICAL ENGI--ETC F/G 9/1
THE ANOMALOUS VOLTAGE RESPONSE OF THE P(+)N-N(+) DEVICE AND ITS--ETC(U)
DEC 77 G W NEUDECK, L R RAZOUK DAAG29-77-G-0191
UNCLASSIFIED TR-EE-77-40 ARO-15322.1-A-EL NL

3 OF 3
AD
A053539

END
DATE
FILMED
6-78
DDC

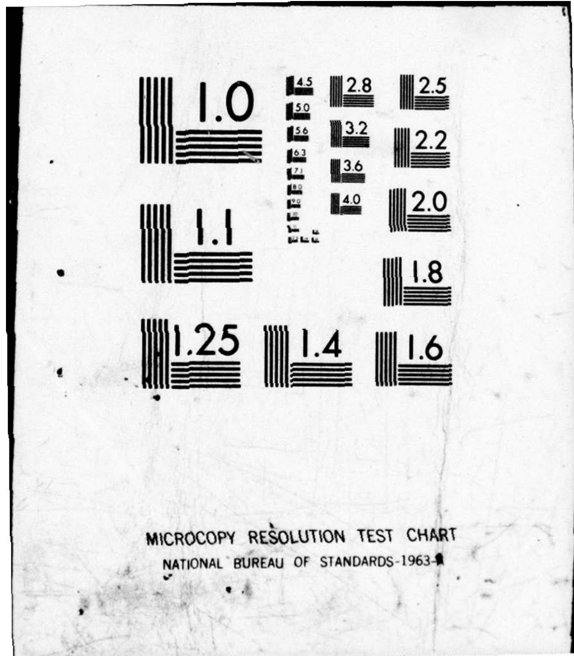
1.0
4.5
5.0
5.6
6.3
2.8
3.2
3.6
4.0
2.5
2.2
2.0
1.1
1.8
1.25
1.4
1.6
MICROCOPY RESOLUTION TEST CHART
NATIONAL BUREAU OF STANDARDS-1963-A

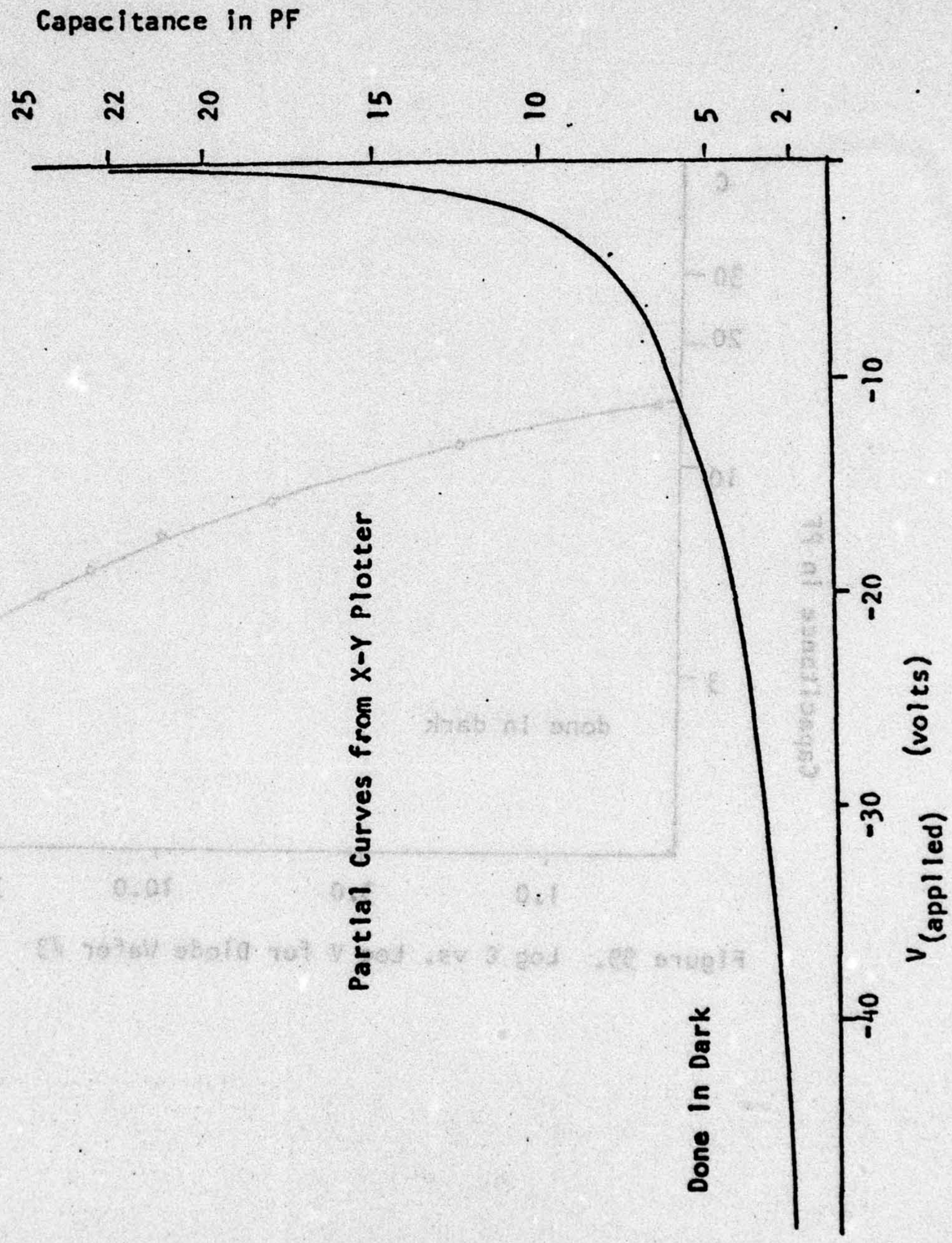

Figure 98. Capacitance vs. Voltage for Diode Wafer #3

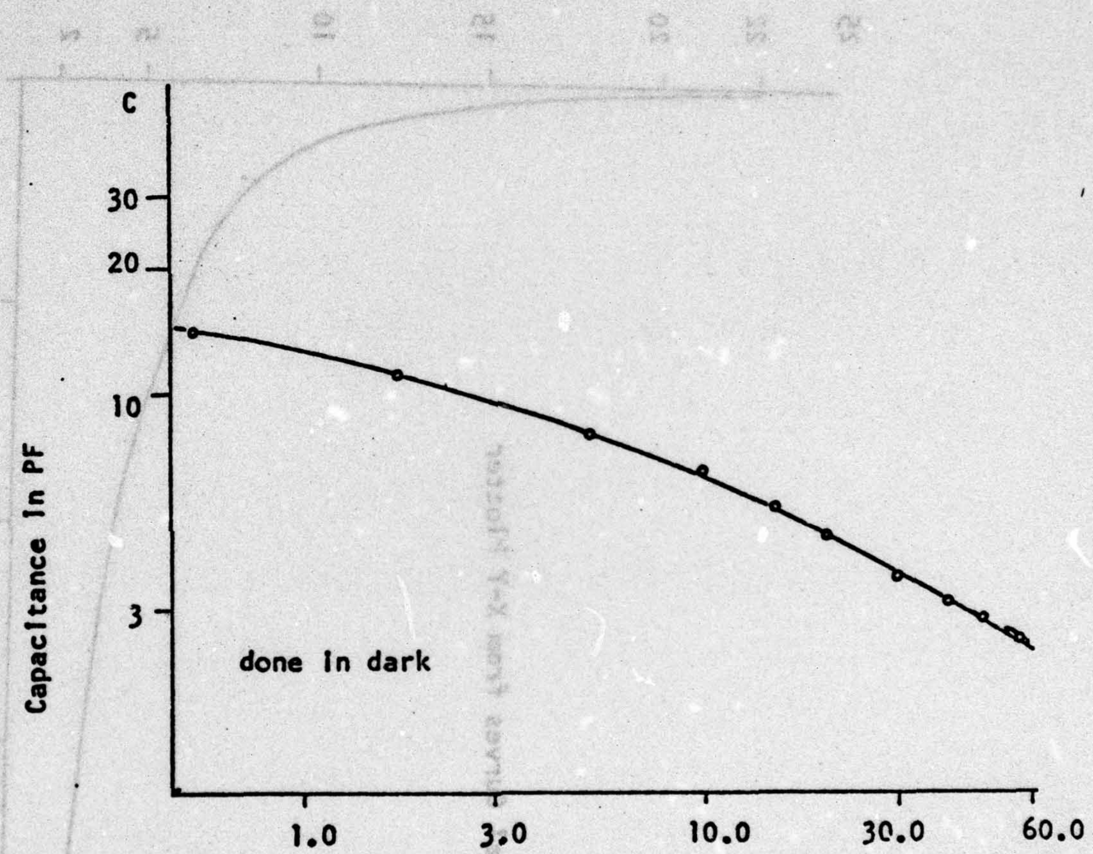

Figure 99. Log C vs. Log V for Diode Wafer #3

abrupt junction. An abrupt junction is known to have a log C vs. log V plot with a -0.5 slope. If the junction is linearly graded, this slope becomes -0.333 [6]. These slopes were found to be -0.29, -0.5, -0.51, and -0.42, for wafers #1, #2, #3, and #4 respectively. For the abrupt junction diodes, the reverse biased C vs. voltage can be used to determine N_D. In this case, the following equations are applicable:

$$C \equiv \frac{dQ_c}{dV} = \sqrt{\frac{q\varepsilon_s N_D A^2}{2(V_{bi} \pm V)}} \tag{126}$$

$$q = 1.602 \times 10^{-19}$$

$\varepsilon_s = \varepsilon_0 \varepsilon_r$ for the semiconductor

A = area of the P^+ region

V_{bi} = built in potential, typically less than 1 volt.

$$\frac{1}{C^2} = \frac{2(V_{bi} \pm V)}{q\varepsilon_s N_D A^2} \tag{127}$$

$$\frac{\Delta\left(\frac{1}{C^2}\right)}{\Delta(V_{bi} \pm V)} = \frac{2}{q\varepsilon_s N_D A^2} \tag{128}$$

Equation (128) indicates the slope of the $1/C^2$ vs. $(V_{bi} \pm V)$ plot and its relationship with N_D. For a uniformly doped N^- region, this slope would be constant. For a non-uniformly doped N^- region, the slope would change and

the plot is not a straight line. Fig. 100 illustrates the $1/C^2$ vs. V plot for wafer #3. The plot is linear. Therefore, the background doping is uniform for this wafer.

The doping profile method consists of plotting the $1/C^2$ vs. V characteristics of the wafer all the way out to the breakdown voltage. $N_D(W)$ is found in the same manner as N_D (diode). In this case, however $N_D(W)$ is found from the slopes of adjacent points on the $1/C^2$ vs. V characteristics. The width W at each point is found from the abrupt junction capacitance equation as follows:

$$W = \frac{\epsilon_s A}{C} \tag{129}$$

Table 6 summarizes the results for N_D. In obtaining these results the abrupt junction approximation was used for all wafers.

Table 6. Results for N_D Using Different Methods

Wafer #	N_D (diode) $(cm)^{-3}$	N_D (rated) $(cm)^{-3}$	N_D (MOS) $(cm)^{-3}$
1		6.0×10^{14}	3.60×10^{14}
4	2.67×10^{14}	1.8×10^{14}	1.65×10^{14}
5	2.64×10^{15}	2.0×10^{15}	1.75×10^{15}
6	3.46×10^{14}	1.7×10^{14}	2.60×10^{14}

Note that the N_D (diode) was higher than the rated value and that MOS data gave a value less than the diode data. This seems reasonable since doping with impurities at high temperatures during the P^+ diffusion for the diodes may add unwanted impurities.

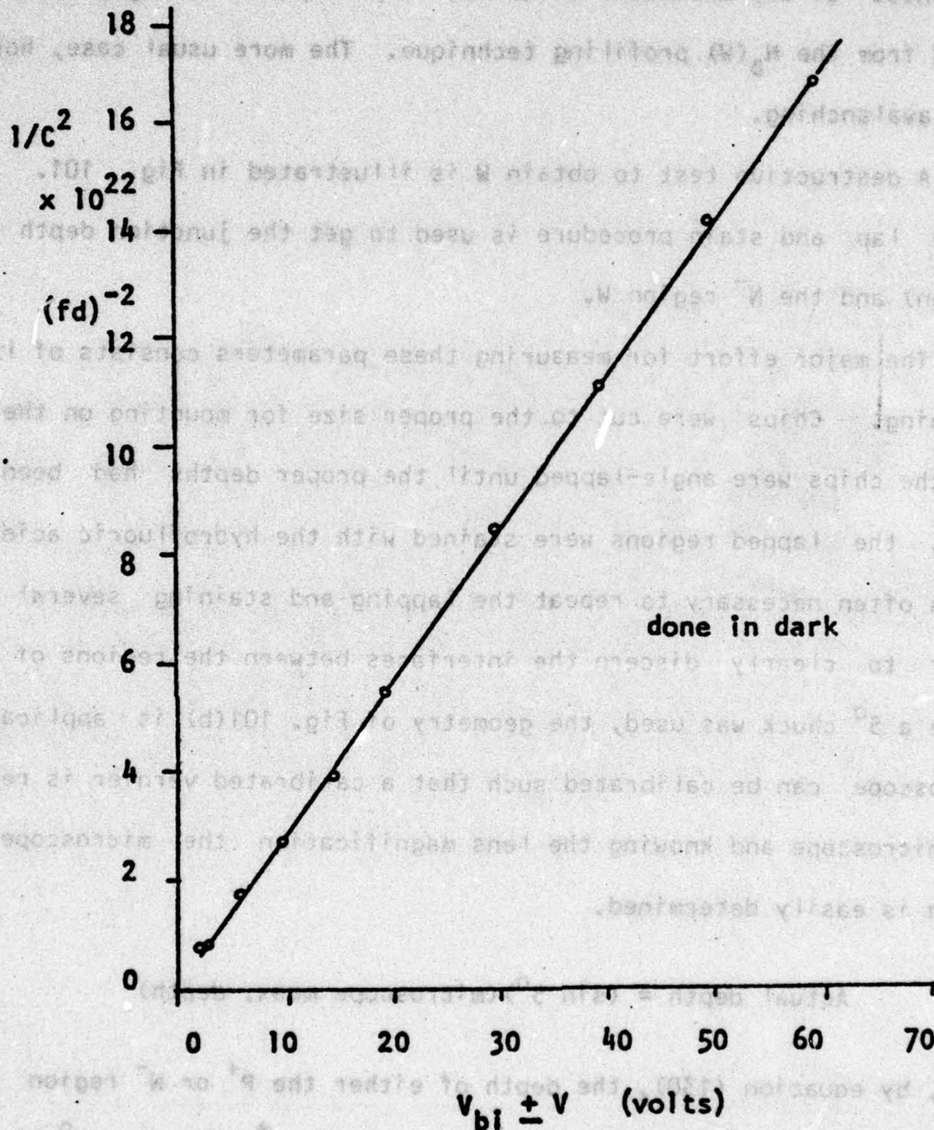

Figure 100. $1/C^2$ vs. volt for diode wafer #3

The Width W

The width of the N^- region is not easily obtained from electrical measurements. If the breakdown mechanism is pure punch-through, then W could be found from the $N_D(W)$ profiling technique. The more usual case, however, is pure avalanching.

A destructive test to obtain W is illustrated in Fig. 101. The same angle lap and stain procedure is used to get the junction depth (of the P^+ region) and the N^- region W.

The major effort for measuring these parameters consists of lapping and staining. Chips were cut to the proper size for mounting on the 5° chuck, and the chips were angle-lapped until the proper depths had been reached. Then, the lapped regions were stained with the hydrofluoric acid solution. It is often necessary to repeat the lapping and staining several times in order to clearly discern the interfaces between the regions of the wafer. Since a 5° chuck was used, the geometry of Fig. 101(b) is applicable. The microscope can be calibrated such that a calibrated vernier is read through the microscope and knowing the lens magnification the microscope measured depth is easily determined.

$$\text{Actual depth} = (\sin 5^o)(\text{microscope meas. depth}) \qquad (130)$$

Then, by equation (130), the depth of either the P^+ or N^- region is calculated. It is recommended that for a shallow P^+ region, a 1° block be used while for a large W a 10° block be used to ease the angle lapping and stain problems.

Table 7 shows the results of determining the P^+ region and N^- region widths by the angle lapping and stain procedures.

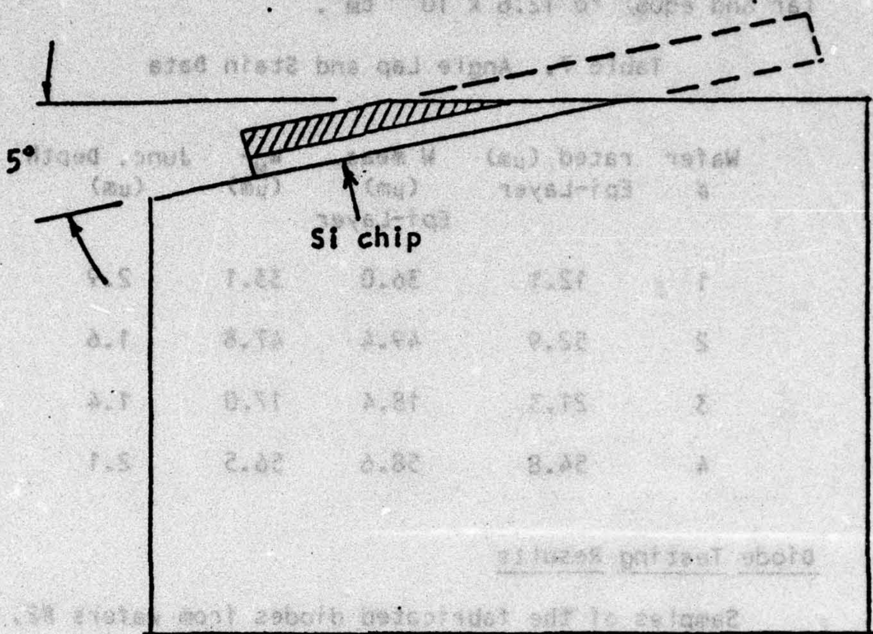

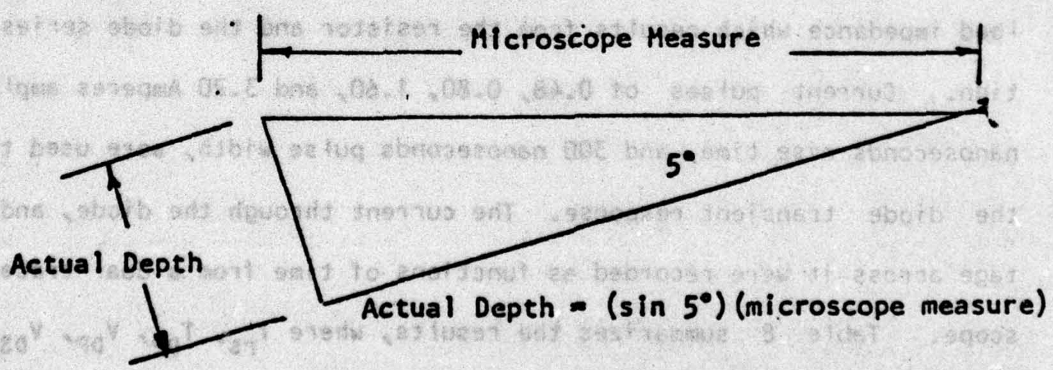

Figure 101. Geometry of Angle Lap and Stain

The diode area is the area of the P^+ diffusion region, which is circular and equal to 12.6×10^{-4} cm^2.

Table 7. Angle Lap and Stain Data

Wafer #	rated (μm) Epi-Layer	W meas. (μm) Epi-Layer	W_N- (μm)	Junc. Depth (μm)
1	12.1	36.0	33.1	2.9
2	52.9	49.4	47.8	1.6
3	21.3	18.4	17.0	1.4
4	54.8	58.6	56.5	2.1

Diode Testing Results

Samples of the fabricated diodes from wafers #2, #3, and #4 were packaged and tested with large forward current pulses. The output voltage of the Velonex pulse generator was applied to the series combination of diode and a 225 ohm resistor. This results in a current pulse through the diode. The Velonex pulse generator has a maximum output voltage of 2.5 kilo volts, with a 30 to 50 nanosecond rise time. This rise time is a function of the load impedance which results from the resistor and the diode series combination. Current pulses of 0.48, 0.80, 1.60, and 3.20 Amperes amplitude, 50 nanoseconds rise time, and 300 nanoseconds pulse width, were used to obtain the diode transient response. The current through the diode, and the voltage across it were recorded as functions of time from a dual trace oscilloscope. Table 8 summarizes the results, where T_{rs}, T_{DP}, V_{DP}, V_{DSS}, and I_D are shown in Fig. 102 along with the general shape of the transient response. The quantities of Table 8 are defined as follows:

T_{rs} is the rise time of the applied current pulse

Figure 102. External applied current and output voltage for experimental data

T_{DP} is the time corresponding to the peak voltage across the diode

V_{DP} is the peak voltage across the diode

V_{DSS} is the steady state voltage across the diode

I_D, J_D are the amplitude of the current pulse in ampers and amp/cm^2

Table 8. Results of pulsing the diodes in the forward direction

Wafer #	T_{rs}	T_{DP}	V_{DP}	V_{DSS}	I_D	J_D
	(n.sec.)	(n.sec.)	(volts)	(volts)	(amp)	(amp cm^2)
2	50	50	11.2	4	0.48	3.81×10^2
2	50	50	13.4	5	0.80	6.35×10^2
2	50	40	23.5	7	1.60	1.27×10^3
2	50	40	36.0	10	3.20	2.54×10^3
3	50	40	3.4	2.0	0.48	3.81×10^2
3	50	40	4.6	2.2	0.80	6.35×10^2
3	50	40	7.6	3.2	1.60	1.27×10^3
3	50	40	15.0	5.0	3.2	2.54×10^3
4	50	30	5.5	2.6	0.48	3.81×10^2
4	50	30	7.3	3.6	0.80	6.35×10^2
4	50	30	10.8	4.6	1.60	1.27×10^3
4	50	35	18.5	7.0	3.10	2.46×10^3

The diodes were also pulsed in the reverse biased direction. The pulsed I-V characteristic is shown in Fig. 103 for wafer #3.

Comparison between Theory and Experiment

Diodes of wafer #3 were chosen for comparison with the computer simulation results under reverse and forward pulsed conditions. A summary of the

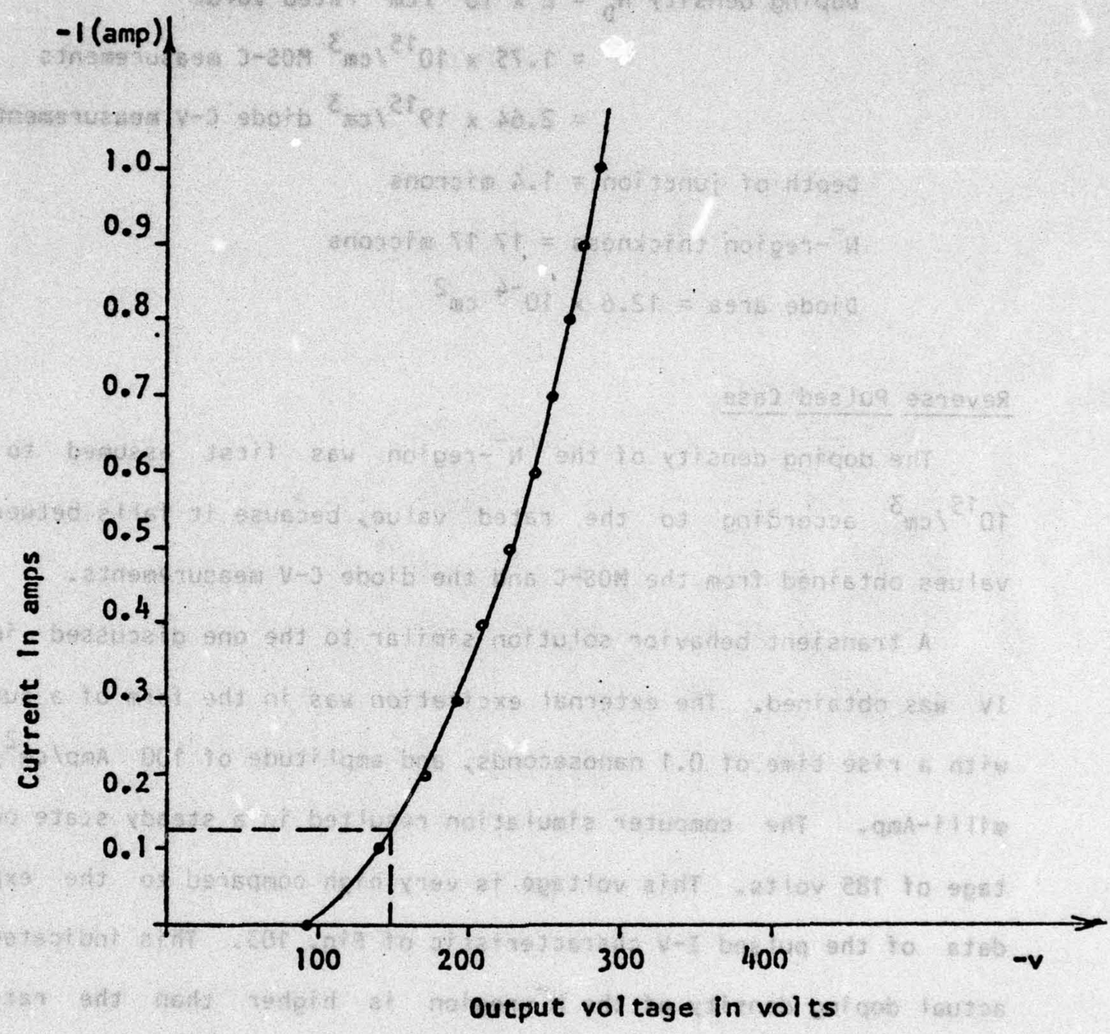

Figure 103. Pulsed reverse biased characteristics for diode wafer #3

measured physical parameters for diodes of wafer #3 are as follows:

Type of junction = abrupt

Doping density $N_D = 2 \times 10^{15}/cm^3$ rated value

$= 1.75 \times 10^{15}/cm^3$ MOS-C measurements

$= 2.64 \times 19^{15}/cm^3$ diode C-V measurements

Depth of junction = 1.4 microns

N^--region thickness = 17 17 microns

Diode area = 12.6×10^{-4} cm^2

Reverse Pulsed Case

The doping density of the N^--region was first assumed to be $2 \times 10^{15}/cm^3$ according to the rated value, because it falls between the two values obtained from the MOS-C and the diode C-V measurements.

A transient behavior solution similar to the one discussed in Chapter IV was obtained. The external excitation was in the form of a current step with a rise time of 0.1 nanoseconds, and amplitude of 100 Amp/cm^2, or 126 milli-Amp. The computer simulation resulted in a steady state output voltage of 185 volts. This voltage is very high compared to the experimental data of the pulsed I-V characteristic of Fig. 103. This indicated that the actual doping density of the N^--region is higher than the rated value. Therefore, the value of N_D obtained from the diode C-V measurements of 2.64 $\times 10^{15}/cm^3$ was assumed. The transient behavior under reverse pulsed conditions for this case is included in Chapter III under the same external excitation previously discussed of 126 milli-Amp amplitude. The result of the output voltage as a function of time is shown in Fig. 39 which shows that the steady state voltage is 150 volts. This value is in excellent agreement with the experimental data of Fig. 103. Therefore, the actual doping density of the N^--region is that obtained from the diode C-V measurements.

According to Sze [6], an approximate expression of the breakdown voltage for a one sided abrupt junction is given by the following equation:

$$V_B = 60(Eg/1.1)^{3/2} (N_D/10^{16})^{-3/4} \text{ volts} \tag{131}$$

where Eg is the band gap in eV(=1.12 eV for Si). Equation (131) results in a breakdown voltage of 167.3 volts which is higher than the actual value of 150 volts. It should also be noted that the approximate equation of (131) predicts a constant breakdown voltage for all current levels, while the steady state condition of the computer simulation depends on the current level according to equations (106) and (107) of Chapter IV.

Chapter III presented the thermal equilibrium condition for this device assuming a total device length of 20 microns. The importance of using non-uniform spatial steps is also discussed in Chapter III.

Forward Pulsed Case

The first part of the measured transient response under forward pulsed conditions, which is described in Table 8, is shown in Fig. 104 for diodes of wafer #3, with a pulse amplitude of 3.2 Amp. (or 2.54×10^3 Amp./cm^2), and a rise time of 50 nanoseconds. One might be tempted to try to simulate this behavior with a current step of long rise time as used experimentally. This proved to be impractical for several reasons. First, it should be noted that a computer simulation does not contain acceleration terms, the carrier response to the electric field is essentially instantaneous. This results in a shorter response time when compared with experimental data. For example, if the measured peak voltage occurs at time T_{DP}, the computer simulation results in a peak voltage at a much shorter time. Therefore, the computer simulation will predict and explain the device behavior with a different time scale. As a result the use of long rise times, as used experi-

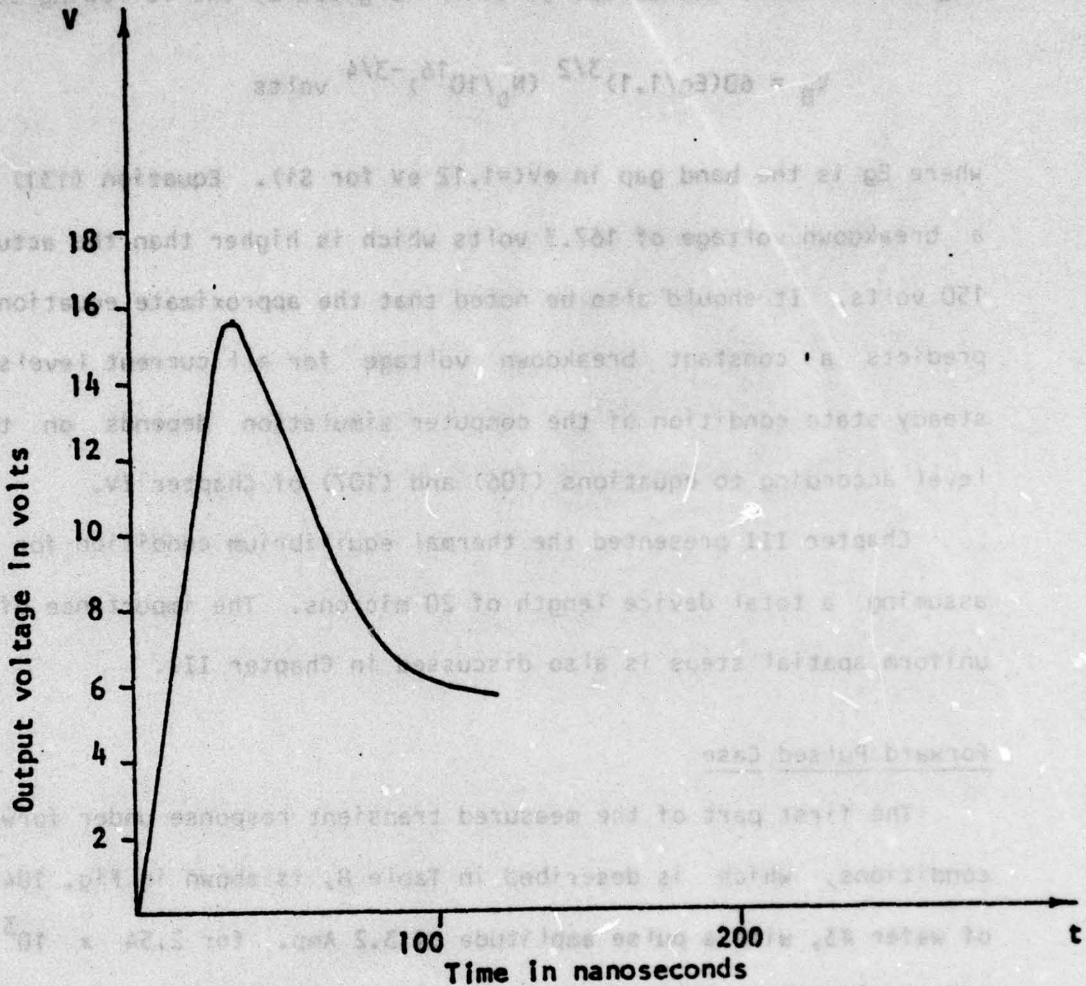

Figure 104. V(t) obtained experimentally for diode #3

mentally, will not yield an exact response. It is also important to realize that the time step required to achieve an accurate converged solution depends very much on the size of the smallest spatial step, as well as the shortest lifetime used. This time step limitation was analyzed in detail for the case of explicit method [2], while due to the complicated nature of the implicit method, a relation between the required time step and the different parameters used is hard to find. Therefore, the use of a non-uniform spatial mesh with small steps near the P^+-N junction limits the time step size. Also, the use of a non-equilibrium transient lifetime adds another restriction to the time step size, due to the presence of very short lifetimes in the beginning of the transient solution. Therefore, in order to reduce the computational time to a practical level a short rise time is used in general. This rise time is further reduced if a transient lifetime is used.

As discussed in Chapter V, the Schockley-Read-Hall lifetime depends on the level of injection. A shorter equilibrium lifetime results in a high steady state voltage, while the use of transient lifetimes results in a higher peak voltage.

Figures 105 and 106 show the transient response of the computer simulation for the experimental device with the external excitation in the form of a current step with an amplitude of 2.54×10^3 Amp/cm^2. Figure 105 shows the result with a rise time of 1 nanosecond, and an equilibrium lifetime of 3.1×10^{-10} seconds. This results in a peak voltage of 11 volts and a steady state voltage of 7.6 volts. It is clear that the steady state voltage is higher than the experimental value which implies that a longer lifetime is required, while the peak voltage which is lower than the experimental value implies the need of using the transient lifetime. Therefore, the

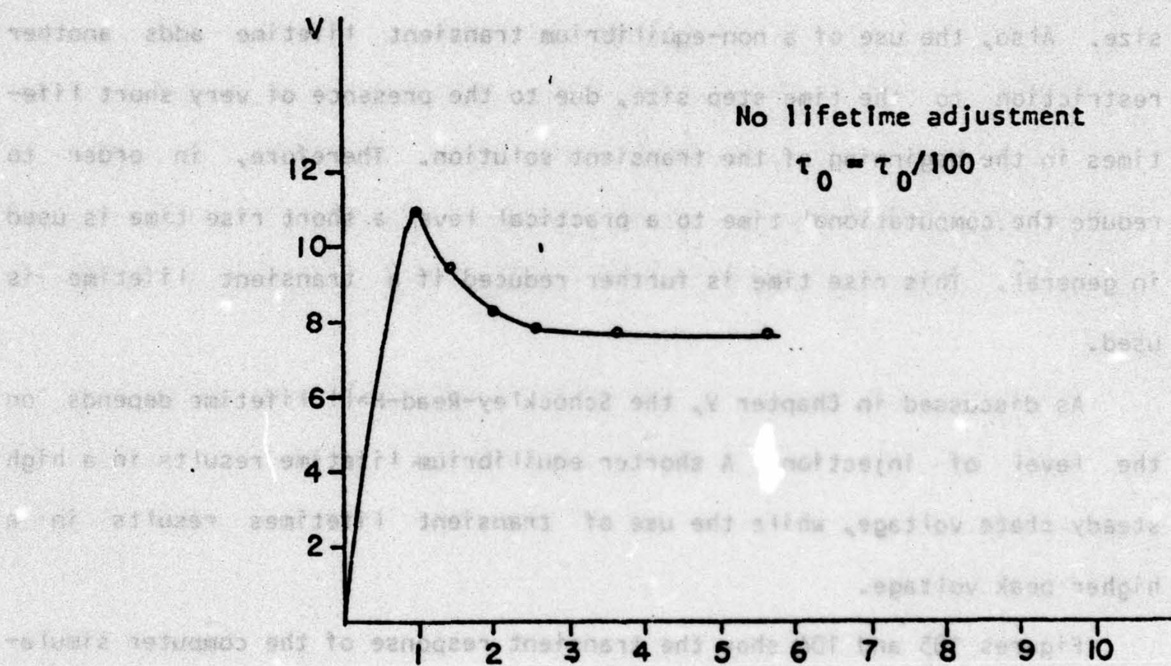

Figure 105. Computer simulation result for v(t) using $\tau_0 = 3.1 \times 10^{-10}$ sec.

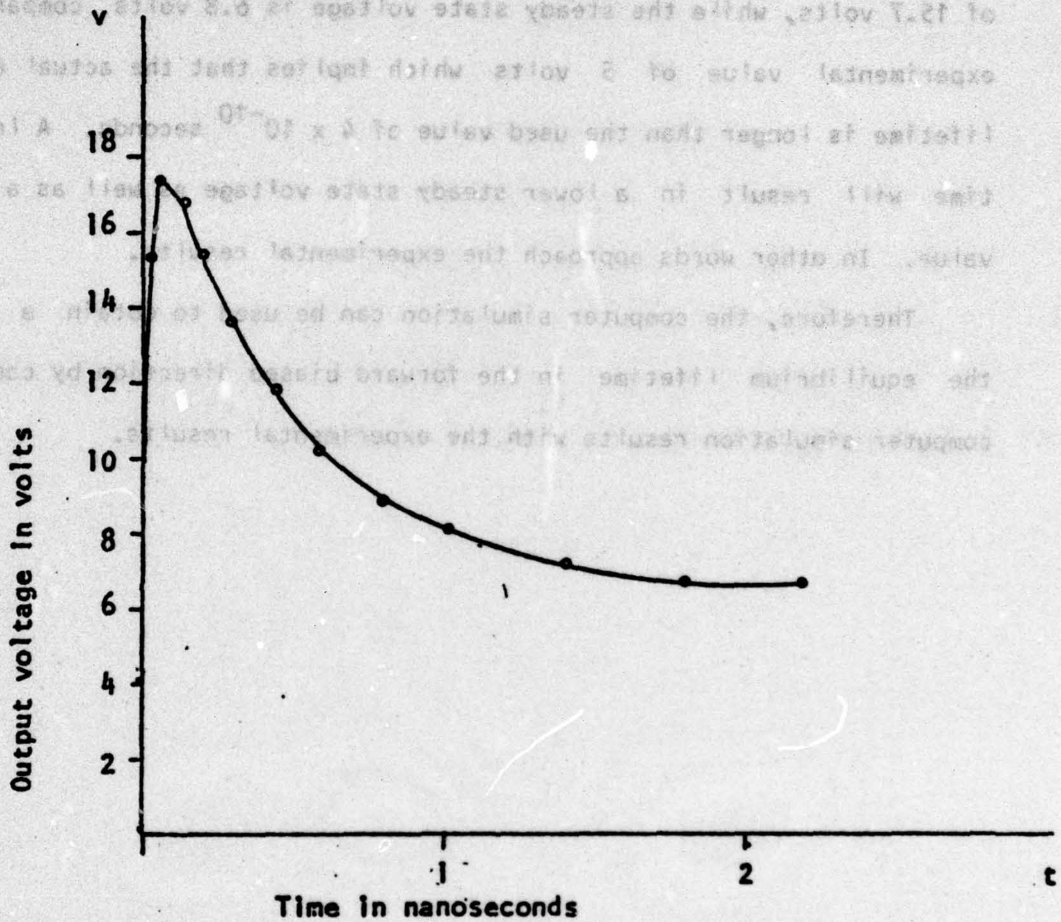

Figure 106. Computer simulation result for v(t) using the transient lifetime and $\tau_0 = 4 \times 10^{-10}$ seconds

simulation was repeated using the transient lifetime adjustment and an equilibrium lifetime of 4×10^{-10} seconds; also the rise time was decreased to 1 picosecond. Figure 106 shows the result of this transient behavior. The peak voltage has a value of 17.4 volts compared to an experimental value of 15.7 volts, while the steady state voltage is 6.8 volts compared to an experimental value of 5 volts which implies that the actual equilibrium lifetime is longer than the used value of 4×10^{-10} seconds. A longer lifetime will result in a lower steady state voltage as well as a lower peak value. In other words approach the experimental results.

Therefore, the computer simulation can be used to obtain a value for the equilibrium lifetime in the forward biased direction by comparing the computer simulation results with the experimental results.

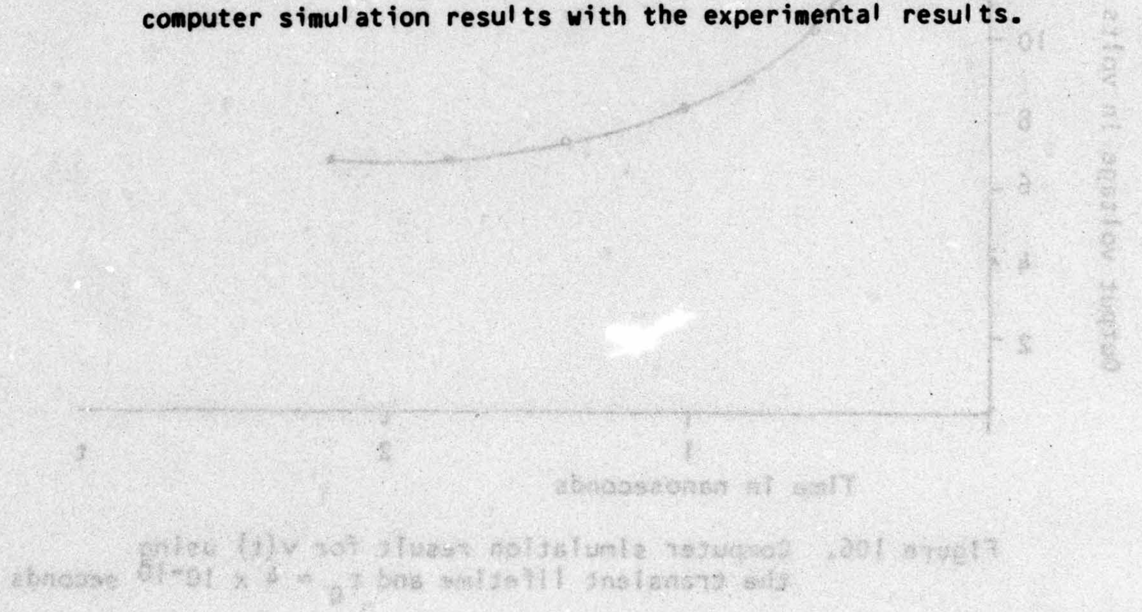

CHAPTER VII

SUMMARY, CONCLUSIONS, AND RECOMMENDATIONS FOR FURTHER STUDY

Summary and conclusions:

A summary of the research presented in this report and the conclusions which may be drawn from this research are given in the present chapter. On the basis of the results of this work, some recommendations are then made for further study.

Numerical methods were used to solve the basic one-dimensional two carrier transport equations coupled with Maxwell's and Poissons's equations. These solutions were used to analyze and to explain the transient behavior of the P^+-N-N^+ structure, in case of extremely high injection levels, for both the reverse and forward directions.

Special effort was directed toward explaining the anomalous voltage that appears across the diode terminals when pulsed in the forward direction with an intense current density of 10^3 amp/cm^2 to 10^6 amp/cm^2. The problem formulations described are of a very general character with none of the conventional assumptions and restrictions introduced. There is freedom in the choice of the doping profile, generation-recombination law, mobility dependencies, and injection level. The boundary conditions are applied at the external ohmic contacts. For a specified arbitrary current excitation, the solution yields the terminal voltage and all the quantities of interest throughout the entire device as functions of position and time.

A comparison between the explicit and the implicit numerical method shows that although the implicit method is complicated and hence is more expensive for each time step Δt, it is more stable numerically and the time step Δt can usually be made very large when the solution approaches steady

state conditions. Since the implicit technique requires a good starting point, the explicit technique is used to obtain a first estimate for the implicit technique. An accurate solution of the thermal equilibrium condition problem is also essential in obtaining a convergent solution of the transient behavior at extreme injection levels.

A numerical method was used to obtain an accurate distribution for the electric field, the hole density, and the electron density at thermal equilibrium. In order to numerically obtain a zero value for both the electron and the hole current densities, different space charge points and field points were used. The thermal equlibrium results show that non-uniform spatial steps are required in the case of large potential variations across the junction.

It was determined that devices with a low doping density and a short N^--region deplete at a relatively fast rate until punch through under reverse-pulsed conditions. The electric field increases uniformly in the N^--region, until the onset of avalanche by impact ionization. On the other hand, a device with high doping density and long N^--region does not fully deplete. In this case, the electric field increases while keeping its triangular shape in the depletion region until it reaches avalanche. In both cases, the steady state condition is satisfied when the rate of generated carriers via avalanche multiplication is balanced by the recombination and depletion rate.

For the forward pulsed case, the use of the standard Shockley-Read-Hall recombination term is adequate in explaining the transient response for relatively low current densities, but it fails to give a physical explanation for extreme current levels, where the device is too far from the eqilibrium condition. This is mainly due to the lack of sufficient recombination dur-

ing the transient behavior. The transient problem can be divided into three stages, the excess diffusion stage near t = 0, the impact ionization stage, and the near steady state stage. In the first stage, the use of the transient lifetimes, which are adjusted in such a way as to limit the increase of majority carriers to that of minority carriers in the two heavily doped regions, is necessary in order to limit the excess diffusion. These transient lifetimes reduce to their equilibrium value as steady state is approached. In the impact ionization stage, the band-to-band Auger recombination is necessary to limit the plasma formation in the avalanched region. The behavior of the near steady state stage necessitates the use of a short equilibrium lifetime which depends on the level of injection to insure that the total current is carried by the majority carriers in the two heavily doped regions.

The results show that the use of transient lifetimes and band-to-band Auger recombination indeed predicts a high terminal voltage across the diode when pulsed with intense current density in the forward direction. A comparison between experiment and theory shows that the computer simulation can be used to explain the anomalously large voltages present in the experimental data.

The effects of this anomalous voltage response that can occur, in the forward and reverse pulsed direction, on second breakdown are as follows:

1. In the forward pulsed case the larger than expected response, at extreme currents at very short pulse times, indicates a larger energy input, hence a shorter time for second breakdown to occur than would be expected. These conditions would only occur for very short intense current pulses in the nanosecond regime and could predict an energy input of 10 to 150 times greater. The net result is to effect (shorten) the time de-

lay before second breakdown occurred.

2. In the reverse pulsed case the diode that breaks down due to punch through has little if any anomalous voltage and therefore would act exactly the same as the normal long current pulse case as far as second breakdown is concerned.

3. The reverse pulsed case with a normal avalanche breakdown will have an excess voltage that exceeds the normal breakdown by up to a factor of 5 to 8. Again this will cause the energy input to exceed the expected value and initiate second breakdown prematurely.

Recommendation for further study:

The computer simulation presented in this report is a very powerful tool. It can be modified to study the transient behavior between thermal equilibrium and steady state or between two steady states, for any one-dimensional, two-terminal semiconductor structure. The simulation can also be modified to analyze the small signal behavior of microwave diodes [10].

This research can be extended by performing more theoretical and experimental comparisons for different diode structures and injection levels in the forward direction. This may lead to relationships describing the dependence of the equilibrium lifetime and the diode parameters, such as the doping density and the length of the N^--region, and on the level of injection, on the transient lifetime and Auger recombination effects.

Also the forward transient behavior can be explained from a physical point of view if one can measure the lifetimes during the transient periods near t = 0.

Due to the limitations of our pulse generator and equipment the full range of the theory could not be tested. Such tests should be conducted.

It would also be of interest to try these simulations and experiments on silicon-on-sapphire devices and make direct comparisons of channeling and second breakdown with the excess energy input.

LIST OF REFERENCES

1. A. De Mari, "An Accurate Numerical One-dimensional Solution of the P-N Junction Under Arbitrary Transient Condition," Solid State Electronics, Pergammon Press 1968, Vol. 11, pp. 1021-1053.

2. D. L. Scharfetter and H. K. Gummel, "Large-Signal Analysis of a Silicon Read Diode Oscillator," IEEE Trans. on Elect. Devices, ED-16, No. 1, January 1969.

3. Charles M. Lee, Ronald J. Lomax, and George I. Haddad, "Semiconductor Device Simulation," IEEE Trans. on Microwave Theory and Techniques, Vol. MTT-22, No. 3, March 1974.

4. Jerry G. Fassum, "Computer-Aided Numerical Analysis of Silicon Solar Cells," Solid-State Electronics, 1976, Vol. 19, pp. 269-277.

5. Richard A. Kiehl, Private communication.

6. S. M. Sze, "Physics of Semiconductor Devices," Wiley, New York, New York, (1969).

7. John L. Moll, "Physics of Semiconductors," McGraw-Hill, Inc., 1964.

8. J. S. Blakemore, "Semiconductor Statistics," Pergammon Press, 1962.

9. Dale U. Von Rosenberg, "Methods for the Numerical Solution of Partial Differential Equations," American Elsevier, New York, 1969.

10. R. R. Razouk, "The Internal Dynamics and Small Signal Analysis of BARITT Diodes," Purdue University, Ph.D. Thesis (1977).

GENERAL REFERENCES

1. H. K. Gummel and D. L. Scharfetter, "Avalanche region of IMPATT diodes," Bell Sys. Tech. J., Vol. 45, pp. 1797-1827, December 1966.

2. C. A. Lee, R. A. Logan, R. L. Batdorf, J. J. Kleimack, and W. Wiegmann, "Ionization rates of holes and electrons in silicon," Phys. Rev., Vol. 137, pp. A761-A773, May 1964.

3. W. Shockley and W. T. Read, Jr., "Statistics of the recombination of hole and electron," Phys. Rev., Vol. 87, pp. 835-842, Sept. 1952.

4. H. K. Gummel, "A self-consistent iterative scheme for one-dimension steady state transistor calculations," IEEE Trans. Electon Devices, Vol. ED-11, pp. 455-465, Oct. 1964.

5. R. W. Hockney, "A fast direct solution of Poisson's equation using Fourier analysis," J. Ass. Comput. Mach., Vol. 12, pp. 95-113, 1965.

6. H. N. Gosh, P. H. de la Moneda, and N. R. Dono, "Computer-aided transistor design characterization and optimization," Solid-State Electron., Vol. 10, pp. 705-726, 1967.

7. D. M. Caughey, "The computer simulation of gigahertz transistors," presented at the IEEE Int. Electron. Conf., Toronto, Ont., Canada, 1967.

8. T. W. Collins, "Two-dimensional numerical analysis of integrated bipolar transistors," presented at the Int. Electron Devices Meeting, Washington, DC, 1968.

9. J. W. Slotboom, "An accurate numerical one-dimensional solution of the p-n junction under arbitrary transient conditions," Solid-State Electron., Vol. 11, pp. 1021-1053, 1968.

10. J. L. Scales and A. L. Ward, "Computer studies of Gunn oscillations in gallium arsenide," Harry Diamond Lab., Rep. TR-1403, Aug. 1968.

11. H. K. Gummel, "Computer device modeling," presented at the European Sem. Develop. Res. Conf., Munich, Germany, 1969.

12. J. W. Slotboom, "Simulation of UHF transistor small signal behavior to 10 GHz for circuit modeling," in Proc. Cornel Conf. Computerized Electron., pp. 369-379, August 1969.

13. D. P. Kennedy and R. R. O'Brien, "Two-dimensional mathematical analysis of a planar type junction field effect transistor," IBM J. Res. Develop., Vol. 13, pp. 662-674, November 1969.

14. V. Arandjelovic, "General iterative scheme for one-dimensional calculations of steady-state electrical properties of transistors," Int. J. Electron., Vol. 27, pp. 459-478, 1969.

15. J. W. Slotboom, "Iterative scheme for 1- and 2-dimensional detransistor simulation," Electron. Lett., Vol. 5, pp. 677-678, December 1969.

16. P. Dubock, "D.c. numerical mode for arbitrarily biased bipolar transistors in two dimensions," Electron. Lett., Vol. 6, pp. 53-55, Feb. 5, 1970.

17. J. W. Slotboom, "Accurate numerical steady-state solutions for a diffused one-dimensional junction diode," Solid-State Electron., Vol. 13, pp. 865-971, 1970.

18. M. Kurata, "Steady-state transistor calculations for higher collector voltages," Proc. IEEE (Lett.), Vol. 58, pp. 485-487, March 1970.

19. B. V. Gokhale, "Numerical solutions for a one-dimensional silicon n-p-n transistor," IEEE Trans. Electron Devices, Vol. ED-17, pp. 594-602, August 1970.

20. V. Arandjelovic, "Accurate numerical steady-state solutions for a diffused one-dimensional junction diode," Solid-State Electron., Vol. 13, pp. 865-871, 1970.

21. P. T. Greiling, "Large-signal characteristics of avalanche-diode oscillators," Ph.D. dissertation, Univ. of Michigan, Ann Arbor, June 1970.

22. D. van Dorpe and N. H. Xuong, "Mathematical 2-dimensional model of semiconductor devices," Electron. Lett., Vol. 7, pp. 47-50, January 1971.

23. J. A. Kilpatrick and W. D. Ryna, "Two-dimensional analysis of lateral-base transistors," Electron. Lett., Vol. 7, pp. 226-227, May 1971.

24. M. Reiser, "Difference methods for the solution of the time-dependent semiconductor flow equations," Electron. Lett., Vol. 7, pp. 353-355, June 1971.

25. S. C. Choo, "Numerical analysis of a forward-biased step-junction P-L-N diode," IEEE Trans. Electron Devices, Vol. ED-18, pp. 574-586, August 1971.

26. D. P. Kennedy and R. R. O'Brien, "Two-dimensional analysis of J.F.E.T. structures containing a low-conductivity substrate," Electron. Lett., Vol. 7, pp. 714-716, December 1971.

27. G. D. Hachtel, R. C. Joy, and J. W. Cooley, "A new efficient one-dimensional analysis program for junction device modeling," Proc. IEEE (Special Issue on Computers in Design), Vol. 60, pp. 86-98, January 1972.

28. J. A. G. Slatter, "Fundamental modeling of cylindrical geometry bipolar transistors," Electron. Lett., Vol. 8, pp. 222-223, May 1972.

29. T. I. Seidman and S. C. Choo, "Iterative scheme for computer simulation of semiconductor devices," Solid-State Electron., Vol. 15, pp. 1229-1235, 1972.

30. D. Van Dorpe, J. Borel, G. Merckel, and P. Saintot, "An accurate two-dimensional numerical analysis of the MOS transistor," Solid-State Electron., Vol. 15, pp. 547-557, 1972.

31. H. H. Heimeier, "A two-dimensional numerical analysis of a silicon N-P-N transistor," IEEE Trans. Electron Devices, Vol. ED-20, pp. 708-714, August 1973.

32. J. W. Slotboom, "Computer-aided two-dimensional analysis of bipolar transistors," IEEE Trans. Electron Devices, Vol. ED-20, pp. 669-679, August 1973.

APPENDIX A

THE FORMULATION FOR THE CONSTRUCTION OF THE MATRIX ELEMENTS IN THE IMPLICIT METHOD

The terms in the matrix elements, of equations (44) to (46) can be calculated as follows:

For E(I) > 0

$$JN(I) = -\,VN(I)\cdot N(J2) - \left|\frac{VN(I)}{E(I)}\right| \cdot \frac{1}{\Delta x}\,[N(J2) - N(J)]$$

$$\frac{\partial JN(1)}{\partial E(I)} = -\,VNE(I)\cdot N(J2) - \frac{\partial\left|\frac{VN(I)}{E(I)}\right|}{\partial E(I)} \cdot \frac{1}{\Delta x}\,[N(J2) - N(J)]$$

$$\frac{\partial JN(I)}{\partial N(J)} = \frac{VN(I)}{E(I)} \cdot \frac{1}{\Delta x}$$

$$\frac{\partial JN(I)}{\partial N(J2)} = -\,VN(I) - \frac{1}{\Delta x} \cdot \left|\frac{VN(I)}{E(I)}\right|$$

$$JP(I) = -\,VP(I)\cdot P(J) + \left|\frac{VP(I)}{E(I)}\right| \cdot \frac{1}{\Delta x}\,[P(J2) - P(J)]$$

$$\frac{\partial JP(I)}{\partial E(I)} = -\,VPE(I)\cdot P(J) + \frac{\partial\left|\frac{VP(I)}{E(I)}\right|}{\partial E(I)}\,\frac{1}{\Delta x}\,[P(J2) - P(J)]$$

$$\frac{\partial JP(I)}{\partial E(I)} = -\,VP(I) - \frac{1}{\Delta x} \cdot \left|\frac{VP(I)}{E(I)}\right|$$

$$\frac{\partial JP(I)}{\partial P(J2)} = \frac{1}{\Delta x} \cdot \left|\frac{VP(I)}{E(I)}\right|$$

For E(I) $\leq$ 0

$$JN(I) = -VN(I) \cdot N(J) - \left|\frac{VN(I)}{E(I)}\right| \cdot \frac{1}{\Delta x}[N(J2) - N(J)]$$

$$\frac{\partial JN(I)}{\partial E(I)} = -VNE(I) \cdot N(J) - \frac{\partial\left|\frac{VN(I)}{E(I)}\right|}{\partial E(I)} \cdot \frac{1}{\Delta x}[N(J2) - N(J)]$$

$$\frac{\partial JN(I)}{\partial N(J)} = -VN(I) + \frac{1}{\Delta x}\left|\frac{VN(I)}{E(I)}\right|$$

$$\frac{\partial JN(I)}{\partial N(J2)} = -\frac{1}{\Delta x}\left|\frac{VN(I)}{E(I)}\right|$$

$$JP(I) = -VP(I) \cdot P(J2) + \left|\frac{VP(I)}{E(I)}\right| \cdot \frac{1}{\Delta x}[P(J2) - P(J)]$$

$$\frac{\partial JP(I)}{\partial E(I)} = -VPE(I) \cdot P(J2) + \frac{\partial\left|\frac{VP(I)}{E(I)}\right|}{\partial E(I)} \cdot \frac{1}{\Delta x}[P(J2) - P(J)]$$

$$\frac{\partial JP(I)}{\partial P(J)} = -\frac{1}{\Delta x}\left|\frac{VP(I)}{E(I)}\right|$$

$$\frac{\partial JP(I)}{\partial P(J2)} = -VP(I) + \frac{1}{\Delta x}\left|\frac{VP(I)}{E(I)}\right|$$

and,

$$G(I) = ALP(I) \cdot |JN(I)| + BET(I) \cdot |JP(I)|$$

$$\frac{\partial G(I)}{\partial E(I)} = ALPE(I) \cdot |JN(I)| + BETE(I) \cdot |JP(I)|$$

$$+ ALP(I) \cdot \frac{\partial JN(I)}{\partial E(I)} \cdot \frac{JN(I)}{|JN(I)|} + BET(I) \cdot \frac{\partial JP(I)}{\partial E(I)} \cdot \frac{JP(I)}{|JP(I)|}$$

$$\frac{\partial G(I)}{\partial N(J)} = ALP(I) \cdot \frac{\partial JN(I)}{\partial N(J)} \cdot \frac{JN(I)}{|JN(I)|}$$

$$\frac{\partial G(I)}{\partial P(J)} = BET(I) \cdot \frac{\partial JP(I)}{\partial P(J)} \cdot \frac{JP(I)}{|JP(I)|}$$

$$\frac{\partial G(I)}{\partial N(J2)} = ALP(I) \cdot \frac{\partial JN(I)}{\partial N(J2)} \cdot \frac{JN(I)}{|JN(I)|}$$

$$\frac{\partial G(I)}{\partial P(J2)} = BET(I) \cdot \frac{\partial JP(I)}{\partial P(J2)} \cdot \frac{JP(I)}{|JP(I)|}$$

$$R(J) = \frac{N(J) \cdot P(J) - 1}{\tau_0[2 + N(J) + P(J)]}$$

$$\frac{\partial R(J)}{\partial N(J)} = \frac{(P(J) + 2)P(J) + 1}{\tau_0[2 + N(J) + P(J)]^2}$$

$$\frac{\partial R(J)}{\partial P(J)} = \frac{(N(J) + 2)N(J) + 1}{\tau_0[2 + N(J) + P(J)]^2}$$

For band-to-band recombination:

$$R_{BB}(J) = B \cdot [P(J) \cdot N(J) - 1]$$

$$\frac{\partial R_{BB}(J)}{\partial P(J)} = B \cdot N(J)$$

$$\frac{\partial R_{BB}(J)}{\partial N(J)} = B \cdot P(J)$$

where,

$$VN(I) = VN[E(I)]$$

$$VNE(I) = \frac{\partial VN(I)}{\partial E(I)}$$

$$VP(I) = VP[E(I)]$$

$$VPE(I) = \frac{\partial VP(I)}{\partial E(I)}$$

$$ALP(I) = \alpha[E(I)]$$

$$ALPE(I) = \frac{\partial ALP(I)}{\partial E(I)}$$

$$BET(I) = \beta[E(I)]$$

$$BETE(I) = \frac{\partial BET(I)}{\partial E(I)}$$

APPENDIX B

THOMAS ALGORITHM FOR TRIDIAGONAL MATRIX [9]

The equations are:

$$a_i u_{i-1} + b_i u_i + c_i u_{i+1} = d_i$$

for $1 \leq i \leq R$
with $a_1 = c_R = 0$

The algorithm is as follows:

First, compute

$$\beta_i = b_i - \frac{a_i c_{i-1}}{\beta_{i-1}} \quad \text{with } \beta_1 = b_1$$

$$\gamma_i = \frac{d_i - a_i \gamma_{i-1}}{\beta_i} \quad \text{with } \gamma_1 = \frac{d_1}{b_1}$$

The values of the dependent variable are then computed from

$$u_R = \gamma_R \quad \text{and} \quad u_i = \gamma_i - \frac{c_i u_{i+1}}{\beta_i}$$

APPENDIX C

ALGORITHM FOR TRI-TRIDIAGONAL MATRIX [9]

The equations are

$$a_i^{(1)}u_{i-1} + a_i^{(2)}v_{i-1} + a_i^{(3)}w_{i-1} + b_i^{(1)}u_i + b_i^{(2)}v_i + b_i^{(3)}w_i$$

$$+ c_i^{(1)}u_{i+1} + c_i^{(2)}v_{i+1} + c_i^{(3)}w_{i+1} = d_i^{(1)}$$

$$a_i^{(4)}u_{i-1} + a_i^{(5)}v_{i-1} + a_i^{(6)}w_{i-1} + b_i^{(4)}u_i + b_i^{(5)}v_i + b_i^{(6)}w_i$$

$$+ c_i^{(4)}u_{i+1} + c_i^{(5)}v_{i+1} + c_i^{(6)}w_{i+1} = d_i^{(2)}$$

$$a_i^{(7)}u_{i-1} + a_i^{(8)}v_{i-1} + a_i^{(9)}w_{i-1} + b_i^{(7)}u_i + b_i^{(8)}v_i + b_i^{(9)}w_i$$

$$+ c_i^{(7)}u_{i+1} + c_i^{(8)}v_{i+1} + c_i^{(9)}w_{i+1} = d_i^{(3)}$$

for $1 \leq i \leq R$

with $a_1^{(m)} = c_R^{(m)} = 0 \quad$ for $1 \leq m \leq 9$

The algorithm is as follows:

First compute

$$\beta_i^{(1)} = b_i^{(1)} - a_i^{(1)}\lambda_{i-1}^{(2)} - a_i^{(2)}\lambda_{i-1}^{(4)} - a_i^{(3)}\lambda_{i-1}^{(7)}$$

$$\beta_i^{(2)} = b_i^{(2)} - a_i^{(1)}\lambda_{i-1}^{(2)} - a_i^{(2)}\lambda_{i-1}^{(5)} - a_i^{(3)}\lambda_{i-1}^{(8)}$$

$$\beta_i^{(3)} = b_i^{(3)} - a_i^{(1)}\lambda_{i-1}^{(3)} - a_i^{(2)}\lambda_{i-1}^{(6)} - a_i^{(3)}\lambda_{i-1}^{(9)}$$

$$\beta_i^{(4)} = b_i^{(4)} - a_i^{(4)}\lambda_{i-1}^{(1)} - a_i^{(5)}\lambda_{i-1}^{(4)} - a_i^{(6)}\lambda_{i-1}^{(7)}$$

$$\beta_i^{(5)} = b_i^{(5)} - a_i^{(4)}\lambda_{i-1}^{(2)} - a_i^{(5)}\lambda_{i-1}^{(5)} - a_i^{(6)}\lambda_{i-1}^{(8)}$$

$$\beta_i^{(6)} = b_i^{(6)} - a_i^{(4)}\lambda_{i-1}^{(3)} - a_i^{(5)}\lambda_{i-1}^{(6)} - a_i^{(6)}\lambda_{i-1}^{(9)}$$

$$\beta_i^{(7)} = b_i^{(7)} - a_i^{(7)}\lambda_{i-1}^{(1)} - a_i^{(8)}\lambda_{i-1}^{(4)} - a_i^{(9)}\lambda_{i-1}^{(7)}$$

$$\beta_i^{(8)} = b_i^{(8)} - a_i^{(7)}\lambda_{i-1}^{(2)} - a_i^{(8)}\lambda_{i-1}^{(5)} - a_i^{(9)}\lambda_{i-1}^{(8)}$$

$$\beta_i^{(9)} = b_i^{(9)} - a_i^{(7)}\lambda_{i-1}^{(3)} - a_i^{(8)}\lambda_{i-1}^{(6)} - a_i^{(9)}\lambda_{i-1}^{(9)}$$

$$\text{with } \beta_1^{(m)} = b_1^{(m)} \quad \text{for } 1 \leq m \leq 9$$

and

$$\delta_i^{(1)} = d_i^{(1)} - a_i^{(1)}\gamma_{i-1}^{(1)} - a_i^{(2)}\gamma_{i-1}^{(2)} - a_i^{(3)}\gamma_{i-1}^{(3)}$$

$$\delta_i^{(2)} = d_i^{(2)} - a_i^{(4)}\gamma_{i-1}^{(1)} - a_i^{(5)}\gamma_{i-1}^{(2)} - a_i^{(6)}\gamma_{i-1}^{(3)}$$

$$\delta_i^{(3)} = d_i^{(3)} - a_i^{(7)}\gamma_{i-1}^{(1)} - a_i^{(8)}\gamma_{i-1}^{(2)} - a_i^{(9)}\gamma_{i-1}^{(3)}$$

$$\text{with } \delta_1^{(m)} = d_1^{(m)} \quad \text{for } 1 \leq m \leq 3$$

The $\beta_i^{(m)}$ are used to compute several more functions and need not be stored after the computation of

$$\theta_i^{(1)} = \beta_i^{(5)}\beta_i^{(9)} - \beta_i^{(6)}\beta_i^{(8)}$$

$$\theta_i^{(2)} = \beta_i^{(6)}\beta_i^{(7)} - \beta_i^{(4)}\beta_i^{(9)}$$

$$\theta_i^{(3)} = \beta_i^{(4)}\beta_i^{(8)} - \beta_i^{(5)}\beta_i^{(7)}$$

$$\theta_i^{(4)} = \beta_i^{(3)}\beta_i^{(8)} - \beta_i^{(2)}\beta_i^{(9)}$$

$$\theta_i^{(5)} = \beta_i^{(1)}\beta_i^{(9)} - \beta_i^{(3)}\beta_i^{(7)}$$

$$\theta_i^{(6)} = \beta_i^{(2)}\beta_i^{(7)} - \beta_i^{(1)}\beta_i^{(8)}$$

$$\theta_i^{(7)} = \beta_i^{(2)}\beta_i^{(6)} - \beta_i^{(3)}\beta_i^{(5)}$$

$$\theta_i^{(8)} = \beta_i^{(3)}\beta_i^{(4)} - \beta_i^{(1)}\beta_i^{(6)}$$

$$\theta_i^{(9)} = \beta_i^{(1)}\beta_i^{(5)} - \beta_i^{(2)}\beta_i^{(4)}$$

$$\mu_i = \theta_i^{(1)}\beta_i^{(1)} + \theta_i^{(2)}\beta_i^{(2)} + \theta_i^{(3)}\beta_i^{(3)}$$

The $\delta_i^{(m)}$, $\theta_i^{(m)}$ and μ_i are used to compute several more functions and need not be stored after the computation of

$$\lambda_i^{(1)} = (\theta_i^{(1)}c_i^{(1)} + \theta_i^{(4)}c_i^{(4)} + \theta_i^{(7)}c_i^{(7)})/\mu_i$$

$$\lambda_i^{(2)} = (\theta_i^{(1)}c_i^{(2)} + \theta_i^{(4)}c_i^{(5)} + \theta_i^{(7)}c_i^{(8)})/\mu_i$$

$$\lambda_i^{(3)} = (\theta_i^{(1)} c_i^{(3)} + \theta_i^{(4)} c_i^{(6)} + \theta_i^{(7)} c_i^{(9)})/\mu_i$$

$$\lambda_i^{(4)} = (\theta_i^{(2)} c_i^{(1)} + \theta_i^{(5)} c_i^{(4)} + \theta_i^{(8)} c_i^{(7)})/\mu_i$$

$$\lambda_i^{(5)} = (\theta_i^{(2)} c_i^{(2)} + \theta_i^{(5)} c_i^{(5)} + \theta_i^{(8)} c_i^{(8)})/\mu_i$$

$$\lambda_i^{(6)} = (\theta_i^{(2)} c_i^{(3)} + \theta_i^{(5)} c_i^{(6)} + \theta_i^{(8)} c_i^{(9)})/\mu_i$$

$$\lambda_i^{(7)} = (\theta_i^{(3)} c_i^{(1)} + \theta_i^{(6)} c_i^{(4)} + \theta_i^{(9)} c_i^{(7)})/\mu_i$$

$$\lambda_i^{(8)} = (\theta_i^{(3)} c_i^{(2)} + \theta_i^{(6)} c_i^{(5)} + \theta_i^{(9)} c_i^{(8)})/\mu_i$$

$$\lambda_i^{(9)} = (\theta_i^{(3)} c_i^{(3)} + \theta_i^{(6)} c_i^{(6)} + \theta_i^{(9)} c_i^{(9)})/\mu_i$$

and

$$\gamma_i^{(1)} = (\theta_i^{(1)} \delta_i^{(1)} + \theta_i^{(4)} \delta_i^{(2)} + \theta_i^{(7)} \delta_i^{(3)})/\mu_i$$

$$\gamma_i^{(2)} = (\theta_i^{(2)} \delta_i^{(1)} + \theta_i^{(5)} \delta_i^{(2)} + \theta_i^{(8)} \delta_i^{(3)})/\mu_i$$

$$\gamma_i^{(3)} = (\theta_i^{(3)} \delta_i^{(1)} + \theta_i^{(6)} \delta_i^{(2)} + \theta_i^{(9)} \delta_i^{(3)})/\mu_i$$

The values of $\lambda_i^{(m)}$ and $\gamma_i^{(m)}$ must be stored, as they are used in the back solution. This is

$$u_R = \gamma_R^{(1)}$$

$$v_R = \gamma_R^{(2)}$$

$$w_R = \gamma_R^{(3)}$$

and

$$u_i = \gamma_i^{(1)} - \lambda_i^{(1)} u_{i+1} - \lambda_i^{(2)} v_{i+1} - \lambda_i^{(3)} w_{i+1}$$

$$v_i = \gamma_i^{(2)} - \lambda_i^{(4)} u_{i+1} - \lambda_i^{(5)} v_{i+1} - \lambda_i^{(6)} w_{i+1}$$

$$w_i = \gamma_i^{(3)} - \lambda_i^{(7)} u_{i+1} - \lambda_i^{(8)} v_{i+1} - \lambda_i^{(9)} w_{i+1}$$

for $(R - 1) \geq i \geq 1$